

Evaporative cooling has proven to be an invaluable technique in atomic physics, allowing for the study of effects such as Bose-Einstein condensation. One main topic of this thesis is the first application of evaporative cooling to cold non-neutral plasmas stored in an ion trap. We (the ALPHA collaboration) have achieved cooling of a cloud of antiprotons to a temperature as low as 9 K, two orders of magnitude lower than ever directly measured previously. The measurements are well-described by appropriate rate equations for the temperature and number of particles.

The technique has direct application to the ongoing attempts to produce trapped samples of antihydrogen. In these experiments the maximum trap depths are extremely shallow ( $\sim 0.6$  K for ground state atoms), and careful control of the trapped antiprotons and positrons used to form the (anti)atoms is essential to success. Since 2006 powerful tools to diagnose and manipulate the antiproton and positron plasmas in the ALPHA apparatus have been developed and used in attempts to trap antihydrogen. These efforts are the second main topic of this thesis.

**Front cover illustration:** Photo showing the gold-plated mixing electrode stack complete with flexible strip line connections. Now installed in the ALPHA apparatus, the mixing electrodes sit at the heart of the device. The intricate design ensures a maximum depth of the magnetostatic atom trap without compromising confinement of charged particles during antihydrogen formation.

# Evaporative cooling of antiprotons and efforts to trap antihydrogen

GORM BRUUN ANDRESEN  
PhD Thesis



FACULTY OF SCIENCE  
AARHUS UNIVERSITY

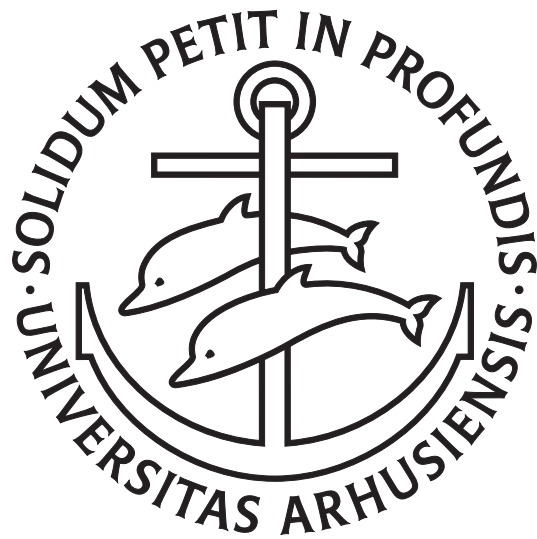


ALPHA  $\alpha$

---

# Evaporative cooling of antiprotons and efforts to trap antihydrogen

---



GORM BRUUN ANDRESEN  
PHD THESIS

The ALPHA collaboration  
Department of Physics and Astronomy  
Aarhus University, Denmark

October 2010  
2nd Edition

Gorm Bruun Andresen  
2nd Edition, October 2010  
1st Edition, August 2010  
Department of Physics and Astronomy  
Aarhus University  
Ny Munkegade, Bld. 1520  
DK-8000 Aarhus C

This document was typeset in L<sup>A</sup>T<sub>E</sub>X.

Front cover illustration: Photo showing the gold-plated mixing electrode stack complete with flexible strip line connections. Now installed in the ALPHA apparatus, the mixing electrodes sit at the heart of the device. The intricate design ensures a maximum depth of the magnetostatic atom trap without compromising confinement of charged particles during antihydrogen formation.

This thesis is submitted to the Faculty of Science at Aarhus University in order to fulfill the requirements of obtaining a PhD degree in physics. The scientific work has been carried out in the ALPHA collaboration under the supervision of Jeffrey S. Hangst, Department of Physics and Astronomy. All the experimental work took place at the Antiproton Decelerator located at CERN, Switzerland.



# Table of Contents

Table of Contents	v
Acknowledgments	ix
List of publications	xi
Outline	xiv
Personal contribution	xvii
List of Figures	xix
List of Tables	xxiii
<b>1 Introduction and background</b>	<b>1</b>
1.1 Some motivations for antimatter research . . . . .	4
1.1.1 The discovery of antimatter . . . . .	5
1.1.2 Antimatter research and <i>CPT</i> -symmetry . . . . .	7
1.1.3 Antimatter gravity . . . . .	8
1.2 Antihydrogen physics . . . . .	9
1.2.1 Antihydrogen formation techniques . . . . .	10
1.2.2 Antihydrogen recombination rates . . . . .	11
1.2.3 Can Antihydrogen be Trapped? . . . . .	11
1.3 Charge particle confinement . . . . .	13
1.3.1 Magnetostatic trap depth . . . . .	14
1.4 Ballistic loss of charged particles . . . . .	15
<b>2 Experimental setup</b>	<b>19</b>
2.0.1 The catching, mixing, and positron transfer region . . . . .	21
2.1 ALPHA control structure . . . . .	22
2.2 The ALPHA magnets . . . . .	22

2.2.1	The main solenoid magnet . . . . .	22
2.2.2	The inner magnet system . . . . .	27
2.3	Electrode design . . . . .	29
2.3.1	Electrode driving circuit . . . . .	31
2.3.2	Thin walled electrodes . . . . .	31
2.3.3	Segmented electrodes . . . . .	32
2.4	Positrons and electrons . . . . .	33
2.4.1	Positrons . . . . .	34
2.4.2	Electrons . . . . .	35
2.5	Plasma diagnostics . . . . .	35
2.5.1	Faraday cup . . . . .	36
2.5.2	Micro channel plate (MCP) . . . . .	36
2.6	Antiproton annihilation detection . . . . .	40
2.6.1	Si detector . . . . .	41
2.6.2	External scintillators . . . . .	43
<b>3</b>	<b>Experimental techniques</b>	<b>45</b>
3.1	Rotating wall compression of antiprotons, electrons and positrons	45
3.1.1	The Rotating wall technique . . . . .	47
3.1.2	Sympathetic compression of antiprotons . . . . .	48
3.2	Temperature diagnostic . . . . .	49
3.2.1	Experimental procedure . . . . .	52
3.2.2	Adiabatic correction . . . . .	54
3.2.3	Space charge correction . . . . .	56
3.2.4	Example: Space charge dominated positron plasma . . .	58
3.2.5	Example: Antiproton dump . . . . .	61
<b>4</b>	<b>Forced evaporative cooling of ions</b>	<b>65</b>
4.1	Comparing evaporation of ions and atoms . . . . .	66
4.2	The dynamics of evaporation . . . . .	68
4.2.1	Dimension of evaporation . . . . .	69
4.2.2	Ion evaporation from a Penning-Malmberg trap . . . . .	69
4.3	The evaporation time scale $\tau_{ev}$ . . . . .	71
4.3.1	Example: The evaporation time scale for atoms (3D) . . .	71
4.3.2	Example: The evaporation time scale for ions (3D) . . . .	72

4.3.3	Example: The evaporation time scale for ions (1D) . . . . .	73
4.4	The collision time constant $\tau_{col}$ . . . . .	75
4.4.1	The Coulomb logarithm $\ln \Lambda$ . . . . .	77
4.5	Evaporation from a plasma . . . . .	77
4.5.1	Evaporation from the radial center . . . . .	79
4.5.2	Radial heat and particle transfer . . . . .	82
4.5.3	Radial expansion of the plasma and Joule heating . . . . .	88
4.6	Conclusion . . . . .	89
<b>5</b>	<b>Forced evaporative cooling: Experimental results</b>	<b>91</b>
5.1	Main results . . . . .	92
5.1.1	Experimental procedure . . . . .	92
5.1.2	Temperature and remaining number . . . . .	94
5.1.3	Radial antiproton distribution . . . . .	97
5.2	The plasma density, self potential, and expansion driven heating	99
5.2.1	Antiproton peak density and collision rate . . . . .	101
5.2.2	Space charge . . . . .	104
5.2.3	Self-potential energy per particle . . . . .	105
5.3	Conclusion . . . . .	106
<b>6</b>	<b>Forced evaporative cooling: Modeling</b>	<b>109</b>
6.1	Model description . . . . .	110
6.1.1	Modeling the evaporation time scale . . . . .	111
6.1.2	Expansion driven (re)heating . . . . .	111
6.1.3	Applying the model . . . . .	114
6.1.4	The effect of radial aperture and heating . . . . .	117
6.2	Increasing the initial number . . . . .	119
6.3	Numerical optimization of the evaporation voltage ramp . . . . .	121
6.4	The effect of radial compression . . . . .	124
6.5	Conclusion . . . . .	125
<b>7</b>	<b>Antihydrogen formation and detection in ALPHA</b>	<b>127</b>
7.1	Signatures of antihydrogen formation . . . . .	128
7.1.1	Spatial detection of antihydrogen annihilations . . . . .	128
7.1.2	Field ionization of antihydrogen . . . . .	131

7.1.3	Mixing with heated positrons . . . . .	132
7.2	Production of antihydrogen in a 1 T magnetic field (2006) . . . . .	133
7.3	Antihydrogen formation in a multipole field (2008) . . . . .	137
7.3.1	Summary of the experiment . . . . .	138
7.3.2	The antihydrogen annihilation pattern in multipole. . . . .	141
7.3.3	Field-ionized antihydrogen . . . . .	144
7.4	Antihydrogen formation in low electric fields (2009) . . . . .	146
7.4.1	Autoresonant manipulation of the antiproton axial energy	147
7.4.2	Autoresonant injection of antiprotons . . . . .	151
7.4.3	Antihydrogen formation in reduced electric fields . . . . .	152
7.5	Conclusion . . . . .	154
<b>8</b>	<b>Search for trapped antihydrogen</b>	<b>155</b>
8.1	Experimental procedure . . . . .	155
8.2	Annihilation identification and cosmic ray rejection . . . . .	160
8.3	Mirror trapping of antiprotons . . . . .	164
8.4	Release signatures of antihydrogen and antiprotons . . . . .	167
8.5	Theoretical estimates . . . . .	170
8.6	Summary and discussion . . . . .	172
<b>9</b>	<b>Outlook</b>	<b>175</b>
<b>A</b>	<b>Modeling evaporative cooling - MatLab code</b>	<b>179</b>
A.1	The collision time constant $\tau_{col}$ . . . . .	179
A.2	Numerical calculation of forced evaporative cooling . . . . .	181
	<b>Bibliography</b>	<b>185</b>

# Acknowledgments

Working in the ALPHA collaboration has been a great experience, and I want to thank my supervisor Jeffrey Hangst for letting me on board. I have enjoyed learning from and with many excellent supervisors and students. As always meetings have been tiring, but the open discussions where the word of a student often carries as much weight as that of a senior scientist have made them worthwhile regardless. I would like to thank all current and previous members of ALPHA. In particular I want to thank: Paul Bowe, Joel Fajans, Francis Robicheaux, Niels Madsen, and Makoto Fujiwara for sharing your experience with me. I would also like to thank: Eoin Butler, Andrew Humphries, Will Bertsche, Daniel Silveira, Steve Chapman, Alex Povilus, Richard Hydromako, James Story, Sara Seif El Nasr, Tim Friesen, Dean Wilding, Crystal Bray, Chukman So, and Matt Jenkins. You have all been great colleagues and some of you have become good friends as well. We have spend countless hours, day and night, working shifts or building and fixing the apparatus. It's amazing we didn't rip each other apart.

A special thanks to the administrative staff at the Department of Physics and Astronomy in Aarhus for helping me sort out my life in two countries. In particular I would like to thank Kate Andersen and Brigitte Henderson for helping me with paper work and travel plans, but most of all for always being kind and smiling.

Thanks to all the family and friends who came to visit us in Geneva. You helped us enjoy the beautiful city and the spectacular surrounding mountains and nature.

I would like to thank my wife Karen and my two-year-old son Karl. Karen I am grateful that you have supported me in following my dream, traveled with me back and forth from Aarhus to Geneva, and endured the demands of an insatiable physics experiment and seemingly endless beam time. Karl you have simply been wonderful. I love you both.

Finally I acknowledge the ALPHA apparatus. During the endless hours I

have spend in your presence you have caused me physical pain, grief, anger,  
and despair too. But in the end you let me have data.

*Gorm Bruun Andresen,  
Aarhus, August 2010.*

# List of publications

The publications [a-i] listed below represents work carried out in the ALPHA collaboration. The work is the result of a collaborative effort, and following the policy of the ALPHA collaboration the author list is alphabetic.

[ a ] **“Search for Trapped Antihydrogen: First Candidate Events.”**

G. B. Andresen, M. D. Ashkezari, M. Baquero-Ruiz, W. Bertsche, P. D. Bowe, C. C. Bray, E. Butler, C. L. Cesar, S. Chapman, M. Charlton, J. Fajans, T. Friesen, M. C. Fujiwara, D. R. Gill, J. S. Hangst, W. N. Hardy, R. S. Hayano, M. E. Hayden, A. Humphries, R. Hydomako, S. Jonsell, L. Kurchaninov, R. Lambo, N. Madsen, S. Menary, P. Nolan, K. Olchanski, A. Olin, A. Povilus, P. Pusa, F. Robicheaux, E. Sarid, D. M. Silveira, C. So, C. H. Storry, R. I. Thompson, D. P. van der Werf, D. Wilding, J. S. Wurtele, and Y. Yamazaki.

*Manuscript in preperation*, (2010)

[ b ] **“Evaporative Cooling of Antiprotons to Cryogenic Temperatures.”**

G. B. Andresen, M. D. Ashkezari, M. Baquero-Ruiz, W. Bertsche, P. D. Bowe, E. Butler, C. L. Cesar, S. Chapman, M. Charlton, J. Fajans, T. Friesen, M. C. Fujiwara, D. R. Gill, J. S. Hangst, W. N. Hardy, R. S. Hayano, M. E. Hayden, A. Humphries, R. Hydomako, S. Jonsell, L. Kurchaninov, R. Lambo, N. Madsen, S. Menary, P. Nolan, K. Olchanski, and A. Olin.

*Phys. Rev. Lett.*, **105**, 013003 (July 2010).

[ c ] **“Antihydrogen formation dynamics in a multipolar neutral anti-atom trap.”**

G. Andresen, W. Bertsche, P. Bowe, C. Bray, E. Butler, C. Cesar, S. Chapman, M. Charlton, J. Fajans, M. Fujiwara, D. Gill, J. Hangst, W. Hardy, R. Hayano, M. Hayden, A. Humphries, R. Hydomako, L. Jørgensen, S. Kerigan, L. Kurchaninov, R. Lambo, N. Madsen, P. Nolan, K. Olchanski, A. Olin, A. Povilus, P. Pusa, F. Robicheaux, E. Sarid, S. S. E. Nasr, D. Sil-

veira, J. Storey, R. Thompson, D. van der Werf, J. Wurtele, and Y. Yamazaki.

*Phys. Lett. B*, **685**, 141 (March 2010).

[ d ] **“Antiproton, positron, and electron imaging with a microchannel plate/phosphor detector.”**

G. B. Andresen, W. Bertsche, P. D. Bowe, C. C. Bray, E. Butler, C. L. Cesar, S. Chapman, M. Charlton, J. Fajans, M. C. Fujiwara, D. R. Gill, J. S. Hangst, W. N. Hardy, R. S. Hayano, M. E. Hayden, A. J. Humphries, R. Hydomako, L. V. Jørgensen, S. J. Kerrigan, L. Kurchaninov, R. Lambo, N. Madsen, P. Nolan, K. Olchanski, A. Olin, A. P. Povilus, P. Pusa, E. Sarid, S. S. E. Nasr, D. M. Silveira, J. W. Storey, R. I. Thompson, D. P. van der Werf, and Y. Yamazaki.

*Rev. Sci. Inst.*, **80**, 123701 (December 2009).

[ e ] **“Magnetic multipole induced zero-rotation frequency bounce-resonant loss in a Penning–Malmberg trap used for antihydrogen trapping.”**

G. B. Andresen, W. Bertsche, C. C. Bray, E. Butler, C. L. Cesar, S. Chapman, M. Charlton, J. Fajans, M. C. Fujiwara, D. R. Gill, W. N. Hardy, R. S. Hayano, M. E. Hayden, A. J. Humphries, R. Hydomako, L. V. Jørgensen, S. J. Kerrigan, J. Keller, L. Kurchaninov, R. Lambo, N. Madsen, P. Nolan, K. Olchanski, A. Olin, A. Povilus, P. Pusa, F. Robicheaux, E. Sarid, S. S. E. Nasr, D. M. Silveira, J. W. Storey, R. I. Thompson, D. P. van der Werf, J. S. Wurtele, and Y. Yamazaki.

*Phys. Plasmas*, **16**, 100702 (October 2009).

[ f ] **“Compression of Antiproton Clouds for Antihydrogen Trapping.”**

G. B. Andresen, W. Bertsche, P. D. Bowe, C. C. Bray, E. Butler, C. L. Cesar, S. Chapman, M. Charlton, J. Fajans, M. C. Fujiwara, R. Funakoshi, D. R. Gill, J. S. Hangst, W. N. Hardy, R. S. Hayano, M. E. Hayden, R. Hydomako, M. J. Jenkins, L. V. Jørgensen, L. Kurchaninov, R. Lambo, N. Madsen, P. Nolan, K. Olchanski, A. Olin, A. Povilus, and P. Pusa.

*Phys. Rev. Lett.*, **100**, 203401 (May 2008).

[g] **“A novel antiproton radial diagnostic based on octupole induced ballistic loss.”**

G. B. Andresen, W. Bertsche, P. D. Bowe, C. C. Bray, E. Butler, C. L. Cesar, S. Chapman, M. Charlton, J. Fajans, M. C. Fujiwara, R. Funakoshi, D. R. Gill, J. S. Hangst, W. N. Hardy, R. S. Hayano, M. E. Hayden, A. J. Humphries, R. Hydomako, M. J. Jenkins, L. V. Jørgensen, L. Kurchaninov, R. Lambo, N. Madsen, P. Nolan, K. Olchanski, A. Olin, R. D. Page, A. Povilus, P. Pusa, F. Robicheaux, E. Sarid, S. S. E. Nasr, D. M. Silveira, J. W. Storey, R. I. Thompson, D. P. van der Werf, J. S. Wurtele, and Y. Yamazaki.

*Phys. Plasmas*, **15**, 032107 (March 2008).

[h] **“Production of antihydrogen at reduced magnetic field for anti-atom trapping.”**

G. B. Andresen, W. Bertsche, A. Boston, P. D. Bowe, C. L. Cesar, S. Chapman, M. Charlton, M. Chartier, A. Deutsch, J. Fajans, M. C. Fujiwara, R. Funakoshi, D. R. Gill, K. Gomberoff, J. S. Hangst, R. S. Hayano, R. Hydomako, M. J. Jenkins, L. V. Jørgensen, L. Kurchaninov, N. Madsen, P. Nolan, K. Olchanski, A. Olin, R. D. Page, A. Povilus, F. Robicheaux, E. Sarid, D. M. Silveira, J. W. Storey, R. I. Thompson, D. P. van der Werf, J. S. Wurtele, and Y. Yamazaki.

*J. Phys. B: At. Mol. Opt. Phys.*, **41**, 011001 (January 2008).

[i] **“Antimatter Plasmas in a Multipole Trap for Antihydrogen.”**

G. Andresen, W. Bertsche, A. Boston, P. D. Bowe, C. L. Cesar, S. Chapman, M. Charlton, M. Chartier, A. Deutsch, J. Fajans, M. C. Fujiwara, R. Funakoshi, D. R. Gill, K. Gomberoff, J. S. Hangst, R. S. Hayano, R. Hydomako, M. J. Jenkins, L. V. Jørgensen, L. Kurchaninov, N. Madsen, P. Nolan, K. Olchanski, A. Olin, A. Povilus, F. Robicheaux, and E. Sarid.

*Phys. Rev. Lett.*, **98**, 023402 (Jan 2007).



# Outline

Currently, the primary goal of the ALPHA collaboration is to trap antihydrogen and the only experiments carried out for their own sake are attempts to trap antihydrogen. The main purpose of any other experiment is to assist in achieving this goal, and once achieved, trapping of antihydrogen atoms will play a similar role in coming spectroscopy measurements.

During the four years I have been working in the ALPHA collaboration, many of the techniques and diagnostic tools we have developed are interesting in their own right. A good example of such a technique is the evaporative cooling of antiprotons, which shows that the technique used with great success to cool atoms can be applied to cool charged particles as well. The theoretical background for and the results of these experiments form a substantial part of this thesis and is the focus of chapter 4 to 6.

I have decided not to divide the thesis in two parts, though, as the title suggests both evaporative cooling of antiprotons and efforts to trap antihydrogen, are discussed. The evaporative cooling technique has been developed with the purpose of achieving cold antiprotons which can be used in antihydrogen trapping attempts, and I found it natural that the two should be viewed in the same context. Obviously, this does not make the evaporative cooling technique any less useful or interesting in a more general setting, and I hope the reader will enjoy the peculiar dynamics of evaporation of trapped charged particles as much as I have.

**Chapter 1:** First an introduction of the two main topics of this thesis followed by a short introduction to antimatter and the motivation of the long term goals in antihydrogen research. At the end of the chapter a short introduction to current and previous antihydrogen trapping experiments.

**Chapter 2:** A technical description of the ALPHA apparatus.

**Chapter 3:** Some of the experimental techniques and analysis tools used in the evaporative cooling experiments and in the most recent antihydrogen trapping attempts are described in some detail. These are: radial compression of antiprotons, and temperature diagnostic of trapped antiprotons and positrons.

**Chapter 4:** The first of three chapters describing evaporative cooling of antiprotons. This chapter is used to introduce and analyze evaporation of trapped charged particles. In particular particles trapped in Penning-Malmberg traps.

**Chapter 5:** Here the experimental results of evaporative cooling of antiprotons in the ALPHA apparatus are discussed and analyzed.

**Chapter 6:** Based on the theory of chapter 4 and the experimental results of chapter 5, a numerical model is used to analyze the evaporative cooling experiments. In addition some scenarios for improving the performance of the technique are investigated.

**Chapter 7:** The development of antihydrogen formation techniques in the ALPHA collaboration is discussed.

**Chapter 8:** A series of antihydrogen trapping attempts carried out in the ALPHA apparatus are described. These experiments resulted in the observation of six candidate events, which could originate from trapped antihydrogen atoms.

**Chapter 9:** A short discussion of future prospects of the antihydrogen trapping experiments, and on how evaporative cooling can be used in antihydrogen trapping experiments.

# Personal contribution

My contribution to the work presented in this thesis is diverse, and I am glad to find it difficult to disentangle my personal contribution from that of my colleagues. The reason is the enormity of the task of trapping antihydrogen. I believe no single person would be able to achieve such a goal alone, and I have found that we have made the greatest progress when one person could take over the work of another seamlessly. Below, I have tried to make a general description of my participation in the work carried out in the ALPHA collaboration, from I joined in August 2006 until now. In addition I have made a more detailed description of my contribution to the two main topics of this thesis.

I have been heavily involved in the construction, maintenance, and retrofitting of the ALPHA apparatus. This work has mainly involved: Cabling of environmental sensors, maintaining the super conductor connections to the ALPHA magnets, and cabling of the electrode stack inside the vacuum chamber. Construction of the electrode stack and support structure in particular construction of the delicate mixing electrode stack (Front cover illustration). Assembly of the vacuum and cryogenic systems. Realignment of the main solenoid magnet. In situ repairs during beam time.

Discussion of physics results and experimental direction has been a continual process where all collaboration members participate. I have been an active part of this process, both at the discussion stage and in implementing new experimental sequences.

During operation I took part in the development and design of experiments and in the necessary monitoring and running of the cryogenic system. My primary task during the experimental run has been to develop the experimental sequences and perform online analysis of data. In several cases I have collected and performed preliminary analysis of data published ALPHA papers. Part of the time in 2008 and 2009 I was given the responsibility of "run coordinator" and was (jointly) responsible for the day to day operation and

experimental direction of the work done during those shifts. I also helped tutor new students in the operation of the apparatus.

## **Efforts to trap antihydrogen**

During my time as a student in ALPHA, one of the primary tasks of myself and a few colleagues has been to manage and develop the antihydrogen formation experiment carried out in the ALPHA apparatus. Often this work has involved incorporating ideas and techniques developed by other members of the collaboration into the sequence of the experiment and to perform preliminary analysis and presentation of the results of these experiments. This work has required me to gain knowledge of all parts of the experiment and, as James so nicely put it, become, "Jack of all Trades and the Ace of none". Thus I found it natural to write about the overall development of the antihydrogen formation experiments, and about some of the key techniques where I have participated directly in the development process.

## **Evaporative cooling of antiprotons**

In January 2009 my supervisor Jeffrey Hangst asked me to start investigating evaporative cooling of antiprotons. Part of the motivation for this investigation was the high antiproton densities and collision rates we had observed the year before, and part was a similar attempt at evaporative cooling of ions trapped in an EBIT (Kinugawa *et al.*, 2001).

During the first half of the year I developed a numerical model of evaporative cooling of antiprotons in a Penning-Malmberg trap to investigate potential problems and estimate the potential of the method. Joel Fajans and Francis Robicheaux helped me in this investigation.

When it was decided to use beam time to attempt the experiment, I led the experimental effort and analysis, with great help from the people on shift. The detailed analysis following the experiments was carried out in close collaboration with Eoin Butler, Joel Fajans, and Francis Robicheaux, and in particular Jeffrey Hangst gave invaluable support during the following write-up of the paper (Andresen *et al.*, 2010c).

# List of Figures

1.1	A. Einstein and P.A.M. Dirac. . . . .	6
1.2	The first observation of antimatter. . . . .	6
1.3	Magnetic field strength vs radius for an ideal quadrupole and an ideal octupole. . . . .	13
1.4	Magnetic field from the octupole and solenoid coils. . . . .	16
1.5	Field lines imaged by passing a circular $e^-$ plasma through the octupole with the octupole off and on. . . . .	16
1.6	$z\phi$ -distribution of the annihilation of bare antiprotons. . . . .	17
2.1	Schematic of the ALPHA apparatus and the attached positron accumulator. . . . .	20
2.2	Block diagram showing the ALPHA control, apparatus monitoring, and data acquisition chain. . . . .	23
2.3	ALPHA magnet placement and on-axis field. . . . .	24
2.4	Cut-away technical drawing of the inner parts of the ALPHA apparatus. . . . .	25
2.5	Main solenoid magnet field map. . . . .	26
2.7	Schematic diagram of the ALPHA electrode stack. . . . .	30
2.8	Technical drawing of the thin electrodes of the mixing region. . . . .	32
2.9	Segmented electrode used for the rotating wall technique. . . . .	33
2.10	Imaging of particle using the combined MCP phosphor screen. . . . .	37
2.11	MCP gain for electrons, positrons, and antiprotons. . . . .	38
2.12	Examples of reconstructed detector events. . . . .	42
3.1	Antiproton and electron images showing the effects of radial compression, and the resulting radial profiles. . . . .	46
3.2	Graphical illustration of conservation of the single particle bounce invariant. . . . .	53
3.3	Graphical illustration of the change in space charge as particles are released. . . . .	56

3.4	Positron dump to determine the temperature. . . . .	58
3.5	Graphical illustration of the on-axis potentials used during a positron dump to determine the temperature. . . . .	60
3.6	Antiproton dump to determine the temperature. . . . .	61
3.7	Estimated correction to the antiproton temperature. . . . .	64
4.1	Truncated Maxwell-Boltzmann energy distribution. . . . .	70
4.2	The collision frequency for magnetized and unmagnetized plasmas. . . . .	75
4.3	Plasma length scales vs temperature. . . . .	77
4.4	Radial plasma density profiles used to illustrate evaporation from the radial center. . . . .	80
4.5	Radial heat and antiproton diffusion across a plasma. . . . .	83
4.6	The time scale of evaporation divided by the plasma diffusion time scales. . . . .	87
5.1	Simplified schematic showing the devices essential to the evaporative cooling experiments, and examples of on-axis potentials used during evaporative cooling of antiprotons. . . . .	93
5.2	Antiproton energy distributions and temperatures before and after evaporative cooling. . . . .	95
5.3	Antiproton temperature and remaining number after evaporative cooling. . . . .	96
5.4	Line-integrated antiproton density profiles before and after evaporative cooling . . . . .	99
5.5	Antiproton cloud radius during evaporative cooling. . . . .	100
5.6	Antiproton density and collision rate during evaporative cooling. . . . .	102
5.7	Antiproton space charge during evaporative cooling. . . . .	105
5.8	Inter-particle potential energy during evaporative cooling. . . . .	106
6.1	The evaporation time scale vs. applied on-axis well depth for five experiments with different ramp times. . . . .	115
6.2	Antiproton temperature and remaining number after evaporative cooling for five experiments with different ramp times. . . . .	116
6.3	The effect of radial aperture and expansion driven heating on forced evaporative cooling. . . . .	118

6.4	The effect of increasing the initial number on forced evaporative cooling. . . . .	120
6.5	Numerically optimized voltage ramp for forced evaporative cooling. . . . .	121
6.6	Fraction remaining and evaporation time scale for the numerically optimized evaporation ramp. . . . .	122
6.7	Temperature vs remaining fraction for the standard ramp and the numerically optimized ramp. . . . .	123
6.8	The effect of a smaller initial radius on forced evaporative cooling.	125
7.1	First detection of cold antihydrogen by the ATHENA collaboration using spatial detection of the antihydrogen annihilation. . . . .	129
7.2	Detection of cold antihydrogen by the ATRAP collaboration using field-ionization. . . . .	131
7.3	Nested potential used during the 2007 experimental run, and antiproton energy distributions after mixing with positrons. . . . .	134
7.4	Scintillation events as a function of time after the start of mixing, for mixing with cold positrons and mixing with heated positrons. Data from the 2006 run. . . . .	135
7.5	The electric and magnetic fields used to create antihydrogen in magnetostatic trap. Antihydrogen is detected using ionizing potentials. . . . .	139
7.6	Projections of the antiproton annihilation vertex distributions during mixing with and without the magnetostatic trap energized. . . . .	142
7.7	Number of intentionally field-ionized antihydrogen atoms detected following ejection, and annihilation events as a function of the depth of the neutral atom trap for ground state antihydrogen. . . . .	144
7.8	Nested on-axis potential used in the 2009 trapping attempts. . . . .	146
7.9	Autoresonant manipulation of the antiproton energy distribution.	148
7.10	Collisional redistribution of energy between the degrees of freedom parallel to and perpendicular to the magnetic field. . . . .	149
7.11	Comparison between the two (vacuum) potential configurations used in the 2008 and the 2009 trapping attempts. . . . .	153

8.1	Simplified schematic, cut-away diagram of the antihydrogen mixing and trapping region of the ALPHA apparatus. . . . .	156
8.2	Illustration of the cuts used to identify antiproton annihilations.	161
8.3	Comparisons of the distributions of the vertex radius and squared residual for events in the trapping experiment and events from the calibration samples that pass the cuts. . . . .	162
8.4	Clearing potentials used to remove mirror trapped antiprotons from the magnetostatic trap. . . . .	165
8.5	Simulated annihilation time and z-distribution of mirror-trapped antiprotons and antihydrogen atoms released from the magnetostatic trap. The simulated distributions are compared to the measured six antihydrogen candidate events. . . . .	167
9.1	Fraction of antiprotons with a total kinetic energy below $0.5 K \times k_B$ .	176

# List of Tables

5.1	Antiproton temperature and remaining number after evaporative cooling. . . . .	98
5.2	Initial antiproton cloud conditions for the three data series: <i>Main</i> , <i>Hot</i> , and <i>Cold</i> . . . . .	101
5.3	Estimates of antiproton density, space charge and cloud dimensions after evaporative cooling. . . . .	103



# Introduction and background

---

Antihydrogen is the bound state of an antiproton and a positron, and represents the simplest pure antimatter atomic system. During recent years, the potential of spectroscopic measurements to probe matter-antimatter equivalence and *CPT*-symmetry has driven a focused experimental effort to study cold antihydrogen atoms. The first cold antihydrogen atoms were produced in 2002 by the ATHENA collaboration (Amoretti *et al.*, 2002) at the Antiproton Decelerator (AD) at CERN, and shortly thereafter by the ATRAP collaboration (Gabrielse *et al.*, 2002a). In these and later experiments, the neutral antihydrogen produced was not confined by the Penning-Malmberg traps used to hold the charged constituent antiprotons and positrons as non-neutral plasmas. Instead, the antihydrogen atoms either escaped to strike the matter making up the apparatus and annihilate, or were ionized by the electric fields present within the trap volume. Before precision spectroscopy and other measurements can be carried out, it is highly desirable to first produce a long-lived sample of antihydrogen in an atomic trap.

All research described in this thesis has been carried out in the ALPHA collaboration, the immediate goal of which is to produce and confine antihydrogen atoms inside an atomic trap in order to pursue the long-term goal of performing spectroscopy on antihydrogen. The experiment combines an antihydrogen production Penning-Malmberg trap with a neutral atom trap Bertsche *et al.* (2006). The strategy behind this device is to mix cold plasmas of antiprotons and positrons near the minimum of magnetic field strength in the combined trap, so that antihydrogen atoms can be "born" trapped. However, only if their kinetic energy does not exceed the effective neutral trap depth, is this possible.

Producing antihydrogen in the combined trap was foreseen to be a challenge (see section 1.3). In this thesis part of the development of the antihydrogen production technique used in the ALPHA experiment to overcome the challenge is described (see chapter 7). In addition, the first systematic attempts to produce and detect trapped antihydrogen, in an experiment with a sensitivity where single annihilations can be detected upon the shut-down of the atom trap, are described (see chapter 8). I have made a significant personal contribution to these experiments, but it is important to me, to point out that the experimental results described in these and other chapters represents the work of the entire collaboration.

Antihydrogen formation is a complicated process and the experiments are rich in details, many of which will not be described in this thesis. In places where the reader is interested in a more details, I hope that these two review articles will help to answer the questions (Holzscheiter *et al.*, 2004; Gabrielse, 2005).

As part of the development of the antihydrogen formation and trapping experiments special techniques are often invented or implemented to solve specific problems. Some of these are discussed in chapter 3.

During the 2009 experimental run at the AD we applied forced evaporative cooling to antiprotons confined in our apparatus and achieved antiproton temperatures as low as 9 K, 2 orders of magnitude lower than any previously reported (Gabrielse *et al.*, 1989). Before, the technique has only found limited applications for trapped ions (at temperatures  $\sim 100$  eV (Kinugawa *et al.*, 2001)) and has never been realized in cold plasmas. The results of the cooling experiments and a discussion of evaporative cooling of trapped charged particles form a central part of this thesis (see chapter 4 to 6). Historically, forced evaporative cooling has been successfully applied to trapped samples of neutral particles (Hess, 1986), and remains the only route to achieve Bose-Einstein condensation in such systems (Anderson *et al.*, 1995).

Evaporative cooling of antiprotons was developed to assist the formation of antihydrogen at temperatures low enough to be confined in our magneto-static trap, and certainly the low temperature range it makes available opens new possibilities for production of cold antihydrogen.

Antihydrogen production techniques can be characterized, from the an-

---

tiproton's standpoint, as either dynamic, when antiprotons are injected into a positron plasma (Amoretti *et al.*, 2002; Gabrielse *et al.*, 2002a) or static, for example, when positronium atoms are introduced into a static antiproton cloud (Charlton, 1990; Storry *et al.*, 2004). In both cases the dominant contribution to the antihydrogen kinetic energy will be that of the antiproton; thus, a low antiproton temperature will obviously increase the number of trappable atoms in the static case. For ground state antihydrogen atoms our neutral atom trap depth is  $0.5 \text{ K} \times k_B$ , where  $k_B$  is Boltzmann's constant. Despite reducing the total antiproton number, the evaporative cooling manipulations described in this thesis increase the absolute number of antiprotons below this depth by about 2 orders of magnitude.

Many of the dynamic techniques rely on the antiprotons to be cooled through collisions with the positrons before antihydrogen is formed, as they, for practical reasons, are injected with a kinetic energy much larger than their thermal energy. In such cases antihydrogen can form before the antiprotons and positrons have equilibrated, resulting in high energy, untrappable atoms (Gabrielse *et al.*, 2004; Madsen *et al.*, 2005). The much colder samples of antiprotons obtained from evaporative cooling can be more precisely controlled and introduced to the positrons with smaller excess energy, resulting in more trappable antihydrogen atoms.

The antihydrogen formation techniques discussed in this thesis all fall in the dynamic category. More specifically, only variations of antihydrogen production techniques which make use of the so-called *nested potential configuration* are described in any detail. Antihydrogen formation in the nested potential configuration is described briefly in section 1.2.1 below and development of the technique in the ALPHA apparatus is the topic of chapter 7.

The reader is assumed to have some familiarity with the basic geometry and dynamics of ion and atom traps. In particular the Penning-Malmberg trap is used to confine charge particles in the ALPHA apparatus. The geometry of this trap is cylindrical symmetrical, and a solenoidal magnetic field is used to confine particles radially. Axial confinement is achieved by electrostatic fields generated by an array of hollow cylindrical electrodes. The basic motion of particles trapped in a Penning-Malmberg trap are: magnetron rotation around the trap axis, cyclotron rotation around magnetic field lines, and

an axial bounce motion. To confine antihydrogen atoms a magnetostatic trap is superimposed on the Penning-Malmberg trap. A minimum of the magnetic field magnitude confines the atoms. The radial component of the trap is generated by an octupole magnet and two short solenoidal coils complete the trap axially. The confinement of atoms in such a trap is discussed in more detail in section 1.2.3 below. A more detailed account of ion and atom traps can be found in (Foot, 2005). An introduction to plasma physics can be found in (Chen, 1974) and a detailed description of non-neutral plasmas in (Davidson, 2001).

While writing I came across an article by Gabrielse (1992) published in *Scientific American*. The article contains a colorful description of the first attempts at trapping antiprotons at CERN. I was 10 years old when this article was written and even younger when the experiments were done. Amazingly to me, I could still recognize the description of the hectic hours before beam time and the die-hard spirit of the scientists from my own experiences almost 20 years later.

## 1.1 Some motivations for antimatter research

The study of cold antihydrogen provides an excellent opportunity to study the fundamental nature of the universe and the laws of physics. Often, such studies are performed in large scale, high energy particle accelerators, and some of the long term physics goals of ALPHA are similar to those of the neighbor experiments at CERN's new Large hadron collider (LHC).

More specifically, the long term goal of the ALPHA collaboration is to use precision spectroscopy to compare the energy spectrum of trapped antihydrogen to that of hydrogen. Such a comparison would constitute a high precision test of fundamental physics and could help guide the way to a deeper understanding of nature. Cold trapped antihydrogen could also be used to study (anti)gravity.

In a universe comprised entirely of matter, antimatter has spectacular properties. In particular the annihilation of antimatter with ordinary matter cause the release of high energy particles which are easily detected. Spatial location of electron-positron annihilations are commonly used in medical facilities to

image cerebral activity, cancer, or other biological phenomena using Positron emission tomography (PET). By spatial imaging of antiproton annihilations, the loss of single particles from a non-neutral plasma can be detected and analyzed to help understanding the dynamics of trapped charged particles (Fujiwara *et al.*, 2004). Other experiments have been able to probe the helium nucleus using cold helium atoms with one electron replaced by an antiproton (Hori *et al.*, 2005). These are only some of the current applications where the unique nature of the matter-antimatter interaction assist in the research of ordinary matter. No doubt a source of cold trapped antihydrogen atoms would allow new types of exciting single atom experiments.

In the following sections the discovery of antimatter and the fundamental physics currently motivating the research in antihydrogen physics are discussed briefly.

### 1.1.1 The discovery of antimatter

*The question remains as to why Nature should have chosen this particular model for the electron instead of being satisfied with the point-charge.*  
(Dirac, 1928).

In early 1928 Paul Dirac combined the new theory of quantum mechanics with Einstein's theory of relativity in an effort to explain the electron spin. This led to a wave equation with exactly two spin-eigenstate solutions of positive energy for the electron — in agreement with observations. However, the same wave equation gave rise to an additional two eigenstates of negative energy and, in principle, allowed transitions to these states (Dirac, 1928). At first the negative energy states were ignored, but only a few years later Dirac, enticed by Robert Oppenheimer, recognized that the negative energy states, if they were ever observed, would manifest themselves as anti-electrons. Particles identical to electrons except for the sign of their charge, and in the case of a collision between an electron and anti-electron the two would annihilate leaving no matter (Dirac, 1931). Shortly afterwards the anti-electron was discovered from cloud chamber images of cosmic rays by Carl D. Anderson, who also coined the term positron (Anderson, 1932, 1933).

The positron was the first experimental evidence of antimatter, but since its discovery in 1932 we have learned that all particles have an antimatter

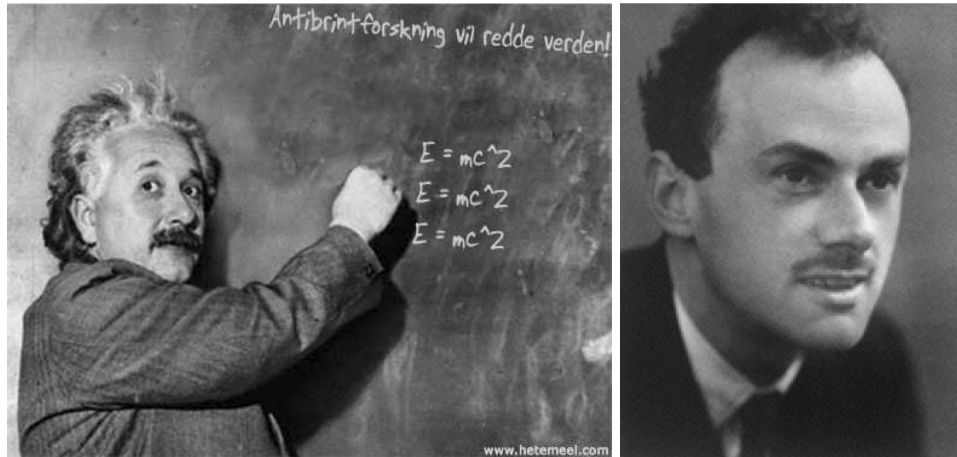


**Figure 1.1:** Left: Albert Einstein (March 14th 1879 - April 18th 1955) Right: Paul Adrien Maurice Dirac (August 8th 1902 - 20. October 20th 1984).

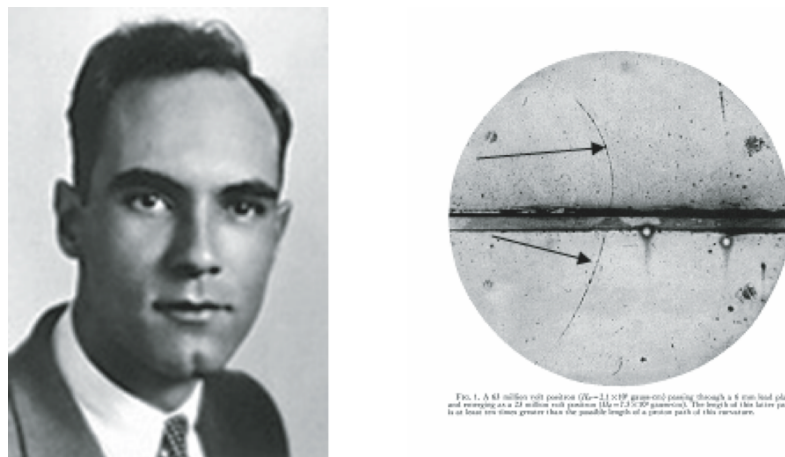


**Figure 1.2:** Left: Carl David Anderson (September 3rd 1905 - January 11th 1991). Right: Photograph of the first observation of a positron. The image was acquired during a cloud chamber study of cosmic rays. The particle track (indicated by arrows and coming from below) was interpreted as a 63 MeV positron passing through a 6 mm lead plate and emerging as a 23 MeV positron (Anderson, 1933).

partner. From being a problematic curiosity which could perhaps be removed when the theory was developed further, antimatter now forms a cornerstone in our understanding of fundamental physics.

Antimatter particles are thought to be perfect mirror images of matter particles. They are created in a reaction where energy is converted to mass, and the corresponding matter particle is always created in the same reaction. The creation of antimatter obeys conservation of energy, momentum, and charge as well as quantities such as lepton number and flavor. To create an antiparticle of mass  $M$ , an energy of at least  $2Mc^2$  must be available. In an annihilation a similar energy is released. As an example the annihilation of an electron with a positron typically results in the emission of two 511 keV photons,  $511 \text{ keV}/c^2$  being the electron mass.

### 1.1.2 Antimatter research and *CPT*-symmetry

The *CPT*-theorem is one of the most basic assertions of modern physics, and it is one of the most fundamental properties of quantum field theories in flat space time, of which the so-called *Standard Model* is the most widely known. The theorem can be derived from the basic requirements of locality, Lorentz invariance and unitarity, and predicts that the reality described by the theory is invariant under the simultaneous application of the three transformations: charge conjugation  $C$  (changing a particle into its antiparticle), parity  $P$ , and time reversal  $T$ . A principal consequence of *CPT*-invariance is the prediction that particles and their antiparticles have equal masses, lifetimes, and an electric charge and magnetic moment of equal magnitude and opposite sign. It also follows that the energy spectrum, i.e., fine structure, hyperfine structure, and Lamb shifts of matter and antimatter bound systems should be identical.

Any attempt to observe a difference between a matter system and its corresponding antimatter system constitutes a test of the *CPT*-theorem and of its underlying assumptions. Already such tests have been carried out with impressive accuracy, e.g., with a precision of  $10^{-12}$  for the difference between the moduli of the magnetic moment of the positron and the electron,  $10^{-11}$  for the difference between the the proton and antiproton charge to mass ratio, and an impressive  $10^{-19}$  for the mass difference between the neutral kaon and antikaon. An up-to-date record of *CPT*-invariance tests can be found in

(Amsler *et al.*, 2008).

At present no violation of *CPT*-invariance has been observed, however, despite the great success of quantum field theory in general and the Standard Model in particular, it is a well known fact that the theory does not offer a complete description of fundamental interactions. Most obviously there is no known way of adapting quantum field theory to include the physics of general relativity, such as gravitation. Another remarkable problem not yet understood, is why and how all of the observed present-day universe is comprised entirely of matter, when, seemingly, matter can only be created if an exactly equal amount of antimatter is created simultaneously.

Antihydrogen atoms, i.e., the bound system of an antiproton and a positron, offers a unique opportunity of a direct comparison between matter and antimatter. Its counterpart, the hydrogen atom, is one of the best known physics systems, and spectroscopy on hydrogen has reached an astounding precision (Hänsch, 2006). If the same experimental methods as developed for hydrogen spectroscopy can be applied to antihydrogen, high-precision comparison of the two systems may be achieved (Cesar *et al.*, 2009).

### 1.1.3 Antimatter gravity

The *weak equivalence principle* (WEP) of Einstein's General theory of relativity requires that the gravitational acceleration of a falling body is independent of its composition. The principle has been tested by philosophers and physicist for centuries, and modern experiments have shown the gravitational acceleration of a variety of composite objects of ordinary matter to be equal with a precision of  $10^{-13}$  (Schlamminger *et al.*, 2008). It is generally thought that antimatter falls exactly like ordinary matter in a gravitational field (Nieto and Goldman, 1991), although the idea that antimatter would fall up instead of down easily comes to mind. So far no experimental test have been carried out to compare the gravitational acceleration of an antimatter object to that of matter, mostly due to the difficulties in shielding of the electromagnetic forces on antimatter particles such as the antiproton.

Antihydrogen, which is a stable, neutral antimatter object, would allow direct experimental tests of the gravitational interaction with the gravitational field of the earth. Such measurements could be free-fall experiments, where

the influence of gravity is observed directly. Alternatively an interferometric method could be used to determine the displacement of a horizontal beam of antihydrogen (Phillips, 1997); or perhaps an (anti)atomic fountain can be created and a technique first used on sodium atoms to determine the gravitational acceleration (Kasevich and Chu, 1992) can be used. None of these measurements would be easy and all require antihydrogen at extremely low energies.

## 1.2 Antihydrogen physics

The study of antihydrogen is a new field in physics starting with the first observation of antihydrogen atoms in 1995 at the LEAR facility at CERN, where 11 such atoms were detected in a beam experiment (Baur *et al.*, 1996). These first atoms were ill-suited for further study mainly because they were created in-flight with about 2 GeV of kinetic energy. To produce antihydrogen at lower energies it was proposed to combine antiprotons confined in a Penning-Malmberg trap with a positron plasma (Gabrielse *et al.*, 1986, 1988).

Some years later, in late 2002, the ATHENA collaboration, working at the Antiproton Decelerator (AD) at CERN (Maury, 1997), reported the production of approximately 50000 cold antihydrogen atoms (Amoretti *et al.*, 2002). The antiatoms were created by merging trapped clouds of about 10000 antiprotons with a low temperature positron plasma in a Penning-Malmberg trap operated at 3 T. Later the same year the ATRAP collaboration, also working at the AD, reported a similar result, this time in a stronger 5.4 T magnetic field (Gabrielse *et al.*, 2002a).

These antihydrogen production experiments paved the way for the current generation antihydrogen experiments, where the aim is to produce and trap antihydrogen in a combined charged particle and atom trap. The ALPHA experiment is one such experiment and another similar experiment is run by the ATRAP collaboration. Recently also the ASACUSA collaboration has begun antihydrogen experiments at the AD.

In the following sections, it will be briefly describe how antihydrogen may be formed from trapped antiprotons and positrons, how antihydrogen can be trapped, and some of the problems of a combined charged particle and

magnetostatic atom trap.

### 1.2.1 Antihydrogen formation techniques

Antihydrogen is formed when an antiproton is combined with a positron. The simplest process is spontaneous radiative recombination, where the two particles combine directly, and the excess energy is removed by a photon:



However, the rate of this process is low under the experimental conditions realized so far. In principle, the rate can be enhanced by laser stimulation to a particular quantum state, but experiments to do so have been inconclusive (Amoretti *et al.*, 2006).

A much higher formation rate can be realized in a three-body process where the excess energy is carried away by a second positron:



This reaction is the one most commonly used to form antihydrogen from trapped particles. In these experiments antiprotons are merged with a dense, low temperature positron plasma in a Penning-Malmberg trap. To realize simultaneous confinement and spatial overlap of negatively charged antiprotons and positive positrons in the electrostatic trap, a so-called *nested potential configuration* is used. In this configuration positrons are confined in a central potential well, and antiprotons are confined at a non-zero axial energy in a longer potential well with the positron well at its center (Gabrielse *et al.*, 1988). A figure illustrating the nested potential can be found in chapter 7 (see Figure 7.1).

An alternative reaction, which has also been used to form antihydrogen, is a charge exchange process where a positronium atom, i.e. the bound system of an electron and a positron, collides with an antiproton (Storry *et al.*, 2004):



Other reactions could also be used to form antihydrogen, but are beyond the scope of this thesis. In fact, only formation of antihydrogen in the nested

potential configuration is discussed in later chapters, though positronium assisted antihydrogen formation would be an obvious use of cold antiprotons as achieved by evaporative cooling. A more detailed account of different antihydrogen formation reactions and techniques can be found in (Holzscheiter *et al.*, 2004; Gabrielse, 2005).

### 1.2.2 Antihydrogen recombination rates

At low temperatures the antiproton-positron recombination rate is dominated by the rate for three body recombination (Holzscheiter *et al.*, 2004), which, in the simplest case where a single antiproton is in equilibrium in a positron plasma, is given as:

$$[2 \times 10^{-27} \text{ cm}^6/\text{s}]n_{e^+} \left( \frac{1\text{eV}}{k_B T_{e^+}} \right)^{-9/2}, \quad (1.4)$$

where  $n_{e^+}$  and  $T_{e^+}$  are the positron plasma density and temperature (Mansbach and Keck, 1969). This result is often quoted in the literature, but it has been pointed out that in the case where the formation happens in a strong magnetic field, the rate goes down by a factor of about ten because the motion of the positron is now tied to magnetic field lines (Glinsky and O'Neil, 1991).

In the experiments done so far, the antiproton is not at rest in the positron plasma, and it is in fact moving in and out of the plasma. This limits the interaction time between the antiproton and the positron plasma, and since the formation of a stable antihydrogen atom is typically a multi-step process it greatly affects the rate. Simulations of this process suggest that the recombination rate is much less dependent on  $T_{e^+}$  and that the length and radius of the positron plasma both have a significant influence (Robicheaux, 2004). Experimentally, some work has been done to determine the temperature dependence of the antihydrogen formation rate. Most recently by Fujiwara *et al.* (2008).

### 1.2.3 Can Antihydrogen be Trapped?

Antihydrogen can, in principle, like many other atoms be trapped through the interaction of the atom's magnetic dipole moment with an inhomogeneous magnetic field. If the atom moves adiabatically, the magnetic moment of the

atom,  $\mu$ , will be parallel or antiparallel to the field, and the interaction energy will then only depend on the magnitude  $B$  of the magnetic field and can be written as:

$$U = -\boldsymbol{\mu} \cdot \mathbf{B} = -\mu B, \quad (1.5)$$

The magnetic moment of the atom is determined by its internal quantum state. In the case of an atom in a magnetic field that is weak compared to the internal fields in the atom the weak field Zeeman coupling gives (Bransden, 2003, chapter 6.2):

$$\mu = g_j m_j \mu_B, \quad (1.6)$$

where  $\mu_B$  is the Bohr magneton,  $m_j$  the magnetic quantum number arising from  $LS$ -coupling and  $g_j$  is the appropriate Landé  $g$ -factor, which is a function of the  $l$ ,  $s$  and  $j$  quantum numbers. The sign of  $m_j$  determines the sign of the interaction energy of the atom with the magnetic field. Atoms with positive  $m_j$  are called *high field seekers* since they are attracted to high field regions, and atoms with negative  $m_j$  are called *low field seekers* because they are attracted to low field regions.

It is impossible to create a local maximum of the magnetic field in free space, but a minimum can be produced. Thus only low field seeking atoms can be trapped. For (anti)hydrogen atom in the ground state the electron spin dominates the magnetic moment of the atom so  $\mu = \mp \mu_b$ . Plugging this into equation (1.5), we see that for a low field seeker the potential trapping depth per Tesla is:

$$\frac{\mu_B}{k_B} = 0.67 \text{ K T}^{-1}, \quad (1.7)$$

Note that it is customary to quote the trap depth in Kelvin and not in energy units.

The prototypical field configuration, developed for trapping hydrogen atoms, is the Ioffe-Pritchard geometry (Pritchard, 1983), where a quadrupole winding and two longitudinal mirror coils produce a minimum in the magnetic field strength at the trap center, so that low field seeking quantum states can be confined. The depth of such a trap is simply given by:

$$\Delta U = \mu \Delta B, \quad (1.8)$$

where  $\Delta B$  is the difference between the maximum and minimum magnetic field strength in the device. (Foot, 2005, chapter 10).

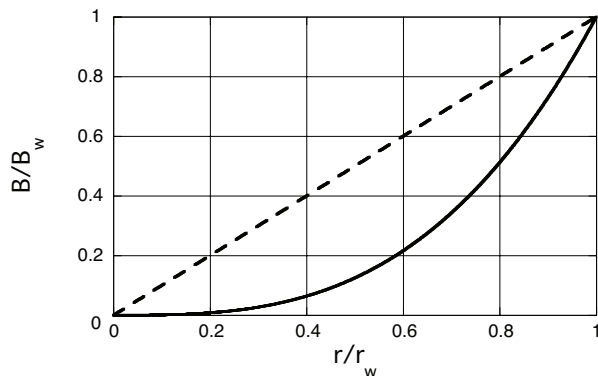


**Figure 1.3:** Magnetic field strength vs radius for an ideal quadrupole (dashed line) and an ideal octupole (solid line).  $B_w$  is the field at the inner electrode wall (radius  $r_w$ ) of the Penning-Malmberg trap. (Adapted from Andresen *et al.*, 2007)

### 1.3 Charge particle confinement in a combined Penning-Malmberg and magnetostatic trap

The ALPHA apparatus features a novel, superconducting magnetostatic atom trap comprising a transverse octupole and longitudinal mirror coils (Bertsche *et al.*, 2006). The octupole was chosen to minimize perturbations of the trapped antiproton and positron plasmas due to the azimuthally asymmetric magnetic fields of a magnetic multipole. As illustrated in Figure 1.3, for equivalent well depths, an octupole has a significantly lower field near the trap axis, where the charged particle plasmas are initially stored.

Plasmas trapped in Penning-Malmberg traps depend on the azimuthal symmetry of the solenoidal field for their stability (O’Neil, 1980), and the presence of a magnetostatic trap breaks this symmetry. For this reason compatibility of a combined device with the requirements of storing and merging non-neutral plasmas to produce antihydrogen while the magnetostatic trap is energized, has previously been the subject of some debate (Squires *et al.*, 2001; Fajans and Schmidt, 2004).

Previous experiments (Fajans *et al.*, 2005) indicates that quadrupole fields, as used for trapping hydrogen (Pritchard, 1983; Cesar *et al.*, 1996), can be problematic. Fajans *et al.* (2005) found that the quadrupole field lead to rapid loss of the charged particles. As a conclusion a high-order multipole is suggested

to replace a quadrupole magnet in the design of the magnetostatic trap, due to its smaller perturbation of the solenoidal magnetic field close to the trap axis. Other latter measurements show similar behavior for quadrupolar magnetic fields, but present a more positive view on their viability in antihydrogen formation and trapping experiments (Gabrielse *et al.*, 2007).

### 1.3.1 Magnetostatic trap depth

Regardless of the choice of multipole, the solenoidal field of the Penning-Malmberg trap defines the "bottom" of the potential well for neutral atoms. The "top" of the trap is determined by the field strength at the inner radius of the Penning-Malmberg trap electrodes (radially) and at the  $z$ -position of the peaks of the mirror coil field (axially). Typically, the maximum depth of the trap is set by the depth of the radial minimum. In this case the relevant  $\Delta B$  is:

$$\Delta B = \sqrt{B_s^2 + B_w^2} - B_s, \quad (1.9)$$

where  $B_s$  is the solenoid field strength, and  $B_w$  is the transverse field strength of the multipole at the inner wall of the Penning-Malmberg trap. Thus there is a conflict between the need for a high solenoidal field to confine charged particles and a low solenoidal field to maximize the well depth for neutrals. In ALPHA,  $B_s = 1$  T and during normal operation  $B_w$  can be as high as 1.55 T (see section 2.2.2). This gives a trap depth of about 0.6 K for ground state antihydrogen (see section 1.2.3).

An important consequence of using a high-order multipole is the rapid change in magnetic field strength close to the magnet windings. For a fixed magnet configuration this means that to maximize  $\Delta B$ , it is imperative to minimize the thickness of the material between the magnet windings and the electrode wall seen by the (trapped) atoms. For a quadrupole magnet the linear decrease in field strength makes this less of a problem (see Figure 1.3). In the ALPHA apparatus the octupole magnet is wound directly on the vacuum chamber and the electrodes are designed to be extremely thin (see chapter 2).

## 1.4 Ballistic loss of charged particles

A very direct and powerful loss mechanism in the combined trap is ballistic transport of particles directly into the electrode wall. So-called *ballistic loss* was described first by Fajans *et al.* (2005). It is a single particle phenomenon, and it is a direct consequence of adding a magnetic multipole field to a solenoidal field. In this case the magnetic field lines will bend away from straight lines and field lines previously parallel to the trap axis can now intersect the cylindrical electrodes. A charged particle following a field line can therefore hit the electrode wall and be lost from the trap.

Figure 1.4 shows a visualization of the magnetic field lines generated by adding an octupole to a solenoid field. The field lines, originating from a circular locus of points in the plane transverse to the solenoid axis of symmetry, form four-fluted cylindrical surfaces with the flutes at each end rotated by  $45^\circ$  with respect to each other.

In Figure 1.5, images of one quadrant of two identically prepared electron plasmas are shown. They were both passed through the region covered by the ALPHA octupole, but in one case the octupole was off and in the other it was on. In the case where octupole was on, a flute as described above is clearly visible. The images are taken with the combined MCP and phosphor screen setup (see section 2.5.2).

When charged particles are confined axially in an electrostatic well of length  $L$ , any particle which moves beyond a certain critical radius  $r_{crit}$  at the axial center of its motion, will be ballistically transported to the wall. More specifically the critical radius can be written as:

$$\frac{r_c}{R_w} = \frac{1}{\sqrt{1 + \frac{B_w}{B_s} \frac{L}{R_w}}}, \quad (1.10)$$

where  $R_w$  is the wall radius and  $B_w$  and  $B_s$  are defined above (see Andresen *et al.*, 2008b, and the references therein). Particles lost in this way strike the electrode wall at distinct points at equally spaced angles. In particular particles in an octupolar magnetic field will strike the wall where the flutes, shown on Figure 1.4 intersect the wall. Figure 1.6 shows an example of antiprotons lost ballistically in the ALPHA trap.

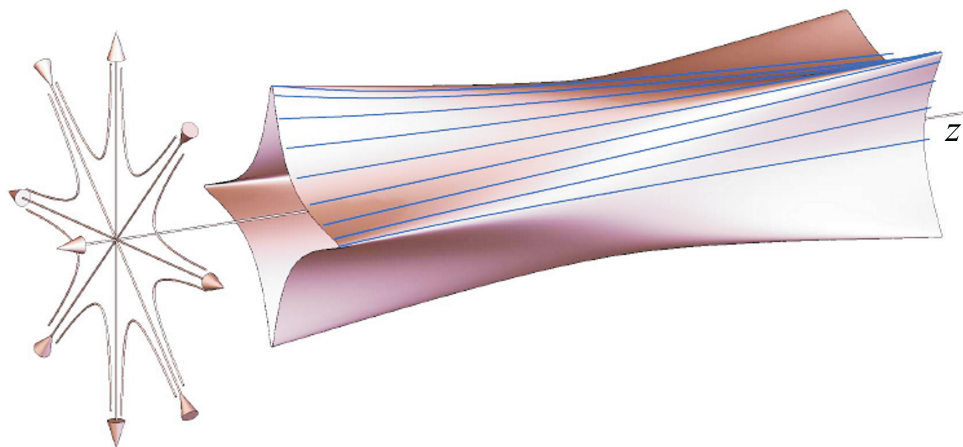


**Figure 1.4:** Magnetic field from the octupole and solenoid coils. The vectors on the left represent the directions of the axially invariant field from these coils. The surface is created by following the field lines from a radially centered circular locus; the lines shown within the surface are field lines. (Adapted from Andresen *et al.*, 2008b)

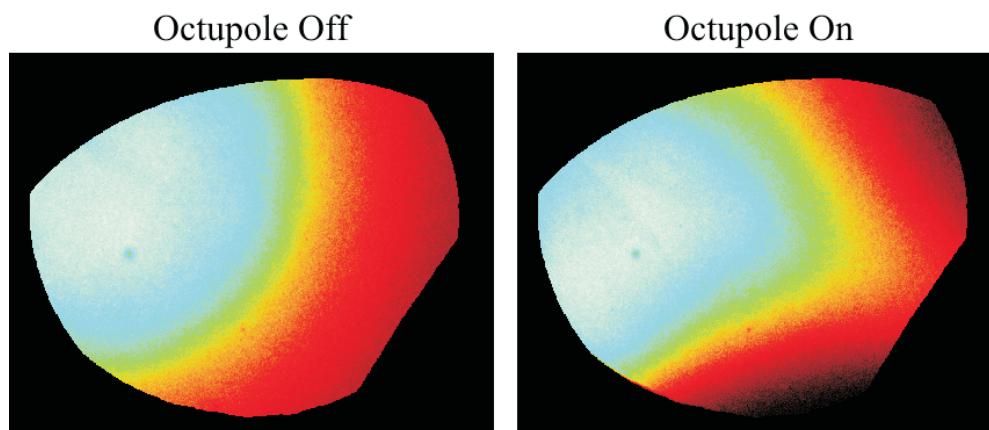


**Figure 1.5:** Field lines imaged by passing a circular  $e^-$  plasma through the octupole with the octupole off and on. Apertures form the image boundaries and limit us to viewing only one quadrant of the octupole field map. The distortion evident in the right-hand image corresponds to one of the flutes at the end of the magnetic surface shown in figure 1.4. (Adapted from Andresen *et al.*, 2008b)

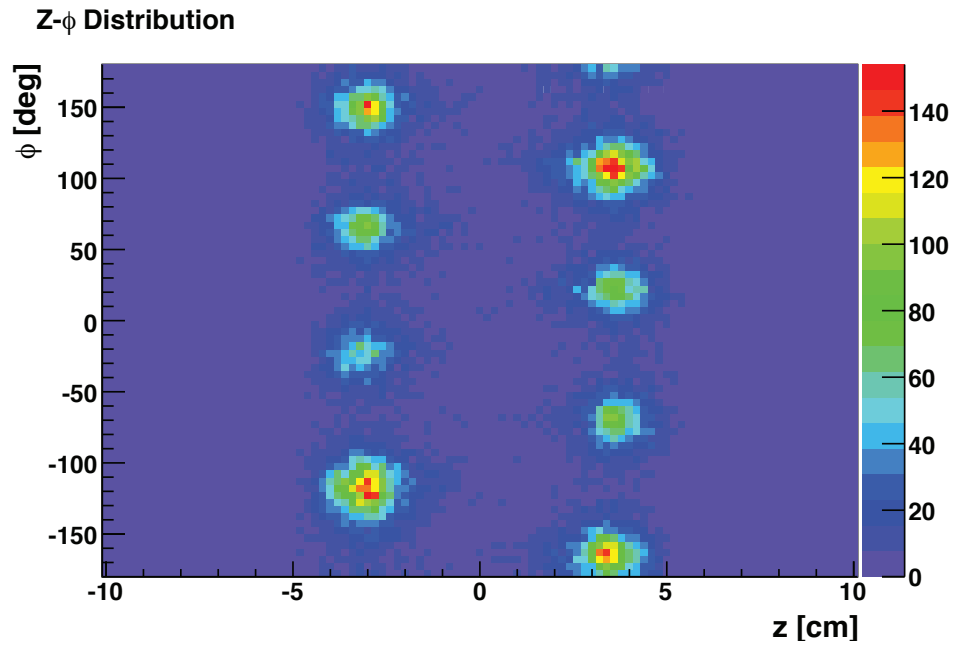


**Figure 1.6:**  $z\phi$ -distribution of the annihilation of bare antiprotons annihilating on the electrode wall while the magnetostatic trap is energized. As described in the text, annihilations occur at a discrete set of points at a particular set of angles.

In the case of a quadrupole,  $r_c$  decreases exponentially with  $L$  making the ballistic loss much more pronounced (Fajans *et al.*, 2008).



# Experimental setup

---

The ALPHA apparatus is a complicated physics device designed to trap antihydrogen atoms created from cold, trapped antiprotons and positrons. The basic idea behind the apparatus is to employ a Penning-Malmberg trap to confine and merge antiprotons and positrons inside a superimposed magnetostatic trap for neutral atoms. Thus any antihydrogen formed in the process will remain confined provided the kinetic energy of the atom is lower than the depth of the magnetostatic trap. Both the ATHENA collaboration and the ATRAP collaboration have synthesized antihydrogen in pure Penning-Malmberg traps (Amoretti *et al.*, 2002; Gabrielse *et al.*, 2002a). An account of the commissioning and basic operation of the ALPHA apparatus was written by Jenkins (2008).

An immediate technical complication of the design comes from the scarcity of both antiprotons and positrons. Antiprotons of sufficiently low energy are only available at the Antiproton decelerator (AD) at CERN (Maury, 1997), and only by placing the apparatus inside the AD can they be acquired. As any accelerator environment the AD requires high power magnet and RF-systems which generates undesirable electronic noise.

To capture the antiprotons delivered from the AD a special trap must be included in the apparatus. The design used in ALPHA is the most typical, and involves intercepting the incoming antiprotons with a metal foil to reduce their energy enough so that some can be captured between two high voltage electrodes located in a strong solenoidal magnetic field (Gabrielse *et al.*, 1986). Positrons are available from radioactive sources, and can be accumulated in a special apparatus (see section 2.4).

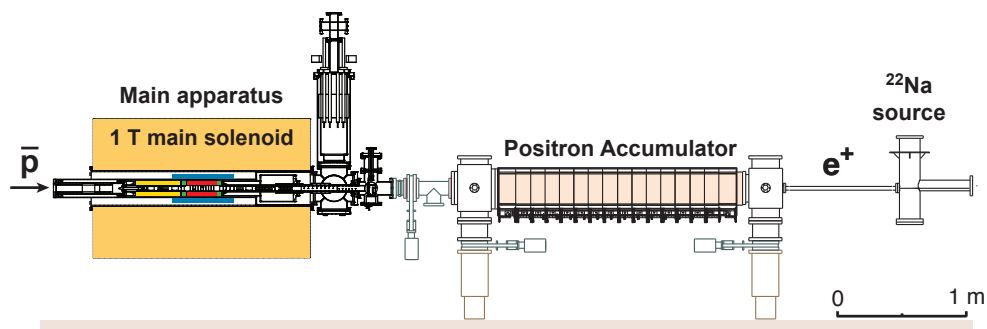


**Figure 2.1:** Schematic diagram showing the ALPHA *main apparatus* and the positron accumulator. The main apparatus is shown in more detail in Figure 2.3 and the inner cryostat (drawn in black), located inside the bore of the main solenoid magnet is shown in Figure 2.4. The inner cryostat contains the ALPHA magnetostatic trap and the electrode stack. The central part of the inner cryostat is surrounded by the ALPHA silicon detector.

In addition to antiprotons and positrons, a source of electrons is installed in the apparatus. The electrons are mixed with the antiprotons and used to cool the antiprotons to low temperatures through collisions. Electrons are the only available matter particle which can coexist with antiprotons, and because of their low mass the electrons have a short cyclotron cooling time and can radiate away the heat absorbed from the antiprotons. As an added benefit electrons can potentially be combined with positrons to form positronium and create antihydrogen through charge exchange with antiprotons.

Figure 2.1 shows the ALPHA *main apparatus* and the positron accumulator. Antiprotons enter the main apparatus from the left (upstream) and electrons and positrons from the right (downstream). Having particles entering the apparatus from both ends complicates thermal and electrical shielding of the central part, where antihydrogen is synthesized.

To be able to detect the annihilation of even low numbers of trapped antihydrogen atoms an advanced silicon detector is built into the apparatus (see section 2.6.1). In order to achieve the best performance of the detector the amount of scattering material between the point of annihilation and the detector must be minimized. Combined with the demand for a deep magnetostatic

---

trap this poses severe space and material constraints on all central parts of the apparatus.

To release and detect trapped atoms on a timescale short enough to avoid significant contamination of the signal from cosmic rays, the magnetostatic trap is designed to be shut down extremely fast. This requires the magnet driving circuit to be able to handle the energy released during the process to avoid permanent damage to the superconductors.

Possibly the largest single barrier to creating trapped antihydrogen comes from achieving antiproton and positron plasmas at cryogenic temperatures and in merging the two without adding energy to the system. Knowing and controlling the plasma characteristics such as density, radius, and temperature is of great importance, and appropriate diagnostic devices are included in the ALPHA apparatus (see section 2.5) as well as special electrodes used to compress the plasmas radially (see section 2.3.3).

Techniques such as the temperature measurement described in section 3.2 and the evaporative cooling described in chapters 4-6 requires a high level of control over the voltages applied to the confining electrodes, and shielding of noise and thermal radiation is of great overall importance.

### **2.0.1 The catching, mixing, and positron transfer region**

For easy reference to a particular region of the ALPHA main apparatus three separate regions are defined: The *catching region* is located furthest upstream and holds the high-voltage electrodes used for catching antiprotons from the AD. This region is covered by the inner solenoid magnet to enhance antiproton capture (see section 2.2). The *mixing region* is at the center of the main apparatus, and is where antiprotons and positrons are merged to form antihydrogen. This region is surrounded by the magnetostatic trap (see section 2.2.2) and the silicon detector (see section 2.6.1). It also holds the mixing electrode stack (see section 2.3.2). Farthest downstream is the *positron transfer region*. This region contains a dynamic aperture, which can be opened to allow electrons and positrons to enter. When closed the aperture blocks thermal radiation from entering.

## 2.1 ALPHA control structure

Figure 2.2 shows a block diagram describing the control, apparatus monitoring, and data acquisition chain of the ALPHA apparatus.

Central to the experiment is the sequencer, which consists of a high level computer interface to create and execute individual experiments. A sequence defines the time dependent voltages applied to each individual electrode and the timing of digital triggers send to and from auxiliary equipment such as the positron accumulator, the magnet power supplies, or the individual detectors.

Sensors to measure temperatures, pressures, voltages, currents, magnetic fields, radiation and other similar parameters are placed in many parts of the apparatus. By means of these the performance and condition of the individual subsystem are monitored and stored in a central database, and warnings or an automatic shutdown of critical components can be issued.

Data acquired during an experiment is timestamped and automatically stored for later access.

## 2.2 The ALPHA magnets

The ALPHA apparatus makes use of two independent magnet systems to generate the magnetic fields necessary to confine both charged particles and neutral antihydrogen atoms. Both systems employs superconductor technology and each system has its own liquid helium cooled cryostat. Figure 2.3 shows the relative placement of the individual magnets.

### 2.2.1 The main solenoid magnet

The outermost part of the apparatus is a 1.7 m long solenoid magnet which is operated in persistence mode. The magnet is normally operated at 1 T, and it forms the backbone of the homogeneous magnetic field used to confine antiprotons, positrons and electrons radially. The quite large 26 cm diameter bore of the magnet is at room temperature.

The magnetic field of the solenoid magnet was measured during the summer 2005 as a part of the initial construction and design of the ALPHA apparatus. Later, in spring 2008, the magnetic field was measured again, and

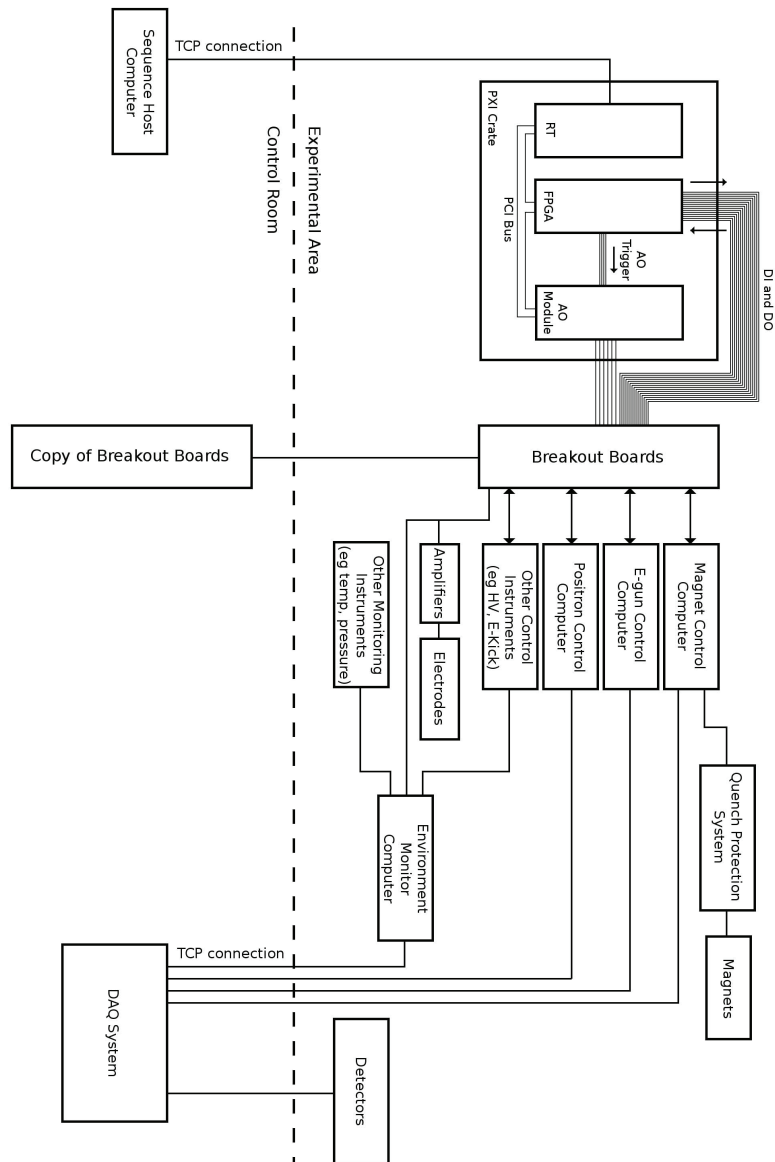


**Figure 2.2:** Block diagram showing the ALPHA control, apparatus monitoring, and data acquisition chain (adapted from Jenkins, 2008).

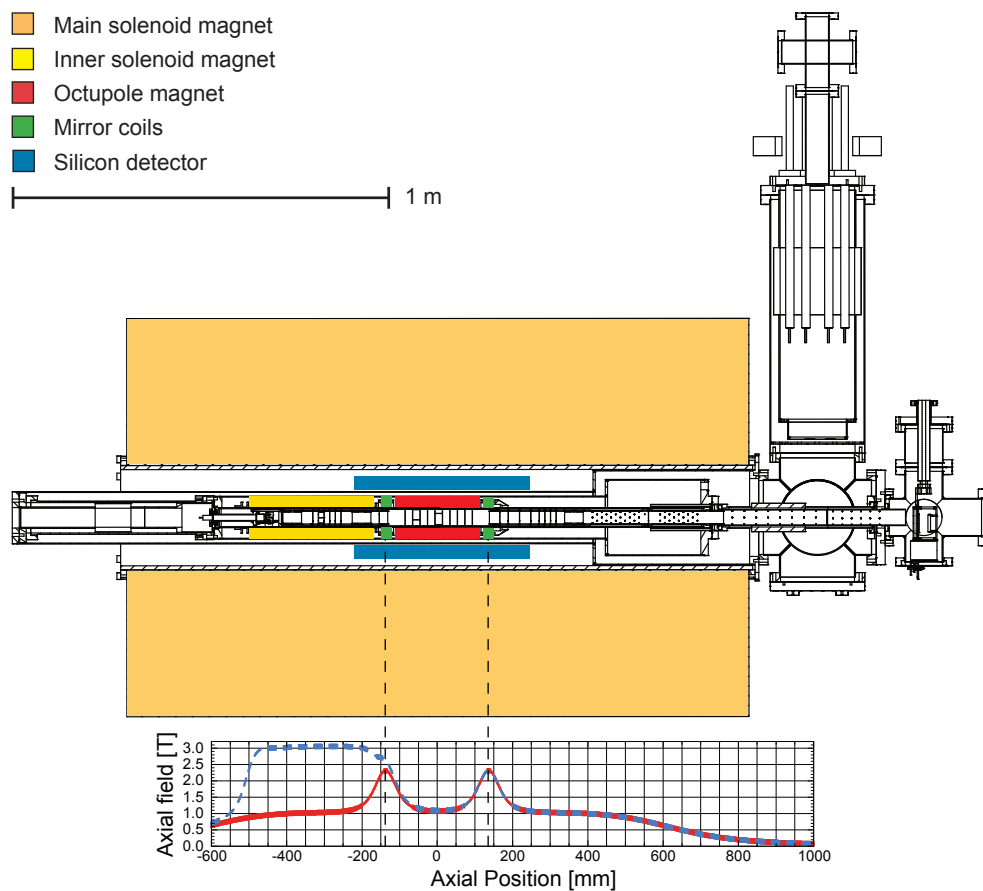


**Figure 2.3:** The position of the main solenoid and the inner magnets is indicated. The lower graph shows the on-axis magnetic field for two typical configurations, both with the main solenoid magnet at 1 T: *Antiproton catching configuration* with the inner solenoid at 2 T (dashed line), and *antihydrogen trapping configuration* with the octupole and mirror coils energized (fully drawn line). The inner cryostat (drawn in black), located inside the bore of the main solenoid magnet is shown in Figure 2.4. The inner cryostat contains the ALPHA magnetostatic trap and the electrode stack. The central part of the inner cryostat is surrounded by the ALPHA silicon detector.

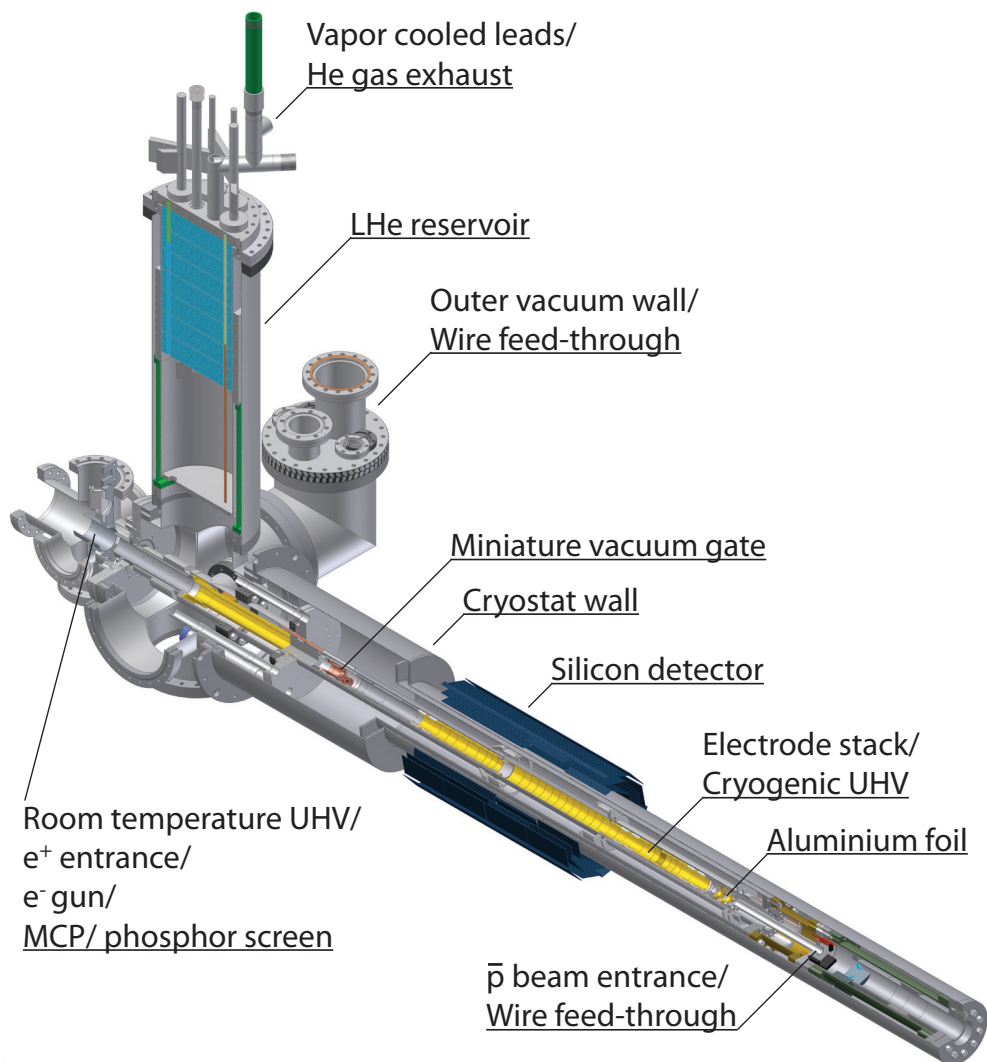


**Figure 2.4:** Cut-away technical drawing showing the inner cryostat, the cold and warm part of the UHV, the electrode stack and the silicon detector. The cryostat is mounted inside the bore of the main solenoid magnet as shown in Figure 2.3.

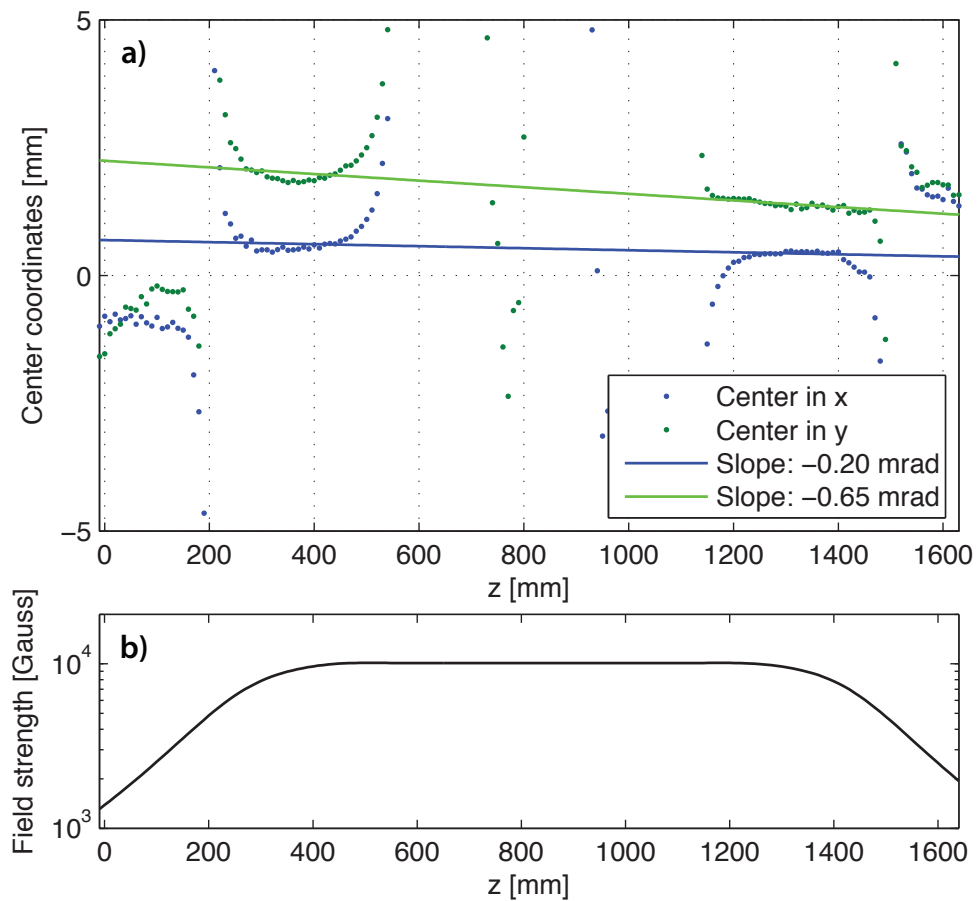


**Figure 2.5:** (a) Measurement of the magnetic axis of the main solenoidal field relative to the mechanical axis of the magnet bore. The  $x$  and  $y$ -axis are in the plane perpendicular to the mechanical axis. (b) Measurement of the magnitude of the main solenoidal field at the bore axis.

the magnet cryostat was opened several times to correct for a 4-5 mrad tilt of the magnetic axis relative to the mechanical axis of the bore. The tilt caused clouds of particles released towards the imaging device, located in the magnet fringe field, to be severely scraped by apertures and was possibly causing radial expansion and heating of trapped plasmas. Figure 2.5 shows the result of a field measurement after the final intervention where the tilt was reduced to less than 1 mrad.

### 2.2.2 The inner magnet system

Mounted inside the bore of the main solenoid magnet is the three layer ALPHA silicon detector and the inner cryostat which contains the second magnet system, the trap vacuum system, and the electrode stack (see Figure 2.4). The cryostat contains four separate superconducting magnets: an octupole, two mirror coils, and a solenoid magnet. All are developed and manufactured with the particular requirements of ALPHA in mind (Bertsche *et al.*, 2006). The four magnets in the inner cryostat make the ALPHA apparatus different from previous devices built to produce antihydrogen. These had only a single solenoid magnet. As seen on Figure 2.4 the inner cryostat has a radial step. This is to allow the silicon detectors to be placed in the room temperature region between the bore wall of the outer magnet and the inner cryostat.

Three of the four magnets are designed to create a magnetostatic trap for antihydrogen atoms. The trap is centered on the mixing region where antiprotons and positrons are merged to create antihydrogen. It consists of two mirror coils which are designed to create a minimum for the magnetic field on the trap axis and an octupole magnet which provides a radial minimum at the trap center. The three magnets are designed to disturb the solenoid field in the center of the trap as little as possible while still providing as deep a magnetic trap as possible. A short description of the reasons behind the choice of the octupole over a quadrupole for radial confinement can be found in section 1.3.

The fourth magnet in the inner cryostat is a solenoid magnet covering about a third of the trap length. This magnet can provide a localized 2 T magnetic field on top of the 1 T external magnetic field to improve antiproton trapping in the antiproton catching region of the apparatus (Bertsche *et al.*, 2006; Andresen *et al.*, 2008a). The higher magnetic field in this region can also

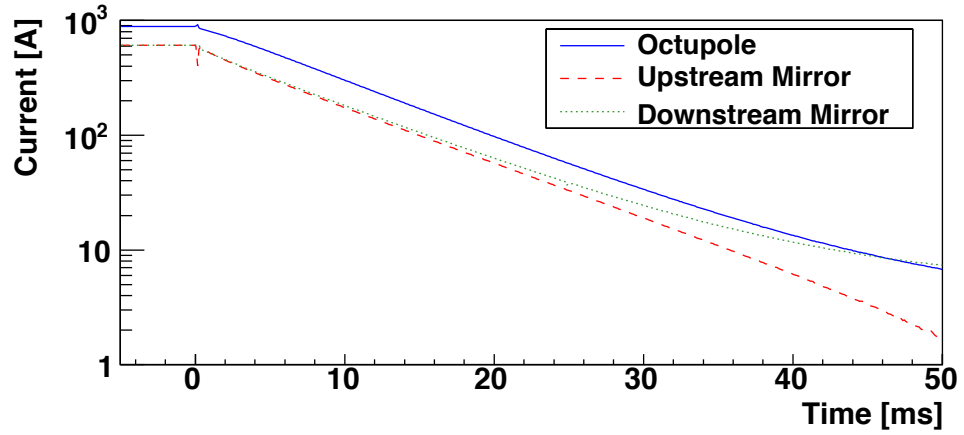


**Figure 2.6:** Current decay in the magnets constituting the magnetostatic trap during a fast shut-down.

be exploited in other ways since it improves cyclotron cooling of electrons and positrons<sup>1</sup> and radial confinement of all charged species. As an example the rotating wall technique described in section 3.1 is more efficient in a high magnetic field.

Notable of the inner magnets is that the superconductors are not run in persistence mode, meaning that the current through them are supplied by power supplies run in constant current mode. Because the magnets are designed with low mutual inductance, the fields they create can be changed on a rather short timescale during an experiment. The inner solenoid and the two mirror coils are typically ramped to their nominal current of 240 A and 600 A in 20 s, and the octupole is typically ramped to 900 A, which is about 80% of its design current, in 60 s. Going higher with the octupole is possible, but it is slow and the magnet becomes much more likely to *quench*, i.e. make the transition to normal conductor. At a current of 900 A the octupole creates a 1.55 T magnetic field at the inner surface of the Penning-Malmberg trap electrodes. Combined with an on-axis field of 1.2 T generated by the mirror coils at 600 A and the 1 T solenoidal bias field the magnetostatic trap depth becomes 0.6 K for ground state antihydrogen (see section 1.2.3).

By design the entire magnetostatic trap can be shut down in about 30 ms

<sup>1</sup>The cyclotron cooling time of antiprotons is irrelevant since it far exceeds any of experimental timescales.

to allow any trapped antihydrogen to escape and be detected in a short time interval, thus reducing the background from cosmic rays. To initiate the fast shutdown an insulated-gate bipolar transistor (IGBT) is used as a switch to force the current in the magnets to flow in an external resistor network where the energy is dissipated as heat. This process induces the superconductor to quench. The current flowing in each magnet is monitored by measuring the voltage drop across a shunt resistor, and we measure an exponential decay of the current with time constants of 9.0 ms for the octupole and 8.5 ms for the mirror coils (see Figure 2.6).

## 2.3 Electrode design

In the ALPHA apparatus all charged particles are confined radially by the solenoidal magnetic field. Axially, they are trapped by electric fields generated by an array of hollow cylindrical electrodes positioned along the entire trap axis. The electrode stack is mounted inside a steel pipe which acts as the wall of the cryogenically cooled part of the trap vacuum system. The stack consists of 36 hollow cylindrical electrodes of various length and radii, and the electrodes are mounted in three separate units: The *antiproton catching electrodes*, the *mixing electrodes*, and the *positron transfer electrodes*. The three units are shown in Figure 2.7, and each electrode has been assigned a name from E1 to E36 for easy reference. In addition the type of coaxial cable running from the room temperature wire feed-through to the cryogenic part of the trap is indicated. To reduce liquid helium consumption most of the wires are made of stainless steel which has a low heat conductance, however, electrodes intended to have better response to fast electrical pulses are connected using copper wires. Three of the electrodes (E1, E9, and E34) are prepared for high voltage and are used to capture antiprotons from the AD. For these electrodes appropriate high voltage cables are used.

The antiproton catching electrodes and the positron transfer electrodes all have an inner diameter of 33.6 mm, leaving room for cables and the electrode support structure between the inner vacuum wall and the electrodes. In contrast are the thin mixing electrodes which are described in more detail below.

All electrodes are thermally anchored to the liquid helium in the inner

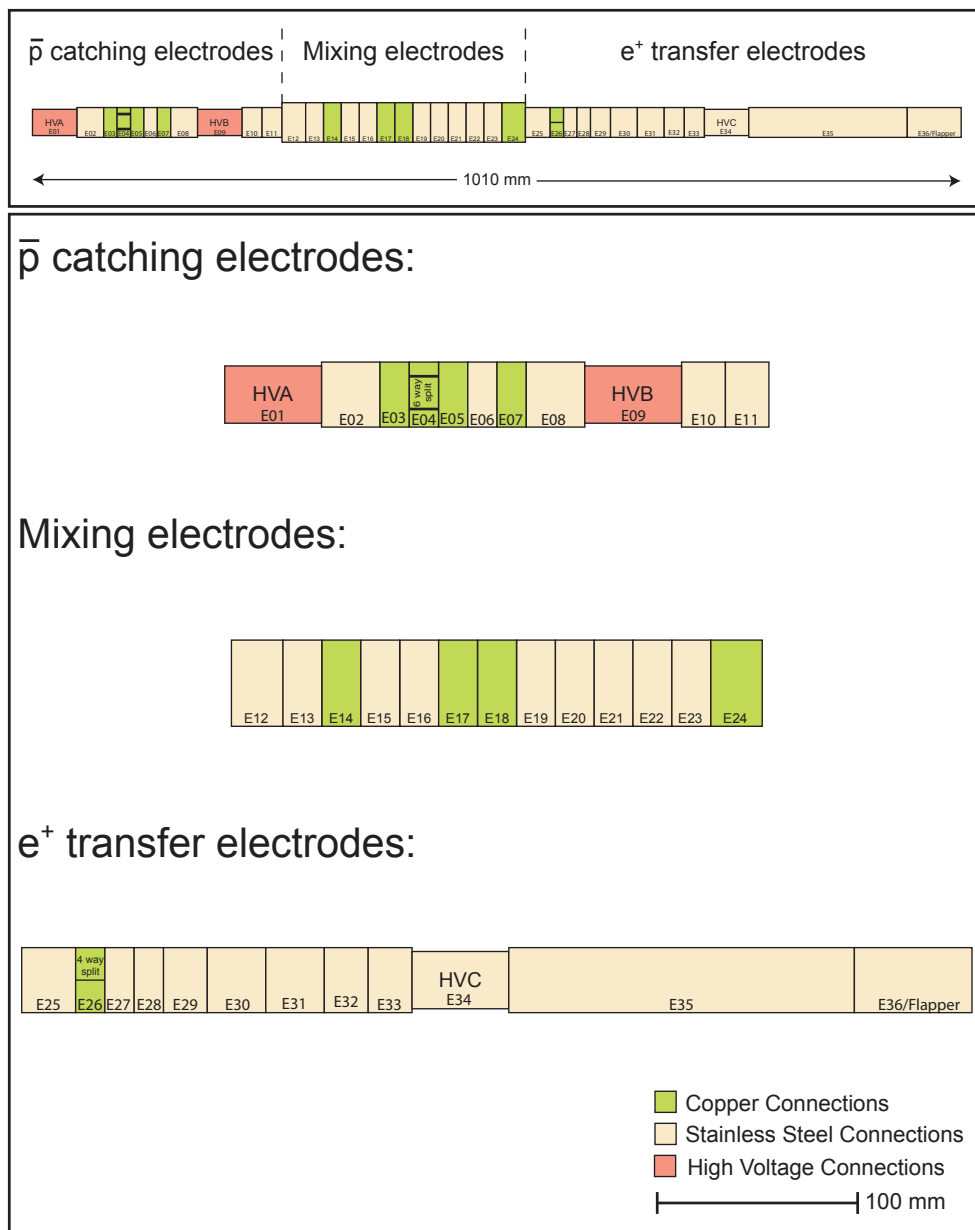


Figure 2.7: Schematic diagram showing the combined ALPHA electrode stack (top panel), and the three separate units (lower panel).

cryostat through the wire connecting the electrode to the electrode driving circuit. In addition they are surrounded by the cold steel vacuum wall on which the super conducting magnets of the magnetostatic trap are wound. Some of the electrodes have CERNOX temperature sensors placed on their outside. Using these we measure a temperature of about 7.5 K during stable operation.

### 2.3.1 Electrode driving circuit

Inside the apparatus each electrode is connected through a coaxial copper cable to a flexible circuit board which is thermally anchored to the liquid helium bath of the inner cryostat. The circuit board runs to a vacuum feedthrough separating the trap vacuum from the isolation vacuum of the inner cryostat. Inside the isolation vacuum the electrode signal is run in coaxial cables of either steel or copper (see Figure 2.7). These are feed-through to a shielded box and run onto a circuit board with a passive RC-filter for each electrode. The filter has a low-pass connection for DC levels and a high-pass connection for fast pulses. The DC-input is connected to an amplifier controlled by the ALPHA sequencer. The amplifiers have a dynamic range of  $\pm 140$  V. The high-pass connection to the RC-filter is only used on electrodes such as the segmented electrodes (see section 2.3.3) or on electrodes where fast pulses are applied to remove electrons, heat positrons using high frequency noise, or to drive other plasma or single particle modes.

### 2.3.2 Thin walled electrodes

The thin walled electrodes of the mixing region are designed to minimize the amount of scattering material between their inner wall and the silicon detector, and to minimize the distance between their inner wall and the windings of the octupole magnet to maximize the depth of the magnetostatic trap (see section 1.3.1). They are manufactured in aluminum which has been gold plated, and they have an inner diameter of 44.55 mm and a wall thickness of 1.5 mm leaving a gap of only  $\sim 0.1$  mm between the outer electrode wall and the inside of the steel vacuum tube. A schematic diagram of the thin electrodes is shown in Figure 2.8.

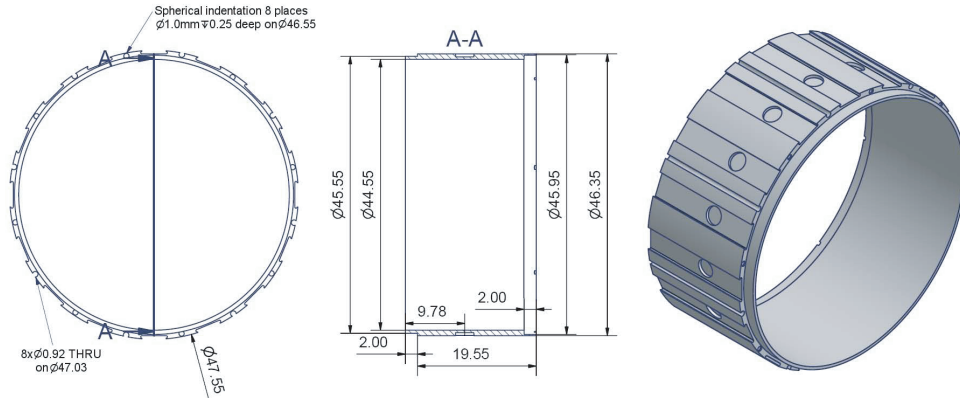


**Figure 2.8:** Technical drawing of the thin electrodes of the mixing region (adapted from Jenkins, 2008).

The electrodes form their own support structure. Small 1 mm diameter ruby balls are used to electrically isolate one electrode from its neighbors, and the electrode stack is held together by a set of aluminum wires running in Kapton<sup>2</sup> plastic tubes along the length of the stack. Each electrode has a set of specially designed grooves on the outside to capture the Kapton tube. The grooves allow part of each Kapton tube to extend radially beyond the radius of the electrode, and when placed inside the vacuum tube the electrode stack is supported solely by the tubes, electrically isolating the stack from the grounded vacuum wall.

Running in another set of grooves are the flat, flexible Kapton coated wires connecting each electrode to the coaxial cable coming from the electrode driving circuit.

### 2.3.3 Segmented electrodes

Some of the electrodes in the ALPHA electrode stack have azimuthal cuts breaking the electrode into sectors electrically isolated from each other (see Figure 2.9). These electrodes are included to allow the rotating wall (RW) technique to be used to radially compress or expand the electron, positron, or combined electron-antiproton plasmas (see section 3.1).

<sup>2</sup>Kapton is, among other things, a UHV friendly plastic.

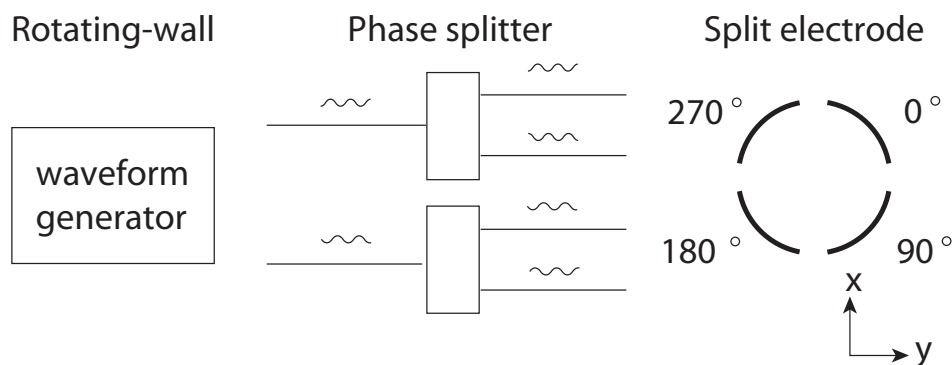


**Figure 2.9:** Schematic diagram showing a segmented electrode and the drive circuit used to apply the rotating wall technique. (Adapted from Funakoshi *et al.*, 2007)

Most of the time the segmented electrodes are operated like any other electrode by driving all sectors to the same DC voltage. This is done by shorting together all of the sectors on the amplifier side of the low pass filter in the electrode driving circuit. However, when the RW technique is used an additional oscillating voltage is applied through the high pass side of the filter. Each sector receives the the signal with a relative phase equal to  $2\pi i/n$ , where  $i$  is the segment number counted either clockwise or anticlockwise, and  $n$  is the total number of segments. The resulting electric field appears to be rotating around the axis of the trap at the oscillation frequency of the applied potential.

In the ALPHA apparatus two electrodes are segmented. E4, located between the two high voltage electrodes in the antiproton catching region, is split into six segments, and E26, located in the positron catching region, is split into four segments. Previously (in 2006 and 2007) one of the thin walled electrodes in the mixing region was also segmented. However, this electrode was replaced to improve the mechanical and electrical properties of the thin walled electrode stack. The phase locked oscillating voltages are generated using a specially designed frequency generator.

## 2.4 Positrons and electrons

Both positrons and electrons enter the apparatus from the downstream end through a series of apertures (see Figure 2.4). Immediately before the particles

are loaded a dynamic aperture (indicated on the figure) is opened to allow access to the cryogenic part of the trap vacuum.

### 2.4.1 Positrons

The positrons are generated and accumulated in the same Surko-type positron accumulator also used by ATHENA (Murphy and Surko, 1992; Jørgensen *et al.*, 2005) with a new  $\beta^+$  3 GBq  $^{22}\text{Na}$  radioactive source installed in 2006. The source generates positrons, and a solid neon moderator is used to reduce their energy. The emerging positrons are directed into the accumulation region, where they are cooled through collisions with molecules of a dilute nitrogen buffer gas and trapped in an electrostatic well. A full accumulation and transfer cycle of 200 s can, under good conditions, give about 100 million positrons in a dense plasma to be transferred to the main apparatus.

Immediately before transferring the positrons to the main apparatus, two cryopumps are used to improve the vacuum in the accumulator by about 4 orders of magnitude, from  $1 \times 10^{-5}$  mbar to about  $1 \times 10^{-9}$  mbar over 40 s. A gate valve is then opened and the positrons are transferred ballistically across a distance of about 2 m before they are recaptured in the mixing region of the main apparatus. Here they cool through cyclotron radiation in the 1 T magnetic field. At the end of the process as many as 70 million positrons are left in a well 2 cm long, 40 V deep electrostatic well.

We have observed the positron plasma to be contaminated with ions, most likely  $\text{H}_2^+$ , the presence of which can cause the plasma to expand radially and heat (Peurrung *et al.*, 1993). The ions can be separated from the positrons by setting up a potential well adjacent to the positron well. A pulsed electric field is then applied to the electrode generating the barrier between the two wells, and only the faster moving positrons are allowed to escape into the new well.

To prepare the positron plasma for antihydrogen formation in the magnetostatic trap it is desirable to achieve as small a plasma radius as possible to minimize the influence of the octupole on the plasma temperature (see section 1.3). Thus the positrons are transferred to the split electrode located in the downstream end of the apparatus, where a rotating-wall electric field is applied to the plasma to decrease the plasma radius (see section 3.1).

In our typical antihydrogen trapping experiments (see chapter 8), the num-

ber of positrons is reduced after transfer, and sometimes only a few million are used. To decrease the number the plasma length is increased and the plasma cut in two by raising a potential wall near the center of the plasma. This method does not affect the radius of the positron plasma. The process is non-adiabatic, and it can be repeated multiple times to lower the number to the desired value.

### 2.4.2 Electrons

An electron gun setup is used to generate and accelerate electrons into the apparatus. The gun is located in the room temperature part of the trap vacuum chamber, in the fringe field of the main solenoid magnet. It is mounted on a linear translator, and it is moved onto the trap axis before it is turned on. The electron gun consists of a barium oxide filament, which emits electrons when heated by an electric current. A positively biased plate with a hole in the center is placed in front of the filament to collimate and accelerate the electrons to a given energy.

Using the electron gun, an electron plasma can be loaded into any region of the trap. By tuning the loading parameters such as the emission current of the electron gun, its position in the fringe field, and the electrostatic potential in the trap, the plasma dimensions and density can be chosen within some constraints.

At the upstream end of the apparatus, a tungsten filament is mounted directly in front of the Faraday cup/degrading foil. This filament is also capable of supplying electrons to the experiment, but since it is thought to have deleterious effects on the trap vacuum, it has so far only been used as a backup electron source.

## 2.5 Plasma diagnostics

To characterize the electron, positron, and antiproton plasmas used in the ALPHA experiment, two plasma diagnostic devices are used: A *Faraday cup* is used to measure the total number of electrons and positrons, and a combined micro channel plate (MCP) and phosphor screen setup is used to create images of the line-integrated charge distribution of all charged species as well as

measuring the temperature of electrons and positrons. The antiproton number and temperature are determined using particle detectors (see section 2.6 below).

### 2.5.1 Faraday cup

In the upstream end of the apparatus an aluminium foil (see Figure 2.4), which is also used to slow down antiprotons from the AD, is electrically isolated from its surroundings and connected through cables to a set of amplifiers and active filters outside the apparatus. The foil is located in the region covered by both solenoid magnets, and is normally operated in a magnetic field of either 1 T or 3 T. By measuring the total charge accumulated on the foil, this arrangement is used as a Faraday cup to count the number of charged particles dumped onto it with a background noise level of about  $10^5$  charges. For millions of electrons and positrons, the result is very repeatable, having reliable counts of particles with  $\leq 5\%$  injection variation during steady operation.

However, this technique does not work for antiprotons since there are significantly fewer of them, and the resulting signal is below the noise level of our electronics. Additionally, even if the noise level was improved, the accumulated charge would not directly indicate the antiproton number since decay products from antiproton annihilations on atomic nuclei may carry away charge. Instead, the Faraday cup is utilized as a beam stop, and antiproton numbers are found by detection of charged annihilation products by nearby scintillators (see section 2.6.2).

### 2.5.2 Micro channel plate (MCP)

Mounted on the same linear translator as the electron gun is a micro channel plate (MCP) with a phosphor screen mounted behind it. This device plays an important role in the temperature diagnostic of electrons and positrons and determination of the spatial density profile of all charge particles in the apparatus. For this reason it will be described in some detail.

Due to spatial constraints the assembly is located at a reduced magnetic field of  $\sim 240$  G in the fringe field of the 1 T main solenoid magnet. When charged particles are incident on the MCP, secondary electrons are emitted and accelerated towards the phosphor screen where they are converted into

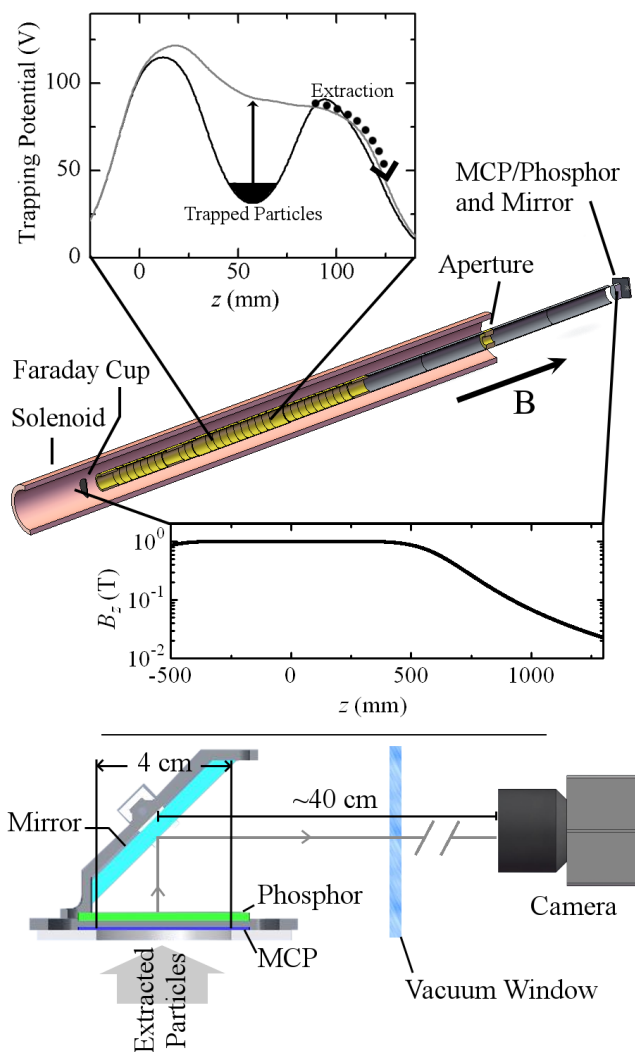


**Figure 2.10:** Simplified schematic of the ALPHA particle trap (top) and MCP imaging system (bottom). Particles are extracted from the trap by slowly (over milliseconds) raising the potential under the trapped particles, allowing them to escape over the lower barrier of the well. Once over the barrier, the particles are ejected with an effective kinetic energy of about 100 eV along the magnetic field. Particles that impact the MCP are amplified and imaged as described in the text. (Adapted from Andresen *et al.*, 2009a)

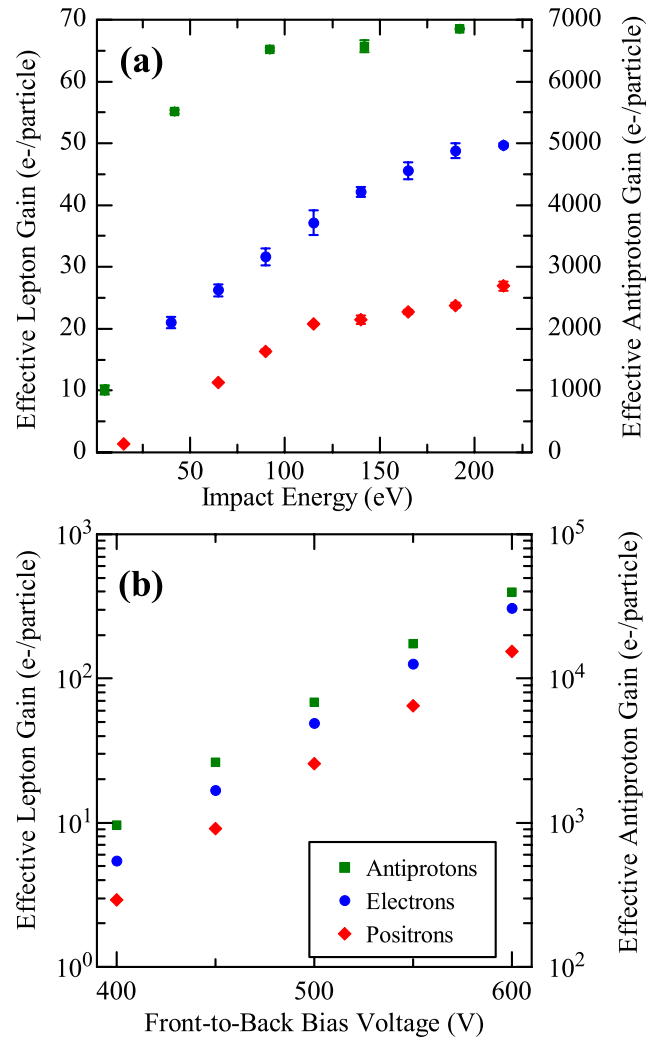


**Figure 2.11:** Effective gain of the MCP for different species of particles while varying the voltages on the front and back plates. Particles are extracted from the trap at  $\sim 100$  eV and accelerated by the front plate voltage. In (a), the front-to-back voltage bias was kept constant at 500 V, while impact energy is varied; in (b), the front-to-back voltage bias is varied while the impact energy is held at 200 eV. The uncertainties in the measurements in (b) are  $<2\%$ . (Adapted from Andresen *et al.*, 2009a)

photons. The light from the phosphor screen travels through a vacuum window and is finally captured by a charge coupled device (CCD) camera mounted outside the vacuum system (see Figure 2.10).

The MCP and phosphor screen assembly has a diameter of 4.0 cm, and the assembly is controlled by three voltages applied to the front and back of the MCP and to the phosphor screen. The voltages can be adjusted to suit the particle species and number. The front voltage accelerates the incoming particles over the last few centimeters of their trajectories to a desired impact energy; this is usually set to give the particles a maximum impact energy of 200 eV. The MCP's back plate voltage relative to the front controls the gain of the MCP and is chosen to avoid saturation. The front-to-back voltage is varied from 900 V for low numbers of trapped particles ( $< 10^5$  electrons and positrons or  $< 10^3$  antiprotons), down to 400 V for large numbers ( $< 10^8$  electrons and positrons or  $< 10^5$  antiprotons). Higher gains (greater front-to-back voltages) saturate the MCP for large numbers of particles.

The camera placed outside the vacuum chamber records a  $688 \times 520$  pixel<sup>2</sup> image from the phosphor screen and the area imaged by each pixel ( $6200 \mu\text{m}^2$ ) is square and contains roughly 30 MCP channels. When particles are extracted onto the MCP/phosphor screen assembly the camera shutter is set to open over the entire extraction cycle, typically 1 ms.

A detailed characterization of the MCP response to electrons, positrons and antiprotons can be found in (Andresen *et al.*, 2009a). Figure 2.11 shows the different gains measured for each species.

There are several apertures in the apparatus limiting the maximum plasma size we can image. For large plasmas this means that only part of the plasma is visible. Since the light electrons and positrons follows the field lines closely, while the heavier antiprotons experience small drifts, the apertures appear different for the different species.

Because the imaging device is placed in a low magnetic field (240 Gauss) outside the area covered by the main solenoid, particles originating from higher field regions will follow the radially expanding field lines. Particle clouds thus increase in radial extend by a factor of  $\sqrt{1 \text{ T}/0.024 \text{ T}} = 6.5$  when released from a 1 T magnetic field and by a factor of  $\sqrt{3 \text{ T}/0.024 \text{ T}} = 11.2$  when released from the 3T.

In addition to being used as part of an imaging device the combined MCP and phosphor screen is also used to measure the temperature of both electron and positron plasmas. In this case the phosphor screen is used as a Faraday cup by integrating the incident charge. The temperature is determined from the time dependent charge distribution as described in detail in section 3.2.

## 2.6 Antiproton annihilation detection

The ATHENA collaboration synthesised and detected antihydrogen atoms using a position sensitive silicon detector to reconstruct the annihilation vertex formed by the tracks of the annihilation products. The detector comprised a two layer silicon detector to detect charged pions from the antiproton annihilation and an array of CsI crystals to detect the two back-to-back 511 keV gamma rays from the annihilation of the positron (Amoretti *et al.*, 2002; Fujiwara *et al.*, 2004). A similar detector has been designed for the ALPHA apparatus. However, in ALPHA, the windings of the octupole magnet are located between the antihydrogen production region and the annihilation detector, and there is a significant chance that a charged particle produced in an annihilation will scatter, reducing the reconstruction performance (Fujiwara, 2005). A third layer of silicon, which allows the tracks to be fitted with curves rather than straight lines helps to alleviate this, and experimental tests and Monte-Carlo simulations have demonstrated that the detector can reconstruct annihilation vertices with a resolution of better than 1 cm (one  $\sigma$ ). Space constraints and the low efficiency of detection of gamma photons through the scattering material precluded the addition of a detector for positron annihilations in ALPHA. The ALPHA silicon detector is described in further detail below.

In addition to the silicon detector, plastic scintillators are placed around the apparatus to monitor the rate of annihilations in the apparatus (see description below), the AD beam intensity, and other sources of radiation in the surrounding accelerator environment. CsI crystals are used to monitor positron annihilations during accumulation and transfer of positrons.

### 2.6.1 Si detector

The silicon detector is used to identify and reconstruct antiproton annihilations from antihydrogen or bare antiprotons striking the electrode wall or annihilating on residual gas in the trap vacuum. The ALPHA detector comprises 60 modules, arranged in three layers in a cylindrical fashion around the mixing region (see Figure 2.4). In each module, a double-sided silicon wafer is divided into 256 strips, of widths 0.9 mm and 0.23 mm in the  $z$  and  $\phi$  directions respectively, oriented in perpendicular directions on the p- and n- sides. The charged products of an annihilation, principally pions, can ionize and leave charge deposits in materials they pass through, and each strip can be individually addressed to measure the amount of charge deposited. Charge exceeding a defined threshold causes the electronics controlling that module to output a digital signal, monitored by a control system.

A coincidence of modules in a 400 ns time interval prompts readout and digitization of the charge collected on all of the detector strips. Each readout of the detector is referred to as an *event*. Strips through which particles passed are identified by charge deposits above noise, with a 96% detection efficiency determined in studies with cosmic rays. Intersection of perpendicular strips defines a hit position. Tracks are constructed by fitting a helix to combinations of three hits, where one hit is drawn from each of the layers of detector modules. Only tracks that produce helices which conform to the expected characteristics of annihilation products are accepted and used to determine the annihilation vertex as the point which minimizes the distances of closest approach. The system achieves a maximum readout rate of 170 Hz.

An example of a reconstructed antiproton annihilation is shown in Figure 2.12(a). The detector is also sensitive to charged particles from cosmic rays, which pass through the detector in a straight line and typically reconstruct as a pair of approximately co-linear tracks, as seen in Figure 2.12(b).

The detector is used as an indicator of antihydrogen production. Antihydrogen atoms that annihilate on the electrodes will produce an azimuthally uniform distribution of vertices. When the octupole field is energized, the trajectories of antiprotons redistributed by the process of antihydrogen production and subsequent ionization can be unstable, giving rise to a component with eightfold symmetry (see Figure 1.6). The distribution of annihilations

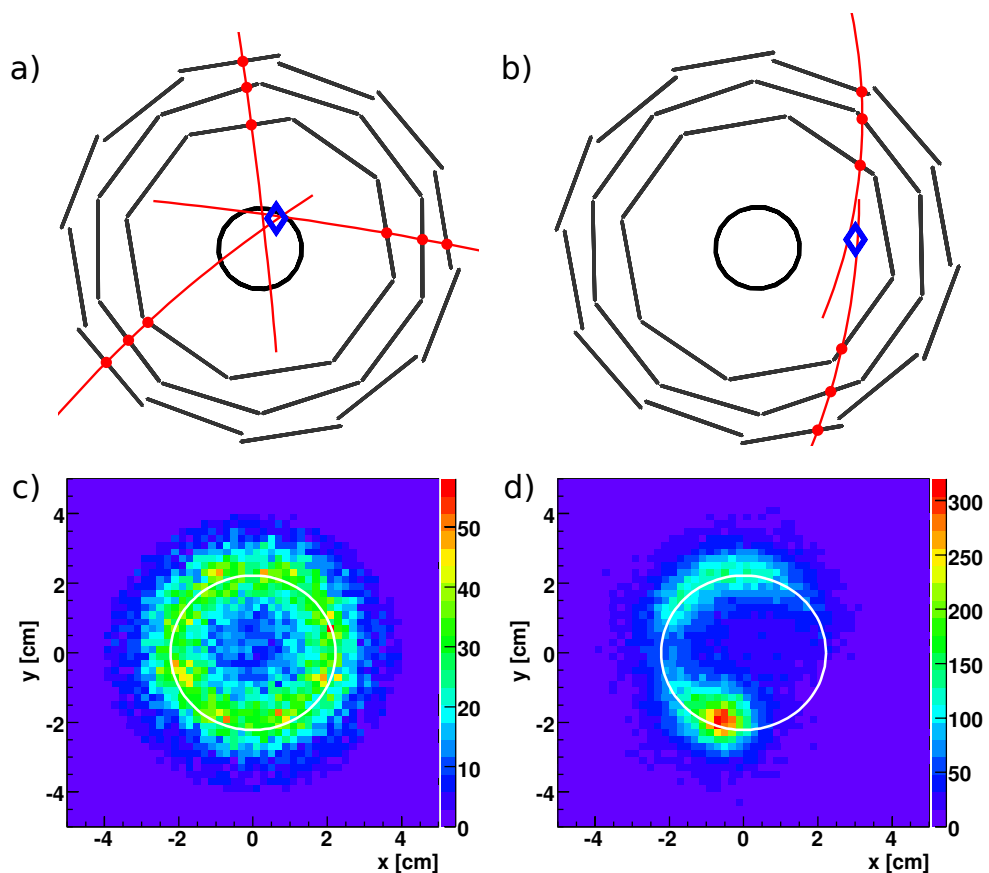


**Figure 2.12:** (a) An example reconstruction of an antihydrogen annihilation and (b) a cosmic ray event. The blue diamond indicates the position of the reconstructed vertex, the red dots the positions of the detected hits, and the inner circle shows the radius of the Penning-Malmberg trap electrodes. (c) The spatial distribution of approximately  $2 \times 10^4$  antihydrogen atoms projected along the z-axis. The distribution is approximately azimuthally uniform and concentrated around the surface of the electrodes, indicated by the white circle. Small non-uniformities are interpreted to be due to the escape of field-ionized antihydrogen. The escape of bare antiprotons tends to produce highly nonuniform distributions, such as that in (d). (Adapted from Andresen *et al.*, 2010b)

measured during the antihydrogen production periods in the trapping experiments described in chapter 8 is shown in Figure 2.12(c). An azimuthally uniform component dominates, and a small contribution from an eightfold symmetric pattern is also present (section 7.3 contains a detailed description of this phenomenon). This can be contrasted to the escape of bare antiprotons, which tend to yield very non-uniform distributions (Fujiwara *et al.*, 2004). An example distribution, created by deliberately destabilizing an antiproton plasma, is shown in Figure 2.12(d). The octupole magnet was not energized for this measurement.

### 2.6.2 External scintillators

Scintillators detect ionizing radiation by emitting light when excited by an energetic particle passing through the scintillating material. Each individual plastic scintillator is shaped as a flat paddle with one end moulded into a funnel-like shape to guide the light traveling inside the plastic. At the end of the funnel the scintillator is coupled to an electronic light-sensitive device, typically a photomultiplier tube (PMT) or a photo diode which both amplifies and converts the light signal to an electric pulse. In ALPHA the scintillators detect charged pions from antiproton annihilations; 511 keV  $\gamma$ -rays from positron-electron annihilations are usually only seen with low efficiencies. In addition to radiation from the intentional antimatter-matter annihilations which are part of the experiment, cosmic rays and other sources of background radiation from the surrounding accelerator environment can also induce a signal in the scintillators.

In ALPHA a variety of plastic scintillators with different light-sensitive devices are used. Of most interest to the physics discussed in this thesis are the three sets of plastic scintillator paddles distributed along the length of the apparatus. These are used to monitor annihilations inside the antimatter trap. Each of these sets consists of four large (40 cm  $\times$  60 cm  $\times$  1 cm) paddles, mounted in two pairs, with one pair on each side of the cryostat containing the main solenoid magnet. A photomultiplier tube is used to read-out each paddle. To reduce the background from cosmic rays the paddles are mounted vertically, and to reduce the number of false counts from noise in the system the electrical signal from all four detectors in a set is combined in the follow-

ing DAQ chain. Thus a count is only registered if a hit is registered simultaneously in both paddles in one or the other pair, such a hit is labeled OR. If a hit is registered simultaneously in all four paddles in a set, the hit is labeled AND.

The scintillators are often used to determine the absolute number of antiprotons in an experiment. This is done in a destructive measurement where the antiprotons are released onto the aluminium foil located in the far upstream end of the apparatus or onto the small gate separating the cold part of the trap vacuum from the room temperature region. The efficiency for detecting a single antiproton annihilation in the trap vacuum depends of the point of annihilation. If the annihilation occurs in the region between two pairs of a set it has a ~25% chance of being detected. However, if many particles are annihilating near simultaneously, such as happens when they are counted, the read-out signal can saturate.

# Experimental techniques

---

This chapter contains a description of two key experimental techniques used in antihydrogen formation and trapping experiments and in the evaporative cooling experiments described in this thesis. The techniques are: radial compression of antiprotons and temperature diagnostic of antiprotons, positrons, and electrons. Detailed knowledge of these techniques is not essential to the understanding of other parts of this thesis.

## 3.1 Rotating wall compression of antiprotons, electrons and positrons

A key problem when trying to create cold antihydrogen in a magnetic trap is the perturbations to the solenoid field caused by the multipole field. These perturbations can cause the charged particles to be immediately lost via the ballistic loss process if their orbit around the trap axis brings them beyond a certain critical radius, and induce increased particle diffusion, radial expansion and heating (see section 1.3).

In the design of ALPHA, two features in particular are implemented to counter deleterious effects of the multipole field. First a relatively high order multipole is used to minimize the perturbations in the central region of the trap and secondly, a number of azimuthally split electrodes are included to allow the rotating wall (RW) technique (described below) to be used to control the radius of the non-neutral plasmas. Generally the perturbations will be smaller for smaller radius plasmas.

Compression using the rotating wall technique requires the plasma to be able to dissipate heat. The technique is used in the ALPHA positron accu-

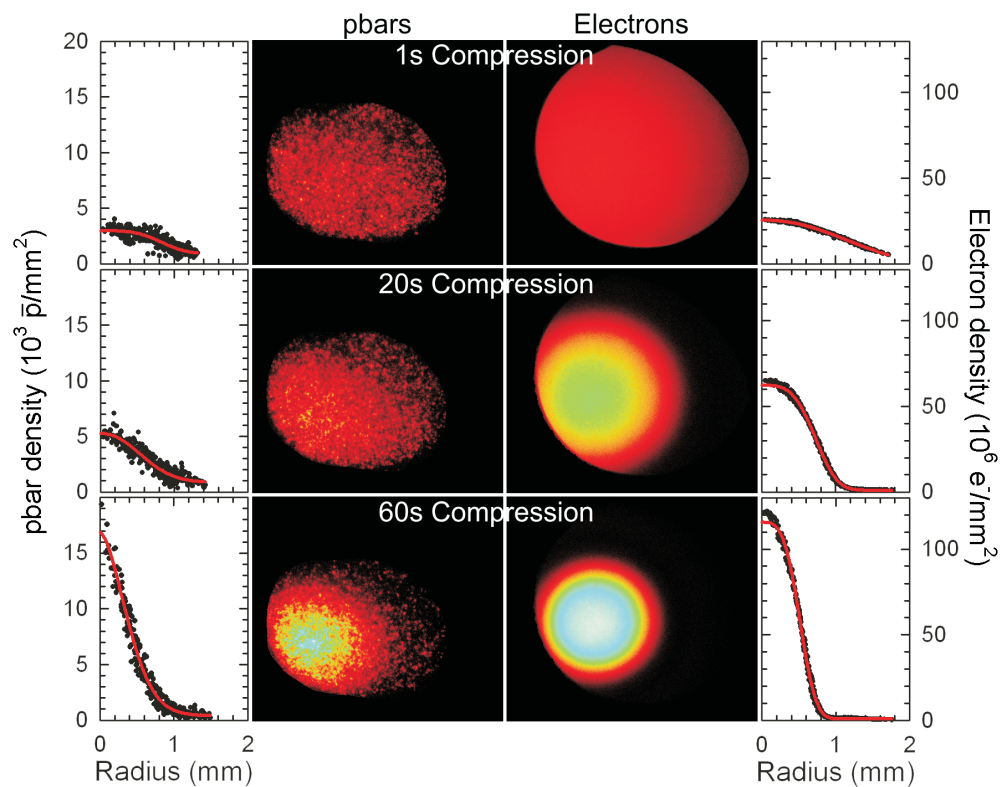


**Figure 3.1:** Antiproton and electron images showing the effects of radial compression, and the resulting radial profiles. The solid (red) lines are Gaussian-like (i.e.,  $\exp[-|r/r_0|^k]$ , where  $k \approx 2$ ) fits to the radial profiles. (Adapted from Andresen *et al.*, 2008c).

mulator, where a nitrogen buffer gas carries away excess energy, and rapid cyclotron cooling ensures that the technique can be readily applied to pure plasmas of electrons and positrons in the 1-3 T field of the main apparatus. Antiprotons on the other hand do not cool fast in these fields due to their larger mass. However, we found that if we apply a rotating wall drive to an electron plasma containing the antiprotons the combined plasma could be compressed. The latter technique was published in (Andresen *et al.*, 2008c) and the antiproton densities achieved have had wide implications for the experimental program in ALPHA. The simultaneous compression of electrons and antiprotons is described below. Direct radial compression of an antiproton cloud held in a 2.5 T magnetic field has been reported by Kuroda *et al.* (2008).

Compared to antiproton clouds reported by ATHENA and ATRAP, the clouds now used in ALPHA are 10-50 times smaller thanks to the radial compression technique. The small antiproton clouds created in this way are well within the critical radius of the octupole for a mixing experiment. The technique has made a whole new range of antiproton densities and radii possible. As an example the evaporative cooling experiments described in later chapters relies on high antiproton collision frequency which becomes possible with high densities. Radial expansion observed in these experiments makes a small initial radius of the antiproton cloud all the more critical.

### **3.1.1 The Rotating wall technique**

A non-neutral plasma confined in a Penning-Malmberg trap will rotate around the trap axis at a frequency determined by the relative strengths of the crossed electric and magnetic fields in the trap. The electric field in a cold plasma is largely determined by the plasma's self-fields, which are strongly dependent on the plasma density (see Davidson, 2001, chapter 3). When a rotating, transverse electric field is applied to the plasma, it will act as a torque on the plasma, and cause the plasma to adjust its frequency of rotation to match that of the drive. To do so, the radius and density of the plasma will also have to adjust to keep the self fields in the plasma consistent with the rotation. If the rotation frequency of the rotating electric field is higher than the plasma rotation frequency, the torque will compress the plasma; if it is lower, it will

expand the plasma.

The rotating wall technique is a method to achieve a rotating, transverse electric field. The technique requires the plasma to be partly contained in an azimuthal segmented electrode, and it works by applying an oscillating electric potential with a certain phase to the individual sectors. Each segment receives the signal with a phase equal to  $2\pi i/n$ , where  $i$  is the segment number counted either clockwise or anticlockwise and  $n$  is the total number of segments. The resulting electric field appears to be rotating around the axis of the trap at the oscillation frequency of the applied potential. Two segmented electrodes are installed in the ALPHA apparatus (see section 2.3.3).

### 3.1.2 Sympathetic compression of antiprotons in an electron plasma

Below the first simultaneous compression of antiprotons and electrons (Andresen *et al.*, 2008c) is described in some detail. Since we first made it to work<sup>1</sup>, the technique has become central to most of the experiments in ALPHA, and it is under constant development. Currently antiproton plasmas containing about 40000 antiprotons can be compressed to radii as small as 0.2 mm when transferred to the 1 T field of the mixing region.

The experimental cycle begins with the preparation of a 30 mm long plasma of about 120 million electrons located in the 3 T catching region. The electrons quickly cool (calculated energy  $e$ -folding time of 0.44 s) via cyclotron radiation in the 3 T field and form a plasma with a radius of  $\sim 0.8$  mm. The radius of the plasma was unchanged by a RW frequency of 400 kHz. If the RW frequency was lower (10 kHz), the plasma expanded to 1.95 mm, and if the frequency was higher (3 MHz), the plasma compressed to radii as small as 0.65 mm.

When used to cool antiprotons captured from the AD, a large radius electron plasma is more efficient, resulting in a higher number of antiprotons remaining in the trap when the high voltage is lowered. Thus the electron plasma was first expanded radially to cool the highest possible number of antiprotons. In total about 11000 antiprotons were collected by the expanded electron plasma from one bunch of antiprotons from the AD.

The combined electron and antiproton plasma was now compressed by

---

<sup>1</sup>ALPHA elog:5387 is a favorite of mine. Thumbs up for the yellow fouines.

applying a constant 10 MHz drive. By varying the drive amplitude we could control the time scale for compression of the electron plasma. We observed that a quick (1 s) compression of the electron plasma would leave the radial antiproton distribution unchanged, whereas a slow ( $\sim 50$  s) compression would allow the antiprotons distribution to follow that of the electrons. Figure 3.1 illustrates successful compression of the combined plasma. The antiproton distributions are imaged after removing the electrons, whereas the electron distributions are imaged in experiments where antiprotons were not allowed to enter the apparatus.

The measurements suggest that the antiprotons come into equilibrium with the electrons and that this equilibrium drives the antiproton cloud radius toward the electron plasma radius. Presumably the charges interact through collisionally mediated drag forces. Such *sympathetic* compression has been observed in laser controlled multispecies ion plasmas (Larson *et al.*, 1986).

### 3.2 Temperature diagnostic

In particular the evaporative cooling experiments described in chapter 5 requires accurate determination of the antiproton temperature. Precise absolute temperature measurements of positrons is also of great importance, as this temperature plays a key role in the antihydrogen formation process. In the following, the measurements of these temperatures will be described in detail. The temperature measurement itself affects the measured temperature, and in order to obtain the true temperature the particles had before the measurement, a set of corrections must be applied. Simple formulas for two such corrections are derived and applied to temperature measurements of antiprotons and positrons. The results are then compared to those obtained in simulations.

The temperature of both electrons, positrons, and antiprotons is measured in a destructive measurement in which one side of the confining potential is lowered and the particles released. Assuming that the particle cloud has reached thermal equilibrium, the particles that are initially released originate from the exponential tail of a Maxwell-Boltzmann distribution, and by mapping the time distribution of escaping particles to the applied blocking poten-

tial over which they escape, their energy distribution can be measured. This allows a fit to be used to determine the temperature of the particles. The technique described here is a simplified variation of the more general technique used to measure the parallel energy distribution of a magnetically confined electron plasma described in (Eggleston *et al.*, 1992).

Figures 3.5 and 3.6 shows examples of measured distributions of positrons and antiprotons. Note that it is custom to plot the integrated distribution, where the integration is done from the applied blocking potential  $qV_{vac}$  to infinity. From the figures it is evident that only the high energy part of the distribution has an exponential behavior. At lower energies the distributions bends over and can become flat. As described in (Eggleston *et al.*, 1992) this effect is due to the space charge  $\phi$  changing as trapped particles are lost. For this reason only the particles which escape while  $\phi$  can still be considered constant can be assumed to follow an exponential. Quantitatively the simple condition  $q\Delta\phi \ll k_B T$ , where  $\Delta\phi$  is an acceptable change in  $\phi$  compared to the temperature  $T$  of the sample, can be used to estimate the number of particles  $\Delta N$ , which can be used in a simple exponential fit. Defining the space charge per particle  $\phi_0 = \phi/N_0$ , where  $N_0$  is the initial number of particles, we can make the estimate  $\Delta\phi = \phi_0\Delta N$ , which allows us to calculate an upper limit for  $\Delta N$ :

$$\Delta N \ll \frac{k_B T}{q\phi_0}. \quad (3.1)$$

The value of  $\phi_0$  varies depending on the plasma dimensions and density. However, since  $\phi$  is proportional to  $N_0$  adding more particles to the distribution will not increase  $\Delta N$ . The temperature on the other hand directly affects the upper bound of  $\Delta N$ . The number of charges available for an exponential fit can easily be as low as a few tens or hundreds for low values of  $T$ , with a reasonable estimate being about a tenth of the upper limit:

$$\Delta N \approx \frac{1}{10} \frac{k_B T}{q\phi_0}. \quad (3.2)$$

In the exponential part of the distribution the temperature can easily be determined from its slope in a log plot. This can be seen by calculating  $d \ln(N_{esc})/d(qV_{vac})$ , where  $N_{esc}$  is the number of particles which have escaped at a particular block-

ing potential. Assuming the one dimensional energy distribution:

$$f(E)dE = \frac{1}{\sqrt{\pi k_B T} \sqrt{E}} e^{-\frac{E}{k_B T}} dE, \quad (3.3)$$

we get the approximate result:

$$\frac{d \ln(N_{esc})}{d(qV_{vac})} \approx -\frac{1}{k_B T}, \quad (3.4)$$

which is accurate to about 5% for  $E/k_B T \gtrsim 2$ .

It is possible to make use of the non-exponential part of the measured energy distribution to determine the temperature of the sample if more sophisticated fitting functions are used. These takes into account the change in space charge as particles escape. A detailed description can be found in (Beck, 1990). In addition a series of measurements performed on identical plasmas can be used to completely characterize the plasma self potentials and possible radial variations in the plasma temperature. This technique is described in (Eggleston *et al.*, 1992). Neither of these more elaborate techniques have been used to analyze the data presented in this thesis.

In order to release the particles to measure their energy distribution it is necessary to change the confining potential. In doing so, it is possible to do work on the confined particles, changing their energy, and to change the dimensions and density of the plasma. Thus the temperature determined directly from the measured energy distribution as described above, does not necessarily represent the temperature of the sample before the measurement. To correct for these so called *finite length effects* one can either attempt to treat each of the effects analytically to calculate a correction to the measured temperature, or simulations of the dynamics of the dump can be used to reproduce the measured data to obtain a correction. Both methods have strength and draw-backs. When treating the problem analytically one often has to make simplifications to obtain useful expressions and different effects are treated separately which can provide useful insight. Simulations on the other hand can in principle include the full set of dynamics and are more likely to include unidentified effects, however presently simulations are time consuming and does not readily help understanding the result. For this reason the method used here is a combination of both simulation and analytic calculation of the correction to the measured temperature. Two effects, important

for the very short plasmas often used in ALPHA, are described in sections 3.2.2 and 3.2.3 below. In addition two examples are used to illustrate how these corrections can be applied to temperature measurements of positrons (section 3.2.4) and antiprotons (section 3.2.5). The results are compared to those predicted by particle-in-cell (PIC) simulations performed by Francis Robicheaux. These simulations include the effect of the time dependent vacuum potentials and plasma self-fields, the possibility of evaporation, and energy exchange between the different translational degrees of freedom.

### 3.2.1 Experimental procedure

In the ALPHA apparatus two different systems are used to detect the released electrons, positrons, and antiprotons. Electrons and positrons are released onto the combined MCP and phosphor screen assembly where the MCP acts as a charge amplifier and the phosphor screen is used as a capacitor to collect the amplified charge. Measuring the voltage across the phosphor screen thus yields a signal proportional to the integral of the released charge. In principle this setup can also be used to measure the antiproton distribution. However, doing so has so far been unsuccessful due to the antiprotons being harder to guide through the apertures onto the MCP in the magnetic fringe field. Instead antiprotons are released onto the aluminium foil located in the upstream end of the apparatus. Here they annihilate and the annihilation signal is recorded using the upstream set of plastic scintillators. Doing so has the advantage of a background consisting of only a few counts per measurement but it suffers from a  $(25 \pm 10)$  % detection efficiency per annihilation.

During the dump one side of the confining potential is lowered in such a way that the escaping particles will gain a few eV of energy relative to ground as they move towards the target. It is our observation, that doing so helps guide the particles onto their target, and often this is achieved by simultaneously raising the bottom of the well and lowering one side. If for instance positrons are kept in a well below ground an intermediate step where the entire well is offset by a positive voltage is necessary.

The time scale of the dump is critical to ensure a good measurement of the energy distribution. A lower limit is set by the bounce time of the particles, since all particles at a particular energy must have time to escape before the

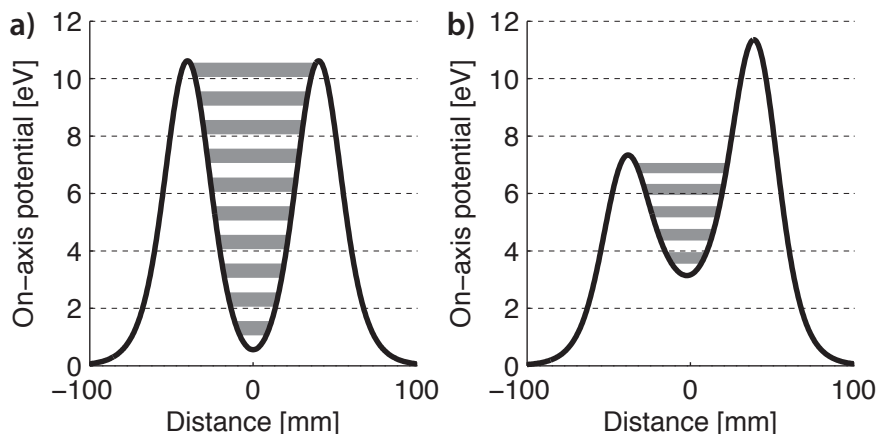


**Figure 3.2:** (a) Example of a confining on-axis potential. White and gray stripes are used to illustrate an energy spacing of 0.5 eV in the potential. (b) The left-most barrier has been partially lowered to allow confined charge to escape. The energy spacing shown in panel (a) has been reduced to  $\sim 0.4$  eV to conserve the single particle bounce invariant.

blocking potential changes significantly. Also this condition insures that the adiabatic invariant associated with the parallel motion of the particles is conserved for particles not yet released (see section 3.2.2 below for more details). However, in the ALPHA apparatus the lower limit is usually set by hardware limitations such as the electrode response time or saturation of the detection device. It is more difficult to set an upper limit for the time scale of the dump. The simplest choice is the collision time of the particles, since collisions will redistribute the energy of the remaining particles and cause premature loss of low energy particles through the process of evaporation. In practice it is desirable to dump the particles as fast as possible to minimize noise on the measurement and to ease the subsequent interpretation of the data. Typically, electrons and positrons are released within less than 1 ms with the entire dump taking 20 ms. Antiprotons are released within a few ms with the entire dump taking 100 ms.

### 3.2.2 Adiabatic correction

A single charged particle confined in a Penning-Malmberg trap will have a periodic motion associated with it moving along the magnetic field lines from one side of the potential to the other. A constant of this motion is the action integral:

$$J = \oint m v_{\parallel} ds, \quad (3.5)$$

where  $m$  is the mass of the particle,  $v_{\parallel}$  the speed of the particle in the direction of the magnetic field and  $ds$  an element of path length (of guiding center) along a magnetic field line. This quantity is known as the *Second adiabatic invariant* or the *Bounce invariant* and is defined for a half-cycle between the two turning points. If the potential is changed adiabatically with respect to the periodic motion,  $J$  is conserved, and in turn the conservation of  $J$  can lead to a non-conservation of the total energy  $E_{tot}$  of the particle (Chen, 1974).

We can express  $J$  in terms of the kinetic energy  $E_{\parallel} = \frac{1}{2} m v_{\parallel}^2$  of the particle, which, since the forces involved are conservative, equals  $E_{tot}$  minus the potential energy  $V$  of the particle. For a given potential  $J$  can then be calculated as:

$$J = \sqrt{2m} \int_a^b \sqrt{E_{tot} - V(z)} dz, \quad (3.6)$$

where the integration is done between the two end points  $a$  and  $b$  of the motion, in the direction of the  $z$ -axis, which is assumed to be parallel to the magnetic field. A simple approximation for  $J$  can easily be derived if  $V$  is assumed to be a square potential:

$$J \approx l \sqrt{2m E_{tot}}. \quad (3.7)$$

Here  $l = b - a$  is the bounce length of the particle. For a harmonic potential equation (3.7) is valid to second order in  $l$ .

When particles are released from a confining potential by lowering one of the side walls, the bounce length  $l_0$  at a fixed value  $E_0$  of  $E_{tot}$  will generally increase. If we define  $l$  as the length, and  $E$  as the energy of the particle such that  $J$  is conserved after the expansion, conservation of  $J$  for each individual particle predicts a decrease of  $E_{tot}$  during a dump to determine the temperature of a distribution of particles. Assuming the approximation (3.7) we get:

$$E = E_0 \left( \frac{l_0}{l} \right)^2 \approx E_0 \left( 1 - 2 \frac{\Delta l}{l_0} \right), \quad (3.8)$$

where  $\Delta l = l - l_0$ .

The temperature of the distribution is proportional to an energy difference  $\Delta E$  so from equation (3.8) we can obtain a relation between the original temperature  $T_0$  of the trapped particles and the temperature  $T$  measured when the charge is released:

$$T = T_0 \left( \frac{l_0}{l} \right)^2 \approx T_0 \left( 1 - 2 \frac{\Delta l}{l_0} \right). \quad (3.9)$$

Figure 3.2 illustrates how the energy distribution is compressed as one side wall is lowered to release the trapped particles, and since energy has been removed from the distribution the temperature  $T$  measured when the charge starts coming out will be lower than the original temperature  $T_0$  of the trapped particles.

Above, the effect of collisions has been ignored, which is only valid when the collisional time scale is long compared to the time scale of the dump. In this case the degree of freedom parallel to the magnetic field does not couple to the two degrees of freedom perpendicular to the magnetic field, and only the parallel part of the energy distribution is affected by the expansion. However, if the effect of collisions cannot be ignored during the dump, the energy lost as a result of expansion in the parallel direction will cause energy from the two perpendicular degrees of freedom to scatter into the parallel degree of freedom. In such collisions the conservation of  $J$  is broken.

In the simple case, where the length is increased much faster than the collisional time scale, whereupon the parallel and the perpendicular temperatures are allowed to rethermalize in the now longer well, equation (3.9) is simply modified to reflect equilibration of energy between all three degrees of freedom. For obvious reasons this is not the case when the particles are being released to measure their temperature:

$$T = T_0 \left( \frac{2}{3} + \frac{1}{3} \left( \frac{l_0}{l} \right)^2 \right) \approx T_0 \left( 1 - \frac{2}{3} \frac{\Delta l}{l_0} \right), \quad (3.10)$$

On the other hand, if the collisional time scale is much faster than the time scale of the dump,  $J$  is only conserved between collisions. This leads to a

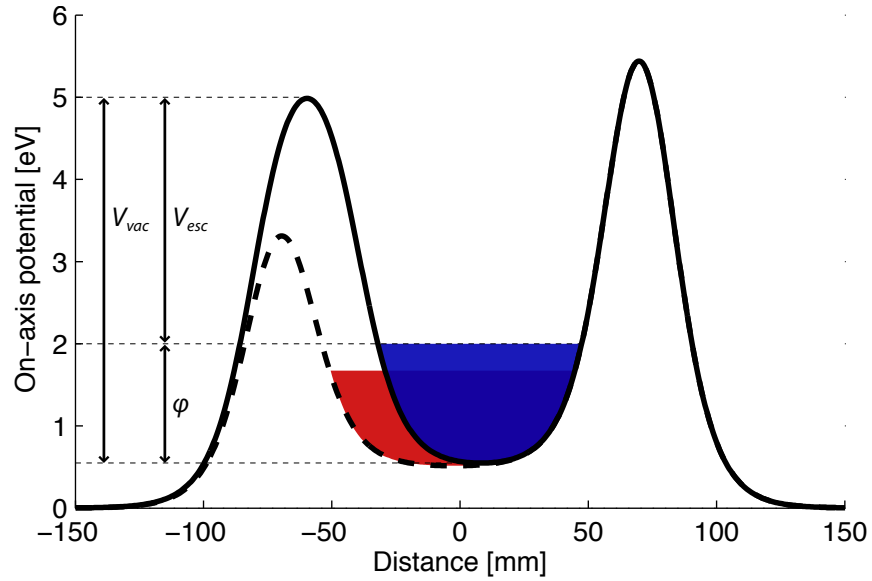


**Figure 3.3:** Example of an on-axis particle holding potential (fully drawn line) and a potential, where the left-most barrier has been partially lowered to allow confined charged to escape (dashed line). Space charge is shown as blue and red. When the barrier is lowered the well becomes longer, and the space charge level is lowered.

different dependence of the final temperature on the length:

$$T = T_0 \left( \frac{l_0}{l} \right)^{2/3} \approx T_0 \left( 1 - \frac{2}{3} \frac{\Delta l}{l_0} \right), \quad (3.11)$$

which for small values of  $\Delta l$  is in fact equal to the simple case above.

When the collection of trapped particles can be described as a plasma, the bounce length of each individual particle is strongly affected by the plasma self potential. In this case the appropriate length to use in the equations above is the length of the plasma.

### 3.2.3 Space charge correction

Another correction to the measured temperature is due to the level of space charge changing, as the confining well is morphed to release the trapped particles. Unlike the correction described in the previous section, this effect does

not directly affect the energy of the trapped particles. Instead it merely affects the mapping between a change in the vacuum well depth and the well depth as seen by the particles in the full electrostatic potential.

The space charge  $\phi$  of the confined particles reduce the depth of the confining potential and the escape barrier becomes:

$$V_{esc} = V_{vac} - \phi. \quad (3.12)$$

In the case where  $\phi$  can be considered a constant while the particles which carry temperature information are being extracted, the space charge will offset the measured energy distribution by approximately  $\phi$ . However, it will have no effect on the temperature inferred from a fit to the exponential part of the measured energy distribution. Indeed, since only the first few particles to escape are used to determine the temperature of the plasma, loss of particles will not cause the space charge to change significantly until the bulk is extracted.

What does cause the value of  $\phi$  to change, even without charge being lost, is the inevitable reshaping of the confining potential as one side is lowered. The reshaping of the well will cause the bounce length at a particular energy to increase, and for a plasma it will cause the length of the plasma to increase. This effect is illustrated in Figure 3.3. If we assume that the charge is evenly distributed in a cylinder of length  $l$  and constant radius  $r_0$ , an increase of the length  $\Delta l$  will cause  $\phi$  to be reduced by the amount:

$$\Delta\phi = -\frac{\phi}{l}\Delta l. \quad (3.13)$$

As described above, the temperature  $T$  inferred from the measured energy distribution is proportional to  $\Delta V_{vac}$ , while the real temperature of the distribution is proportional to  $\Delta V_{esc}$ . From equation (3.12) we see that a change in  $V_{vac}$  leads to a smaller change in  $V_{esc}$  when the space charge is reduced simultaneously:

$$\Delta V_{esc} = \Delta V_{vac} - \Delta\phi, \quad (3.14)$$

and thus we expect the original temperature  $T_0$  to be smaller than the measured temperature  $T$ . Note that  $\Delta V_{vac}$ ,  $\Delta V_{esc}$  and  $\Delta\phi$  are all negative quantities during a dump.

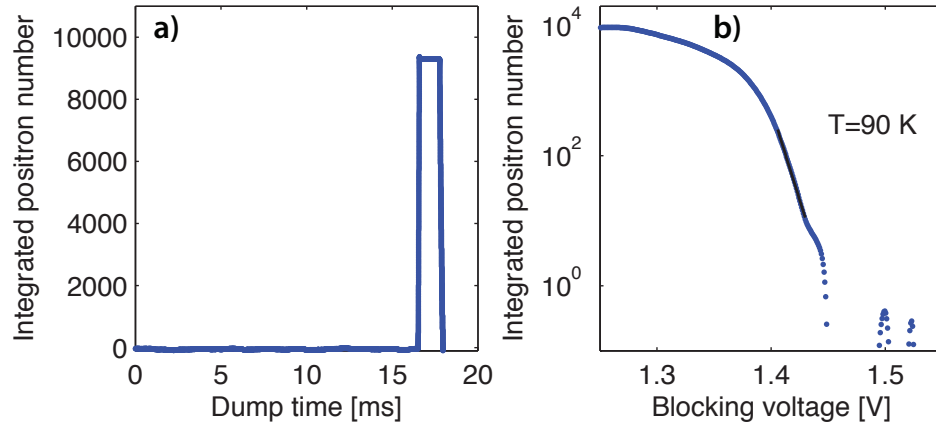


**Figure 3.4:** (a) Integrated number of positrons released vs. the dump time. The particles come out at approximately 16.6 ms (83 % into the dump). Notice that the signal amplifier saturates at  $\sim 10^4$  positrons. (b) The time in panel (a) has been mapped to the applied on-axis blocking voltage and the range of the axis has been reduced to show only the onset of the positron signal. Positron numbers have been corrected for a linear background and are displayed on a log scale. An estimate of the temperature is obtained from a fit to the exponential part of the curve and yields a temperature of 90 K.

Rewriting equation (3.14) in terms of the temperatures  $T_0$  and  $T$ , and inserting the above approximation of  $\Delta\phi$  we get the relationship:

$$T_0 = T \left( 1 + \frac{\phi}{l} \frac{\Delta l}{\Delta V_{vac}} \right), \quad (3.15)$$

between the two temperatures. Since  $\Delta V_{vac}$  is negative this means that the real temperature  $T_0$  is actually smaller than the measured temperature  $T$  as expected from the argument above. Note that  $\Delta l / \Delta V_{vac}$  should in principle be evaluated as the instantaneous plasma length change  $dl/dV_{vac}$  at the time when particles are escaping. Unfortunately, this can be tricky as  $dl/dV_{vac}$  diverges near the point where the bulk of the plasma escapes.

### 3.2.4 Example: Space charge dominated positron plasma

In the following a dump to determine the temperature of the positron plasma used in a 2009 mixing and trapping attempt will be described and used to

show how the two corrections described above can be estimated and applied to the measured temperature. Auxiliary measurements have been used to determine the positron number and radial distribution. These measurements show that the sample contains about 4 million positrons and a self-consistent solution to the Poisson-Boltzmann equation suggests a peak density of  $7 \times 10^7 \text{ cm}^{-3}$  and a space charge of about 2.1 V, which gives an initial barrier voltage of about 0.5 V.

Since the potential used to confine the positrons is a nested potential below ground, an intermediate step is introduced to both lift the positrons above ground and to remove the side walls intended to store antiprotons. The positrons are stored for 10 ms in the 49 V deep pre-dump potential well to allow thermalization between the parallel and the perpendicular degrees of freedom, before they are released onto the combined MCP and phosphor screen, where they are detected. The dump takes 20 ms total, but since the positron space charge is small compared to the depth of the well, they are released late in the dump as shown in Figure 3.4(a). Figure 3.4(b) shows how the temperature is determined from the time distribution which have been mapped to the applied on-axis blocking voltage. In this case, the measured temperature is 90 K and the space charge at the time when particles are released can be estimated to be about 1.4 V. The later value is lower than expected from equilibrium calculations. Inserting these values in equation (3.2) the estimated number of particles in the exponential part of the distribution is about 2000, on the figure the trace starts to be noticeably non-exponential after the first 1,000 particles have escaped.

Figure 3.5 illustrates how the original energy distribution maps to the measured distribution assuming conservation of the single particle bounce invariant (equation (3.6)). The point at which the first charges are released has been estimated as the point at which a particle at the level of the 2.1 V space charge estimate would escape. At this point the single particle bounce length is about 80% of the original length. Assuming equation (3.11) this slight compression gives a correction factor of  $(1/0.8)^{2/3} = 1.16$  from conservation of the second adiabatic invariant. The depth of the potential is 3.7 V and it has a maximum length of 25 mm with  $dl/dV_{vac} \approx -2.5 \text{ mm/V}$ , which when used in equation (3.15) gives a correction factor of  $(1-3.7 \text{ V}/25 \text{ mm} \times 2.5 \text{ mm/V})=0.63$  due to the

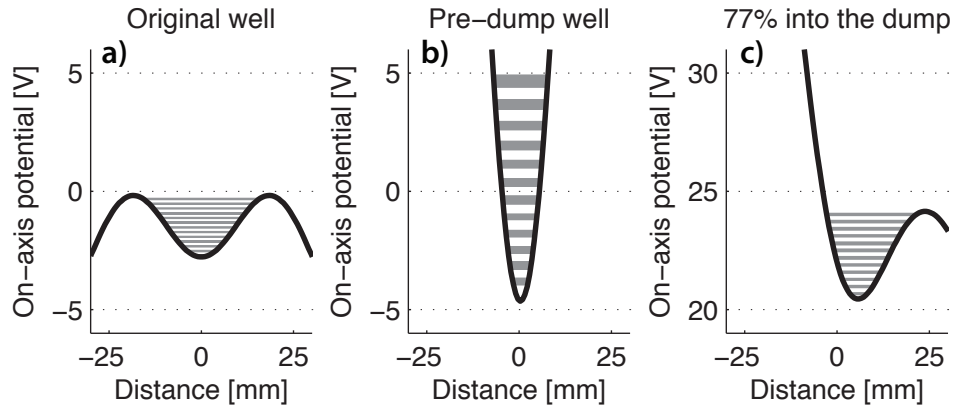


**Figure 3.5:** (a) Initial positron holding potential. White and gray stripes are used to illustrate an energy spacing of 0.1 eV in the potential. (b) Intermediate 49 V deep pre-dump potential. The energy spacing of panel (a) has been compressed adiabatically assuming conservation of the single particle bounce invariant. (c) 77% into the dump. The first positrons are assumed to escape at this point. As in panel (b) the energy spacing has been mapped adiabatically from (a).

space charge moving as the plasma length expands. Thus the original temperature of the sample is expected to be lower than the measured temperature by a factor of  $(1/1.16) \times 0.63 = 0.54$  i.e.  $T_0 = 0.54 \times 90 \text{ K} = 49 \text{ K}$ . A simulation of the dump yields a correction factor, which is in very good agreement with the above estimate.

In the above example both corrections were in the direction of a lower original temperature, which leads to a large combined correction factor. Often it is the case that the two corrections will be in opposite directions, as the length usually increase when going from the initial potential to the potential at which particles escape. In such cases conservation of the bounce invariant leads to a lower measured temperature while the correction due to the space charge moving leads to a higher measured temperature. However, the intermediate potential used in this example causes the length to be reduced by a large factor, which is not wholly canceled by the subsequent expansion (see Figure 3.5).

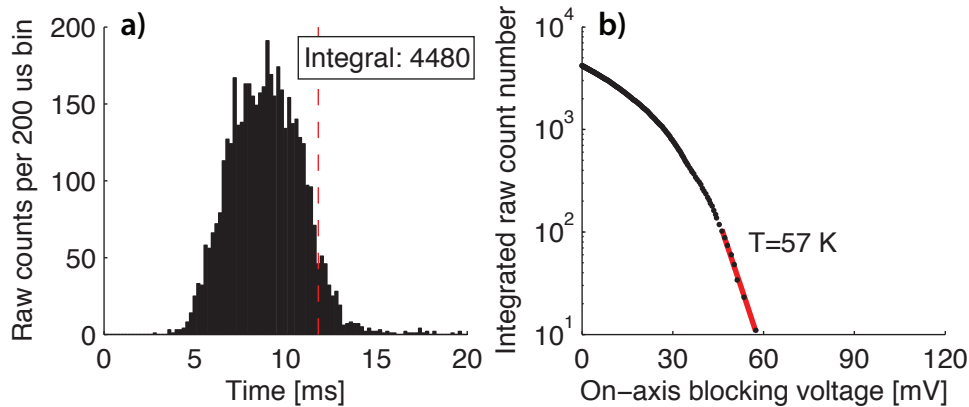


**Figure 3.6:** (a) Number of detected antiproton annihilations vs. time during a dump to determine the temperature of the antiproton distribution. The total number of antiprotons released is obtained by correcting for the 25% detection efficiency. The time at which the well disappears on axis is indicated by the (red) dashed line. (b) The time distribution has been integrated and plotted against the applied on-axis blocking voltage. The well depth is ramped from high to low; thus, time flows from right to left in the figure. A fit to the exponential part of the distribution is used to determine its temperature. (Adapted from Andresen *et al.*, 2010c)

### 3.2.5 Example: Antiproton dump

The following example illustrates a typical dump to determine the temperature and total number of a sample of antiprotons. The initial potential used to store the antiprotons has a depth of  $V_0 = 116$  mV and is the final potential of an evaporative cooling ramp (see chapter 5). The antiprotons have been stored in this potentials for 10 s prior to the measurement. Like in the example above auxiliary measurements have been used to determine the antiproton radial distribution and a self-consistent solution to the Poisson-Boltzmann equation suggests a peak density of  $3 \times 10^6$  cm $^{-3}$  and a space charge of about 30 mV.

Unlike the above example no intermediate potential is used prior to the dump. The initial potential is already below ground, and as one side of the well is lowered (see Figure 3.7(a)), the particles are released directly onto the aluminium foil where they annihilate. Figure 3.6(a) shows the number of detected annihilations against time, and we see that all particles are re-

leased within the first 15 ms of the 100 ms dump. Correcting for the 25% detector efficiency the total number of antiprotons can be determined to be  $4480/0.25 \approx 18000$ . In Figure 3.6(b) the measured distribution has been integrated in time and mapped to the applied on-axis blocking voltage. A fit to the exponential part of the distribution yields a measured temperature of 57 K. About 100 signal counts were used to determine the temperature, a number which could be improved by increasing the annihilation detection efficiency. The upper bound on the useful number calculated from equation (3.2) is  $(18000/10) \times (57 \text{ K}/30 \text{ mV})(k_b/e) \approx 310$ .

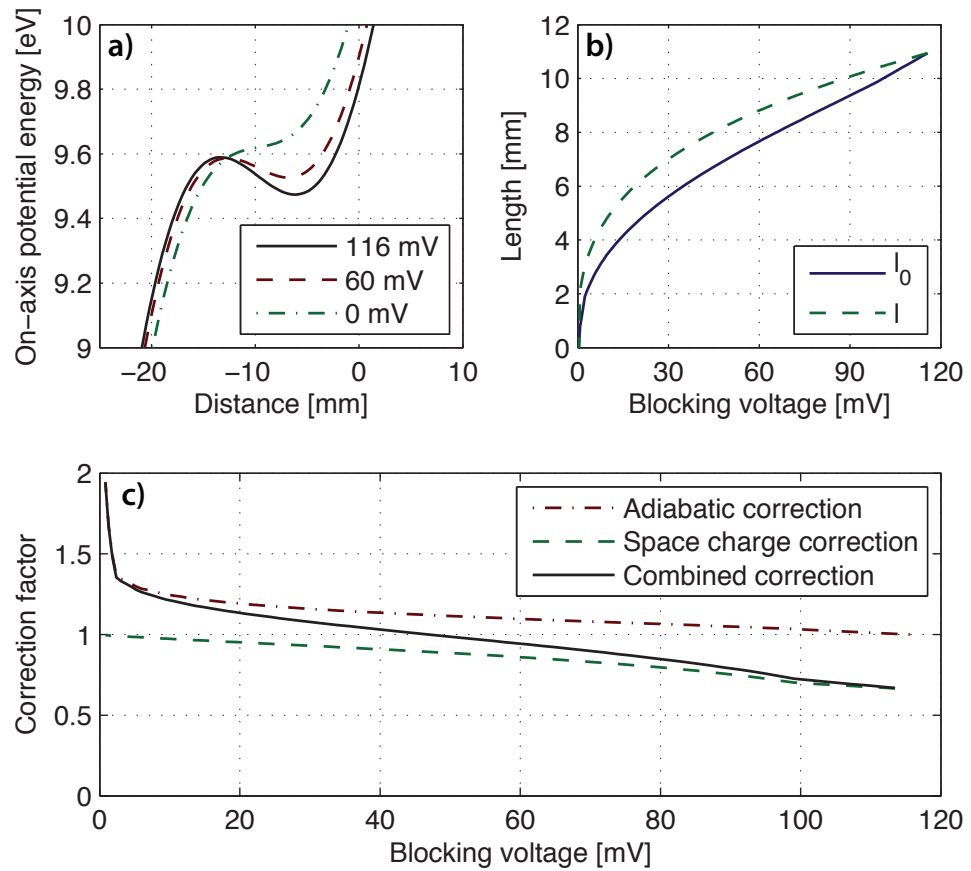
The time at which the first particles escape can be shifted for a constant temperature and number of particles. This is done by varying the space charge potential which is proportional to the particle density. Assuming that the particles, used to determine the temperature, escape at a particular blocking voltage  $V_{esc}$ , the two correction factors described above can be estimated by calculating the change in bounce length. Figure 3.7(b) shows the bounce length  $l$  of a single particle just about to escape, and the bounce length  $l_0$  in the initial potential is calculated assuming conservation of the bounce invariant (equation (3.7)). The ratio  $l/l_0$  determines the adiabatic correction factor as shown in section 3.2.2, here equation (3.11) is used. A rough estimate of the correction due to changes in the space charge potential of  $1 + (V_{esc}/l)(\Delta l/\Delta V)$  can be obtained using a simplified version of equation (3.15). Here the space charge  $\phi$  has been assumed to equal  $V_{esc}$ ,  $\Delta V = V_{esc} - V_0$  and  $\Delta l = l - l_0$ .

Figure 3.7c shows a calculation of the above estimates of the two correction factors together with the combined factor. The two separate correction factors are in opposite directions with the adiabatic correction dominating if the first particles escape at low blocking voltages whereas the space charge correction dominates at high blocking voltages. Around 60 mV where charge actually escapes in the data shown in Figure 3.6 the two correction factors roughly balance each other. Simulations to determine the combined factor yields measured temperatures which are about 15% higher than the true temperature.

It is important to note that to determine the magnitude of the two correction factors above only the two lengths  $l$  and  $l_0$  were used. If, like in example 3.2.4 above, an intermediate step, where the confining potential is morphed before the dump starts, is introduced, a third length, say  $l'$ , enters. In this case

---

the adiabatic correction factor is still determined by the ratio  $l/l_0$ , however, to determine the space charge correction  $\Delta l$  should be calculated as  $l - l'$ . Often  $l'$  and  $l$  can be tuned while  $l_0$  is determined by the type of experiment being diagnosed. Knowing the approximate temperature and space charge, such tuning can be used to tailor a dump where the combined correction factor is close to one, reducing the need of calculating the exact factor.



**Figure 3.7:** (a) The applied on-axis potential used to hold the antiprotons. The potential is plotted at three different stages of the dump: the initial potential (116 mV), 4.3 ms into the dump (60 mV) and 15 ms into the dump (0 mV). Each curve is labeled by the on-axis blocking voltage. (b) Single particle bounce length vs. the applied on-axis blocking voltage. The curve labeled  $l$  shows the bounce length of a single particle just about to escape and the bounce length  $l_0$  in the initial potential is calculated assuming conservation of the bounce invariant (equation (3.7)). (c) An estimate of the correction factor which should be applied to the measured temperature to obtain the original temperature is plotted against the applied on-axis blocking voltage (see text). The two contributing factors are plotted together with their product.

# Forced evaporative cooling of ions confined in a Penning-Malmberg trap

---

The process of evaporation is a well-known phenomenon in everyday life, and it is usually associated with a liquid converting to the gaseous state. Microscopically, a particle in the liquid can only evaporate if it gains enough energy to overcome the binding energy of the liquid. This happens naturally since there are always high energy particles in the Maxwell-Boltzmann distribution. The warmer the liquid the faster it will evaporate. Evaporation results in cooling of the liquid, since the evaporating particles carries away more than the average energy of a particle in the liquid, which in turn leads to a slower rate of evaporation. To control the rate of evaporation, the process can be forced. Either by heating the liquid or by manipulating the binding energy of the liquid.

In a more general sense, the term evaporation can be used to describe the process of energetic particles leaving a system with a finite binding energy, and, historically, forced evaporative cooling has been successfully applied to cool trapped samples of neutral atoms to sub-Kelvin temperatures (Hess, 1986), and remains the only route to achieve Bose-Einstein Condensation (BEC) (Anderson *et al.*, 1995). However, the technique has only found limited applications for trapped ions (at temperatures  $\sim 100$  eV (Kinugawa *et al.*, 2001)) and has not before been realized in cold plasmas.

Access to pure samples of low temperature antiprotons can ease formation of low temperature antihydrogen, and while antiprotons can be collisionally

cooled in a cryogenic electron plasma, the electrons must be removed before the antiprotons are mixed with a positron plasma to form antihydrogen. Electrons can deplete the positron plasma through positronium formation, destroy antihydrogen atoms through charge exchange, or partially neutralize and destabilize the positron plasma (Peurrung *et al.*, 1993). We also find that the relevant electron plasmas do not necessarily reach thermal equilibrium with their cryogenic surroundings (7.5 K), as they are subject to heating by electronic noise, plasma instabilities, and leakage of thermal radiation from higher temperature surfaces. After significant study and optimization, pulsed electric field removal of electrons in our apparatus results in antiproton temperatures of 200-300 K at best.

In the first part of this chapter, a simple theoretical framework is used to describe forced evaporative cooling in general and evaporation of ions is compared to that of atoms. Later, details more specific to evaporation of ions will be described. The aim of the chapter is to identify and include the dynamics particular to evaporation of antiprotons trapped in a Penning-Malmberg trap. In chapter 6 these are included in a numerical model to describe forced evaporative cooling, and the results of evaporative cooling experiments performed in the ALPHA apparatus (see chapters 5) are discussed in the context of these effects.

## 4.1 Comparing evaporation of ions and atoms

There are two very important differences between evaporative cooling of ions and neutral atoms. Not surprisingly, both are related to the charge of the ion.

The first and most obvious difference is due to the different interactions used to confine atoms and ions. Atoms used in evaporative cooling experiments are typically confined in magnetostatic traps which rely on the magnetic dipole moment of the atom for confinement (see section 1.2.3). The coupling is weak, and large magnetic fields are required to create even small confining potentials. As an example the maximum depth of the ALPHA magnetostatic trap, which employs state of the art superconductor technology, is a mere  $0.5 \text{ K} \times k_B$  or  $43 \text{ } \mu\text{eV}$  deep for ground state (anti)hydrogen. On the

other hand, the Penning-Malmberg trap used to confine charged particles in the same apparatus, can create electrostatic wells for particles with a single charge with a depth of up to 40 to 60 million  $\text{K} \times k_B$  using high voltage electrodes energized to 4 to 5 keV. As a consequence the magnetostatic trap can easily be operated at a sub-Kelvin scale; a simple change of 1 A in the superconductor corresponds to about  $0.5 \text{ mK} \times k_B$  change in the trap depth. In contrast, to create a  $1 \text{ K} \times k_B$  deep electrostatic well for antiprotons requires a voltage control better than about  $100 \mu\text{V}$  which is very difficult at best. The minimum temperature which can be achieved by means of forced evaporative cooling is on the order of 1/10 of the minimum well depth one can create. For antiprotons trapped in the ALPHA apparatus this means that to even approach temperatures close to the depth of the magnetostatic trap the voltage control capabilities of the Penning-Malmberg trap must be stretched to its limit.

The second reason why evaporative cooling of ions is fundamentally different to that of atoms is the fact that the ions can interact over long distances through the Coulomb interaction. This interaction causes the elastic collision rate of ions to be much higher than that of neutrals of similar density and temperature making evaporative cooling of much lower numbers and densities of particles feasible. In addition, intraspecies loss channels from inelastic collisions are non-existent. However, the electric field generated by each individual trapped particle gives rise to a non-zero mean field which must be added to the confining electric field generated by the trap electrodes. The combined confining potential will always have a smaller depth than due to the vacuum potential alone. If the magnitude of the ion self-field becomes a substantial fraction of the vacuum well depth, it makes controlling the well depth non-trivial. The ion self field will generally be largest in the spatial center of the ion distribution. This can cause the effective well depth to be larger at the edge of the ion cloud and evaporation to occur primarily from the cloud center. The consequence of such localized evaporation can be local depletion of ion density and destabilization of the entire cloud. In a Penning-Malmberg trap evaporation from the center only, can cause the cloud to expand radially due to conservation of total angular momentum. The effect of the ion self field is strongest when the cloud can be characterized as a plasma.

## 4.2 The dynamics of evaporation

In the standard theory of evaporation of trapped atoms as presented in (Ketterle and Van Druten, 1996), two coupled first order differential equations are used to link particle loss to temperature:

$$\frac{dN}{dt} = -\frac{N}{\tau_{ev}}, \quad (4.1)$$

$$\frac{dT}{dt} = -\alpha \frac{T}{\tau_{ev}}. \quad (4.2)$$

Here  $N$  is particle number,  $T$  temperature,  $t$  time,  $\tau_{ev}$  the time constant of evaporation, and  $\alpha$  the ratio of the average excess energy carried away by an escaping particle to the average energy of a trapped particle. At the end of this chapter these equations are modified to include effects particular to evaporation of ions from a Penning-Malmberg trap.

When computing  $\alpha$  and  $\tau_{ev}$  it is convenient to use a set of dimensionless parameters:  $\eta$ ,  $\kappa$  and  $\delta$ . The most important of the three is  $\eta$ , which is defined as the ratio between the potential barrier a particle must overcome to escape the well and Boltzmann's constant times the temperature:

$$\eta = \frac{eV}{k_B T}. \quad (4.3)$$

Here the unit of the potential barrier  $V$  is in volts.

The sum  $(\eta + \kappa)k_B T$  is the average energy of a particle escaping the well, and  $\kappa$  is a measure of how much a particle overshoots the potential barrier on average. Any additional energy carried away in degrees of freedom not directly coupled to the barrier, is also included in  $\kappa$ . The expression  $(\delta + 3/2)k_B T$  is the average energy of a trapped particle with three translational degrees of freedom. In a 3D-harmonic potential  $\delta = 3/2$ , and in a 1D-harmonic potential  $\delta = 1/2$ . A square well would have  $\delta = 0$ . Returning to the definition of  $\alpha$  from above, we can now write:

$$\alpha = \frac{\eta + \kappa}{\delta + 3/2} - 1. \quad (4.4)$$

Typically values of  $\alpha$  is a few, say 5 or less, and to achieve efficient cooling from evaporation  $\alpha$  should be maximized.

By eliminating  $\tau_{ev}$  from equations (4.1) and (4.2) we see that  $\alpha$  is the slope of the curve defined by  $(N(t), T(t))$  in a log-log plot:

$$\frac{d \ln T}{d \ln N} = \alpha. \quad (4.5)$$

From this equation we see that with a constant  $\alpha$  of 5, a one order of magnitude decrease in number would lead to a five order of magnitude decrease in temperature<sup>1</sup>. However, for evaporation of ions this relation is modified and the slope of the curve  $(N(t), T(t))$  in a log-log plot is no longer equal to  $\alpha$  (see section 6.1.2).

### 4.2.1 Dimension of evaporation

Often the escape barrier for particles trapped in a potential well will not be equally high in all directions, and evaporation will be limited to the directions where the barrier is sufficiently low. In such a situation it is not enough for a particle to acquire enough energy to overcome the barrier, the particle must also be moving in the right direction. This limits the volume in velocity space a particle can escape from, and in turn increases the time scale of evaporation. If we let  $\vec{v} = (v_x, v_y, v_z)$  denote the velocity of a particle we can define a barrier for each of the three velocity components. The dimension of evaporation can then be defined as the number of barriers a particle can realistically overcome. As we shall see in section 4.3 the evaporation time scale depends exponentially on  $\eta$ , and thus a small difference in barrier height for each velocity component can cause one direction to dominate.

The dimension of evaporation can, in principle, be non-integer if the potential barrier along a certain direction changes in space. A dimension of evaporation lower than 1 can be an issue for a plasma where the self-fields are large compared to the escape barrier.

### 4.2.2 Ion evaporation from a Penning-Malmberg trap

Ions trapped in a Penning-Malmberg trap are confined radially by strong magnetic fields and conservation of total angular momentum prevents par-

---

<sup>1</sup>Reality is not that generous.

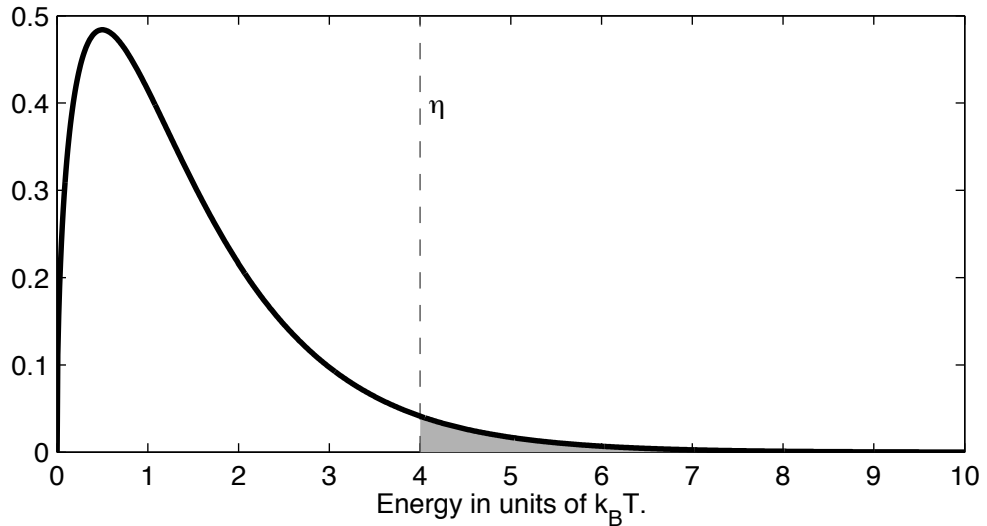


**Figure 4.1:** Maxwell-Boltzmann energy distribution with three harmonic degrees of freedom. In a truncated distribution particles in the (grayed out) high energy tail above the threshold  $\eta$  are removed.

ticles from escaping radially. Axially the particles are confined by electric potential wells, and if the value of  $\eta$  for a given potential configuration and temperature is low enough, particles have a finite chance of escaping along the trap axis by evaporation. In this case the dimension of evaporation is one.

The average energy carried away by an escaping particle is  $(\eta + \kappa)k_B T$ , where  $\eta$  is set by the depth of the potential well in the axial direction, and  $\kappa$  is the average energy, in units of  $k_B T$ , along the two translational degrees of freedom transverse to the magnetic field plus a small number (between 0 and 1) to account for particles overshooting the potential barrier (Ketterle and Van Druten, 1996). Often the applied axial potential can be approximated by a harmonic potential and  $\delta \approx 1/2$ . However, the plasma self-field can flatten the potential seen by the particles substantially, and as a consequence  $\delta$  can be smaller than  $1/2$ , close to that of a square potential.

### 4.3 The evaporation time scale $\tau_{ev}$

During evaporation the finite depth of the confining potential results in an energy distribution truncated at the depth of the well (see Figure 4.1). However, if  $\eta$  is large, the truncated energy distribution can be assumed to closely resemble a complete Maxwell-Boltzmann distribution. In this case the rate of evaporation can be linked to the rate at which particles with an energy of more than  $\eta k_B T$  are produced through elastic collisions in the untruncated distribution. By the principle of detailed balance such particles are produced at the same rate as particles with an energy larger than  $\eta k_B T$  are removed from the high energy tail of the distribution by collisions. Assuming that every collision involving a particle in the high energy tail removes that particle from the tail, we can calculate the evaporation rate as the number of particles with an energy larger than  $\eta k_B T$  divided by their collision time. Note that if evaporation only happens along one dimension only particles with sufficient energy along that particular dimension should be considered (Ketterle and Van Druten, 1996).

#### 4.3.1 Example: The evaporation time scale for atoms (3D)

For a distribution of  $N$  atoms of constant density  $n$ , where the cross section  $\sigma$  for a collision can be assumed to be independent of the atom velocity, it is easy to make an estimate of the evaporation time scale. Assuming a Maxwell-Boltzmann energy distribution with three harmonic degrees of freedom, the fraction  $f$  of atoms with an energy greater than  $\eta k_B T$  approaches  $2e^{-\eta} \sqrt{\eta/\pi}$  (for  $\eta$  greater than  $\sim 4$ ), and the collision time for the atoms in the high energy tail can be estimated as  $n\sigma v_\eta$ , where  $v_\eta$  is the velocity of atoms with energy  $\eta k_B T$ . Introducing  $\bar{v}$  as the average velocity of atoms in the distribution,  $v_\eta$  can be calculated as  $\sqrt{2\eta k_B T/m} = \sqrt{\pi\eta} \bar{v}/2$ . As described above, we can now calculate the rate of collisions involving an atom in the high energy part of the untruncated distribution, and thus the loss due to evaporation in the truncated distribution:

$$\frac{dN}{dt} = -fNn\sigma v_\eta = -n\sigma \frac{\eta}{e^\eta} \bar{v} N \equiv -\frac{N}{\tau_{ev}}. \quad (4.6)$$

This relation defines the evaporation time constant  $\tau_{ev}$ , and in units of the average collision time  $\tau_{el}$  in the distribution the evaporation time constant

can be expressed as the dimensionless parameter  $\lambda$ :

$$\lambda = \frac{\tau_{ev}}{\tau_{el}} = \sqrt{2} \frac{e^\eta}{\eta}, \quad (4.7)$$

where  $1/\tau_{el} = n\sigma \sqrt{2}\bar{v}$ . Here  $\sqrt{2}\bar{v}$  is the average relative velocity between two atoms (Ketterle and Van Druten, 1996).

### 4.3.2 Example: The evaporation time scale for ions (3D)

As in the case of atoms, we can determine the rate of ions crossing the energy boundary  $\eta k_B T$  in an untruncated Maxwell-Boltzmann distribution to calculate the evaporation rate for a distribution truncated at that energy. However, for an ion in the distribution the elastic collision cross section is highly dependent on the speed of the ion, and thus it is appropriate to perform the calculation in velocity space instead. In the case of three dimensional evaporation the ion speed boundary becomes  $v_\eta = \sqrt{2\eta k_B T/m}$ , and the rate of ions leaving the high energy tail can then be written as:

$$\left. \frac{dN}{dt} \right|_{v=v_\eta} = - \left( \frac{dN}{dv} \frac{dv}{dt} \right) \Big|_{v=v_\eta}, \quad (4.8)$$

where  $dN/dv$  is simply the Maxwell-Boltzmann distribution of speeds with temperature  $T$ :

$$\frac{dN}{dv} = N 4\pi v^2 \left( \frac{m}{2\pi k_B T} \right)^{3/2} e^{-\frac{mv^2}{2k_B T}}, \quad (4.9)$$

and  $dv/dt$  is the relaxation rate for slowing down an ion in such a distribution. The later is given in (Huba, 2009) and for ion-ion self collisions it reduces to:

$$\frac{d\vec{v}}{dt} = - \frac{2(eZ)^4 n \ln \Lambda}{4\pi \epsilon_0^2 m^2} \frac{\vec{v}}{v^3}, \quad (4.10)$$

when  $v$  can be assumed to be large compared to the characteristic thermal velocity of the distribution  $v_{th} = \sqrt{2k_B T/m}$ . Here  $eZ$  is the ion charge,  $n$  the density, and  $\ln \Lambda$  the Coulomb logarithm. The later is discussed in further detail in section 4.4.1.

Inserting equations (4.9) and (4.10) in equation (4.8) above, we get the following rate of three dimensional evaporation from a distribution of ions:

$$\frac{dN}{dt} = -N e^{-\eta} \frac{\sqrt{2}(eZ)^4 n \ln \Lambda}{\pi^{3/2} \epsilon_0^2 \sqrt{m} (k_B T)^{3/2}}. \quad (4.11)$$

As done in the example of three dimensional evaporation of atoms, we can now define the evaporation time constant  $\tau_{ev}$  and calculate the dimensionless parameter  $\lambda$  as the ratio:

$$\lambda_{3D} = \frac{\tau_{ev}}{\tau_{col}} = \frac{1}{12}e^\eta, \quad (4.12)$$

where  $\tau_{col}$  is the ion-ion collisional time scale for momentum transfer between test ions with speed  $v_{th} = \sqrt{2K_B T/m}$  and the field particles in the distribution. For a plasma in a low magnetic field  $\tau_{col}$  can be written as (Hinton, 1983):

$$\tau_{col} = \frac{6\sqrt{2}\pi^{3/2}\epsilon_0^2\sqrt{m}(k_B T)^{3/2}}{n(Ze)^4 \ln \Lambda}. \quad (4.13)$$

In earlier work by (Fussmann *et al.*, 1999) and (Kinugawa *et al.*, 2001) this expression for  $\tau_{col}$  is used. However, for antiproton plasmas with low temperatures which are immersed in a high magnetic field a more general expression must be used as the plasma can become magnetized (see section 4.4).

The result for three dimensional evaporation from a distribution of ions can be directly compared to that obtained for atoms by comparing  $\lambda$  for the two cases. Doing so shows that the evaporation time scale is a factor of  $\eta$  longer for ions for distributions with similar collision frequencies. This discrepancy is due to the different collisional dynamics in the two cases. For atoms the collision frequency is simply proportional to the speed of the atom, which means that faster atoms will collide more often than the average atom. The collision frequency for fast moving ions on the other hand is suppressed by a factor of  $v^2$  as is seen from equation (4.10).

### 4.3.3 Example: The evaporation time scale for ions (1D)

In a Penning-Malmberg trap such as the ALPHA apparatus, ions can only escape the confining potential parallel to the magnetic field lines, thus evaporation can only occur along one dimension. In this case the ions must have a velocity of  $v_{\parallel} = \sqrt{2k_B T/m}$  parallel to the magnetic field to cross the boundary in velocity space and evaporate from the trap. Again we can calculate the rate of ions crossing this boundary in the direction of lower speed in an untruncated Maxwell-Boltzmann distribution to obtain the rate of evaporation in the truncated distribution. In this case it is most easily done in cartesian velocity

coordinates  $\vec{v} = (v_x, v_y, v_z)$ , where  $v_z$  is the coordinate parallel to the magnetic field.

The evaporation rate can now be written as:

$$\left. \frac{dN}{dt} \right|_{|v_z|=\bar{v}_\parallel} = 2 \iint dv_x dv_y \left. \frac{dN_{v_x v_y}}{dt} \right|_{v_z=v_\parallel}, \quad (4.14)$$

where the integrand is the evaporation rate from a small volume element at  $\vec{v} = (v_x, v_y, v_\parallel)$  in velocity space and the factor 2 comes from including both negative and positive values of  $v_z$ . Using the chain rule of differentiation we can write:

$$\frac{dN_{v_x v_y}}{dt} = - \frac{dN_{v_x v_y}}{dv_z} \frac{dv_z}{dt}. \quad (4.15)$$

The first factor on the right hand side is then the Maxwell-Boltzmann velocity distribution with temperature  $T$ :

$$\frac{dN_{v_x v_y}}{dv_z} = N \left( \frac{m}{2\pi k_B T} \right)^{3/2} e^{-\frac{m(v_x^2 + v_y^2 + v_z^2)}{2k_B T}} \quad (4.16)$$

and the second factor is simply the third component of equation (4.10).

Unfortunately, actually solving the integral (4.14) requires integrating a function of the form  $e^{-x^2}/(x^2 + a^2)^{3/2}$ , which have no analytic solution. Instead we can make the approximation  $v_z/v^3 = 1/v_z^2$  in equation (4.10), which is an upper bound. In this case the evaporation rate takes the form:

$$\frac{dN}{dt} = -N \frac{e^{-\eta}}{4\eta} \frac{\sqrt{2}(eZ)^4 n \ln \Lambda}{\pi^{3/2} \varepsilon_0^2 \sqrt{m} (k_B T)^{3/2}}, \quad (4.17)$$

which is a factor of  $1/(4\eta)$  lower than the rate for three dimensional evaporation (equation (4.11)). The same factor has been obtained from geometrical considerations in (Ketterle and Van Druten, 1996). The value of the evaporation time constant is increased accordingly, giving a  $\lambda$  of:

$$\lambda_{1D} = \frac{\tau_{ev}}{\tau_{col}} = \frac{1}{3} \eta e^\eta, \quad (4.18)$$

Note that the evaporation time constant calculated here is a factor of  $\sqrt{2}$  lower than that obtained through a similar derivation in (Fussmann *et al.*, 1999) and used in (Kinugawa *et al.*, 2001). I believe the above result to be correct, however, the difference has no great practical implications.

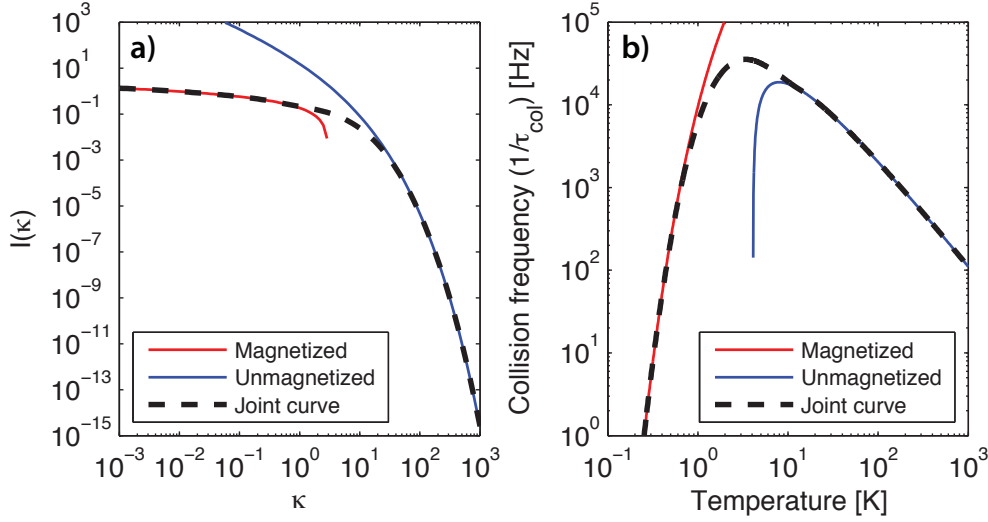


**Figure 4.2:** (a) Evaluation of  $I(\bar{\kappa})$  for a plasma of antiprotons in a 1 T field. Three cases are shown: A magnetized plasma ( $\bar{\kappa} \ll 1$ ), an unmagnetized plasma ( $\bar{\kappa} \gg 1$ ), and equation (4.22) joining the two. (b) Collision frequency for antiprotons of density  $5 \times 10^6 \text{ cm}^{-3}$ . Note that  $\bar{\kappa} = 1$  for a temperature of 8.5 K.

#### 4.4 The collision time constant $\tau_{col}$

For a nonneutral plasma immersed in a uniform magnetic field of magnitude  $B$ , the ion-ion collisional time scale depends on whether the plasma can be considered to be *highly correlated*, such as in a Coulomb crystal, or if the plasma is *uncorrelated*. The former is also called a *magnetized* plasma and the latter an *unmagnetized* plasma. Following the treatment in (Glinsky *et al.*, 1992), the two regimes can be characterized by the parameter  $\bar{\kappa} = (\bar{b}/r_c)$ , where  $\bar{b} = 2e^2/4\pi\epsilon_0k_B T$  is twice the distance of closest approach and  $r_c = v_{th}/\Omega_c$  the cyclotron radius.  $v_{th} = \sqrt{2k_B T/m}$  is the thermal velocity and  $\Omega_c = eB/m$  the cyclotron frequency. For a strongly magnetized plasma ( $\bar{\kappa} \gg 1$ ) the collisional rate is exponentially small, and for a weakly magnetized plasma ( $\bar{\kappa} \ll 1$ ) the rate is similar to that of an unmagnetized plasma (see equation (4.13)). Antiprotons in a 1 T magnetic field have  $\kappa = 1$  for a temperature of 8.5 K. For electrons and positrons the corresponding temperature is 104 K due to their smaller mass.

The collision frequency  $\nu_{col} = 1/\tau_{col}$  can be written in a simple form where

the magnetic field  $B$  only enters through a function  $I(\bar{\kappa})$ :

$$v_{col} = \frac{5}{\sqrt{2}} n \bar{b}^2 v_{th} I(\bar{\kappa}). \quad (4.19)$$

Here  $n$  is the density, usually the peak density, and  $\bar{b}$  and  $v_{th}$  depends only on the temperature. The factor  $5/\sqrt{2}$  is necessary to make  $v_{col}$  coincide with the asymptotic expression (equation (4.13)). In (Glinsky *et al.*, 1992) where  $I(\bar{\kappa})$  is determined a slightly different prefactor is used. For completeness the two asymptotic expressions for  $I(\bar{\kappa})$  are given below. The former is for a magnetized plasma, the later for an unmagnetized plasma:

$$I_{magnetized}(\bar{\kappa}) \approx \exp\left[\frac{-5(3\pi\bar{\kappa})^{2/5}}{6}\right] \left(1.83 \cdot \bar{\kappa}^{-7/15} + 20.9 \cdot \bar{\kappa}^{-11/15} + 0.347 \cdot \bar{\kappa}^{-13/15} + 87.8 \cdot \bar{\kappa}^{-15/15} + 6.68 \cdot \bar{\kappa}^{-17/15}\right), \quad (4.20)$$

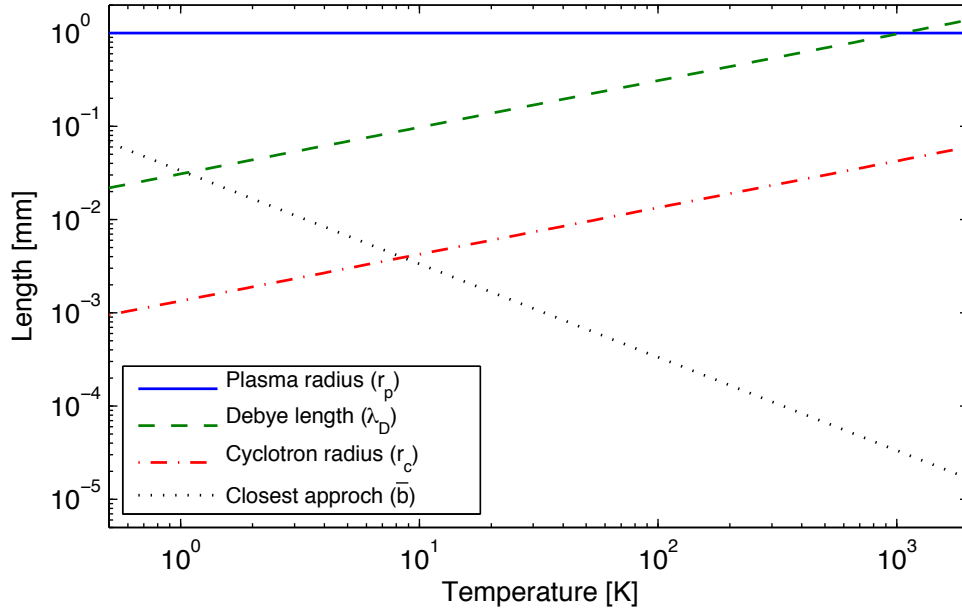
$$I_{unmagnetized}(\bar{\kappa}) = -\frac{\sqrt{2\pi}}{15} \ln\left(\frac{\bar{\kappa}}{3}\right). \quad (4.21)$$

Figure 4.2(a) shows  $I(\bar{\kappa})$  for three cases: a magnetized plasma, an unmagnetized plasma and a joint curve. The joint curve equals that of a magnetized plasma for  $\bar{\kappa} < 0.5$  and that of an unmagnetized plasma for  $\bar{\kappa} > 100$ . In the transition region a function of the form:

$$I_{transition}(\bar{\kappa}) = e^{a \ln(\bar{\kappa}) + b \ln(\bar{\kappa}) + c \ln(\bar{\kappa}) + d} \quad (4.22)$$

is used to join the two asymptotic curves in a smooth manner.

Figure 4.2(b) shows the collision frequency as a function of temperature, calculated for an antiproton plasma of constant density in a 1 T magnetic field using the three choices of  $I(\bar{\kappa})$  described above. From the figure we see that the transition from a magnetized to an unmagnetized plasma happens roughly between 0.5 and 10 K, and that both of the asymptotic expressions diverge rapidly from the joined curve in this region. We see that to investigate evaporative cooling of antiprotons to temperatures close to- or lower than 10 K one must use the more general joined curve as calculated in (Glinsky *et al.*, 1992). In addition it seems futile to attempt evaporative cooling of antiprotons to temperatures lower than about 0.5 K as the collision rate, which drives the evaporation, drops rapidly beyond this point.



**Figure 4.3:** Plasma length scales vs temperature. An antiproton density of  $5 \times 10^6 \text{ cm}^{-3}$  and a magnetic field of 1 T was used in the calculations.

#### 4.4.1 The Coulomb logarithm $\ln \Lambda$

The Coulomb logarithm  $\ln \Lambda$ , used first in equation (4.10), describes the factor by which small-angle collisions are more effective than large-angle collisions in a plasma. Several convenient expressions for  $\ln \Lambda$  exist, typically of the form  $\ln \Lambda = \ln(r_a/\bar{b})$ , where  $r_a$  is the smallest of the cyclotron radius  $r_c$ , the plasma radius  $r_p$ , or the Debye length  $\lambda_D$ , and  $\bar{b}$  is the distance of closest approach (see (Huba, 2009)). Figure 4.3 shows an example of how the different plasma length scales vary as a function of temperature for a plasma antiprotons with density  $5 \times 10^6 \text{ cm}^{-3}$ .

In the expression for the collision frequency used in this section (equation (4.19))  $I(\bar{\kappa})$  takes the place of the Coulomb logarithm.

## 4.5 Evaporation from a plasma

Many of the effects particular to evaporation of ions are most pronounced if the ion cloud can be considered to be a (nonneutral) plasma. A simple

criterion for when this is the case is to require that  $\lambda_D \ll L$ , where  $\lambda_D$  is the Debye length (see definition below), and  $L$  is the smallest of the cloud length and radius (Chen, 1974).

$$\lambda_D = \sqrt{\frac{\epsilon_0 k_B T}{e^2 n}}. \quad (4.23)$$

Figure 4.3 shows a calculation of  $\lambda_D$  as a function of temperature for a typical antiproton density observed in the ALPHA apparatus ( $5 \times 10^6 \text{ cm}^{-3}$ ). On the figure the 1 T cyclotron radius  $r_c$  and the thermal distance of closest approach  $\bar{b}$  are also graphed and can be compared to a typical 1 mm plasma radius.

The most obvious effect of a plasma on evaporation is the reduction in the evaporation barrier  $V$  caused by the plasma self field. For an infinite plasma column of density  $n$  and radius  $r_p$  surrounded by a conducting wall with radius  $R_w$ , the self potential as a function of the radius  $r$  is given as:

$$\phi_{inf}(r) = \frac{qnR^2}{2\epsilon_0} \left( \ln \frac{R_w}{R} + \frac{1}{2} \right), \quad (4.24)$$

where  $q$  is the charge of an ion. For antiprotons with  $n = 5 \times 10^6 \text{ cm}^{-3}$ ,  $r_p = 1 \text{ mm}$  and  $R_w = 22 \text{ mm}$  the central self potential is  $\phi_{inf}(0) = -162 \text{ mV}$ , and the potential drop across the plasma is 23 mV. Note that for plasmas of finite length the self potential will be lower, though typically not by a large factor.

When calculating  $V$ , the self potential must be added to the vacuum potential generated by the confining electrodes. If we assume a relatively high plasma temperature of 1000 K and a vacuum well depth of 1 V,  $\eta = eV/k_B T$  would change by about 1.9 from 11.6 to 9.7 at the center and by a little less (1.6) at the cloud edge. If instead we assume a situation somewhat deeper into the plasma regime with a temperature of 300 K and a vacuum well depth of 300 mV, the change in  $\eta$  due to the plasma self field is 6.2 at the center and 5.4 at the plasma edge. Since  $\eta$  enters exponentially in the expression for the evaporation time scale  $\tau_{ev}$  (see section 4.3) even small changes can have a large effect on the rate of evaporation both for the plasma as a whole and spatially as a function of  $r$ .

The effect of a reduced evaporation time scale for the plasma as a whole is simple to include in equations (4.1) and (4.2), which describe the evaporation process, by calculating the barrier potential, and thus  $\eta$ , by taking into

account the ion self potential. However, the effect of variations in  $V$  across the plasma are more subtle and can result in a nonuniform temperature and density profile in the plasma and in an increasing plasma radius. In the following the extent and the effects of localized evaporation will be investigated in detail.

#### 4.5.1 Equilibrium plasma profiles and evaporation from the radial center

As described in (Prasad and O'Neil, 1979) the equilibrium density profile of a plasma can be calculated by solving Poisson's equation. In the case of global thermal equilibrium the potential  $\phi(r, z)$  must be determined self-consistently, and the equation takes the form:

$$\frac{1}{r} \frac{\partial}{\partial r} r \frac{\partial \phi}{\partial r} + \frac{\partial^2 \phi}{\partial z^2} = - \frac{-en_0}{\epsilon_0} \exp\left(-\left[-e\phi(r, z) + \frac{1}{2}m\omega(\Omega_c - \omega)r^2\right]/k_B T\right), \quad (4.25)$$

where  $-e$  is the charge of an antiproton,  $n_0$  the central density,  $\Omega_c = eB/mc$  the cyclotron frequency, and  $\omega$  a frequency determined from the boundary conditions of the system. Following (Prasad and O'Neil, 1979) equation (4.25) can be scaled to reduce the number of parameters. The reduced variables are:

$$\begin{aligned} \rho &\equiv \frac{r}{\lambda_D}, & \xi &\equiv \frac{z}{\lambda_D}, \\ \psi &\equiv \frac{e\phi}{k_B T} - \frac{m\omega(\Omega_c - \omega)r^2}{2k_B T}, \\ \gamma &\equiv \frac{2\epsilon_0 m\omega(\Omega_c - \omega)}{n_0 e^2} - 1. \end{aligned} \quad (4.26)$$

Applying these variables equation (4.25) takes the form:

$$\frac{1}{\rho} \frac{\partial}{\partial \rho} \rho \frac{\partial \psi}{\partial \rho} + \frac{\partial^2 \psi}{\partial \xi^2} = e^\psi - 1 - \gamma, \quad (4.27)$$

and the density is given by  $n(\rho, \xi) = n_0 \exp[\psi(\rho, \xi)]$ .

To gain insight in how the plasma is depleted when particles evaporate, it is not necessary to obtain the full solution to equation (4.27). Instead we can assume that the plasma is symmetric in  $z$  in which case  $\partial^2 \psi / \partial \xi^2$  is constant.

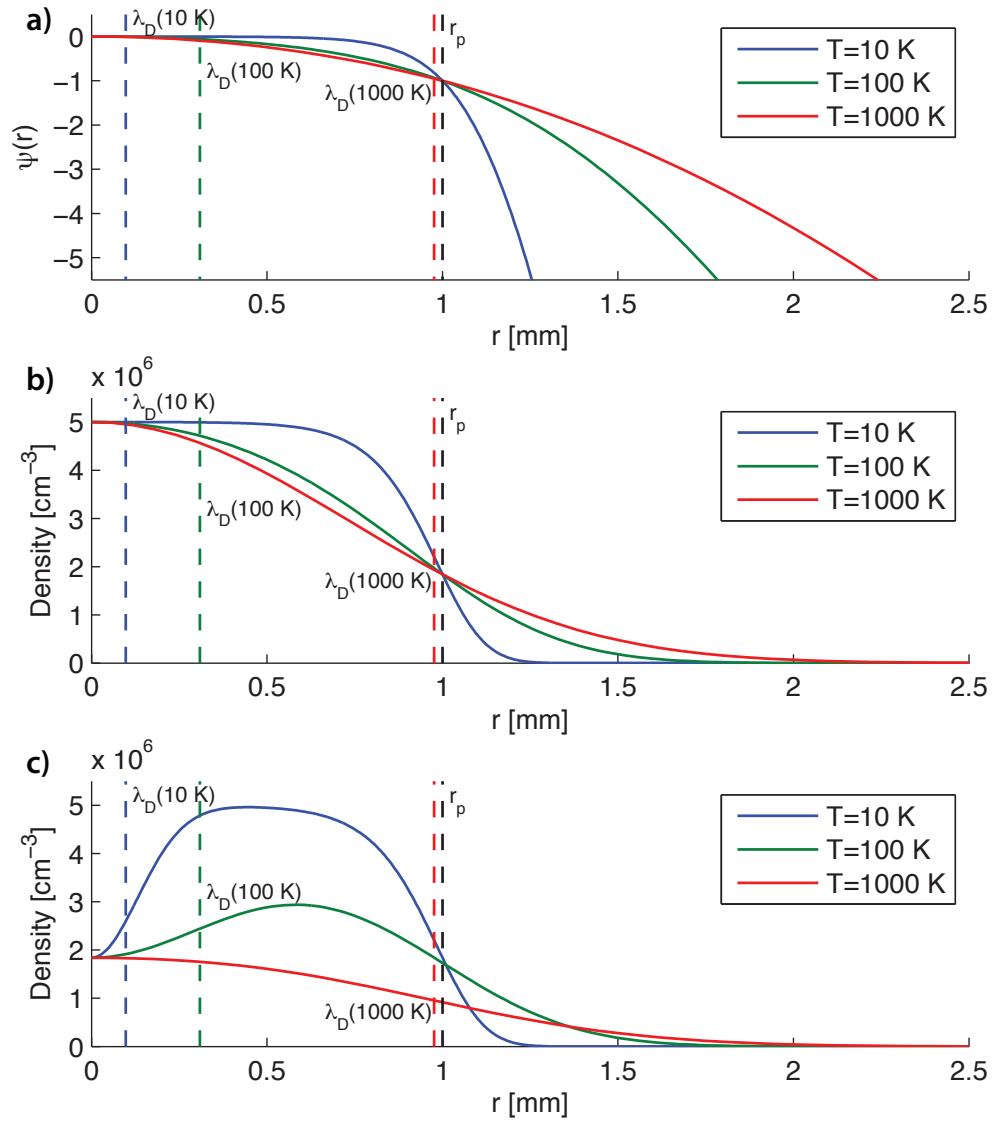


**Figure 4.4:** (a)  $\psi$  vs radius in real units.  $\psi$  is calculate by numerical integration of equation (4.28) for three plasmas of central density  $n_0 = 5 \times 10^6 \text{ cm}^{-3}$ , radius  $r_p = 1 \text{ mm}$ , and temperatures  $T$  of 10, 100, and 1000 K. The Debye length  $\lambda_D$  for each plasma and  $r_p$  is indicated by dashed vertical lines. (b) Global thermal equilibrium density profiles calculated as  $n(r) = n_0 \exp(-\psi(r))$ . (c) Density profiles depleted due to evaporation calculated as  $n - \Delta n$  (see equation (4.32)).

To keep the calculation simple we let  $\partial^2\psi/\partial\xi^2 = 0$ , as is the case for an infinite plasma column:

$$\frac{1}{\rho} \frac{\partial}{\partial\rho} \rho \frac{\partial\psi}{\partial\rho} = e^\psi - 1 - \gamma. \quad (4.28)$$

We now define the plasma radius  $r_p$  (in scaled units  $\rho_p$ ) to be the radius where  $\psi(\rho_p) = -1$ . This implies that  $n(r_p) = n_0 \exp(-1)$ . A solution to equation (4.28) is now fully specified by the three parameters  $T$ ,  $n_0$ , and  $r_p$  and the requirements  $\psi(\rho = 0) = 0$  and  $\partial\psi/\partial\rho|_{\rho=0} = 0$ , the latter arising from the cylindrical symmetry of the problem.

Figure 4.4(a) shows  $\psi$  for three plasmas of central density  $n_0 = 5 \times 10^6 \text{ cm}^{-3}$ , radius  $r_p = 1 \text{ mm}$ , and temperatures  $T$  of 10, 100, and 1000 K. The solutions were obtained by numerical integration of equation (4.28), and the values of  $\gamma$  were determined numerically from the requirement  $\psi(\rho_p) = -1$  to be  $3.4 \times 10^{-4}$ , 0.22, and 3.6 in order of increasing temperature. For plasmas with  $\gamma \ll 1$  the value of  $\gamma$  is approximately equal to (Dubin and O'Neil, 1999):

$$\gamma \approx \sqrt{\frac{2\pi r_p}{\lambda_D}} \exp\left[-\frac{r_p}{\lambda_D}\right]. \quad (4.29)$$

The radial density distributions for the three plasmas are displayed in Figure 4.4(b). The 10 K plasma has a flat density profile at the center and a well defined edge of the plasma, both of which are characteristics of a plasma with  $\lambda_D \ll r_p$ . The 100 and the 1000 K plasmas on the other hand both have a more gradual decrease in density and no well defined edge. In the case of the 1000 K plasma  $\lambda_D \approx r_p$  and thus it hardly qualifies as a plasma. However, it does have a set of parameters close to those of some antiproton clouds observed in the ALPHA apparatus. Such clouds were used as initial conditions for some of the evaporative cooling experiments described in chapter 5.

Using the definitions (4.26) we can rewrite the expression for  $\psi$  as:

$$\psi = -\frac{e\phi}{k_B T} - \frac{1 + \gamma}{4} \rho^2. \quad (4.30)$$

We can now assume that to evaporate, a particle has to overcome a potential  $-eV_0$  which is constant in  $r$ . For this to happen the particle must overcome the barrier  $V = -e(V_0 - \phi)$  or, using the notation of section 4.2, it must achieve an

$\eta = -e(V_0 - \phi)/k_B T$ . Defining  $\eta_0 = -eV_0/k_B T$  equation (4.31) can be written as:

$$\eta = \eta_0 + \psi + \frac{1 + \gamma}{4} \rho^2. \quad (4.31)$$

From this expression we immediately see that  $\eta$  changes on the order of  $\lambda_D$ . The evaporation time  $\tau_{ev}$  depends exponentially on  $\eta$  (see equation (6.1.1)) and the change in the radial density profile  $\Delta n$  can be calculated from the expression for  $dN/dt$  given by equation (4.1). We thus obtain:

$$\Delta n = -\frac{ne^{-\eta}}{\eta} \Delta t, \quad (4.32)$$

where all constants are absorbed in the time step  $\Delta t$ .

Figure 4.4(c) shows  $n - \Delta n$  for the three plasmas described above using  $\eta_0 = 10$ . The value of  $\Delta t$  has been chosen to reduce the central density to  $n_0/\exp(1)$  in all cases. This choice was made to ensure that the change in the density profile becomes clearly visible, but since  $\Delta n$  is proportional to  $\Delta t$  any time step would have similar features.

For all three plasmas we see that the density changes most for  $r < \lambda_D$ , though the fractional change in density is nearly uniform in  $r$  for the 1000 K plasma. In the case of the 10 and the 100 K plasma a dip in the density profile appears at the center of the plasma, showing that evaporation from the center is favored. In the calculation above we assumed that the barrier voltage  $V_0$  was independent of radius. In a typical real potential well  $V_0$  is an increasing function of  $r$ , favoring evaporation from the radial center even more.

Evaporation localized in  $r$  has unfavorable consequences for evaporative cooling: the evaporation time is increased since only part of the distribution contributes efficiently, only the center is cooled making cooling of the entire plasma rely on heat transfer across the plasma, and the center can be depleted if particle transport across the plasma is unable to repopulate the center. In addition conservation of angular momentum can cause the plasma radius to grow.

#### 4.5.2 Radial heat and particle transfer

When particles primarily evaporate from the radial center of the plasma, as is the case if the Debye length  $\lambda_D$  is smaller than the plasma radius  $r_p$ , both

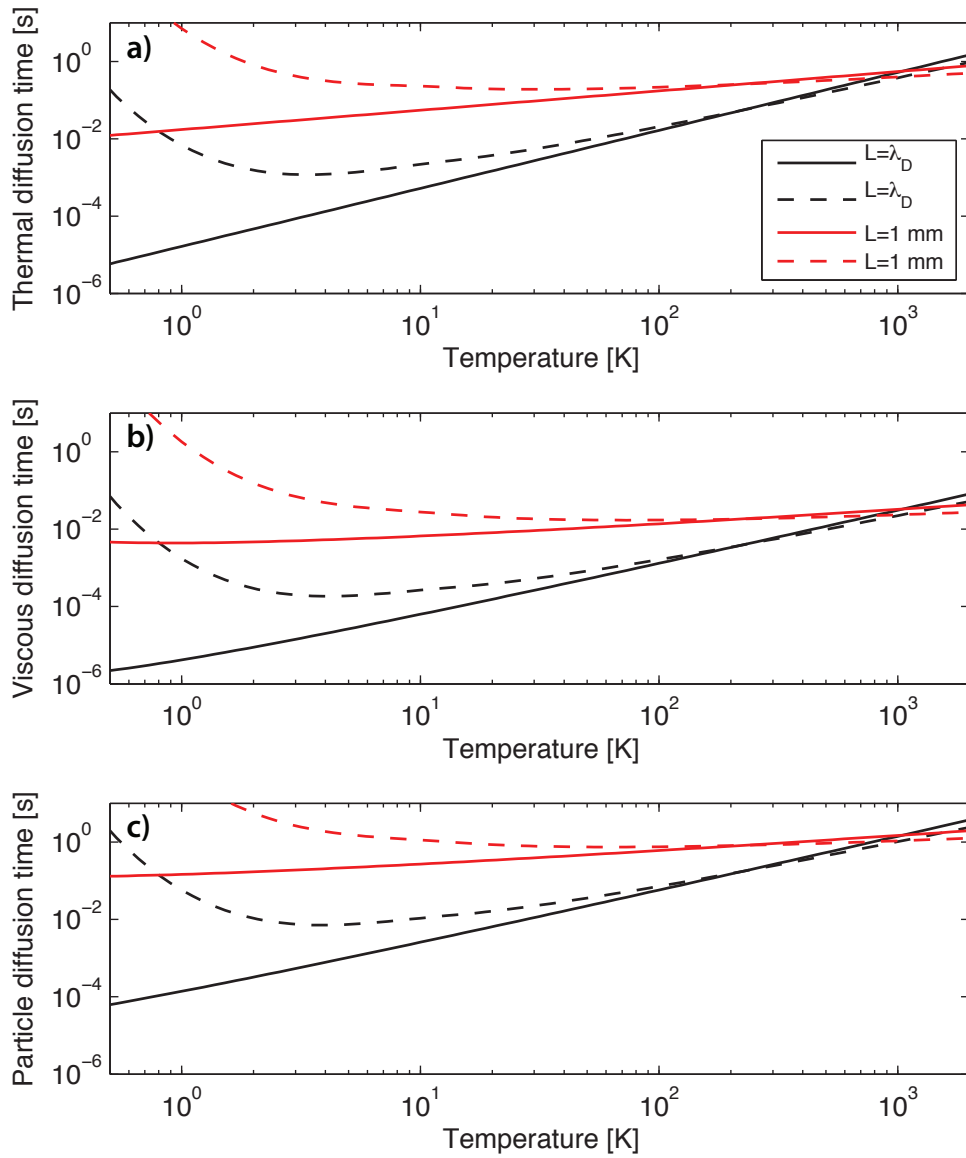


**Figure 4.5:** Antiproton diffusion times vs temperature for the three diffusion mechanisms described in the text: Diffusion of heat ( $\tau_\chi$ ), viscous diffusion ( $\tau_{\eta_{\text{visc}}/mm}$ ), and normal diffusion of particles ( $\tau_D$ ). Each calculation was performed using two different length scales  $L = \lambda_D$ , and  $L = 1 \text{ mm}$ , and a density of  $5 \times 10^6 \text{ cm}^{-3}$ . Two different expressions for the collision frequency was used: The simple expression  $v_c = nv_{th}\bar{b}^2/4\sqrt{2}$  (fully drawn lines), or  $v_{col}$  as defined by equation (4.19).

heat and particles must be able to move across the plasma for the evaporative cooling to be efficient. If heat does not flow to the center on a time scale which is faster than the evaporation timescale  $\tau_{ev}$  only the central part is cooled, and if particles are not transported towards the center, the central region can eventually become depleted.

The rates for three different energy- and particle transport mechanisms for ions trapped in a Penning-Malmberg trap can be found in (Dubin, 1998), and each of these three rates will be briefly discussed in the following. The three mechanisms are: *Heat conduction*, which does not involve transport of particles; *viscous diffusion*, which acts to make the plasma shear free; and *normal diffusion* of particles.

Heat conduction across the plasma can be characterized by the thermal diffusivity  $\chi$ , which is the thermal conductivity divided by the volumetric heat capacity. The expression for  $\chi$  found in (Dubin, 1998) depends on the simplified collision frequency  $\nu_c = nv_{th}\bar{b}^2/(4\sqrt{2})$  times  $\lambda_D^2$ :

$$\chi = 0.48\nu_c\lambda_D^2. \quad (4.33)$$

The odd factor  $1/4\sqrt{2}$  in  $\nu_c$  has been introduced to account for a difference in how the thermal velocity  $v_{th}$  and the distance of closest approach  $\bar{b}$  are defined in this chapter and in (Dubin, 1998). Inserting the definitions of  $\lambda_D$  and  $\nu_c$  in equation (4.33) we get an expression for  $\chi$  which only depends on the temperature:  $\chi = 0.48e^2 / ((4\pi)^2 \epsilon_0 \sqrt{mk_B T})$ . For heat diffusing across a fixed distance this means that the rate is independent of both the magnetic field and the density. However, the simplified expression for the collision frequency used in equation (4.33) is only a good approximation for a weakly magnetized plasma (see section 4.4). Instead we could chose to use the more accurate expression described by equation (4.19).

Figure 4.5(a) shows an approximate time scale for heat diffusion  $\tau_\chi$ :

$$\tau_\chi = \frac{L^2}{\chi}. \quad (4.34)$$

The calculation has been carried out for two different diffusion length scales:  $L = \lambda_D$ , and  $L = 1$  mm. The former describes the radius of the evaporating region, and the later a typical plasma radius in the ALPHA apparatus. Both

the simple and the more detailed expressions for the collision frequency has been used for each length. From the figure we see that heat transport across the entire plasma happens in a few hundred ms for temperatures in the range 1 to 1000 K. This time scale is independent of the density. On the scale of  $\lambda_D$  heat diffusion is faster by 2 to 3 orders of magnitude, however, since  $\lambda_D^2$  is inversely proportional to the density so is  $\tau_\chi$ .

The kinematic viscosity  $\eta_{visc}/nm$  describes the viscous diffusion in the plasma, and like  $\chi$  it is proportional to the collision rate times the square of  $\lambda_D$ . Viscous diffusion involves transport of particles and momentum, and acts to minimize shear in the plasma. A plasma with an equilibrium density distribution, as those described in section 4.5.1, are shear free because they rotate as a rigid body around the trap axis (Davidson, 2001). An expression for  $\eta_{visc}/nm$ , valid for *floppy* plasmas, i.e. plasmas with a low axial bounce frequency compared to the rotation frequency, is given in (Dubin, 1998):

$$\frac{\eta_{visc}}{nm} = 1.8v_c\lambda_D^2 \ln\left(\frac{v_{th}}{(D_v\lambda_D)^{1/3}}\right), \quad (4.35)$$

where  $D_v \approx v_c v_{th}^2/2$  is the velocity-space diffusion coefficient. For *rigid* plasmas which have a high bounce frequency relative to the rotation frequency the rate is higher (Dubin, 1998; Driscoll *et al.*, 2002).

An approximate time scale for viscous diffusion can be calculated as:

$$\tau_{\eta_{visc}/nm} = \frac{L^2}{\eta_{visc}/nm}, \quad (4.36)$$

and Figure 4.5(b) shows a calculation of  $\tau_\chi$  for  $L = \lambda_D$  and  $L = 1$  mm. Like in the case of heat diffusion,  $\tau_{\eta_{visc}/nm}$  has been calculated twice for each value of  $L$  using the two expressions for the collision rate. In the temperature range 2 to 2000 K, the figure shows time scales of only a few ms for viscous diffusion across the entire plasma ( $L = 1$  mm).

The last diffusion mechanism discussed here is normal diffusion as described by Fick's law. Unlike viscous diffusion, normal diffusion is present even if the plasma as a whole is in global thermal equilibrium and the density profile constant. The diffusion constant  $D$  is proportional to the collision rate

times the square of the cyclotron radius  $r_c = v_{th}/\Omega_c$ , and thus scales with the magnetic field as  $1/B^2$  unlike both the heat and the viscous diffusion constants (Dubin, 1998):

$$D = 6 \sqrt{\pi} v_c r_c^2 \ln \left( \frac{v_{th}}{(D_v \sqrt{\lambda_D r_c})^{1/3}} \right) \ln \left( \frac{\lambda_D}{r_c} \right). \quad (4.37)$$

The diffusion time  $\tau_D$  can be calculated as:

$$\tau_D = \frac{L^2}{D}, \quad (4.38)$$

and is plotted for  $L = \lambda_D$  and  $L = 1$  mm in Figure 4.5(c) using both expressions for the collision frequency. We see that for diffusion across the entire plasma ( $L = 1$  mm), normal diffusion has the longest time scale ( $\sim 1$  s) of the three diffusion mechanisms investigated here, and unlike the other two it scales with the plasma density ( $v_c r_c^2 \propto n$ ). The density used in the calculations displayed on the figure was  $5 \times 10^6 \text{ cm}^{-3}$ .

To summarize; if  $\lambda_D < r_p$  heat and particles must flow into the central region ( $r < \lambda_D$ ) of the plasma on a time scale faster or at least comparable to the time scale of evaporation. If this does not occur the outer part of the plasma is not cooled and the central region can be depleted, hollowing out the plasma. The time scale of evaporation  $\tau_{ev}$  can be calculated using equation (6.1.1). If we assume  $\eta = 10$  and a collisional time scale of 1 ms (see figure 4.2), we get  $\tau_{ev} \approx 70$  s decreasing to  $\sim 250$  ms for  $\eta = 5$ . Compared to these time scales viscous diffusion is very fast, and should be able to maintain a near equilibrium density profile across the entire plasma. Thermal diffusion has a time scale of a few hundred ms which is comparable to the lower estimate of  $\tau_{ev}$ , and normal diffusion with time scales of about 1 s across the entire plasma is somewhat faster than the high estimate of  $\tau_{ev}$ . Thus it is likely that evaporation does not cause the plasma temperature or density profile to deviate from global equilibrium.

For temperatures below say 2 K, an increase in all three diffusion time scales is seen for the calculations performed using equation (4.33) for the collision rate. One worry could be that the very long diffusion time scales seen for these temperatures would cause the plasma to deviate from equilibrium.

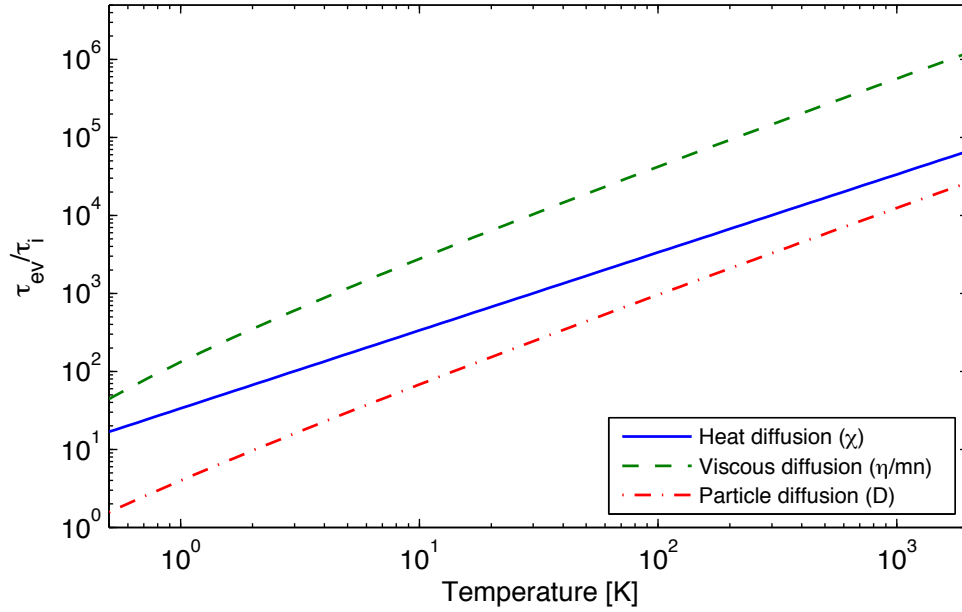


**Figure 4.6:** The time scale of evaporation divided by the plasma diffusion time scales ( $\tau_{ev}/\tau_i$ ) vs plasma temperature. The ratio for each of the three diffusion mechanisms described in the text: Diffusion of heat ( $\tau_\chi$ ), viscous diffusion ( $\tau_{\eta_{visc}/mn}$ ), and normal diffusion of particles ( $\tau_D$ ). Each ratio should be as large as possible for the plasma to remain close to global thermal equilibrium during the evaporation process.

However, this increase is caused by a similar increase in the collision time, and therefore  $\tau_{ev}$  will follow. In fact the ratio  $\tau_{ev}/\tau_i$ , where  $\tau_i$  is one of the three diffusion time scales, is independent of the collision rate.

Figure 4.6 shows  $\tau_{ev}/\tau_i$  calculated for  $L = 1$  mm for all three diffusion mechanisms, and the figure summarizes the above discussion. For the density used in the figure ( $5 \times 10^6 \text{ cm}^{-3}$ ) all three ratios are higher than 1 over the entire 0.5 to 2000 K range of the plot. The ratio of  $\tau_{ev}$  to the time scale for both the heat- and the viscous diffusion is proportional to  $\lambda_D^2/L^2$ , and  $\tau_{ev}/\tau_D$  is proportional to  $r_c^2/L^2$ . This means that a decrease in density due to an increasing radius will only affect the later, and a decrease in density for a fixed radius will actually increase both of the former two ratios.

### 4.5.3 Radial expansion of the plasma and Joule heating

As described in (O'Neil, 1980), the total canonical angular momentum  $L = \sum r_i^2$  is a conserved quantity for a cloud of ions confined in a Penning-Malmberg trap. However, when a particle leaves the cloud due to evaporation it will reduce  $L$  by an amount proportional to the radius  $r_i$  of its orbit around the trap axis. Now, if evaporation occurs primarily at the radial center of the cloud, very little angular momentum is removed and  $L$  stays largely unchanged. As we have seen in section 4.5.2 viscous diffusion is often very fast, and to eliminate the shear introduced by a lower central density, the plasma will quickly refill the center.

If we assume that all evaporating particles leave the plasma at  $r = 0$  it is easy to see, that conservation of  $L$  during the refilling process requires the plasma radius to grow. For convenience we can make use of the plasma mean square radius  $\sqrt{\langle r^2 \rangle} = \sqrt{L/N}$ , where  $N$  is the number of particles. Thus if the cloud initially contains  $N_0$  particles and has a mean square radius of  $\sqrt{\langle r_0^2 \rangle}$  we can calculate  $\sqrt{\langle r^2 \rangle}$  at some later time using the relation:

$$\frac{\langle r^2 \rangle}{\langle r_0^2 \rangle} = \frac{N_0}{N}. \quad (4.39)$$

Equation (4.39) sets an upper limit on the amount of radial expansion due to conservation of angular momentum, since it is assumed that all particles are lost at  $r = 0$ . If instead some particles are lost from a finite radius they will carry away angular momentum and the expansion will be smaller.

An unfortunate consequence of radial expansion is the release of potential energy stored in the plasma. For an infinite plasma column of radius  $R$  surrounded by a conducting wall of radius  $R_w$  the potential energy stored due to the inter particle potential is given as:

$$u_{inf} = \frac{e}{4\pi\epsilon_0} \frac{N}{l} \left( \ln\left(\frac{R_w}{R}\right) + \frac{1}{4} \right). \quad (4.40)$$

Here  $N/l$  is the number of particles per unit length. For a constant number of particles  $u_{inf}$  is a decreasing function of  $R$ , and the energy released due to expansion of the plasma will be converted to thermal energy thus increasing the temperature. The conversion of stored potential energy to thermal energy

is referred to as *Joule heating* (or *expansion driven (re)heating*), and to account for this heating mechanism an extra term proportional to  $du/dt$  must be added to the expression for  $dT/dt$  (equation (4.2)).

## 4.6 Conclusion

We have seen, that to describe evaporation of ions confined in a Penning-Malmberg trap one must include the effects of the ion self fields when calculating the key parameter  $\eta$ . When the ion cloud can be considered a plasma, the estimate of  $\eta$  is significantly reduced if the ion self fields are included. This leads to a dramatic decrease in the evaporation time scale  $\tau_{ev}$ . In addition the self fields introduce radial variations in the evaporation barrier  $V$ , which can cause the evaporation to be localized at the radial center of the cloud and lead to an increase in the plasma radius. In turn the radial increase can result in Joule heating of the ions. The heating term must be included in the the expression for  $dT/dt$  found at the beginning of this chapter (section 4.2). A modified set of differential equations for the temperature  $T$  and the number  $N$  takes the form:

$$\frac{dN}{dt} = -\frac{N}{\tau_{ev}} + \gamma N, \quad (4.41)$$

$$\frac{dT}{dt} = -\alpha \frac{T}{\tau_{ev}} + P. \quad (4.42)$$

Here  $\gamma$  is the loss rate per particle due to processes other than evaporation, and  $P$  is a heating rate which must include expansion driven Joule heating and possibly other heating sources as well. For antiprotons  $\gamma$  is a measure of the number of annihilation on rest gas per time. In chapter 6 these equations are used to compare numerical estimates of evaporative cooling to the results of the experiments described in chapter 5.



# Forced evaporative cooling: Experimental results

---

The results of the first implementation of forced evaporative cooling of antiprotons is presented in this chapter. A large portion of the data have recently been published in (Andresen *et al.*, 2010c). The focus of the chapter is twofold: In the first part of the chapter, the experimental procedure is described and it is shown that evaporative cooling can indeed be used to obtain antiprotons at low temperatures. In the second part, a number of additional measurements are introduced, and together with the Main data series, these will be used to make estimates of the plasma density, space charge potential, and stored self-potential energy. The estimates are then used to develop and evaluate the quality of a set of simple models, and, here and in the following chapter, it is shown how plasma properties strongly affect the dynamics of the evaporation process. The results of this investigation feeds into the development of a model used to describe the evaporation process (see chapter 6).

Most of the figures shown in this chapter have either number, temperature or well depth on the first axis. During a forced evaporative cooling experiment, these numbers will all naturally be decreasing and the reader is encouraged to read the figures from right to left.

Throughout the chapter well depth will be quoted as the on-axis value due to the confining electrodes only. Space charge potentials are considered separately.

## 5.1 Main results

The data here dubbed the *Main* series is the data series used in (Andresen *et al.*, 2010c). The experiments which resulted in this data series were carried out very systematically under as stable and well characterized experimental conditions.

### 5.1.1 Experimental procedure

Each evaporative cooling experiment begins with the preparation of a cloud of 45000 antiprotons with a radius of 0.6 mm and a density of  $7.5 \times 10^6 \text{ cm}^{-3}$ . The antiprotons are produced and slowed to 5.3 MeV in the AD, and as they enter the apparatus through the aluminium foil (see Figure 5.1(a)) they are further slowed. Inside the apparatus we capture 70000 of the antiprotons in a 3 T magnetic field between two high voltage electrodes (not shown) excited to 4 kV. Typically 65% of the captured antiprotons spatially overlap a 0.5 mm radius, pre-loaded, electron plasma with 15 million particles. The electrons are self-cooled by cyclotron radiation and in turn cool the antiprotons through collisions. Antiprotons which do not overlap the electron plasma remain energetic and are lost when the high voltage is lowered.

The combined antiproton and electron plasma is then compressed radially using the rotating-wall technique described in section 3.1. The magnetic field is ramped to 1 T, and the particles moved to the mixing region where a set of low-noise amplifiers is used to drive the confining electrodes. Pulsed electric fields are used to selectively remove the electrons, and the antiprotons remain in a potential well of depth 1500 mV (see Figure 5.1(b)).

To perform evaporative cooling, the depth of the initially 1500 mV deep well was reduced by linearly ramping the voltage applied to one of the electrodes to one of six different predetermined values (see examples on Figure 5.1(b)). The shallowest well investigated had a depth of  $(10 \pm 4)$  mV. Then the antiprotons were allowed to re-equilibrate for 10 s before being ejected to measure either their temperature and remaining number (see section 3.2.5) or their spatial distribution (see section 2.5.2). During the ramp only one side of the confining potential is lowered, so that escaping particles are guided by the magnetic field onto the aluminium foil, where they annihilate. Monitor-

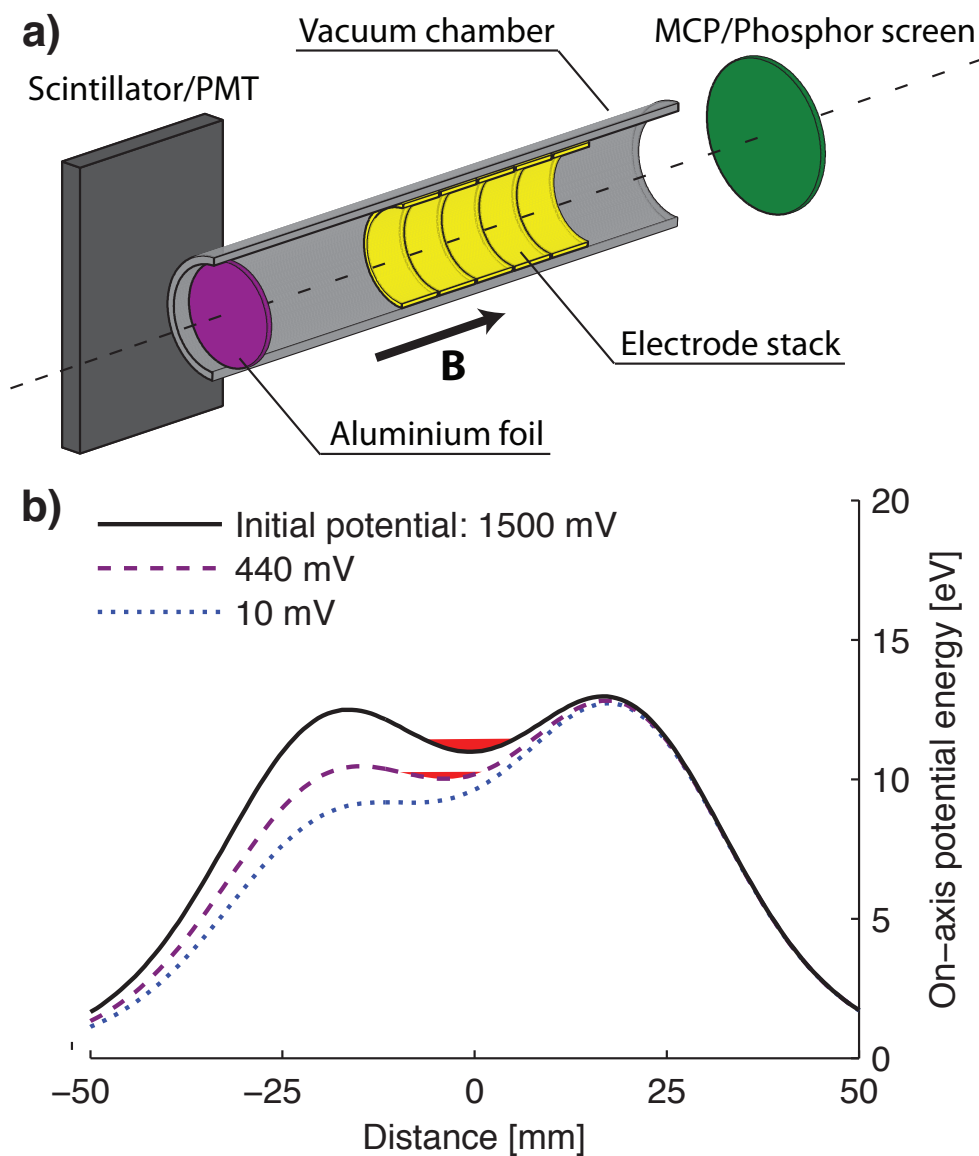


**Figure 5.1:** (a) Simplified schematic of the Penning-Malmberg trap used to confine the antiprotons and of the two diagnostic devices used. The direction of the magnetic field is indicated by the arrow. (b) Potential wells used to confine the antiprotons during the evaporative cooling ramp. The antiprotons are indicated at the bottom of the potential well (red), and the different wells are labelled by their on-axis depth. (Adapted from Andresen *et al.*, 2010c)

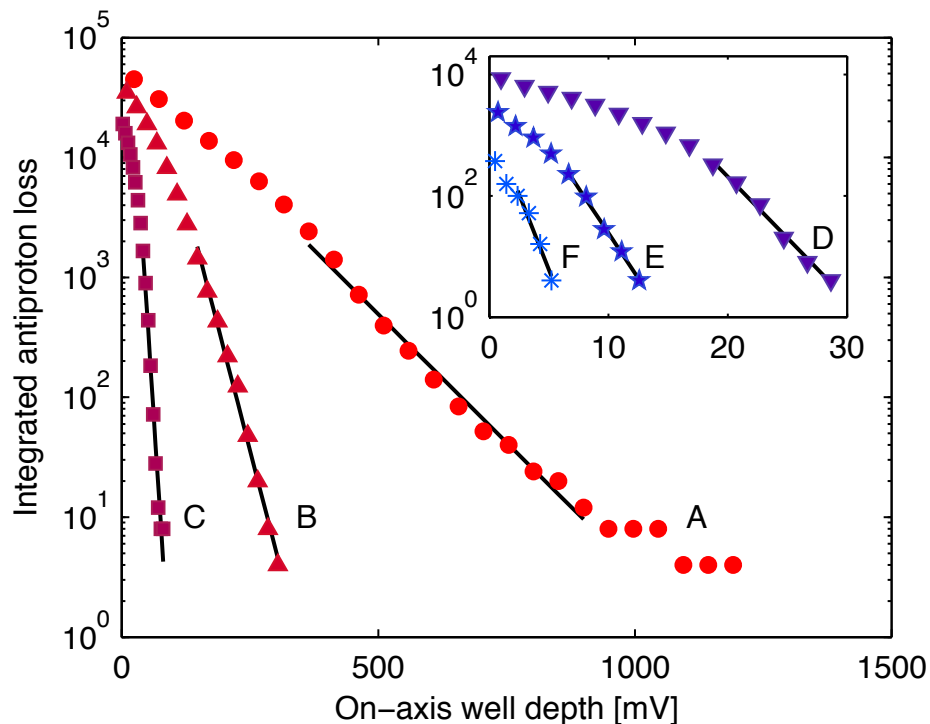
ing the annihilation signal allows us to calculate the number of antiprotons remaining at any time by summing all antiproton losses and subtracting the measured cosmic background. For each of the six well depths, five different times (300, 100, 30, 10, and 1 s) for ramping down the confining potential were tried. Unless otherwise stated the magnetostatic trap was not energized and the evaporative cooling was performed in a homogeneous 1 T solenoidal field.

Figure 5.1(a) shows a schematic diagram of the apparatus, with only the devices most important to the evaporative cooling experiment shown. To the left, antiprotons can be released towards the aluminium foil, on which they annihilate. The annihilation products are detected by the upstream set of plastic scintillators with an efficiency of  $(25 \pm 10)\%$  per annihilation. The background signal from cosmic rays was measured during each experimental cycle and was approximately 40 Hz. To the right, antiprotons can be released onto the combined MCP and phosphor screen assembly, to measure the antiproton cloud's spatial density profile, integrated along the axis of cylindrical symmetry. The thin walled electrodes, of which only a subset is shown, are used to generate the confining potentials shown in Figure 5.1(b).

### 5.1.2 Temperature and remaining number

The temperature of the antiprotons was determined from an exponential fit to the energy distribution of the particles. As described in detail in section 3.2 this distribution can be obtained from the annihilation time distribution when the antiprotons are released onto the aluminium foil at the end of the experiment. The measured temperature was then corrected by a factor determined by particle-in-cell (PIC) simulations, which suggests that the measured temperature is about 16% higher than the true temperature. The distribution labelled A in Figure 5.2 yields a corrected temperature of  $(1040 \pm 45)$  K before evaporative cooling; the others are examples of evaporatively cooled antiprotons.

The number of antiprotons remaining at the final dump was measured as the integrated number of annihilations during the 100 ms dump to measure the temperature. However, since we observe approximately 10% variation in the number of antiprotons captured, the number remaining is converted to a *cooling efficiency* (also referred to as *remaining fraction*), which is calculated



**Figure 5.2:** The number of antiprotons lost from the well as its depth is reduced is integrated over time and plotted against the well depth. The well depth is ramped from high to low; thus, time flows from right to left in the figure. The measured number is corrected for the 25% detection efficiency. The curves are labelled in decreasing order of the temperatures extracted from an exponential fit, shown as the solid lines. The temperatures (corrected as described in the text) are: A: 1,040 K B: 325 K C: 57 K D: 23 K E: 19 K F: 9 K. As the antiprotons get colder, fewer can be used to determine their temperature, an effect described in section 3.2. (Adapted from Andresen *et al.*, 2010c)

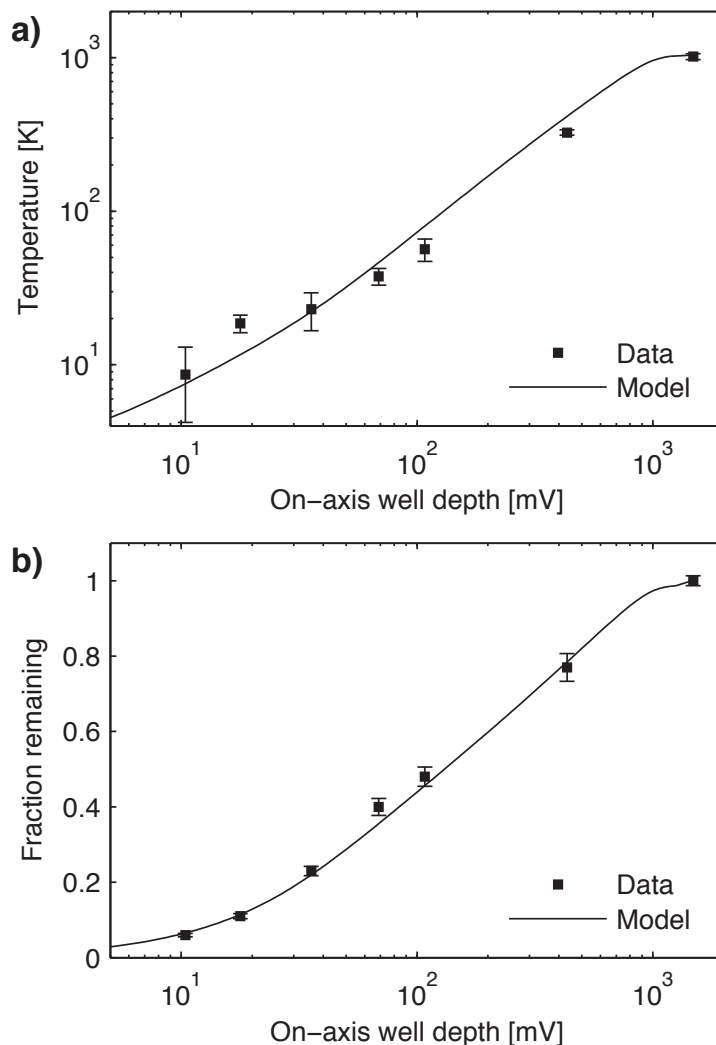


**Figure 5.3:** (a) Temperature vs. the on-axis well depth. The error is the combined statistical uncertainty from the temperature fit and an uncertainty associated with the applied potentials (one  $\sigma$ ). The model calculation (solid line) are those of (Andresen *et al.*, 2010c) (see the introduction of Chapter 6 for more details). (b) The fraction of antiprotons remaining after evaporative cooling vs. the on-axis well depth. The uncertainty on each point is propagated from the counting error (one  $\sigma$ ). The initial number of antiprotons was approximately 45000, for an on-axis well depth of  $(1484 \pm 14)$  mV. (Adapted from Andresen *et al.*, 2010c)

as the remaining number divided by the total number of antiprotons before evaporative cooling. The latter number is estimated as the sum of all annihilations observed during the ramp, the subsequent 10 s waiting time and the final dump minus the measured average background signal.

The results of a series of evaporative cooling experiment, where the final depth is varied, is shown in Figure 5.3. For each of the points shown, the ramp time was 100 s followed by a 10 s wait; thus the ramp rate is slightly higher for lower well depths. Figure 5.3(a) shows the temperature obtained during evaporative cooling as a function of the well depth. We observe an almost linear relationship, and in the case of the most shallow well, we estimate the temperature to be  $(9 \pm 4)$  K. The fraction of antiprotons remaining at the various well depths is shown on Figure 5.3(b), where it is found that  $(6 \pm 1)\%$  of the initial 45,000 antiprotons remain in the shallowest well.

Table 5.1 shows temperatures and fractions remaining for the complete matrix of well depths and ramp times. The table shows that the final temperature and fraction remaining were essentially independent of the ramp time except for the 1 s case, for which less than 0.1% of the particles survived to the most shallow well.

### 5.1.3 Radial antiproton distribution

For a subset of the matrix presented in Table 5.1 an additional set of measurements was carried out to determine the transverse antiproton density profile as a function of well depth. For these studies the antiprotons were released onto the combined MCP and phosphor screen assembly (see Figure 5.1(a)). Some examples of radial profiles measured in these experiments are shown in Figure 5.4.

To determine the radius of the measured distribution a two dimensional Gaussian with a constant offset was fitted to the measure line-integrated density profiles:

$$f(x, y) = Ae^{-\frac{(x-x_0)^2+(y-y_0)^2}{b^2}} + C, \quad (5.1)$$

where the amplitude  $A$  and the radius  $b$  are determined from the fit. The center of the distribution  $(x_0, y_0)$  was determined from an image of the initial antiproton distribution. The constant background  $C$  was determined from a

Ramp time	1 s	10 s	30 s	100 s	300 s
433 mV	65(2)% 339(33) K	73(2)% 324(24) K	75(3)% 295(19) K	77(4)% 325(13) K	76(7)% 314(23) K
108 mV	27(1)% 80(14) K	36(1)% 40(9) K	43(2)% 40(9) K	48(3)% 57(10) K	52(5)% 37(14) K
68.8 mV	8(1)% 52(12) K	32(1)% 36(10) K	37(1)% 30(10) K	40(2)% 37(5) K	42(4)% 31(6) K
35.6 mV	3(1)% 21(6) K	19(1)% 19(4) K	22(1)% 19(5) K	23(1)% 23(6) K	24(2)% 23(5) K
17.8 mV	1(1)% 19(8) K	- -	10(1)% 9(3) K	11(1)% 19(2) K	11(1)% 11(4) K
10.4 mV	< 0.1% -	5(1)% 11(6) K	5(1)% 11(6) K	6(1)% 9(4) K	6(1)% 10(3) K

**Table 5.1:** Fraction remaining and final temperature after evaporative cooling of initially 45000 antiprotons. The initial temperature was measured to be  $(1040 \pm 45)$  K and the well depth  $(1484 \pm 14)$  mV. Uncertainties are given in brackets after the number it self. The uncertainty associated with the fraction remaining is propagated from the counting error (one  $\sigma$ ). The uncertainty on the temperature is the combined statistical uncertainty from the temperature fit and an uncertainty associated with the applied potentials (one  $\sigma$ ).

large featureless portion of each image. In most cases the antiproton clouds had a radial extent sufficiently small for most of the distribution to be imaged successfully, and visual inspection shows good agreement between fit and data. However, for some clouds only the central part could be imaged, resulting in a fit with a high uncertainty on  $b$ . Scaled to the measured number instead of measured light intensity  $A = N/\pi b^2$ .

A striking feature of the antiproton images is the radial expansion of the cloud with decreasing well depth, from an initial radius  $b_0$  of 0.6 mm to approximately 3 mm for the shallowest well. In section 4.5.3 it is described how loss from the radial center of the cloud can lead to radial expansion through conservation of total canonical angular momentum. Figure 5.5 shows good agreement between the measured radius and that predicted from equa-

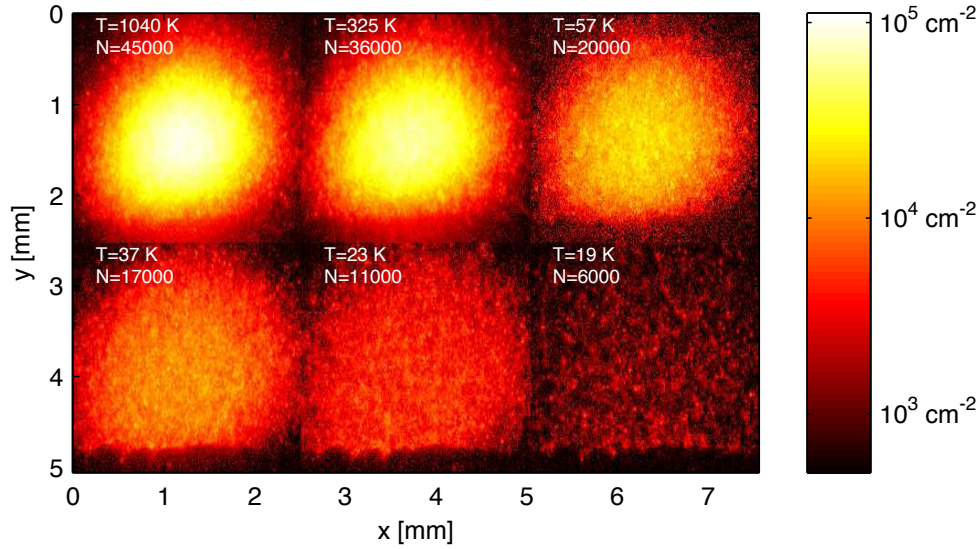


**Figure 5.4:** Examples of the line-integrated density profile for six different antiproton temperatures and numbers (logarithmic color scale). A rough estimate of the density can be obtained by dividing the shown areal density by a plasma length of 1 cm. The image in the top left corner shows a measurement of the radial antiproton distribution before evaporative cooling; all other shows the distribution after evaporative cooling. The temperature and number associated with each distribution was measured in a separate measurement.

tion (4.39), which have been rearranged and written in terms of the measured radius  $b$  below:

$$b = b_0 \sqrt{N/N_0}. \quad (5.2)$$

Here  $b_0$  is the cloud radius before evaporative cooling and  $N/N_0$  the fraction remaining after evaporative cooling.

## 5.2 The plasma density, self potential, and expansion driven heating

The measured radial antiproton distribution, number, and temperature can be used to solve the Poisson-Boltzmann equation to obtain the full three dimen-

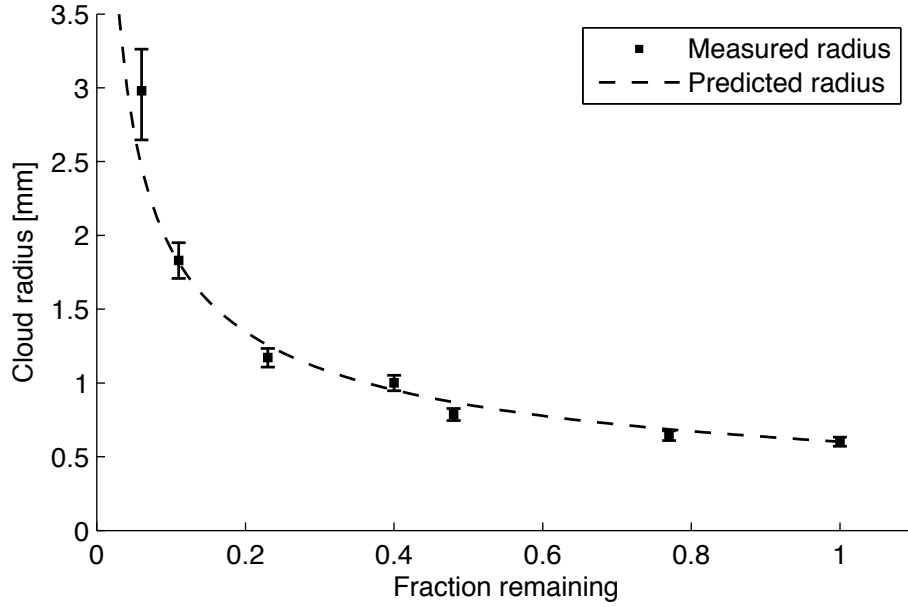


**Figure 5.5:** Antiproton cloud radius ( $b$ ) vs. fraction remaining after evaporative cooling for a constant ramp time of 100 s. Measurements are shown with error estimates, which are calculated as the most extreme values obtained when combining the 95% confidence interval of the fit with an assumed 10% uncertainty on the 240 Gauss magnetic field at the MCP. The dashed line shows the predicted radial expansion (equation (5.2)).

sional density distribution and electric potential. Doing so provides useful estimates of the peak antiproton density, the cloud length  $l$ , the on-axis space charge potential  $\phi$ , and the potential energy  $U$  stored in the cloud; all of which plays important roles in the dynamics of the evaporation process. Below the results of such calculations are used to compare simple models of the plasma to measurements for three data series: *Main*, *Hot* and *Cold*, which only differ in the antiproton cloud conditions immediately before the evaporative cooling ramp is initiated. All three series share a common ramp time of 100 s and the applied potentials are identical. The Main series is a subset of the measurements presented in the previous sections, while the Hot and Cold series were done separately, with different settings for the pulsed electric field used to remove the electrons. The initial antiproton conditions for each series are summarized in Table 5.2.

Series	Number	Temperature	Radius ( $b$ )	Peak density
Main	45000	1040 K	0.60 mm	$7.5 \times 10^6 \text{ cm}^{-3}$
Hot	33000	1570 K	0.83 mm	$2.6 \times 10^6 \text{ cm}^{-3}$
Cold	33000	526 K	0.35 mm	$2.0 \times 10^7 \text{ cm}^{-3}$

**Table 5.2:** Initial antiproton cloud conditions for the three series described in section 5.2.

Table 5.3 is a summary of the results of a calculation to determine three dimensional density distribution after evaporative cooling for the Main series. Similar results have been obtain for both the Hot and the Cold series and are added to the figures in this section.

### 5.2.1 Antiproton peak density and collision rate

The antiproton density peaks at the radial center of the cloud, and together with the temperature it determines the rate of collisions which drives the evaporation (see section 4.3). Figure 5.6(a) shows the peak density estimates obtained from the equilibrium calculations as a function of the number of antiprotons remaining in the well. Estimates of the antiproton collision rate (equation 4.19) are shown as a function of the remaining number (panel (b)) and the temperature (panel (c)). A first investigation of the data shows that with the exception of only a few points, the peak densities estimated for each series falls on a line with a slope of about 1.5 in the log-log plot of Figure 5.6(a). Thus, a one order of magnitude decrease in number is followed by a 1.5 order of magnitude decrease in density. This observation is consistent with an increasing volume of the cloud. Below simple considerations are used to derive a model for the density as a function of the remaining number.

The zero temperature global thermal equilibrium of a charge distribution in a 3D harmonic potential consists of an ellipsoid of constant density  $n_{\text{ellipsoid}}$  (Davidson, 2001). Assuming such a distribution we get:

$$n_{\text{ellipsoid}} = \frac{N}{\frac{4}{3}\pi b^2(\frac{l}{2})}, \quad (5.3)$$

where  $b$  is the cloud radius,  $l/2$  the half length and  $N$  the number of par-

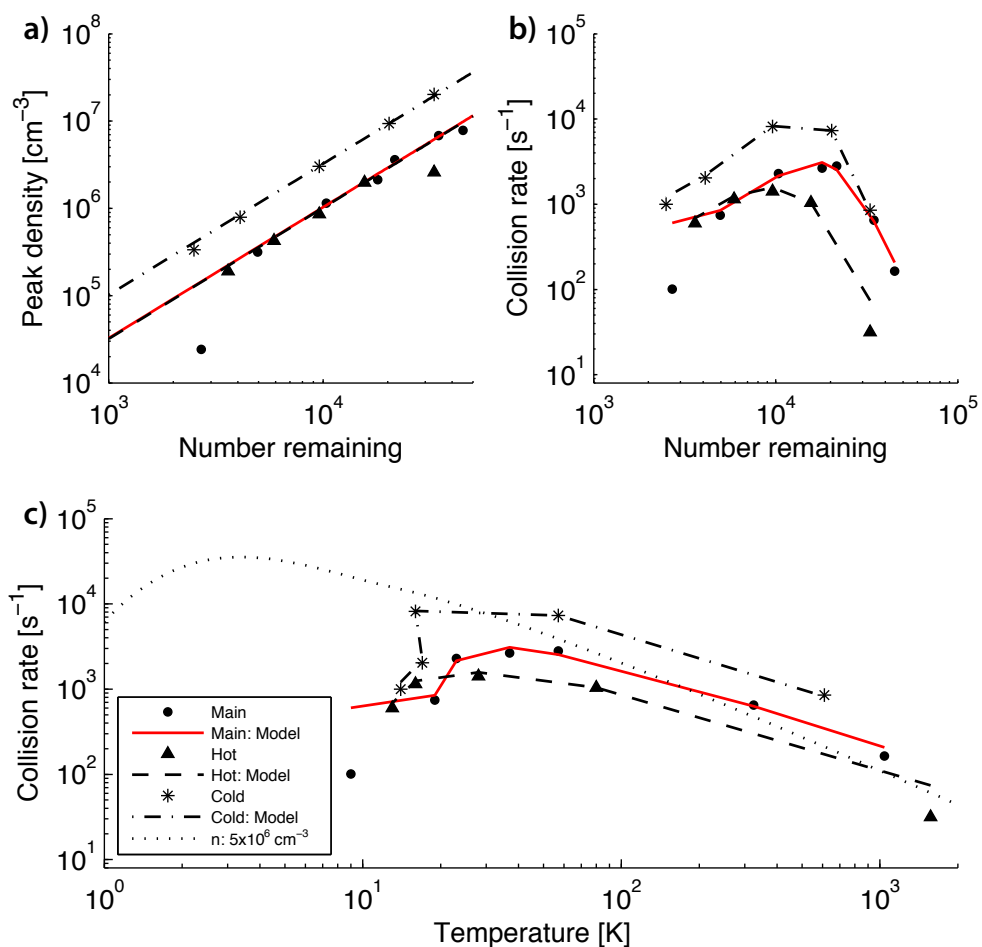


**Figure 5.6:** (a) Peak density vs. the number remaining after evaporative cooling. Points are used to indicate the estimate obtained from a self consistent solution to the Poisson-Boltzman equations. The lines indicate a density estimated using the simple model described by equation (5.4). (b) Estimated collision rate vs. remaining number. (c) Estimated collision rate vs. temperature. The dotted line indicates the rate for a plasma with a constant density of  $5 \times 10^6 \text{ cm}^{-3}$ .

Depth [mV]	$N$ [-]	$T$ [K]	$b$ [mm]	$l$ [mm]	Density [cm <sup>-3</sup> ]	$\phi$ [mV]	$u$ [meV]
1484	45000	1040	0.60	12.0	$7.8 \times 10^6$	57	20.0
433	34650	325	0.64	8.5	$6.8 \times 10^6$	51	18.0
108	21600	57	0.79	5.6	$3.6 \times 10^6$	34	12.2
68.8	18000	37	1.00	5.0	$2.1 \times 10^6$	26	9.3
35.6	10350	23	1.17	4.0	$1.2 \times 10^6$	14	5.1
17.8	4950	19	1.83	3.5	$3.5 \times 10^5$	5	1.8
10.4	2700	9	2.98	4.4	$2.4 \times 10^4$	1	0.3

**Table 5.3:** Main series: Summary table showing estimates of the plasma length  $l$ , peak density, on-axis space charge  $\phi$  and the summed inter-particle potential energy  $u$  per particle. The estimates are obtained by solving the Poisson-Boltzmann equation for seven samples of antiprotons associated with the evaporative cooling experiments described in the text. The input parameters are the vacuum potential (summarized here by the on-axis well depth), the number of antiprotons  $N$ , the temperature  $T$  and the cloud radius  $b$ .

ticles. In section 5.1.3 we saw that the radius of the measured antiproton clouds increase as  $1/\sqrt{N}$  as the number of antiprotons remaining in the well is decreased (equation (5.2)). The length, on the other hand, is decreasing as the number remaining decreases. From Table 5.3 we see that for a one order of magnitude decrease in number, the length is reduced by a factor  $12/3.5 = 3.4 \approx \sqrt{10}$ . Making the assumption that the on-axis plasma space charge  $\phi$  is a linear function of the number, we can let  $\phi_0 N = \frac{1}{2}k(l/2)^2$ , where the left hand side is the space charge and the right hand side a harmonic on-axis potential evaluated at  $z = l/2$ . We can now estimate the length as:  $l = l_0 \sqrt{N}$ , where  $l_0$  is a constant. Combining the estimates of  $b$  and  $l$  with equation (5.3) we get the following expression for the peak density:

$$n_{peak} = \frac{3}{2} A_0 \frac{N^{1.5}}{\pi b_0^2 l_0 \sqrt{N_0}}, \quad (5.4)$$

where  $A_0$  is a factor introduced to correct for a non-uniform charge distribution both radially and along the axis of the plasma.

Figure 5.6(a) shows the peak density calculated from equation (5.4) for

each of the three data series. In each case the constants  $b_0$ ,  $l_0$  and  $N_0$  has been determined from a single data point and  $A_0$  has been set to 1.4. As an example the data point used in the Main series is the row in Table 5.3 which gives:  $b_0 = 0.64$  mm,  $l_0 = 8.5$  mm /  $\sqrt{34650} = 46$   $\mu$ m and  $N_0 = 34650$ . It is clear from the figure that this simple model agrees quite well with the estimates obtained from the measurements with the exception of only a few points.

Returning to the estimates of the antiproton collision rate shown on Figure 5.6(b) and (c), we see that there is a rapid decrease in rate for temperatures lower than about 20 K. The rate is indeed expected to decrease at low temperatures as the plasma enters the magnetized regime, however, as illustrated by the constant density curve in panel (c), this is not expected to happen until the temperature is smaller than about 2 K. Thus the observed decrease is caused by the rapidly decreasing peak density.

## 5.2.2 Space charge

To escape the well an antiproton has to overcome the potential barrier set by the applied potentials minus the self potential generated by the charge distribution. In a Penning-Malmberg trap the potential barrier generated by the electrodes will always have a minimum on the trap axis, and for a typical charge distribution the self potential will have a maximum on the trap axis. Thus the minimum potential barrier is on the trap axis too.

Figure 5.7 shows the estimated on-axis space charge potential  $\phi$  as a function of the number remaining for the three data series. We see that there is a near linear dependence of  $\phi$  on the number remaining, and for each series a linear fit has been used to estimate the on-axis space charge per antiproton.

The measured space charge affects the dynamics of the evaporation strongly; especially at low and intermediate well depths. To exemplify this consider the 1.4  $\mu$ V per antiproton space charge estimate for the Main series. With 45000 antiprotons in the initial 1500 mV well, the best estimate of  $\phi$  is 57 mV which is a correction of about 4%. However, with 21600 antiprotons left in the 108 mV well,  $\phi$  is estimated to be 34 mV; a 31% correction to the potential barrier. For the temperature measured, this corresponds to a change in the estimate of  $\eta$  from 22 to 15 and a change in the evaporation timescale  $\tau_{ev}$  of about three orders of magnitude.

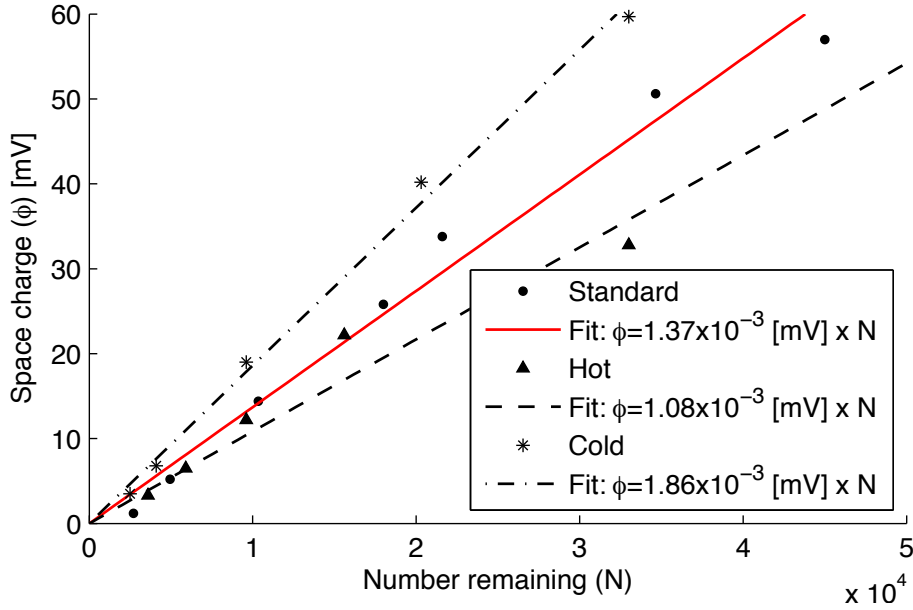


**Figure 5.7:** On-axis space charge vs. the number remaining after evaporative cooling. Points are used to indicate the estimate obtained from a self consistent solution to the Poisson-Boltzman equations. The dashed line indicates a least squares linear fit to the points.

### 5.2.3 Self-potential energy per particle

When the cloud expands as a result of particle loss from the radial center some of the potential energy stored in the charge distribution will be released. This can cause Joule heating of the distribution as the potential energy is converted into thermal energy of the particles. From the calculated charge distributions we can estimate the potential energy stored in the plasma as the energy required to assemble the cloud in the vacuum field. Table 5.3 shows the potential energy per particle  $u$  estimated for the Main series, and we see that the the initial value of 20 meV per particle drops to less than 1 meV as the charge escapes. Figure 5.8 shows that all three series follow the same trend. On the same graph a calculation of  $u_{inf}$  which is the energy stored per particle in an infinite plasma column surrounded by a conducting cylinder is shown (see equation (4.40)). The wall radius used in the calculation is  $R_w = 22$  mm, the length  $l = 10$  mm and the radius  $R$  is calculated using equation (5.2).

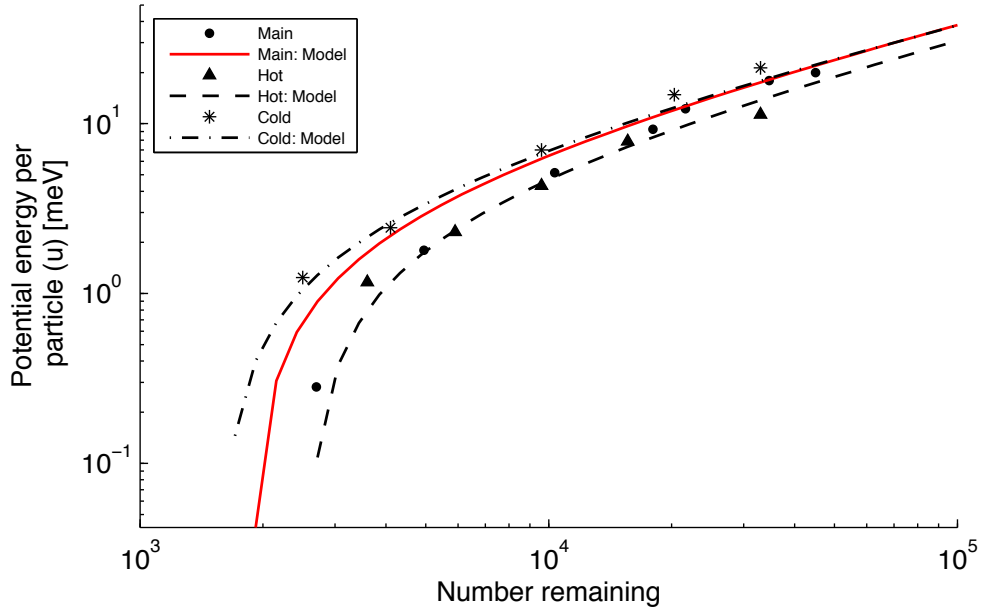


**Figure 5.8:** Potential energy per particle vs. the number remaining for each of the three data series described in the text. The lines indicate the energy per particle predicted from equation (4.40) with an offset of  $-3$  meV.

In addition, the calculation of  $u_{inf}$  was offset by  $-3$  meV in order to achieve reasonable agreement with the measurements. However, since heating from the release of potential energy depends on the slope of the curve, doing so does not change the estimate. The heating is discussed in more details in section 6.1.2 of next chapter.

### 5.3 Conclusion

In this chapter we have seen that low temperature samples of antiprotons can be obtained using forced evaporative cooling. The coldest samples obtained from an initial sample of 45000 antiprotons have temperatures of about 10 K and contains several thousand antiprotons. If we assume that all antiprotons were converted directly into antihydrogen atoms, the fraction with a total energy below the 0.5 K depth of the magnetostatic trap would be increased by about three orders of magnitude. Thus, despite the lower total number, the number of trappable atoms would be increased from less than one atom in the

initial distribution to more than 10 in the 10 K distribution.

From measurements of the radial distribution of evaporative cooled samples of antiprotons we see that the antiproton cloud expands radially as more antiprotons are lost. The expansion is likely to be driven by evaporation from the radial center of the cloud, and occurs when angular momentum is redistributed among fewer particles.

Using the measured antiproton number, temperature and radial distribution after evaporative cooling, estimates of the plasma length, density and self potential have been obtained from self-consistent solutions to the Poisson-Boltzmann equations. These estimates have been used to develop a set of simple models to describe the plasma properties as a function of number and temperature. Furthermore, the estimates have been used to show how the density affects the antiproton collision time, how the evaporation time scale is affected by the space charge, and to estimate the self-potential energy. All of these observations will be used in the following chapter to model the evaporation process.

The possibility of low temperatures makes evaporative cooling a strong candidate to replace electron cooling of antiprotons as the final cooling step when preparing pure samples of antiprotons for production of cold antihydrogen. In principle, the technique can be used to obtain temperatures lower than the temperature of the surrounding apparatus, and perhaps even sub-Kelvin plasmas, foreseen to be a prerequisite for proposed measurements of gravitational forces on antimatter (Drobychev *et al.*, 2007), can be achieved. As we shall see in the following chapter, reheating caused by the release of self-potential energy, unfortunately, limits the efficiency at very low temperatures.



# Forced evaporative cooling: Modeling

---

To predict the effect of forced evaporative cooling of antiprotons in the trap, we can model the process numerically. Such a model allows us to investigate the impact of the different effects particular to evaporation of charged particles, and can provide a guideline to optimizing the evaporation process.

The model makes use of the theory of evaporation presented in chapter 4 as well as the simple models used to describe the measurements in chapter 5. The MatLab functions used to perform the numerical calculations can be found in appendix A.

A similar model to the one described in this chapter was used to perform the numerical calculations shown in Andresen *et al.* (2010c). However, in these calculations a constant cloud length was used, and the heating term was larger by about a factor 4. Further investigation of the data show that including length variations improves the estimate of density in particular, and a more careful analysis of the expansion driven reheating of the plasma shows that some terms previously included are likely not contributing to the reheating process (see section 6.1.2).

The first section of this chapter includes a full description of the numerical model and a discussion of the most important effects. The later sections are examples of how the model can be applied to investigate different variations of the forced evaporative cooling.

## 6.1 Model description

The evaporation process is governed by the rate equations (4.41) and (4.42) describing the time evolution of the temperature  $T$ , and the number of particles trapped  $N$ :

$$\begin{aligned}\frac{dN}{dt} &= -\frac{N}{\tau_{ev}} + \gamma N, \\ \frac{dT}{dt} &= -\alpha \frac{T}{\tau_{ev}} + P.\end{aligned}$$

To solve the equations the initial number  $N_0$  and temperature  $T_0$  of the antiprotons must be supplied as well as the time dependent depth of the confining potential  $V_{vac}(t)$ . In addition all other quantities entering the model ( $\gamma$ ,  $\alpha$ ,  $\tau_{ev}$ , and  $P$ ) must be expressed in terms of the model variables  $t$ ,  $N$ , and  $T$ .

The loss term  $\gamma$  represents antiproton annihilations with residual gas. The rate can be measured directly using our position sensitive silicon detector to observe the number of antiprotons annihilating at the center of the trap when a cloud is confined for an extended period of time. We observe a  $\gamma \approx 1 \times 10^{-4} \text{ s}^{-1}$  per antiproton.

The average cooling per particle evaporating is contained in  $\alpha$ , which depends on the three variables  $\eta$ ,  $\kappa$ , and  $\delta$  (equation (4.4)):

$$\alpha = \frac{\eta + \kappa}{\delta + 3/2} - 1.$$

Two of these can be approximated by constants:  $\kappa = 1$  and  $\delta = 3/2$ , as described in section 4.2. The third, is defined as (equation (4.3)):

$$\eta = \frac{eV}{k_B T},$$

where the well depth  $V$  is the combination of the on-axis vacuum well depth and the space charge potential  $\phi$ :

$$V = V_{vac}(t) - \phi. \quad (6.1)$$

The latter is approximated by a constant value, determined by measurements, times  $N$  (see section 5.2.2). A typical estimate is  $\phi \approx 1.4 \times 10^{-3} \text{ [mV]} \times N$ .

In the previous chapter, we found simple analytical expressions for the the antiproton cloud radius  $r$ , length  $l$ , density  $n$ , and stored self-potential

energy per particle  $u$  all as functions of  $N$  and  $T$ . When compared to the measurements, these expressions provided a reasonable description over the range of the measurements. In the following these estimates will be used to obtain model expressions for the evaporation time  $\tau_{ev}$  and for the heating rate  $P$ .

### 6.1.1 Modeling the evaporation time scale

In section 4.3.3 we found the evaporation timescale for ions confined in a Penning-Malmberg trap to be:

$$\lambda_{1D} = \frac{\tau_{ev}}{\tau_{col}} = \frac{1}{3}\eta e^\eta,$$

However, this expression assumes evaporation at equal rate for all radii. As explained in section 4.5.1 the radial change in the plasma self-potential cause evaporation to occur from within approximately one Debye length  $\lambda_D$  of the radial center only. To account for this effect,  $\tau_{ev}$  is increased by the ratio of the transverse area of the entire plasma to the area of the evaporating part of the plasma:

$$f = \frac{r^2}{\lambda_D^2}. \quad (6.2)$$

Thus, the evaporation time constant is modeled as:

$$\tau_{ev} = f\lambda_{1D}\tau_{col}, \quad (6.3)$$

where the expression for the collisional time scale  $\tau_{col}$  is given in section 4.4. The expression for  $\tau_{col}$  depends on the density and temperature of the plasma. The temperature is a model variable and the density can be expressed in terms of the number. This is done in section 5.2.1 where a simple equation describing the measured peak density as a function of the number was found and applied to estimate the collision frequency.

### 6.1.2 Expansion driven (re)heating

When a particle evaporates it can cause the release of some of the self-potential energy stored in the plasma. Some of the released energy can be carried away by the particle itself, and some can couple to the kinetic energy of the plasma

causing an increase of the plasma temperature. In the following we will estimate the source and magnitude of such heating.

The measured self-potential energy of the plasmas used in the evaporative cooling experiments can be approximated by the energy stored per particle in an infinite plasma column of constant density and radius  $r$ , surrounded by a conducting cylindrical wall of radius  $R_w$  (see section 5.2.3):

$$u = \frac{e^2}{4\pi\epsilon_0} \frac{N}{l} \left( \ln\left(\frac{R_w}{r}\right) + \frac{1}{4} \right), \quad (6.4)$$

where  $eN/l$  is the charge per unit length. The number of particles  $N$  is a decreasing function of time as particles evaporate, and both  $r$  and  $l$  can change as well. Thus the change in  $u$  as a function of time can be written as:

$$\frac{du}{dt} = \frac{\partial u}{\partial N} \frac{dN}{dt} + \frac{\partial u}{\partial r} \frac{dr}{dt} + \frac{\partial u}{\partial l} \frac{dl}{dt}. \quad (6.5)$$

In the analysis of the evaporative cooling experiments, we found that  $r$  and  $l$  could be expressed in terms of  $N$  as:

$$r = r_0 \sqrt{N_0/N}, \quad (6.6)$$

$$l = l_0 \sqrt{N/N_0}, \quad (6.7)$$

where  $r_0$  is the initial plasma radius,  $l_0$  the initial plasma length, and  $N_0$  the initial number of particles (Note though, the expression for  $l$  is not very accurate and could be improved).

Using these expressions the first term on the right side of equation (6.5) becomes:

$$\frac{\partial u}{\partial N} \frac{dN}{dt} = \frac{e^2}{4\pi\epsilon_0} \frac{1}{l_0} \sqrt{\frac{N_0}{N}} \left( \ln\left(\frac{R_w}{r}\right) + \frac{1}{4} \right) \frac{dN}{dt}. \quad (6.8)$$

This term can be interpreted as the potential energy carried away by a particle evaporating from the distribution. The second term becomes:

$$\frac{\partial u}{\partial r} \frac{dr}{dt} = \frac{e^2}{4\pi\epsilon_0} \frac{1}{2l_0} \sqrt{\frac{N_0}{N}} \frac{dN}{dt}, \quad (6.9)$$

and it express the energy released as the plasma radius expands after a particle has left. During this expansion, work is done on the plasma, converting

potential energy to kinetic energy, thus heating the plasma. The last term becomes:

$$\frac{\partial u}{\partial l} \frac{dl}{dt} = -\frac{e^2}{4\pi\epsilon_0} \frac{1}{2l_0} \sqrt{\frac{N_0}{N}} \left( \ln\left(\frac{R_w}{r}\right) + \frac{1}{4} \right) \frac{dN}{dt}, \quad (6.10)$$

and is the increase in energy as the plasma length is shortened after a particle has left. Since evaporation involves fast moving particles the potential change due to evaporation is non-adiabatic, and no work is done on the plasma during this process.

In this analysis only the second term of equation (6.5) is assumed to contribute to heating of the plasma. In this case the total temperature change can be written as:

$$\begin{aligned} P &= \frac{1}{\frac{3}{2}k_B} \frac{\partial u}{\partial r} \frac{dr}{dt} \\ &= \frac{1}{\frac{3}{2}k_B} \frac{e^2}{4\pi\epsilon_0} \frac{1}{2l_0} \sqrt{\frac{N_0}{N}} \frac{dN}{dt}. \end{aligned} \quad (6.11)$$

However, finite length effects may cause more of the released self-potential energy to be converted to heat during the process of evaporation. An upper limit of such effects can be found by assuming that the entire change in self-potential energy is converted to heat. Assuming  $\ln(R_w/r) \approx 3$  ( $R_w = 22$  mm and  $r \approx 1$  mm), all three terms of equation (6.5) are easily compared, and we find a heating rate about 4 times higher than that of the  $r$  dependent term alone.

Finally, we can now define the dimensionless quantity:

$$\begin{aligned} \alpha_{Heat} &= \frac{N}{3/2k_B T} \frac{\partial u}{\partial r} \frac{dr}{dN} \\ &= \frac{1}{3/2k_B T} \frac{e^2}{4\pi\epsilon_0} \frac{\sqrt{NN_0}}{2l_0}, \end{aligned} \quad (6.12)$$

and rewrite the differential equation describing the evaporation process as:

$$\frac{dN}{dt} = -\frac{N}{\tau_{ev}} + \gamma N, \quad (6.13)$$

$$\frac{dT}{dt} = -(\alpha - \alpha_{Heat}) \frac{T}{\tau_{ev}} + P'. \quad (6.14)$$

where  $P'$  includes heating from sources other than the release of self-potential energy.

As mentioned at the end of section 4.2 the slope of the curve  $(N(t), T(t))$  in a log-log plot does not equal  $\alpha$  in the case of evaporation of ions (from a Penning-Malmberg trap). Instead, we see from the equations above that:

$$\frac{d \ln T}{d \ln N} \approx (\alpha - \alpha_{Heat}). \quad (6.15)$$

This means that achieving conditions where  $\alpha$  (and  $\eta$ ) is relatively high does not guarantee that the distribution is cooled efficiently from evaporation.

The equation (6.12) describing  $\alpha_{Heat}$  scales as  $\sqrt{N}/T$ , which means that even in the case where the cooling is incredibly efficient, i.e. a negligible change in  $N$  leads to a large decrease in  $T$ ,  $\alpha_{Heat}$  will increase. At some temperature  $\alpha_{Heat}$  will equal  $\alpha$  and no evaporative cooling beyond that point is possible. This effect is illustrated in section 6.1.4 below.

### 6.1.3 Applying the model

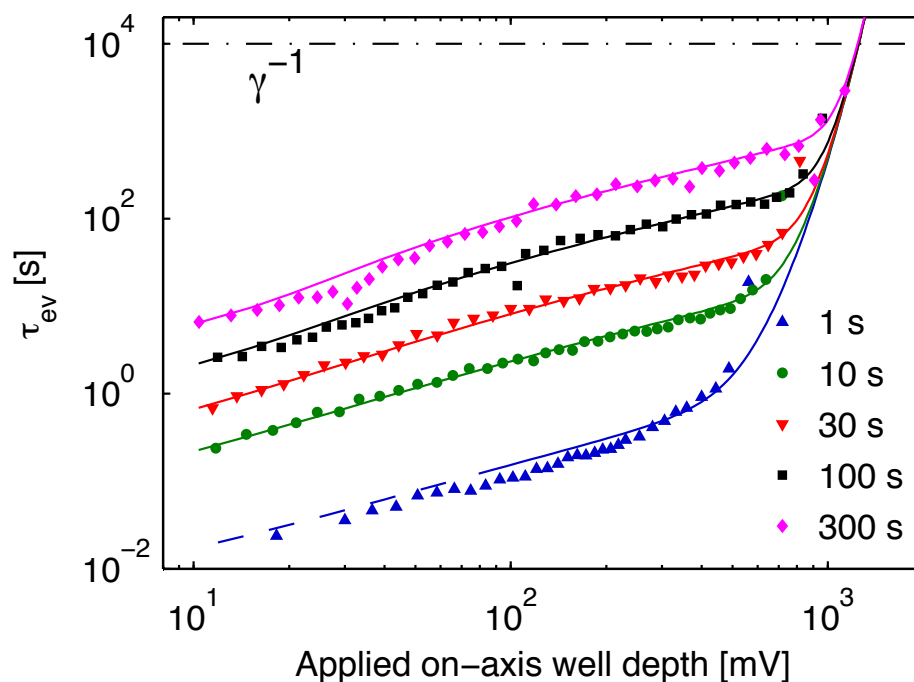
The numerical model, as described by equations (6.13) and (6.14) above, can be applied to calculate  $N$  and  $T$  for a given evaporation ramp  $V_{vac}(t)$  if we assume  $P' = 0$ . It is not clear that the release of self-potential energy is the only heating source, and as we shall see, the heating term included in the model does not allow complete agreement with the measurements. However, attempts to include another heating source shows that, if present, it must be of similar magnitude as the one already included.

Figure 6.1 shows the evaporation time scale calculated as:

$$\tau_{ev} = -(d \log N/dt + \gamma)^{-1}, \quad (6.16)$$

for five different experimental data sets of the Main series (see section 5.1). In each case the ramp was from the initially 1500 mV deep well to the most shallow 10 mV deep well. The total time of the ramp was varied between 1 and 300 s. Also shown are model calculations of the five ramps. The good agreement between the measurement and the model calculation shows that we can predict  $\tau_{ev}$  over a wide range of well depth and ramp times.

Figure 6.2 shows a plot of all the data points of the Main series (see Table 5.1). Each point is the result of a forced evaporation experiment, where the well depth was changed from 1500 mV to the well depth indicated on the first axis, and in each case the ramp time is indicated by the data marker and



**Figure 6.1:** The evaporation time scale vs applied on-axis well depth for five experiments with different ramp times. The on-axis well depth at the end of the ramp is  $(10 \pm 4)$  mv in all cases.  $\gamma^{-1}$  is indicated by the dot-dashed line, model calculations are shown as lines and, dashed lines indicate  $\eta < 4$  in the model calculation.

color. Thus, all similar data points share the same ramp time, but the ramp rates differ slightly. Model calculations are shown as lines, and each point on one of the lines represents a calculation of a ramp to a particular well depth, with the total time of the ramp indicated by the color of the line (101 calculations per line). In Figure 6.1, discussed above, all points on the same line belongs to the same single calculation.

The model calculations of temperature and remaining fraction shown in Figure 6.2(a) and (b) are in reasonably good agreement with the data points. However, at low well depth the temperature predicted by the model appears to be slightly lower than the measured temperature (panel (a)) and the remaining fraction appears slightly higher than the measured fraction (panel (b)). A possible explanation of this phenomenon is that the heating term due to re-

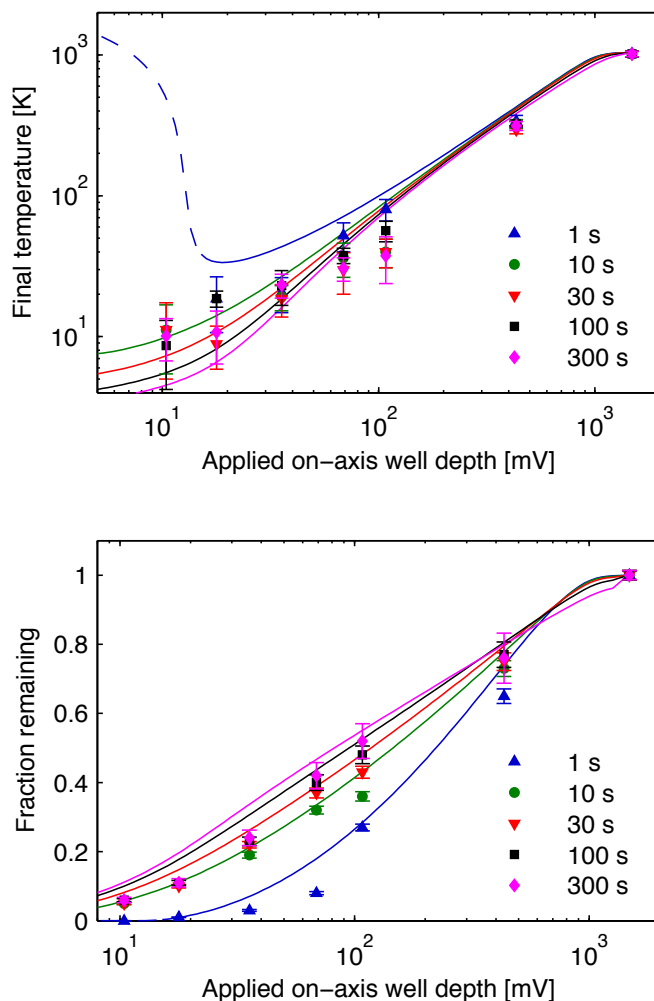


**Figure 6.2:** (a) Temperature vs. the on-axis well depth. The error on the data points is the combined statistical uncertainty from the temperature fit and an uncertainty associated with the applied potentials (one  $\sigma$ ). The legend indicates the ramp time. The model calculations (solid lines) are described in the text, dashed lines indicate  $\eta < 4$  in the model calculation. (b) The fraction of antiprotons remaining after evaporative cooling vs. the on-axis well depth. The uncertainty on each point is propagated from the counting error (one  $\sigma$ ). The initial number of antiprotons was approximately 45000, for an on-axis well depth of  $(1484 \pm 14)$  mV.

lease of self-potential energy  $\alpha_{Heat}$  is too small, or that some other mechanism such as electronic noise heat the particles (non-zero  $P'$ ). If  $\alpha_{Heat}$  is increased by a factor of  $\sim 4$  to include the entire change in self-potential energy, and not just that due to radial expansion, a better match to the data can be achieved. This indicates that any other heating mechanism is of the same order as  $\alpha_{Heat}$ .

The model explains the excessive particle loss observed for the 1 s ramps. Here  $\tau_{ev}$  becomes too short for rethermalization, and  $\eta$  is forced below one.

Over all, the numerical calculations agrees well with the measured data, indicating that the most important physics is captured in the model. In the following section two of these effects will be investigated, and in later sections different attempts to improve the number remaining at low temperatures (10 K) are evaluated.

#### 6.1.4 The effect of radial aperture and heating

Two effects, in particular, limit the evaporative cooling at low temperatures. One is the aperture effect of evaporation from the radial center, characterized by the ratio  $f$  defined by equation (6.2). The other is the heating caused by the release of self-potential energy, characterized by  $\alpha_{Heat}$  defined above in equation (6.12).

If we ignore both of these effects, evaporation is only limited by the collision rate which is determined by the temperature and density. As discussed in section 4.4 the collision rate increase for decreasing temperature until at some point the plasma becomes strongly magnetized. For antiprotons in a 1 T magnetic field the collision rate drops quickly beyond about 0.5 K.

Figure 6.3 shows three different model calculations, all starting with the same conditions. In the first case the full model is used, including the effect of aperture and heating ( $f$  and  $\alpha_{Heat}$ ), in the second case  $\alpha_{Heat} = 0$ , and in the third case  $f = 1$  as well. For the calculations here the initial antiproton number was 45000, the initial length 10 mm, and the initial radius 0.6 mm. The ramp starts at an applied well depth of 1500 mV and ends at varying well depth down to 2.5 mV. The duration of the ramp was chosen to be 100 s.

In the case where both effects are ignored evaporation is very efficient with about 45% of the initial number left at 10 K and about 30% at 1 K. In this case  $\alpha \approx 3$  is the slope of the curve in the log-log plot.

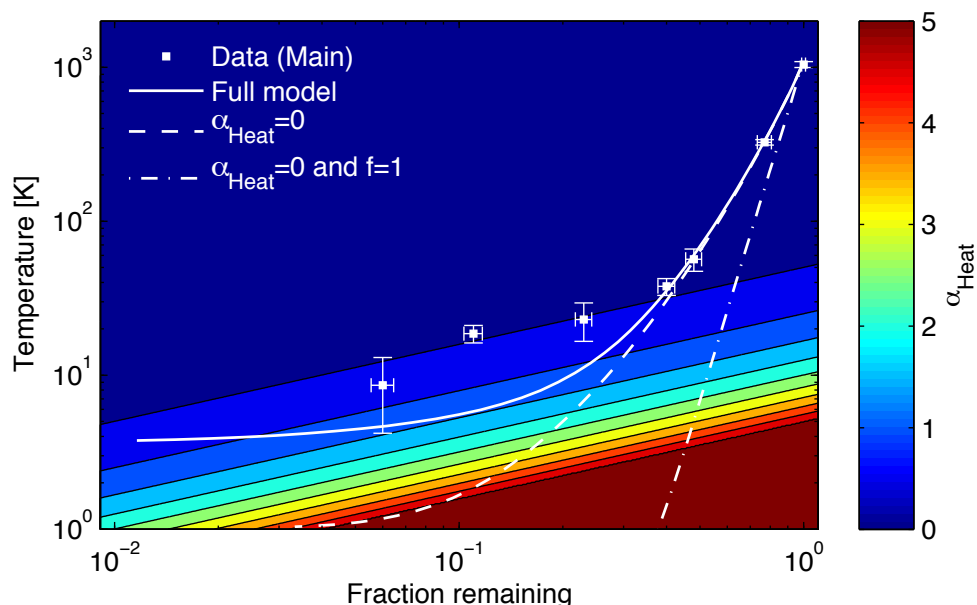


**Figure 6.3:** The effect of radial aperture and expansion driven heating on forced evaporative cooling. Numerical model calculations using an initial number of 45000 antiprotons, length of 10 mm and radius of 0.6 mm. The ramp starts at an applied well depth of 1500 mV and ends at a varying well depth down to 2.5 mV. The duration of the ramp was chosen to be 100 s.

Adding the effect of aperture ( $f$ ), the model starts to follow the measured data at temperatures higher than about 30 K, and it is clear that even at the beginning of the ramp, the aperture effect play an important role. In principle, the effect of the aperture can be canceled by a longer ramp time, since its only direct effect is a lower rate of evaporation. Thus the aperture does not limit the maximum efficiency at a given temperature.

When  $\alpha_{Heat}$  is included in the model, a limit on the best possible efficiency is introduced. The value of  $\alpha_{Heat}$  is indicated as contours on the figure, and at low temperatures (here below  $\sim 10$  K) it increases rapidly. For all practical purposes, it is not possible to enter the region where  $\alpha_{Heat}$  exceeds 5. In fact as soon as  $\alpha_{Heat}$  becomes about 0.5 the slope of the  $(N, T)$  curve starts to change noticeably on the log-log plot.

In summary, both the aperture effect and the heating caused by the release of self-potential energy are important to include when modeling the evapora-

tion experiments at low temperatures. The effect of the former is noticeable even at the start of the evaporation ramp, and the later limits the maximum efficiency which can be achieved for a given temperature.

## 6.2 Increasing the initial number

The evaporation process is driven by collisions, and it seems reasonable to increase the collision rate by increasing the density. The main reason for doing so would be to increase the number of antiprotons remaining at a particular temperature.

When the number is increased the space charge is also increased, and in turn this affects the well depth experienced by the particles. This is expressed by equation (6.1). If we follow the model for the length of the cloud described by equation (6.7), the length will increase as the square root of the number as we add more particles. Unlike the length, the radius of the cloud will stay unchanged.

Figure 6.4(a)-(d) shows four different calculations starting with  $k = 0.5, 1, 5,$  and  $10$  times the initial number of the Main data series. In this case the initial number is  $N_0 = 45000$ . The initial length is  $\sqrt{k} \times 10$  mm, and the radius is  $0.6$  mm. The ramp starts at a an applied well depth of  $1500$  mV and ends at a varying well depth down to  $2.5$  mV. The duration of the ramp was chosen to be  $100$  s. Also shown is a line indicating  $10$  K, and contours show the magnitude of  $\alpha_{Heat}$  in each case.

The applied well depth where the temperature reaches  $10$  K will be different in each case because the space charge potential is higher when more antiprotons are in the well. Thus to find out which of the four cases is the most favorable, we can compare the fraction remaining at  $10$  K in each case. Such a comparison shows that a slightly lower fraction remains when more particles are added to the distribution. In all cases the curve bends of when it enters a region of large  $\alpha_{Heat}$ , and for higher numbers the increase in  $\alpha_{Heat}$  happens at a higher temperature.

We can conclude, that since  $\alpha_{Heat}$  increase with the number of antiprotons in the well, the gain in collision frequency from a higher density is counter-acted.

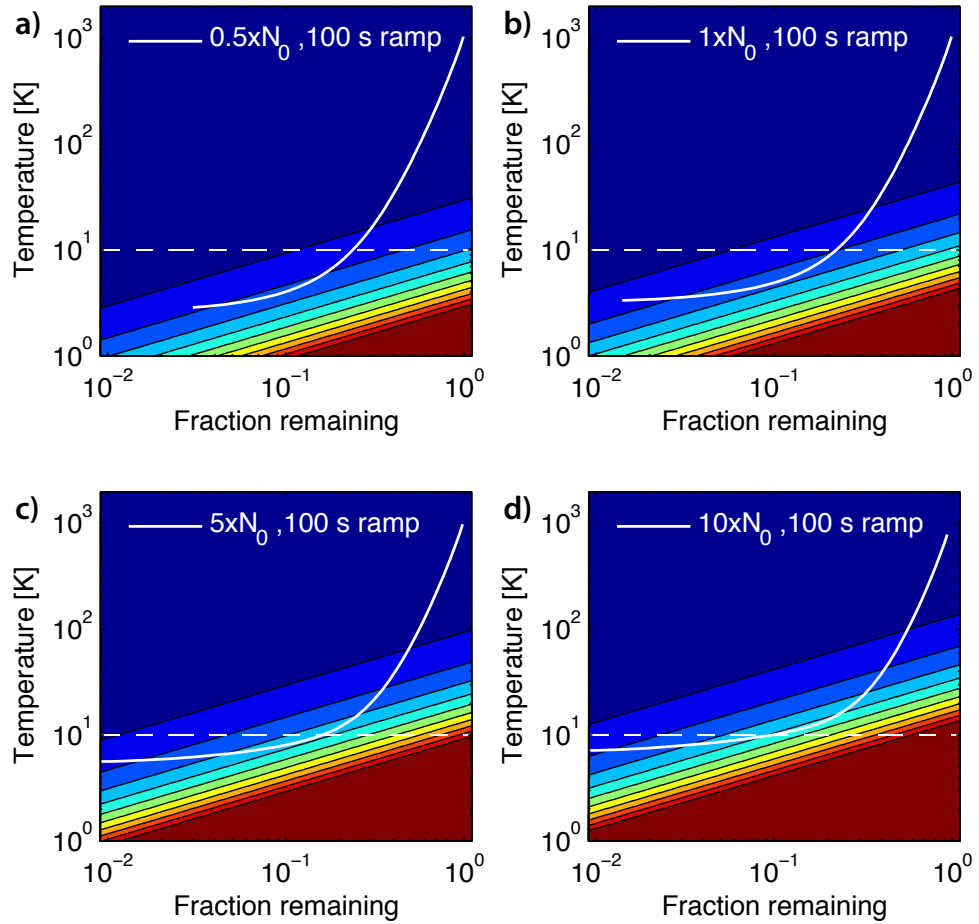


**Figure 6.4:** The effect of increasing the initial number on forced evaporative cooling. Numerical model calculations for four different initial numbers of antiprotons (see text). For higher numbers the release of self-potential energy cause heating to be problematic at higher temperatures. Contours indicate the value of  $\alpha_{Heat}$  with the same color scale as used in Figure 6.3.

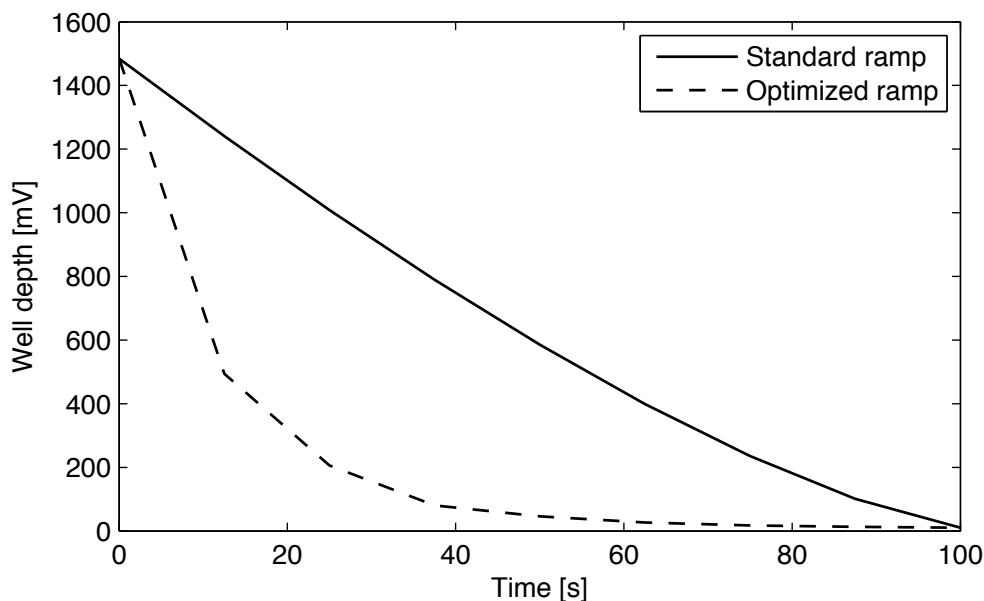


**Figure 6.5:** Numerically optimized voltage ramp for forced evaporative cooling (dashed line). The standard ramp applied in the experiments using the most shallow 10 mV final well depth is drawn for comparison (solid line).

### 6.3 Numerical optimization of the evaporation voltage ramp

In the forced evaporative cooling experiments described in the previous chapter, the depth of the applied potential well was changed by linearly ramping the voltage applied to one of the electrodes. As a result the depth changes in a near linear way near the axis too. Figure 6.5 shows the vacuum well depth as a function of time for a ramp to the most shallow well investigated.

Using the numerical model, we can attempt to optimize the shape of the voltage ramp to increase the number of antiprotons remaining at the end of the ramp. This was done in a numerical simulation where a *standard ramp* was broken into 8 separate linear pieces of equal length in time. By choosing a piece at random and then randomly changing the slope of that particular piece and that of its right neighbor, a new ramp was generated. If the new ramp resulted in a higher number of surviving particles the change was kept; if not the change was discarded. The process was repeated 200 times after

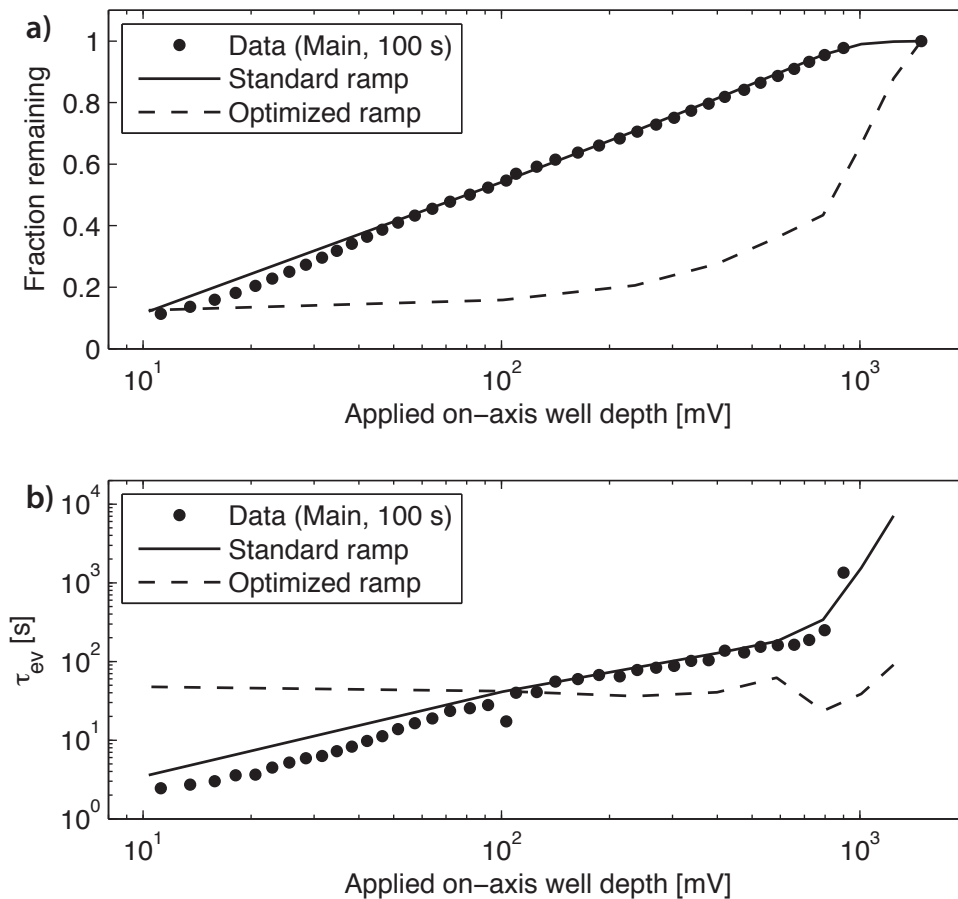


**Figure 6.6:** (a) Remaining fraction as a function of well depth for the standard ramp (solid line), the numerically optimized ramp (dashed line), and the experimental data. In all cases the total ramp time was 100 s. (b) The evaporation time scale for all three cases.

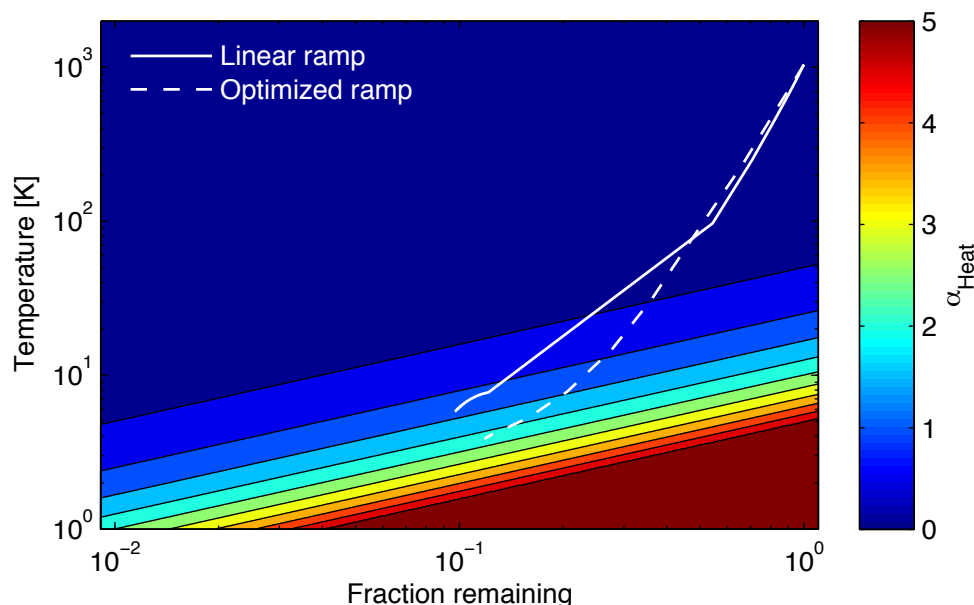


**Figure 6.7:** Temperature vs remaining fraction for the standard ramp (solid line) and the numerically optimized ramp (dashed line). The value of  $\alpha_{Heat}$  is indicated by contours.

which the shape of the ramp was observed to be reasonably stable, meaning that a high number of additional iterations was required for any new change to be accepted.

The initial conditions used for the numerical optimization was those of the Main data series described in the previous chapter, i.e. 45000 antiprotons of length 10 mm and radius 0.6 mm. The ramp started at a depth of 1500 mV and ended with a 10 mV deep final well. The duration of the ramp was chosen to be 100 s.

Figure 6.5 shows the standard ramp and the optimized ramp as a function of time. Clearly, the optimized ramp is much different from the standard ramp with a fast initial decrease in well depth followed by a slow decrease to the final depth. The fraction surviving is shown as a function of well depth in Figure 6.6(a). Also shown is the measured fraction of antiprotons remaining in an experiment where the standard ramp was used. Qualitatively, the two curves are very different with the optimized ramp exhibiting a quick decrease in number in the beginning followed by a slow decay. The standard ramp

has a more gradual decrease in number as the well depth becomes lower. However, the final fraction remaining only differs by about 0.02 between the two ramps.

Figure 6.6(b) shows the evaporation time scale  $\tau_{ev}$  for both ramps as well as for the experimental data. Here we see that the optimized ramp achieves a near constant  $\tau_{ev}$  as a function of well depth, whereas  $\tau_{ev}$  is a decreasing function of well depth for the standard ramp. It is perhaps not surprising that keeping  $\tau_{ev}$  constant is a more efficient solution.

Finally, Figure 6.7 shows the temperature as a function of number for the two ramps. The optimized ramp clearly achieves the lowest temperature, but as the heating term  $\alpha_{Heat}$  starts to increase the curve bends off, limiting the surviving number. If the well depth is lowered further (not shown), both curves roughly follow the slope indicated by the contours of  $\alpha_{Heat}$ .

In conclusion, the optimal ramp appears to be one where  $\tau_{ev}$  is kept constant, which can be achieved by adjusting the ramp rate to be faster at the beginning of the ramp and slower at the end. However, the surviving number is increased very little by changing the standard linear ramp to an optimized ramp. In this calculation, about 10% of the initial number survived to the final well depth for the standard ramp compared to 12% survival for the optimized ramp.

## 6.4 The effect of radial compression

Radial compression of the initial antiproton distribution will increase the density  $n$ , and since  $\alpha_{Heat}$  is independent of the initial radius, it will remain unchanged. Increasing the density has the effect of increasing the rate of evaporation by increasing the collision rate. However, the Debye length will decrease as well, enhancing the aperture effect. The overall change in evaporation rate will scale like  $\sqrt{n}$ , and radial compression should be favorable.

Figure 6.8 shows a calculation performed with different initial radii (0.1, 0.5, 1, and 2 times  $r_0$ ). The initial condition of the calculation had 45000 antiprotons, a cloud length of 10 mm, and  $r_0 = 0.6$  mm. As expected, evaporative cooling is more efficient for smaller radii, favoring radial compression before evaporation.

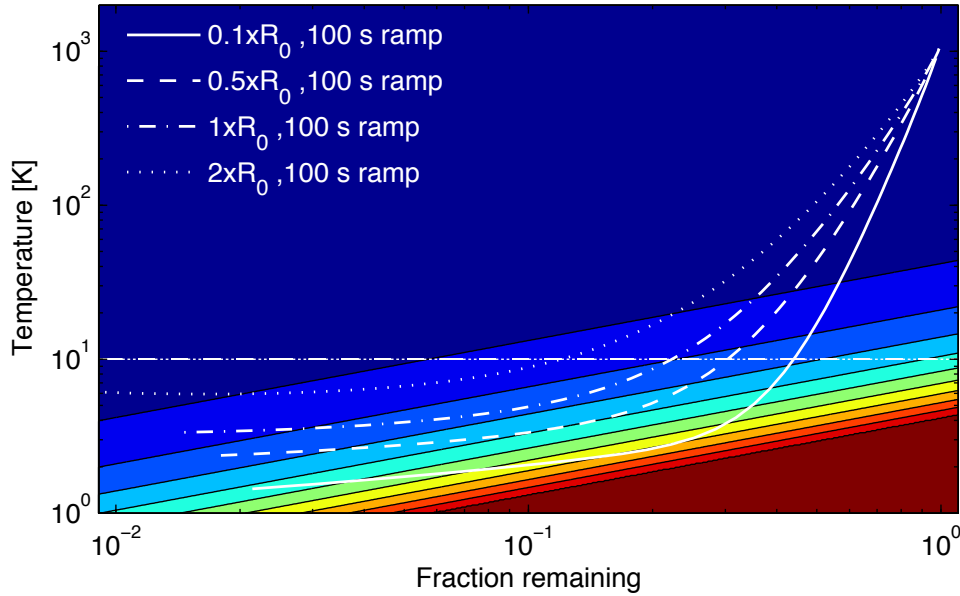


**Figure 6.8:** The effect of a smaller initial radius on forced evaporative cooling. Numerical model calculations using an initial number of 45000 antiprotons, length of 10 mm and  $r_0 = 0.6$  mm. The ramp starts at an applied well depth of 1500 mV and ends at a varying well depth down to 2.5 mV. The duration of the ramp was chosen to be 100 s. The value of  $\alpha_{Heat}$  is indicated by contours.

A small cloud radius is preferable for other reasons too. As described in section 1.3 the perturbations of the magnetostatic trap on the charged particles is smaller near the axis, and as described in later chapters the energy associated with the antiproton magnetron motion can lead to antihydrogen formed at energies too high to be trapped (see section 8.5 and chapter 9).

The increase in cloud radius due to evaporative cooling scales with the fraction remaining (see equation (6.6)), and with a higher fraction surviving at a smaller initial radius the relative change in radius becomes smaller too. Thus a smaller initial radius results in a much smaller final radius.

## 6.5 Conclusion

In this chapter, a numerical model was compared to the results of evaporative cooling of antiprotons. We found reasonable agreement between the data and

the model, and were able to investigate the effect of a decrease in evaporation rate, due to evaporation occurring primarily from within one Debye length of the radial center, and the effect of heating due to the release of self-potential energy. The former was found to decrease the efficiency of evaporation even at relative high temperatures, and the later to limit the maximum efficiency at a given temperature.

Using the model, different strategies to enhance the fraction remaining at a given temperature (here 10 K) was investigated. Increasing the initial number was found to decrease the fraction surviving, numerical optimization of the evaporation ramp resulted in a small increase in the fraction remaining, and radial compression of the cloud before evaporative cooling was found to increase the fraction remaining at 10 K significantly. In addition, the later had the added benefit of a much smaller final cloud radius.

# Antihydrogen formation and detection in the ALPHA apparatus

---

The aim of this chapter is to show how antihydrogen production in the ALPHA apparatus has evolved since the apparatus was commissioned in 2006. Three different experiments are discussed, and in all three cases the technique used to form antihydrogen are variations of the nested potential scheme described briefly in section 1.2.1 of the introduction.

The first experiment is mixing of antiprotons and positrons in the most basic configuration of the ALPHA apparatus (see section 7.2). In these experiments the magnetostatic trap was not energized and the mixing procedure mimics that used previously by the ATHENA experiment; though this time in a lower solenoidal field. Previous experiments Amoretti *et al.* (2002); Gabrielse *et al.* (2002a) employed much higher magnetic fields to confine the charged constituents in the antihydrogen formation region.

The next step was to demonstrate antihydrogen production with the magnetostatic trap on (see section 7.3). The ALPHA apparatus is designed to produce antihydrogen inside a magnetostatic trap, but as described in section 1.3 the presence of a multipolar field introduced by such a trap, can be problematic. For this reason verification of antihydrogen production in the combined trap has been of utmost importance in the early phase of ALPHA.

The mixing experiments used to demonstrate antihydrogen production in the magnetostatic trap employed new techniques such as radial compression of the antiproton cloud and a new way of injecting the antiprotons into

the positron plasma. Also ionization of antihydrogen was used in concert with spatial detection of annihilations to strengthen detection of antihydrogen and to identify particular signatures of antihydrogen formed in the magnetostatic trap.

At the end of the chapter some of the details concerning the most recent antihydrogen trapping attempts performed during the 2009 experimental run at the AD, are described (see section 7.4). These experiments are discussed in more detail in chapter 8.

However, first, the methods which have currently been used to identify formation of antihydrogen from trapped antiprotons and positrons are discussed in section 7.1.

## 7.1 Signatures of antihydrogen formation

The ultimate signature of antihydrogen would be direct observation of the (anti)hydrogen energy spectrum from trapped atoms. But, fortunately, other methods are available until this can be realized.

So far three methods for detecting antihydrogen are available in the ALPHA apparatus. These are: spatial detection of annihilations, field-ionization of antihydrogen, and heating of the positron plasma to inhibit antihydrogen formation. In the following sections each of these methods will be discussed in the context of the experiments where they were first used.

### 7.1.1 Spatial detection of antihydrogen annihilations

Antihydrogen atoms produced during the interaction between trapped antiprotons and positrons in a nested potential configuration (shown in Figure 7.1(b)) was first detected by the ATHENA collaboration using a combined silicon strip and CsI detector. The neutral antihydrogen produced in these experiments was not confined by the Penning-Malmberg trap used to hold its charged constituents, and would annihilate on the surrounding electrode wall quickly after being formed.

A typical antiproton annihilation results in the emission of three charged pions, and the annihilation of a positron results in the emission of two back-to-back 511 keV photons (Yao *et al.*, 2006). In the event where three pions were

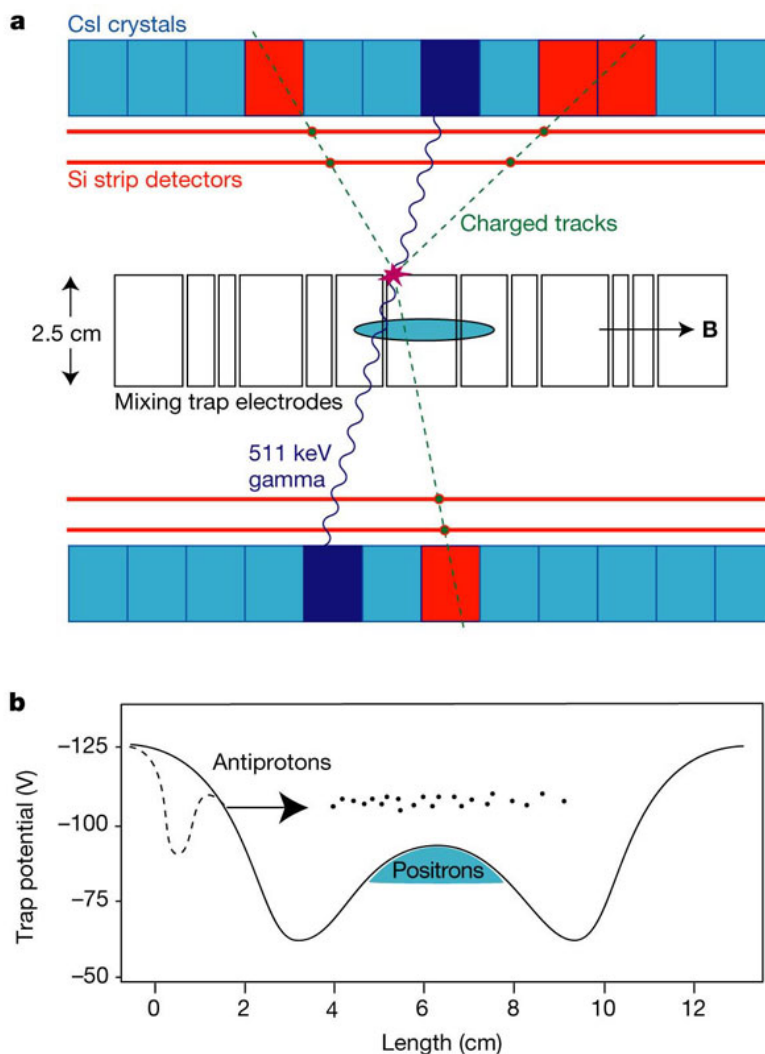


**Figure 7.1:** First detection of cold antihydrogen by the ATHENA collaboration using spatial detection of the antihydrogen annihilation. (a) Schematic diagram illustrating detection of an antihydrogen atom annihilating on the electrode wall in the ATHENA apparatus. Three charge ions and two back-to-back 511 keV photons are emitted and detected in the combined silicon strip and CsI crystal detector. Coincidence and spatial overlap between the location of the antiproton and the positron annihilation is used as a proxy for antihydrogen. (b) Antiprotons are injected into a nested potential to interact with a preloaded positron plasma. (Adapted from Amoretti *et al.*, 2002).

successfully detected in both layers of the silicon detector, the location of the antiproton annihilation could be identified as the vertex formed by the pion tracks. Likewise, if two 511 keV photons were detected in the CsI crystals, a straight line drawn between the two activated crystals indicates the path followed by the photons. Coincidence between an antiproton and a positron annihilation and overlap between the antiproton annihilation vertex and the photon path was thus used as a proxy for antihydrogen. A graphical illustration of antihydrogen annihilation and detection in the ATHENA apparatus is shown in Figure 7.1(a). In the ATHENA experiment the efficiency for detecting an antihydrogen annihilation as described above was estimated to be  $2.5 \times 10^{-3}$  (Amoretti *et al.*, 2002).

The very stringent cuts initially used to identify antihydrogen was later used to characterize other signatures of antihydrogen production, showing that nearly all antiprotons observed to annihilate on the electrode wall during mixing of antiprotons and positrons could be attributed to antihydrogen (Amoretti *et al.*, 2004b; Madsen *et al.*, 2005). Fujiwara *et al.* (2004) showed that bare antiprotons striking the electrode wall tend to annihilate in *hot spots*, i.e. at a discrete set of point, the location of which is assumed to be determined by field inhomogeneities particular to the individual apparatus. In contrast antihydrogen is observed to annihilate in a pattern with no angular dependence (Amoretti *et al.*, 2002; Fujiwara, 2005). Thus by observing the spatial distribution of antiproton annihilations during mixing the solid angle for antihydrogen detection can be made very large. With a position sensitive detector covering the entire mixing region a coverage close to  $4\pi$  can be achieved.

In the ALPHA apparatus detection of positron annihilations is very limited, and only reconstruction of the antiproton annihilation vertex is possible. Thus identification of antihydrogen annihilations rely on the spatial distribution of antiproton annihilations as described above.

The time dependent antihydrogen signal measured by the ATHENA collaboration can be found in Amoretti *et al.* (2004b). These experiments showed the antihydrogen formation rate to peak within a few tens of milliseconds followed by a slow decay lasting more than 100 s.

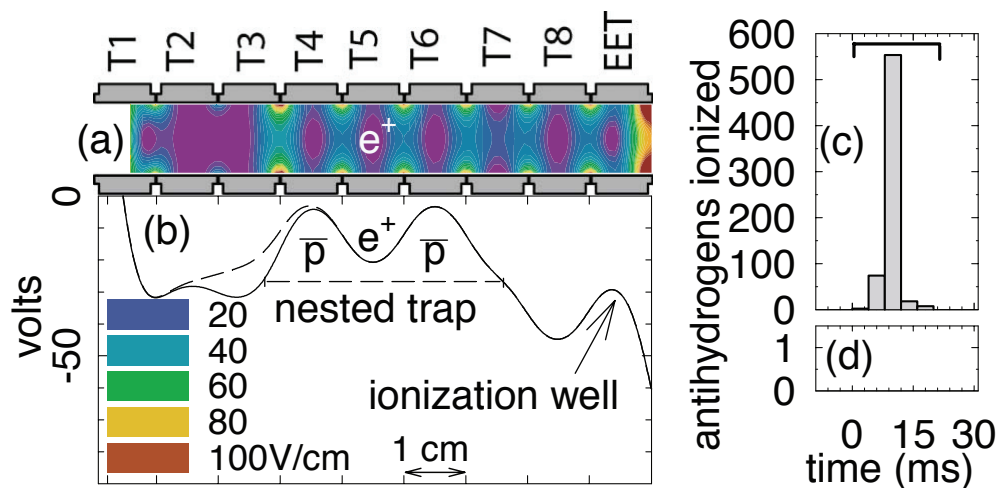


**Figure 7.2:** Detection of cold antihydrogen by the ATRAP collaboration using field-ionization. (a) Electrodes for the nested Penning-Malmberg trap. Inside is a representation of the magnitude of the electric field that strips antihydrogen atoms. (b) Nested potential used to mix antiprotons and positrons (solid line) with the (dashed line) modification used to launch antiprotons into the well. (c) Antiprotons from field-ionization are released from the ionization well during a 20 ms time window. (d) No antiprotons are counted when no positrons are in the trap. (Adapted from Gabrielse *et al.*, 2002a).

### 7.1.2 Field ionization of antihydrogen

A second, complementary, method to establish antihydrogen formation is to intentionally field-ionize weakly bound antihydrogen atoms, and trap the antiproton in the process. Later the number of antiprotons caught in this way can be counted by quickly releasing them onto a matter target. The method works by exploiting the fact that bare antiprotons cannot traverse an electric potential barrier higher than their kinetic energy and become trapped in the so-called *ionization well*. Antihydrogen atoms, on the other hand, are neutral and can move through the barrier. Once past the barrier an electrode is used to generate an electric field strong enough to ionize weakly bound atoms. Field-ionization was first developed as a technique to identify antihydrogen atoms by the ATRAP collaboration. Figure 7.2 illustrates the first detection of antihydrogen atoms using this technique (Gabrielse *et al.*, 2002a).

One advantage of using field-ionization as a detection method is the in-

formation about the antihydrogen binding energy gained in the process. The electric field the atom has to traverse to enter the ionization-well sets a lower limit on the binding energy, and the field used to ionize the atom sets an upper limit. Using this method part of the distribution of atomic states produced in the antihydrogen formation process has been measured (Gabrielse *et al.*, 2002b). Unfortunately, it is typically not feasible to apply fields much greater than  $\sim 100$  V/cm corresponding to a Rydberg state of about 40, and the formation rate of lower lying Rydberg states remains a theoretical question.

As an antihydrogen detection method, field-ionization of antihydrogen suffers from a small cross section for detection. To be detected an atom is required to have a binding energy in the interval described above, and it must be emitted in the direction of the detection region. A typical solid angle from spatial separation of production and detection is a few percent of  $4\pi$  at most. This number can be compared to the near complete solid angle coverage achieved when using position sensitive detection of the antihydrogen annihilation (see section 7.1.1 above).

In section 7.3 a novel way of combining the ionization of antihydrogen with spatial detection of antiproton annihilations is described in some detail. This method only applies when a multipolar magnetic field is added to the solenoidal field of a Penning-Malmberg trap either during or immediately after antihydrogen formation.

### 7.1.3 Mixing with heated positrons

Theoretical estimates of the antihydrogen formation rate shows a strong dependence on the positron temperature (see section 1.2.2). In addition to showing simultaneous and co-located annihilation of antiprotons and positrons, the ATHENA collaboration used heating of the positron plasma to inhibit antihydrogen formation. In the initial experiments heating of the positron plasma reduced the average rate of antiproton annihilations by a factor of 4 and the peak rate by a factor of 10. Investigations of the spatial distribution of the annihilations during this so-called *hot mixing* showed a distribution peaked at the radial center as opposed to a distribution peaked at the radius of the electrode wall observed for *cold mixing* (Amoretti *et al.*, 2002).

Further development and analysis of the ATHENA results has firmly es-

tablished heating of the positron plasma as a reliable null measurement for antihydrogen formation and has provided experimental insight in the temperature scaling of the antihydrogen formation rate (Amoretti *et al.*, 2003, 2004b; Fujiwara *et al.*, 2008).

A comparison between hot and cold mixing of antiprotons and positrons measured during the commissioning of the ALPHA apparatus can be seen in Figure 7.4 (further details can be found in section 7.2 below).

## 7.2 Production of antihydrogen in a 1 T magnetic field (2006)

During the commissioning of the ALPHA apparatus in 2006, production of antihydrogen was shown to be possible in a 1 T solenoidal field. In previous experiments antihydrogen was formed in higher fields (ATHENA 3 T and ATRAP 5 T). Understanding the signatures of antihydrogen production in the low field is a very important step towards making trappable antihydrogen, and showing that the ALPHA apparatus is capable of synthesizing antihydrogen in the most basic configuration was essential. The measurements described in this section were reported in (Andresen *et al.*, 2008a).

The experiment starts with the stacking and cooling of three bunches of antiprotons from the AD. One bunch is delivered every 100 s and contains 2 to  $3 \times 10^7$  antiprotons at a kinetic energy of 5 MeV. The antiprotons are slowed in a thin metal foil allowing a fraction to be caught between the two high-voltage electrodes in the catching region (Gabrielse *et al.*, 1986, 2002c). Between the arrival of each bunch, the captured antiprotons cool by interactions with a preloaded electron plasma and after about 40 s of cooling most are fully contained in the electron plasma. To optimize the antiproton catching efficiency, both solenoids in the apparatus were energized to yield a combined field of 3 T (Bertsche *et al.*, 2006; Andresen *et al.*, 2008a). After catching and cooling the final bunch of antiprotons, the electrons were removed by applying a series of 30, 200 ns pulses to quickly lower one of the confining electric potentials.

The antiproton cloud was then transferred from the catching region to the mixing region of the apparatus. This was done by ramping adjacent elec-

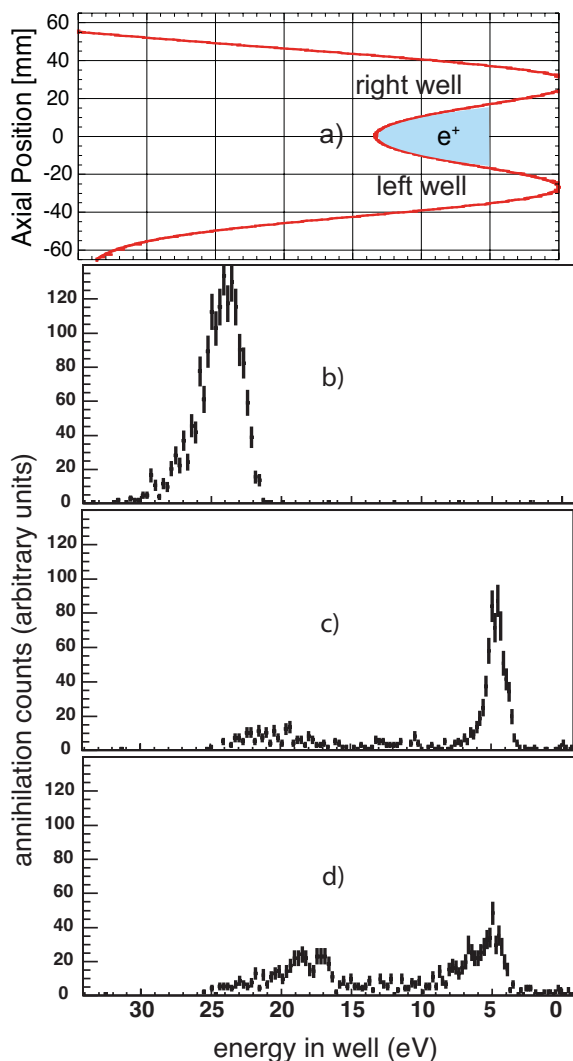


**Figure 7.3:** (a) The on-axis vacuum potential in the nested trap. The blue-shaded region is the portion of the center well that is flattened by the positron space charge potential. (b)-(d) Antiproton energy distributions in the nested trap potential measured by ramping down the left potential wall. The relative number of released antiprotons is plotted versus energy for (b) antiprotons only, (c) mixing with cold positrons and (d) mixing with heated positrons. In all three cases, the antiprotons were released in 200 ms, 50 s after being injected into the nested potential. The horizontal axis scale is common to all four figures. The uncertainties reflect counting statistics only (1 sigma). (Adapted from Andresen *et al.*, 2008a).

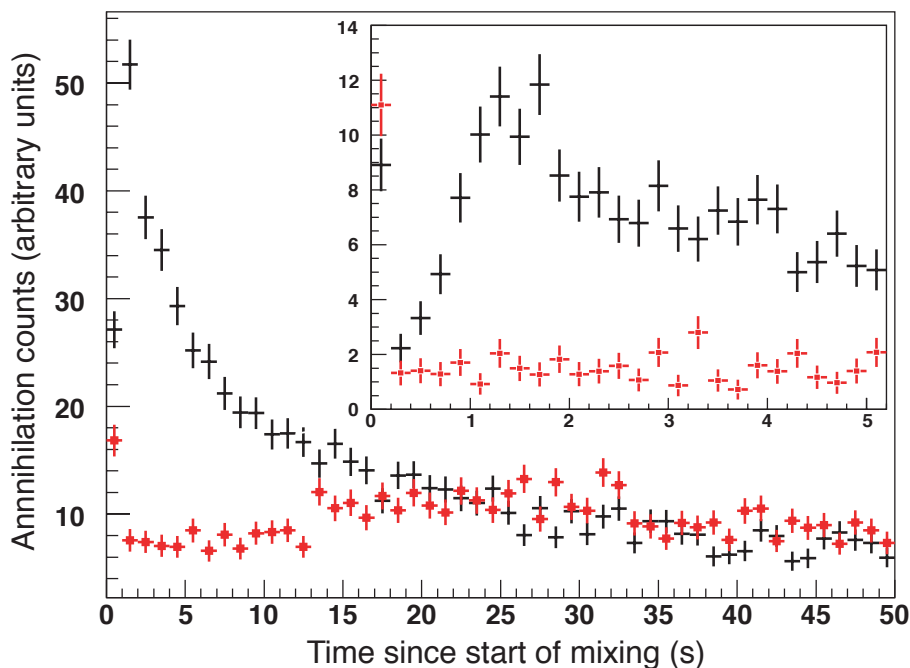


**Figure 7.4:** Scintillation events as a function of time after the start of mixing, for mixing with cold positrons (black) and mixing with heated positrons (red). The time bins are 1 s long. The data are for 10 mixing cycles, normalized to one cycle. The inset is a plot of the first 5 s of the same data, re-binned into 200 ms bins to illustrate the rise time of the antihydrogen production. The uncertainties reflect counting statistics only (1 sigma). (Adapted from Andresen *et al.*, 2008a).

trodes to create a potential well of close to constant depth and length, moving slowly with respect to the antiproton axial bounce time, along the trap axis. In the region where the solenoidal field changes from 3 to 1 T, great care had to be taken to avoid losing particles since the radius of the antiproton cloud expands radially by a factor of  $\sqrt{3} \approx 1.7$  as the particles follow the magnetic field lines. To smooth the transition from 3 to 1 T, the left-most mirror coil was energized. After optimization, the transfer was accomplished with less than 10% loss of antiprotons, leaving about 7000 antiprotons to be mixed with positrons.

While the antiprotons were being prepared, a plasma of typically 30 mil-

lion positrons was loaded from the ALPHA positron accumulator into the mixing region of the main apparatus. Here they were allowed to cool by emission of synchrotron radiation for tens of seconds in the 1 T solenoid field.

With both antiprotons and positrons in the mixing region a nested potential was formed around the particles. The potential is shown in Figure 7.3(a) and is similar to that used in the ATHENA experiment (see Figure 7.1(b)). Antiprotons were initially held in a preinjection well and were released with an energy of about 12 eV above the level where the positrons are held. As the antiprotons bounce back and forth, they are slowed by Coulomb interactions with the positron plasma and cooling similar to that previously seen in higher magnetic fields (Gabrielse *et al.*, 2001; Amoretti *et al.*, 2004c) was observed. Here the antiprotons were allowed to interact with the positron plasma for 50 s before the remaining particles were dumped and counted. Figure 7.3 demonstrates positron cooling of antiprotons in the ALPHA apparatus. With no positrons in the central positron well, the antiprotons remain at the injection energy (Figure 7.3(b)). With positrons present, the antiprotons cool to an energy approximately corresponding to the potential at which the positron plasma is held (Figure 7.3(c)). In ATHENA, cooling to this level was shown to be correlated with the onset of antihydrogen production, though the exact level where antihydrogen formation can be said to begin is not well defined (Madsen *et al.*, 2005).

For the experiment described here the ALPHA silicon detector had not yet been installed. Instead the apparatus was equipped with four scintillation detectors read out by Avalanche photo diodes (APD). The detectors were placed inside the main solenoid and adjacent to the mixing region covering a solid angle of about 35% of  $4\pi$ . An event was registered if two or more of the detectors fired in coincidence (100 ns window). Coincidence is used to lower the background count rate caused by cosmic rays. Since an antiproton annihilating will send out multiple charged pions it will have a high probability of setting off multiple detectors whereas a cosmic ray will often only hit opposite pairs.

Figure 7.4 shows the time development of the annihilation event rate after the start of mixing. The two cases shown are *normal mixing*, as described above, and mixing in which the positron plasma is heated to suppress anti-

hydrogen formation. The heating is achieved by driving the axial bounce frequency of the positron plasma during mixing, a technique previously shown to be a reliable null measurement (see section 7.1.3). In the case of normal mixing we observe a signal similar to that observed by ATHENA but with a considerably longer rise time - about 1 s as opposed to a few tens of milliseconds. The longer rise time is probably due to a lower positron plasma density and a higher positron temperature in the 1 T field, although these could not be quantified at the time. Also the absolute number of positrons used in the experiments described here was a factor of 2 to 3 lower than that used by Amoretti *et al.* (2004c).

With heated positron plasmas the antiprotons are observed to interact with the positrons as seen on Figure 7.3(d). However, no significant antiproton loss is detected. (The events in the very first time bin of Figure 7.4, include antiproton losses caused by the rapid potential manipulations used to inject the particles into the nested trap). Thus the annihilation signal for normal mixing can be interpreted as being due to a time-varying antihydrogen production superimposed on a largely flat background due to cosmic rays and slow antiproton losses. We estimate that up to 15% of the injected antiprotons could have formed antihydrogen in these first mixing experiments performed in the ALPHA apparatus. The number is comparable to that observed by Amoretti *et al.* (2004b).

### 7.3 Antihydrogen formation in a multipole field and injection from below (2008)

The antihydrogen production experiments described in this section are very similar to the experiments described above (section 7.2). However, there are some very important differences which will be described below. The primary aim of these experiments was to demonstrate antihydrogen production in the ALPHA apparatus with the full magnetostatic trap energized. A secondary, though perhaps equally important goal, was to study different signatures of antihydrogen production in the presence of a multipolar magnetic field. To strengthen identification of antihydrogen two complementary antihydrogen

identification methods were used: The spatial distribution of antiproton annihilations detected during antihydrogen formation, and ionization of antihydrogen atoms.

The experiments described here were carried out during the 2008 AD beam time over a period of 4-6 weeks, and the results are published in (Andresen *et al.*, 2010a).

### 7.3.1 Summary of the experiment

Like the experiment described in section 7.2 the first step is to capture antiprotons from the AD, and cool them using a preloaded electron plasma. The initial capture takes place in the 3 T solenoidal field of the catching region. In this case antiprotons were caught from a total of 8 bunches of antiprotons. As a result the combined electron-antiproton plasma comprised about  $2 \times 10^5$  antiprotons and  $2 \times 10^7$  electrons - one order of magnitude more antiprotons than used previously in ALPHA.

Following the capture, the combined plasma was compressed radially using the rotating wall technique described in section 3.1.2. The electrons were removed using pulsed electric fields, the magnetic field ramped to 1 T, and the antiprotons transferred to the mixing region of the apparatus.

In the mean time, a positrons plasma was prepared in the mixing region. The plasma had a radius of  $\sim 1.5$  mm and a density of  $\sim 7 \times 10^8$  cm<sup>-3</sup>.

At this point, the antiprotons are not yet placed inside the nested potential. Instead they are located in a so-called *injection well* to the left of the nested potential. The positrons are placed at the center of the nested potential. With the particles in this configuration the magnetostatic trap is set to the desired depth by ramping up the current in the octupole and the two mirror coil magnets. Once the ramp is complete, the antiprotons are injected into the leftmost side well of the nested potential. However, instead of letting the antiprotons traverse the positron plasma immediately, they are placed at a non-zero axial energy, just below the level of the positrons. By slowly changing the voltage that confines the positrons, over a period of typically 100 s, we now bring the two particle species into contact and form antihydrogen. This process is illustrated in Figure 7.5, where the total change in the potential used to confine the positrons is illustrated.

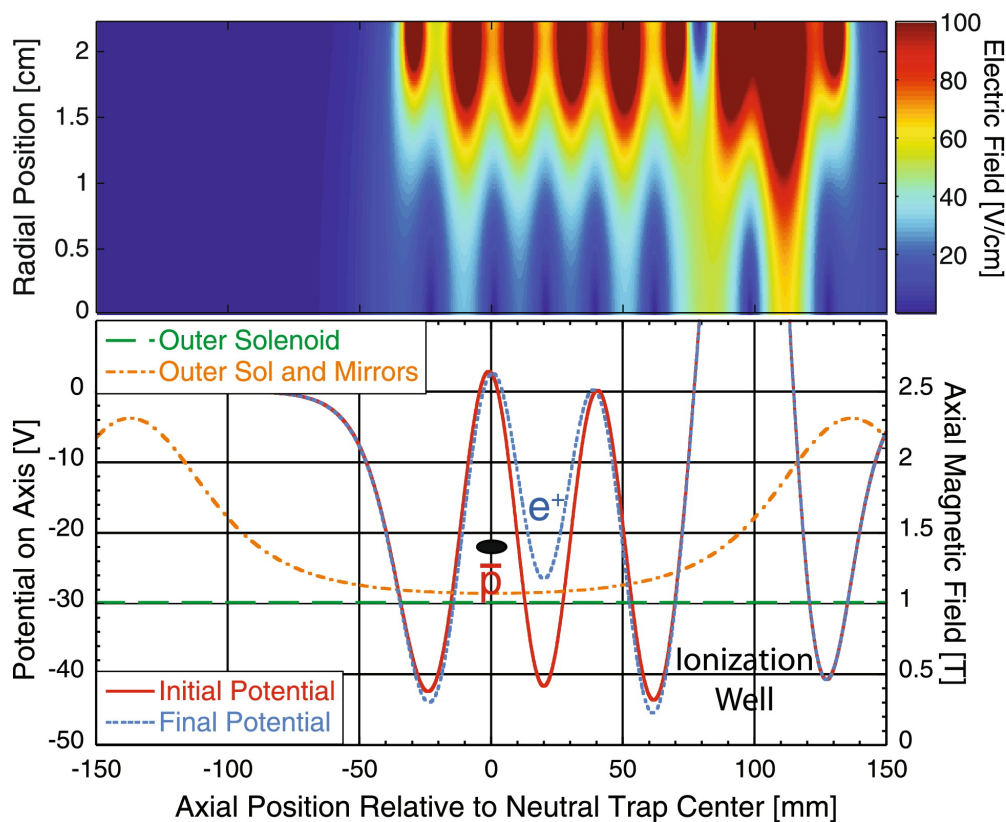


**Figure 7.5:** Plots of the electric and magnetic fields used to create antihydrogen in magnetostatic trap. Antihydrogen is formed in the positron plasma at the center of the nested potential. To the far right a deep potential well has been created to capture field-ionized antihydrogen atoms. The (lower) plot shows the axial magnetic fields with (yellow, dot-dashed line) and without (dashed line) the magnetic mirrors and the electric potential on axis at the beginning (solid line) and at the end (dotted line) of the mixing cycle. The black ellipse indicates the initial energy and axial location of the antiprotons. The (top) plot shows the corresponding total electric field strength versus radius and axial position at the end of the mixing. (Adapted from Andresen *et al.*, 2010a).

We call this way of merging antiprotons and positrons for *injection from below*. The idea behind the method is to avoid introducing antiprotons with very high axial energies to the positrons and thus to avoid forming very high energy antihydrogen. In addition, antiprotons which becomes decoupled from the positron plasma by colliding into one of the side wells will have some chance of being reinjected as the level of the positrons is moving. The method was later changed to the *autoresonant injection* technique described in section 7.4.1. In (Gabrielse *et al.*, 2008) a moving positron level was also used, and the experiment was simulated in Ordonez and Weathers (2008).

At the end of the mixing ramp all remaining particles are ejected for counting.

During the mixing of antiprotons and positrons, the silicon detector was used to record the number of annihilations on the electrode wall and to reconstruct the point of annihilation. A simple trigger, which requires a minimum of two triggered silicon modules, was used as a proxy for the absolute number of antihydrogen produced. From Monte Carlo simulations, we estimate that this trigger has an efficiency of about 95% for antiproton annihilation events. However, to determine which fraction of antiproton annihilations are in fact due to antihydrogen, the full vertex distribution must be analysed. In these experiments<sup>1</sup> about 20% of the recorded annihilations could be reconstructed.

Figure 7.6 shows the spatial distribution of the annihilation events which could be reconstructed. The left-most column shows the results of mixing in the pure solenoidal field, and the right-most column shows the result of mixing with the magnetostatic trap fully energized. The former is consistent with antihydrogen production as described in section 7.1.1. The latter shows a more complicated structure which will be discussed below.

The total number of detected annihilations is shown in Figure 7.7 where all values have been normalized to a total number of  $10^5$  antiprotons brought into mixing. Also shown on the figure is the number of antiprotons caught in the ionization-well. Common to both quantities is a gradual decrease in signal as a function of increasing magnetostatic well depth. To investigate the cause of this decrease, a number of control experiments were carried out. In these experiments, some of the magnets comprising the magnetostatic trap

---

<sup>1</sup>The silicon detector was not fully deployed until the following year (2009).

were not energized.

When the experiment was conducted with only the mirror coils energized, it gave the same mixing results as that with a pure 1 T solenoidal field. With only the octupole field, the results were equivalent to mixing in the full magnetostatic trap, implying that it is the octupole which is responsible for the drop in antihydrogen formation. Indeed other, later, measurements indicate an increase in the temperature of the positron plasma when the octupole is energized. The decrease in antihydrogen production described above differ from an earlier report by the ATRAP collaboration (Gabrielse *et al.*, 2008) where an increase in antihydrogen formation was observed when the depth of their trap was increased. However, the increase was also present without their multipole (quadrupole) fields. A likely explanation for this is that since their mirror coils are closer together than in our experiment, the axial magnetic field in the formation region increases significantly (from 1.0 T to 2.2 T) when their trapping field is turned on. In ALPHA the mirrors add only 0.1 T to the 1.0 T solenoidal field in the antihydrogen formation region. Increasing the axial field will increase the positron synchrotron cooling rate and can increase the plasma density substantially. Both higher densities and lower temperatures were observed by the ATHENA collaboration to increase formation rates (Amoretti *et al.*, 2004a; Funakoshi *et al.*, 2007).

### 7.3.2 The antihydrogen annihilation pattern in multipolar magnetic field

When antiprotons are mixed with positrons in a nested potential configuration, there are a number of possible outcomes which can cause annihilation of antiprotons. The most common of these are listed here. Two of the outcomes involve an antiproton combining with a positron to form antihydrogen. These are: (1) Antihydrogen which is formed with a relatively high amount of kinetic energy and with a binding energy great enough to survive the electric fields in the trap. Such atoms will approximately follow straight line trajectories and annihilate on the electrode wall. (2) Atoms which are weakly bound and ionized in the trap volume. In this case the antiproton may end up being re-trapped, typically closer to the electrode wall, or it can be lost to annihilate on the electrode wall. Two additional outcomes does not necessarily involve

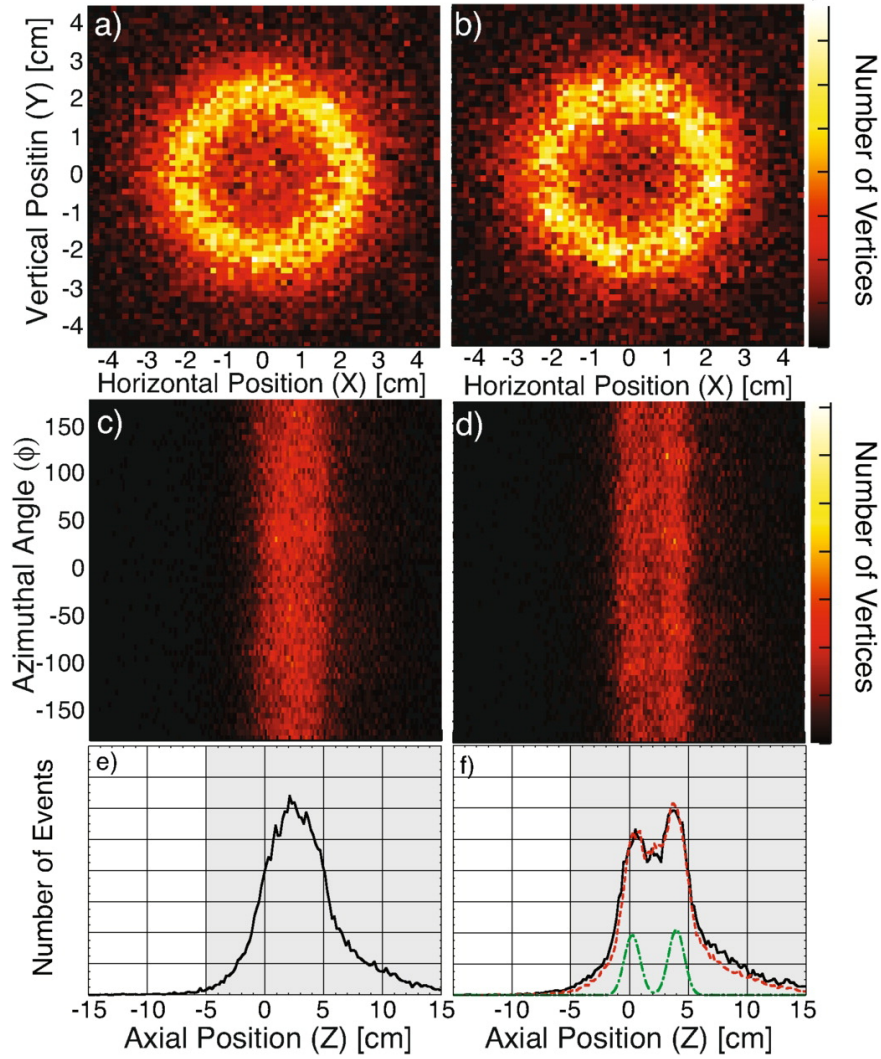


**Figure 7.6:** (a)-(b) Azimuthal projections of the antiproton annihilation vertex distributions during mixing with (a) no magnetostatic trap and (b) the full trap energized. (c)-(d) Corresponding  $z - \phi$  distributions. (e)-(f) Corresponding axial projections. (f) Fit to the full distribution (red, dashed line) and the off-center component of the fit (green, dot-dashed line). The fit is described in the text. For these measurement only part of the silicon detector was deployed. The shaded area marks the region covered by three layers of silicon. Left of this area the detector has only one layer of silicon. The slight asymmetry in the axial distributions (in particular the tails) is due to the lower reconstruction efficiency outside the three layer section. For clarity the plots have been normalized to have the same total number of events. The zero axial position is the center of the neutral atom trap. (Adapted from Andresen *et al.*, 2010a).

formation of antihydrogen: (3) An antiproton can annihilate with a residual gas atom or ion. (4) A bare antiproton is transported to the electrode wall by means of diffusion or plasma instabilities.

Antidrogen directly detected as atoms striking the electrode wall during antihydrogen formation belongs to case (1), and as described in section 7.1.1 the angular distribution of such annihilations has been observed to be uniform. The antihydrogen atoms detected using field-ionization (see section 7.1.2) are a subset of case (2), though, in principle, atoms belonging to case (1) can also be detected using this method provided the ionizing field is strong enough.

When a multipolar magnetic field is superimposed on the antihydrogen formation region, the cases (1)-(4) still apply. Having a relatively high kinetic energy the trajectory of atoms belonging to case (1) are largely unaffected by the magnetic field, and the expected angular distribution remains uniform. On the other hand, the presence of a multipolar field can cause bare antiprotons from case (2) or (4) to be transported to the electrode wall. As described in section 1.4 such transport results in an annihilation pattern consisting of a discrete set of points in the  $z\phi$ -plane.

Figure 7.6 shows annihilation patterns for antiprotons striking the electrode wall during antihydrogen formation. The left hand column shows the results of antiproton and positron mixing in a pure solenoidal field, and the right hand column shows the results of similar mixing in the combined solenoidal and multipolar magnetic field. As mentioned earlier, a uniform angular distribution can be observed in the first case, consistent with antihydrogen formation seen in previous experiments (see section 7.1.1). When the multipolar field is added the annihilation pattern develops structure compatible with that expected from so-called ballistic loss of bare antiprotons (see section 1.4). When the annihilation distribution is projected onto the  $z$ -axis, as is done in panels (e) and (f), two side peaks clearly distinguish the pattern observed in the combined magnetic field from that observed in the pure solenoidal field.

We can estimate the fraction of antihydrogen directly impacting the wall in the combined field measurement by assuming that the shape of the axial annihilation distribution of strongly bound antihydrogen remains unaltered when the multipolar field is added. A fit with the sum of a constant times the

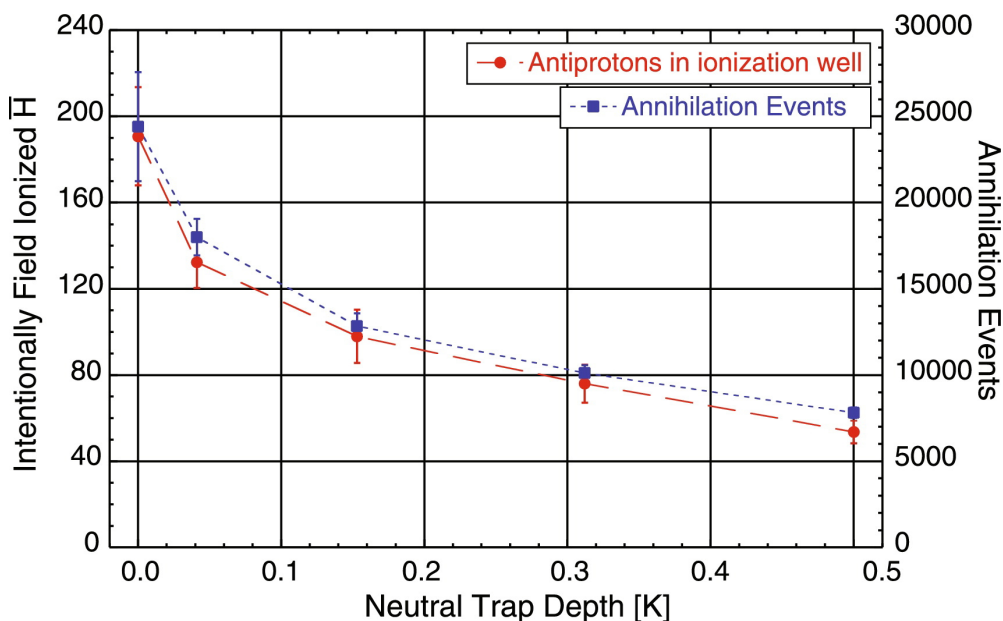


**Figure 7.7:** Number of intentionally field-ionized antihydrogen atoms detected following ejection, and annihilation events as a function of the depth of the neutral atom trap for ground state antihydrogen. The depth of the well has been converted to a temperature as described in section 1.2.3. The uncertainties represent variations between a number of experiments. All values are normalized to  $10^5$  antiprotons brought into mixing. The scaling accidentally makes the numbers overlap at zero field. (Adapted from Andresen *et al.*, 2010a).

unperturbed distribution (Figure 7.6(e)) and two additional Gaussian peaks representing the annihilations from antiprotons lost ballistically, is overlaid on the measured distribution in Figure 7.6(f). The fit results in side peaks of width  $\sim 7$  mm (dot-dashed green curve). From the fit we estimate that  $(83 \pm 5)\%$  of the events observed in presence of the maximum multipolar field are due to strongly bound antihydrogen atoms hitting the wall directly, with the remainder originating from field ionized antihydrogen.

### 7.3.3 Field-ionized antihydrogen

Antihydrogen which is formed in weakly bound states can ionize in the high electric fields near the trap wall or become ionized in a region covered by an ionization well. The potential configuration used for the experiments de-

scribed here have an ionization well located to the far right of the nested potential (see Figure 7.5). Depending on the distribution of atomic states, the solid angle covered by the ionization well is between 1.8 and 5% of  $4\pi$ . However, if we are able to count all antihydrogen atoms field-ionized in the trapping volume, a much greater solid angle can be achieved. For the same binding energies as those stripped in the ionization well on axis, the full trapping potentials ionize over a total solid angle of about 80% of  $4\pi$ .

In the case where the mixing is done in a pure solenoidal magnetic field it is possible to selectively count the number of antiprotons trapped beyond a certain radius. By ramping up the multipolar field after the mixing has been concluded, particles trapped at a radius higher than the critical radius  $r_{crit}$  are guided to the electrode wall where they annihilate (see section 1.4). This technique is described in detail in (Andresen *et al.*, 2008b). We find that  $(6.1 \pm 0.2)\%$  of the total number of antiprotons annihilate when we ramp up our octupole magnet after mixing, and using the combined MCP and phosphor screen (see section 2.5.2) we find that the bulk of the remaining antiprotons (69%) are left with the same radial distribution as before mixing. Thus we assume that antiprotons have been transported to high radii as weakly bound antihydrogen atoms. The number of antiprotons caught in the ionization well is  $(0.19 \pm 0.02)\%$  of the total number. Scaling this number by the difference in solid angle for ionization in the ionization well (1.8 to 5% of  $4\pi$ ) and in the full trapping field (80%), we thus expect between 3 to 8% of the total number of antiprotons to annihilate during the ramp up, which is consistent with the measurement. However, the agreement can be a coincidence as antihydrogen atoms are not necessarily created with similar axial and radial distribution of speeds. Indeed additional measurements using a lower positron density indicates a different ratio of the number emitted axially and radially.

When antihydrogen is formed in the combined magnetic field, an antihydrogen atom ionized beyond  $r_{crit}$  will be detected immediately as the antiproton is transported directly to the electrode wall. In this case the number of field ionized atoms can be estimated from the area of the two side peaks of the axial distribution of annihilations as described in the previous section.

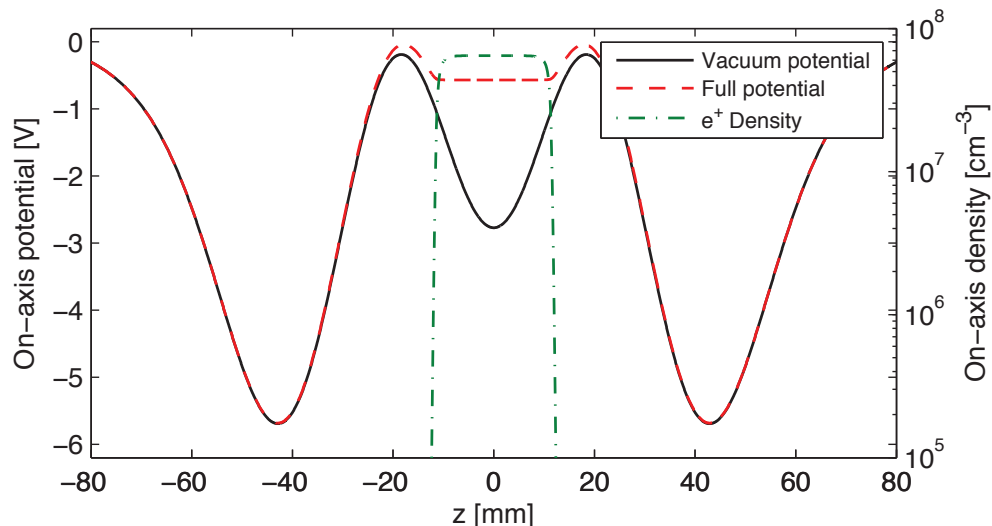


**Figure 7.8:** Nested on-axis potential used in the 2009 trapping attempts (see chapter 8). The vacuum potential generated by the electrodes (black) is shown together with the full potential (red, dashed line) obtained from a self-consistent solution to the Poisson-Boltzmann equations using the measured line-integrated positron density profile and temperature. In addition the calculated axial positron density distribution is shown (green, dash-dotted line).

#### 7.4 Antihydrogen formation in low electric fields and autoresonant injection (2009)

During the 2009 experimental run at the AD, many of the tools and diagnostics described in this thesis were combined in a new antihydrogen mixing experiment. We were able to quantify parameters such as positron density and temperature before, during, and after mixing, which allowed us to make simple order of magnitude theoretical predictions of the probability of trapping single atoms. In addition the development of a new technique for injecting the antiprotons into the positron plasma allowed better control and understanding of the injection process. A full description of these trapping experiments is the topic of chapter 8. However, a description of the autoresonant injection technique and the nested potential configuration used in the experiments is kept in this chapter.

### 7.4.1 Autoresonant manipulation of the antiproton axial energy

If the electric potential well confining the antiprotons is anharmonic, the bounce frequency of the antiprotons can be made to be a decreasing function of the oscillator energy. Only close to the bottom of the well, is the oscillation frequency close to the linear well oscillation frequency. By applying a sinusoidal drive to one of the confining electrodes, and letting the frequency of the drive sweep downwards through the linear well oscillation frequency, the antiprotons can be made to oscillate with the drive frequency. With appropriate choice of drive parameters, the antiprotons autoresonantly lock to the drive such that their longitudinal energy adjusts to keep their oscillation frequency matched to the drive frequency (McMillan, 1945; Fajans *et al.*, 1999; Barth *et al.*, 2009). This method allows the parallel energy of the antiprotons to be quickly and precisely changed with little impact on the energy distribution transverse to the magnetic field.

Figure 7.9 shows the result of a test experiment where the energy distribution of about 16000 antiprotons with a density of about  $2 \times 10^6 \text{ cm}^{-3}$  were given a non-zero energy offset relative to the bottom of the potential well. The single particle axial oscillation frequency in the particular well is shown as a function of energy in panel (a). At zero axial energy the oscillation frequency is about 400 kHz decreasing slowly to about 280 kHz at an axial energy of 3.5 eV. Close to the top of the well barrier, at about 3.8 eV, an abrupt change in the character of the antiproton orbits occurs with a corresponding singularity in the antiproton oscillation frequency.

In the test experiments the antiprotons were initially placed at the bottom of the well. A sinusoidal drive of frequency 500 kHz was then applied to one of the confining electrodes, and over 20 ms the frequency was decreased. In one case to 370 kHz and in another to 350 kHz. Panel (b) of Figure 7.9 shows the antiproton energy distribution before and after applying the autoresonant drive. Clearly the distribution is shifted to a higher energy by the drive, and comparing to the frequency vs energy curve in panel (a), we observe reasonable agreement between the mean energy of the distribution and the applied end frequency.

Another set of measurements highlights a problem which occurs when

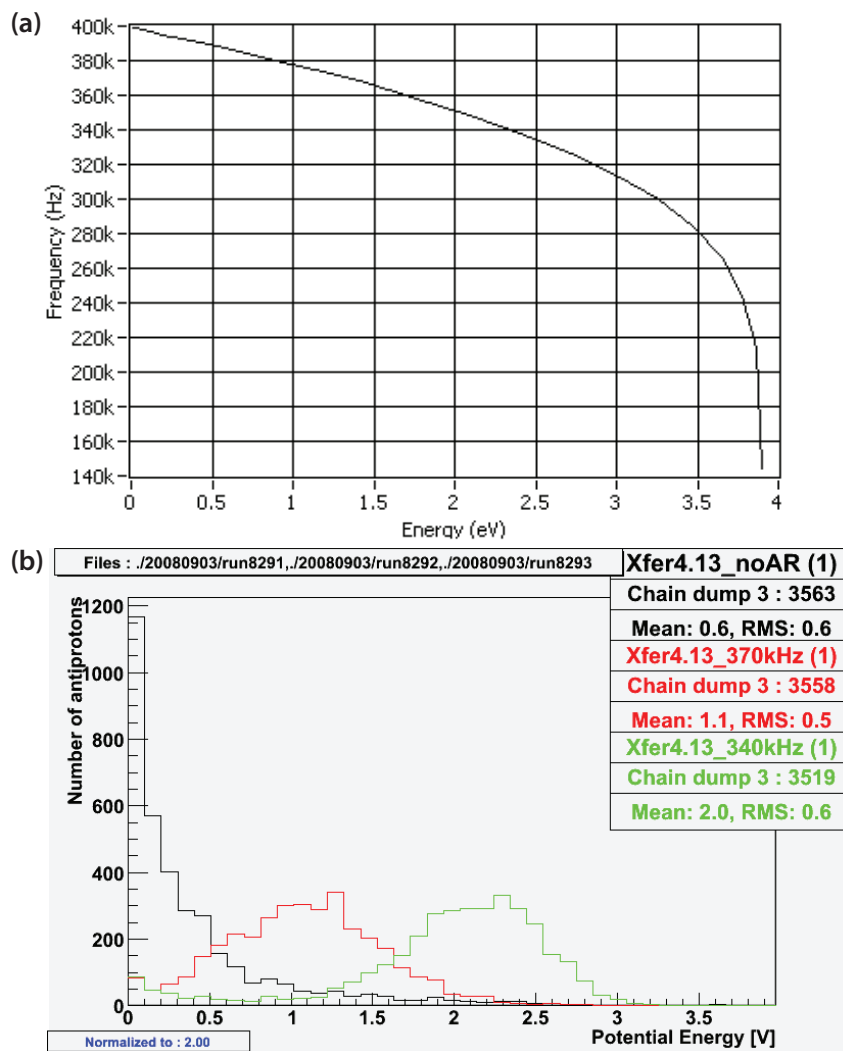


**Figure 7.9:** Autoresonant manipulation of the antiproton energy distribution. (a) The single particle axial oscillation frequency for an antiproton in a 3.8 V deep anharmonic potential well. (b) The antiproton energy distribution before (black) and after applying the autoresonant drive. A sinusoidal drive of frequency 500 kHz was applied to one of the confining electrodes, and over 20 ms the frequency was decreased. In one case to 370 kHz (red) and in another to 350 kHz (green).

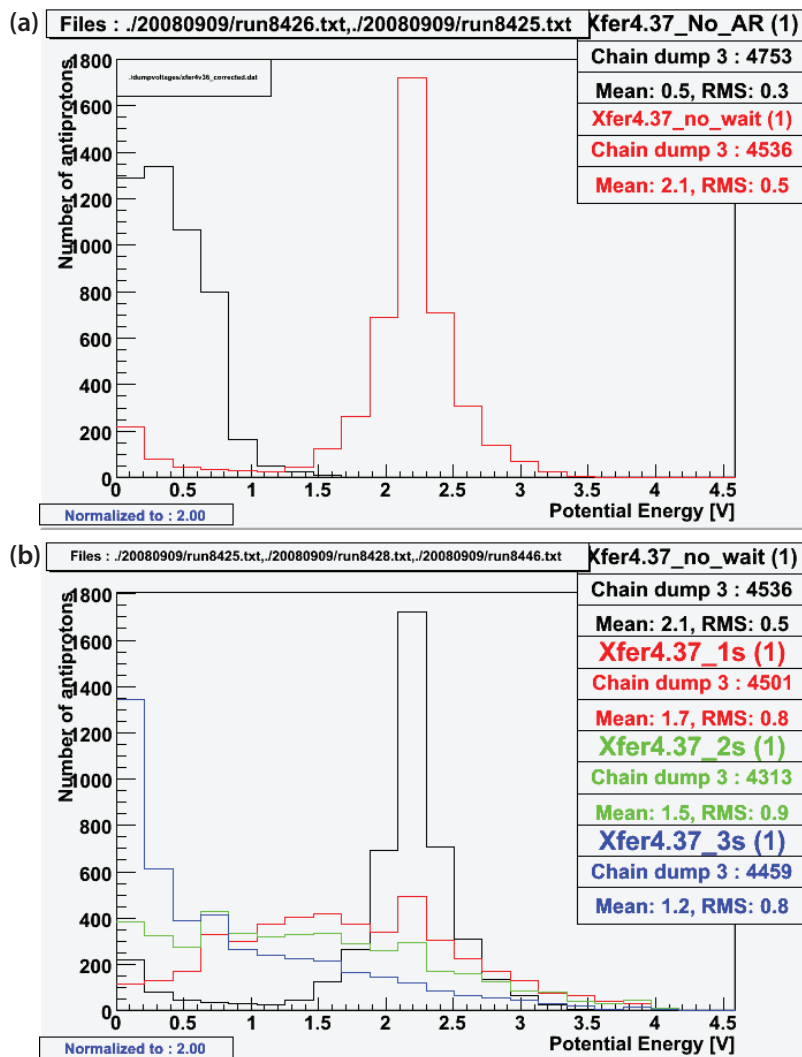


**Figure 7.10:** Collisional redistribution of energy between the degrees of freedom parallel to and perpendicular to the magnetic field. (a) The initial (black) and the offset (red) distribution. The later distribution was measured immediately after the autoresonant drive was turned off and shows a distribution peaked at about 2.2 eV. (b) Measurements of the distribution 0 (black), 1 (red), 2 (green), and 3 s (blue) after the drive was turned of.

the axial energy distribution of the antiprotons is offset from the bottom of the confining well. Figure 7.10(a) shows the initial and the offset distribution. The later distribution was measured immediately after the autoresonant drive was turned off and shows a distribution peaked at about 2.2 eV. Panel (b) in the same figure shows measurements of the distribution 0, 1, 2, and 3 s after the drive was turned off. During this time the offset distribution spreads out and shifts to a lower mean energy. A measurement (not shown) of the distribution 60 s after the drive had been turned off is consistent with the distribution measured after 3 s.

We interpret the change in the energy distribution as collisional redistribution of energy between the degrees of freedom parallel to and perpendicular to the magnetic field. The autoresonant drive affects only the two parallel degrees of freedom<sup>2</sup> increasing their mean energy from about 0.5 eV to about 2.1 eV. Assuming equilibrium between all four degrees of freedom before the drive was applied, the mean energy associated with the two transverse degrees of freedom is:  $(2 \times 0.5)$  eV. Thus the total energy after applying the drive is 5.2 eV or about 1.3 eV per degree of freedom, close to the 1.2 eV measured for the 3 s distribution.

In previous experiments, such as that described in section 7.2 above, antiprotons were not observed to redistribute energy between the degrees of freedom perpendicular and transverse to the magnetic field. As an example the results shown in Figure 7.3(b) shows no cooling of the axial motion of the antiprotons over a period of 100 s. However, radial compression of the antiproton cloud has led to at least an order of magnitude increase in antiproton density, and the total number of antiprotons per experiment has been increased as well. In addition the energy distribution of Figure 7.3(b) has a width of about 5 eV, which is about one order of magnitude more than that discussed above, indicating a much higher antiproton temperature. In section 4.4 the antiproton-antiproton collisional time constant is shown to depend on both density and temperature, and it is likely to be many orders of magnitude shorter in the more recent experiments.

As mentioned above these measurements shed light on part of the mix-

---

<sup>2</sup>The Hamiltonian of a single particle one dimensional harmonic oscillator has two quadratic terms and thus two harmonic degrees of freedom.

ing dynamics of the experiments where antiprotons were injected in the left-most side well just below the level of the positrons. In these experiments the positron level was then slowly changed to let antiprotons traverse the full length of the nested potential and form antihydrogen. The antiproton density (approximately  $1 \times 10^7 \text{ cm}^{-3}$ ) was higher than that used in the autoresonant experiments described above and the temperature comparable. Thus, most likely, the antiproton energy distribution quickly spread out and shifted to lower energies. As a consequence the positron level would have to be moved much further than expected in the absence of collisions to inject a large number of antiproton into the positron plasma. In addition the mean energy of the transverse energy distribution would be increased, and though the axial energy of an antiproton entering the positron plasma was kept low in this scheme, the transverse energy was increased.

#### 7.4.2 Autoresonant injection of antiprotons

Autoresonant excitation of the antiproton motion can be used to inject the antiprotons into the positron plasma. Initially the antiprotons are kept at the bottom of the left-most side well of the nested potential with the positrons in the center. As described above, a fast frequency sweep is then used to excite their parallel motion. When the antiprotons have sufficient energy to enter the positron plasma, an abrupt change in the character of the antiproton orbits occurs with a corresponding abrupt change in the antiprotons' oscillation frequency. They decouple from the drive and cease to resonantly gain energy from the drive.

This technique was used in the antiprotons trapping attempts during the 2009 experimental run at the AD (see chapter 8). With about 45000 antiprotons starting in the left side well of the potential shown in Figure 7.8 we employed a 1 ms long drive, swept from 320 to 200 kHz, producing a  $\sim 55$  mV amplitude oscillation on the trap axis. This injects 70% of the antiprotons in approximately 200  $\mu\text{s}$ , with the remainder staying below the energy needed to enter the positrons.

Such quick injection of a large fraction of the antiprotons exactly at the positron level ensures a high initial rate of antihydrogen production. It also avoids redistribution of energy between the different degrees of freedom even

at relative high densities and low temperatures. In fact a low initial temperature helps precise manipulation of the antiproton distribution as discussed by Barth *et al.* (2009). Antiprotons will still be able to collide and scatter energy into the perpendicular degrees of freedom, however, when an antiproton loses parallel energy, it will immediately fall into one of the two side wells and decouple from the positron plasma. This way antihydrogen is most likely produced primarily from antiprotons with relatively low perpendicular energy.

It is worthwhile to note that a drive at the axial bounce frequency of the antiprotons was previously used by Gabrielse *et al.* (2002b) to control antihydrogen production. However, the nature of the drive used in these experiments was fundamentally different from the autoresonant drive described here. Instead of sweeping the frequency to excite the entire population as a whole, a single frequency was used to continuously heat individual antiprotons to bring them into contact with the positron plasma. In this case the perpendicular motion of the antiproton is likely to be heated as well. Possibly to several eV of energy.

### 7.4.3 Antihydrogen formation in reduced electric fields

The nested potential configuration primarily used during the 2009 experimental run was different from previous configurations in that it used voltages about one order of magnitude lower than previously used. Figure 7.11 shows a comparison between the potentials used during the 2008 run (see section 7.3) and during the 2009 run. Also shown in the figure are a comparison between the maximum electric fields in the antihydrogen trapping volume.

With lower electric fields in the trapping volume antihydrogen formed in weakly bound states will not be so easily ionized, and thus the fraction of antihydrogen which can survive the fields and potentially be considered trap-pable is increased. However the increase is only a few percent as discussed in section 7.3.3.

Another benefit from using lower voltages to generate the nested trap potential is more flexibility in the choice of amplifiers used to drive the electrodes. During the 2009 run some of the amplifiers used in the mixing region had been modified to reduce electronic noise. Part of the modification involved halving the dynamic range of the output.

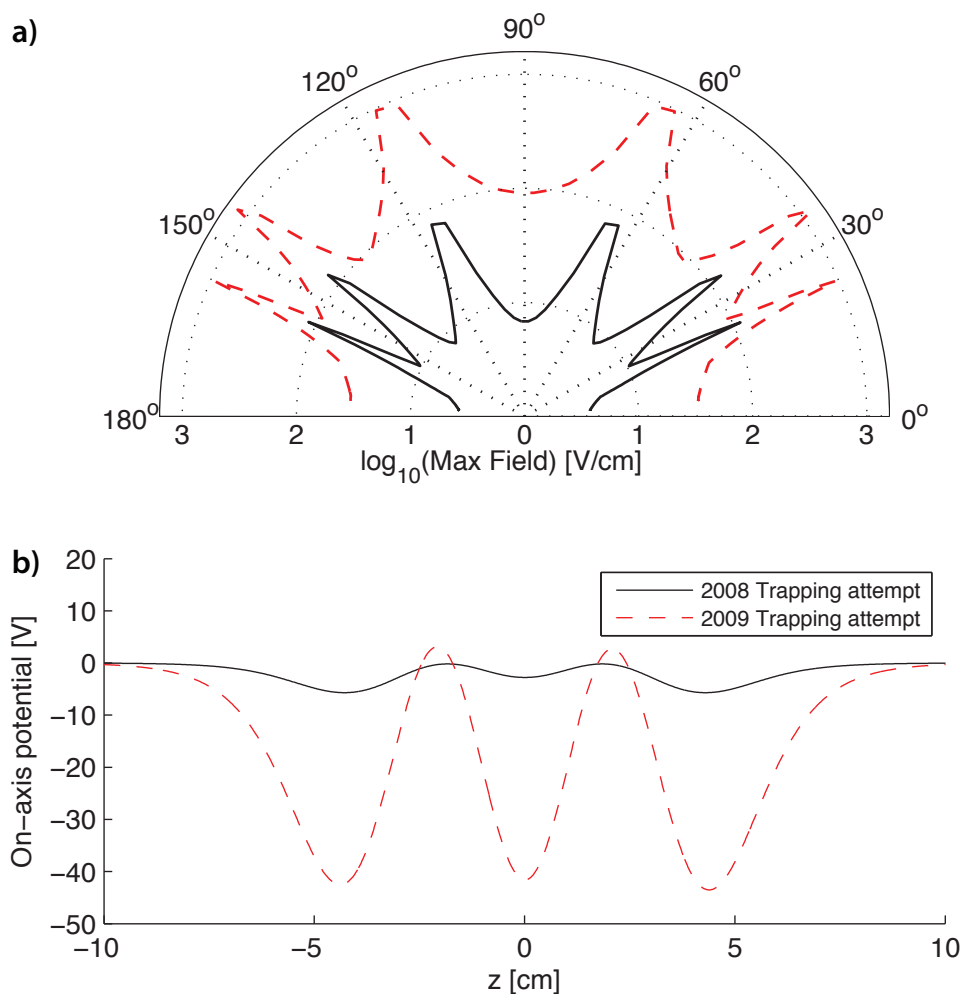


**Figure 7.11:** Comparison between the two (vacuum) potential configurations used in the 2008 (red, dashed line) and the 2009 (black line) trapping attempts. (a) Maximum field encountered by antihydrogen atoms emitted from the center of the nested potential vs emission angle in the RZ-plane. (b) On-axis nested potentials used during the mixing of antiprotons and positrons. The positrons are confined in the central well (at  $z=0$ ). The antiprotons are made to traverse the positrons with their motion bounded by the (negative voltage) side walls. The 2009 potential is shown in more detail in Figure 7.8.

The most important reason for minimizing the depth of the nested potential was to improve injection of antiprotons into the positron plasma. Figure 7.8 shows a calculation of the nested potential used with the positron self-field included. From the figure we see that a barrier of only  $\sim 0.5$  V separates antiprotons kept in the left side well from the level of the positrons in the center. Such a small difference allows quick injection of the antiprotons as described in the section above.

Finally, the low maximum depth of the nested potential limits the chance of antiprotons gaining several tens of eV kinetic energy transverse to the magnetic field. Such particles can become mirror trapped and mimic antihydrogen atom during detection of these (see section 8.3).

## 7.5 Conclusion

In conclusion, development of the nested potential antihydrogen formation technique in the ALPHA apparatus has reached a point, where antihydrogen can be produced in the magnetostatic trap. In addition, new techniques allows much better control of the antiproton and positron merging process than was previously available. In the following chapter, an antihydrogen trapping experiment where these techniques are applied, will be described.

# Search for trapped antihydrogen

---

Over a three week period in late October and early November 2009, a systematic search for trapped antihydrogen was conducted in the ALPHA apparatus. We carried out the trapping attempts under controlled and well-determined experimental conditions. During previous years other trapping attempts have been tried, but for the first time simple theoretical estimates predict a good probability of detecting a small number of trapped antihydrogen atoms.

A total of 212 repetitions of the experiment was carried out. During these attempts six events consistent with the release of trapped antihydrogen was observed. However, more experimental work is needed to definitively identify the six events as antihydrogen atoms.

In the following the trapping experiment and the subsequent data analysis will be described. More than any other topic in this thesis, the work described in this chapter represents the joint effort of the entire ALPHA collaboration. My personal contribution has primarily been to the development, debugging, and execution of the experimental effort, preliminary analysis of data, and review of the final analysis. The work is the subject of a coming publication Andresen *et al.* (2010b).

## 8.1 Experimental procedure

The experimental procedure is a variation of the antihydrogen production experiments described in section 7.2 and 7.3, and, as in the case of the latter, the full magnetostatic trap was energized. Some of the differences to these earlier experiments are in the choice of nested potential and the autoresonant technique used to initiate the antihydrogen formation. These differences are

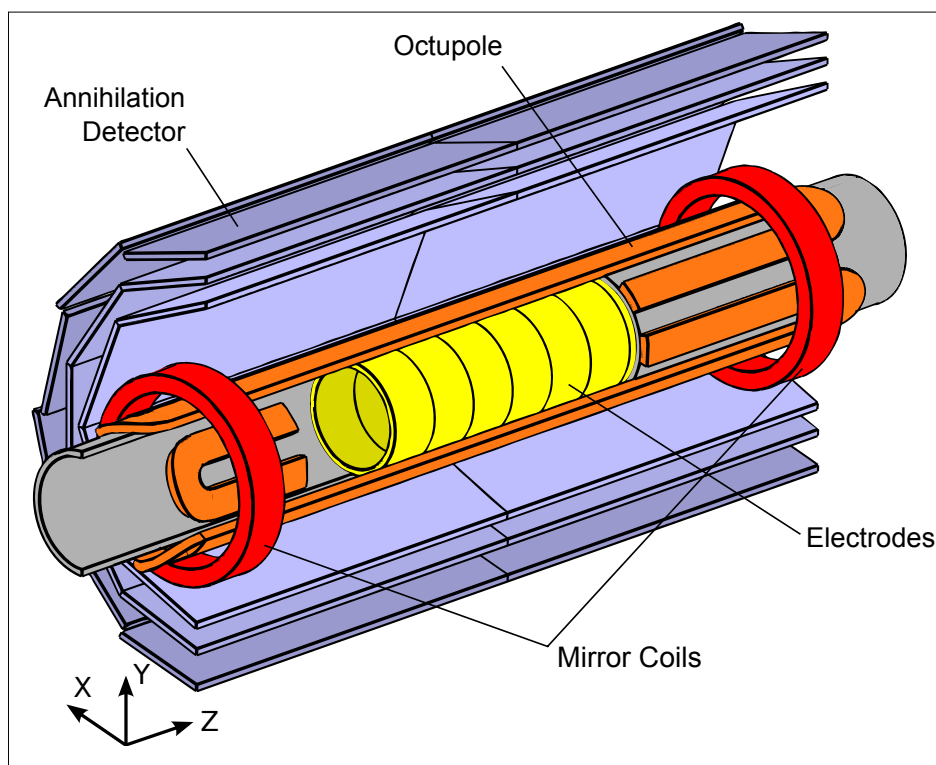


**Figure 8.1:** Simplified schematic, cut-away diagram of the antihydrogen mixing and trapping region of the ALPHA apparatus, showing the relative positions of the Penning-Malmberg electrodes, the magnetostatic trap magnets and the annihilation detector. The components are not drawn to scale. (Adapted from Andresen *et al.*, 2010b)

described in section 7.4. In the following the trapping experiment will be described with a focus on details particular to this experiment in addition to details relevant to detection and identification of trapped antihydrogen.

The experiment begins with the capture of about  $4.5 \times 10^4$  antiprotons from one bunch of antiprotons delivered by the AD. The antiprotons are cooled through collisions with a 0.5 mm radius, pre-loaded electron plasma of  $1.5 \times 10^7$  particles in the 3 T magnetic field of the catching region (Gabrielse *et al.*, 1989). The resulting two-component plasma is then compressed radially using the sympathetic rotating wall technique described in section 3.1.2.

The solenoidal magnetic field was lowered to 1 T before the particles were

transferred to the antihydrogen mixing region, where the magnetostatic trap is located (see Figure 8.1). For the experiments described here a set of heavily filtered, low-noise amplifiers were used to drive the thin mixing trap electrodes (see section 2.3.2) to reduce the level of electronic noise which may undesirably heat the plasmas. A series of electric field pulses were then used to separate the electrons from the antiprotons, taking advantage of the much higher velocity of the electrons.

In parallel with this operation, a plasma of positrons was accumulated in the ALPHA positron accumulator and transferred to the mixing region of the main apparatus. There, the number of positrons was adjusted to a desired level and the plasma compressed using the rotating-wall technique (see section 2.4.1).

In auxiliary measurements the radial density profiles of each of the types of plasmas was directly measured by destructively extracting the plasma onto the combined MCP and phosphor screen assembly (see section 2.5.2). We observed good reproducibility of the plasmas. By changing the parameters of the rotating-wall compression fields and measuring the effect, we were able to tailor the mixing potential and the positron density, and to ensure complete radial overlap of antiprotons and positrons. For the experiment described here, the positron plasma was prepared to be 1 cm long in the  $z$ -direction, have a radius of 1 mm, and a peak density of  $7 \times 10^7 \text{ cm}^{-3}$ . The radius of the antiproton plasma was 0.8 mm.

In addition the antiproton and positron temperatures were measured using the technique described in section 3.2. However, the temperatures quoted in this chapter represents the temperatures extracted directly from a fit to the measured energy distributions and not the temperature obtained when the appropriate corrections are applied. To do so requires the particular potential manipulations used in the measurements to be further scrutinized. A preliminary analysis indicates that the temperature obtained from these measurements are higher than the true temperature by a factor between 1.5 and 2 for the positron plasma, and around 1.15 for the antiproton plasma.

In contrast to the first cold antihydrogen experiments (Amoretti *et al.*, 2002; Gabrielse *et al.*, 2002a) the positron and antiproton clouds are placed in adjacent potential wells in a variation of the nested-trap arrangement. The space-

charge ( $\sim 2.1$  V) of the positron plasma fills most of the central well so that the antiprotons and positrons are separated by a potential barrier of approximately 500 mV (see Figure 7.8). With both species in-place to be mixed the magnetostatic trap was fully energized to a depth of  $0.6 K \times k_B$  for ground state (anti)hydrogen (see section 2.2.2). In this configuration the temperature of the positron plasma was measured to be  $(71 \pm 10)$  K, which is significantly higher than the  $\sim 7$  K temperature of the surrounding electrodes. Once the antiprotons have been separated from the cooling electrons, they are no longer effectively cooled, and we measured their temperature to be  $(358 \pm 55)$  K. The uncertainty quoted here is one standard deviation of a collection of measurements.

As described in section 7.4, injection of the antiprotons into the positron plasma is achieved by autoresonantly exciting the motion of the antiprotons parallel to the magnetic field. This method allows the parallel energy of the antiprotons to be quickly and precisely changed with little impact on the transverse energy and avoids letting antiprotons traverse the positron plasma with many eV of kinetic energy as was done previously (Amoretti *et al.*, 2002; Gabrielse *et al.*, 2002a). We employed a 1 ms long drive, swept from 320 to 200 kHz, producing a  $\sim 55$  mV amplitude oscillation on the trap axis. This injects 70% of the antiprotons in approximately 200  $\mu$ s, with the remainder staying below the energy needed to enter the positrons. For reasons that are not yet well understood, the temperature of the positron plasma increases to  $(194 \pm 23)$  K after injection of the antiprotons. Collision calculations indicate that the antiprotons quickly equilibrate to this temperature while inside the positron plasma (Hurt *et al.*, 2008). Previous experiments using a different injection method observed antihydrogen formation to begin at higher temperatures (Gabrielse *et al.*, 2004; Madsen *et al.*, 2005).

Once inside the positron plasma, the antiprotons can combine with the positrons to form antihydrogen atoms. As described in section 7.3, most of the antihydrogen has a kinetic energy too high to be trapped and escapes the trap volume to annihilate on the surrounding apparatus. The interaction is allowed to continue for 1 s, during which we observe  $(2700 \pm 700)$  annihilation counts per experimental cycle.

Following the analysis of section 7.3, we consider two possible sources of

annihilations: Antihydrogen immediately striking the wall, or weakly-bound antihydrogen that has been ionized by the electric fields at high radius, and are guided by the magnetic field to the wall. Comparing the vertex distribution to that obtained when the octupole is not energised allows us to estimate the fraction of the annihilations that correspond to antihydrogen that is strongly enough bound to not be ionized before reaching the wall. From this procedure, we estimate that between 70% and 85% of the detector counts are due to antihydrogen strongly enough bound to survive at least one pass through the electric fields. Only these atoms can potentially remain trapped.

Following the 1 s mixing period, uncombined antiprotons and positrons were ejected from the trap by manipulating the confining potentials. The bulk of the remaining charged particles are removed in a single pulse by simply opening the nested potential. However, a small number of charged particles remain trapped by the gradient magnetic fields of the magnetostatic trap (see section 8.3 below). To clear these, a series of four identical electric field pulses were applied across the length of the trap. Each pulse had a maximum average electric field of approximately  $2.5 \text{ Vcm}^{-1}$  which was applied for 10 ms (see Figure 8.4). We observe detector counts corresponding to a few tens of antiprotons coincident with the first pulse, showing that antiprotons can indeed become mirror-trapped, and that this method can remove at least some of them. During the following three clearing pulses a number of detector counts, consistent with the measured background rate, were observed.

Removal of the charged particles takes a total of 80 ms, following which the neutral trap remains energized for a further 50 ms before the shut-down of the magnetostatic trap is triggered. As the magnetic field falls, any antihydrogen held in the trap will escape and annihilate on the surrounding apparatus. After 30 ms, the depth of the magnetic minimum has fallen to less than 0.1% of its initial value; this defines the time window in which we search for escaping trapped antihydrogen. Before the shut-down, electrostatic barriers at either end of the trapping volume are erected to prevent any charged particles not cleared from the trapping volume to escape along the trap axis, though some can still escape radially. These barriers are lowered 100 ms after the shut-down was initiated to look for remaining mirror trapped bare antiprotons. The number of detector counts observed during this dump was

consistent with the expected number of background counts.

## 8.2 Annihilation identification and cosmic ray rejection

Our experiment is designed to identify trapped antihydrogen by releasing it from the magnetostatic trap and detecting the antiproton annihilation when the atom strikes the surrounding apparatus. It is vitally important in this scheme to have a sensitive and efficient method of distinguishing annihilations from cosmic rays.

Antiproton annihilations and cosmic rays exhibit distinct features characterized by their event topology (see Figure 2.12(a) and (b).) These features were studied by collecting a sample of cosmic ray events, consisting of approximately  $3.1 \times 10^5$  events, recorded over 20 hours during which no antiprotons were delivered to the apparatus. We compared this sample to approximately  $2.4 \times 10^4$  events recorded during a total of 170 s of antihydrogen production in the magnetostatic trap. These events overwhelmingly consist of antihydrogen annihilations. As a result of the study we were able to choose and optimize a method for identifying antiproton annihilations. No reference was made to the data recorded during the trapping experiments, so the possibility of experimenter bias influencing the analysis was eliminated.

If our reconstruction algorithm successfully identifies an annihilation vertex, i.e., at least two tracks, we use the topology of the event to distinguish antiprotons from the cosmic background. Our analysis procedure parameterizes each event in terms of the number of tracks present, the radial position of the vertex, and the squared residual from a linear fit to the hit positions. It accepts or rejects events as annihilations based on the values of these parameters relative to thresholds or *cuts*. The vertices are subdivided into two groups characterized by the number of tracks. Events with exactly two tracks form one group, and events with three or more tracks form the second group. Each of these two groups has a specific set of cuts. Figure 8.2 compares the distributions of the three parameters for the samples of cosmic ray events and antiproton annihilation events and illustrates the cuts associated with each parameter. Note that due to the distinction between two-track events and more than two track events, panels (c) and (d) both show distributions of squared

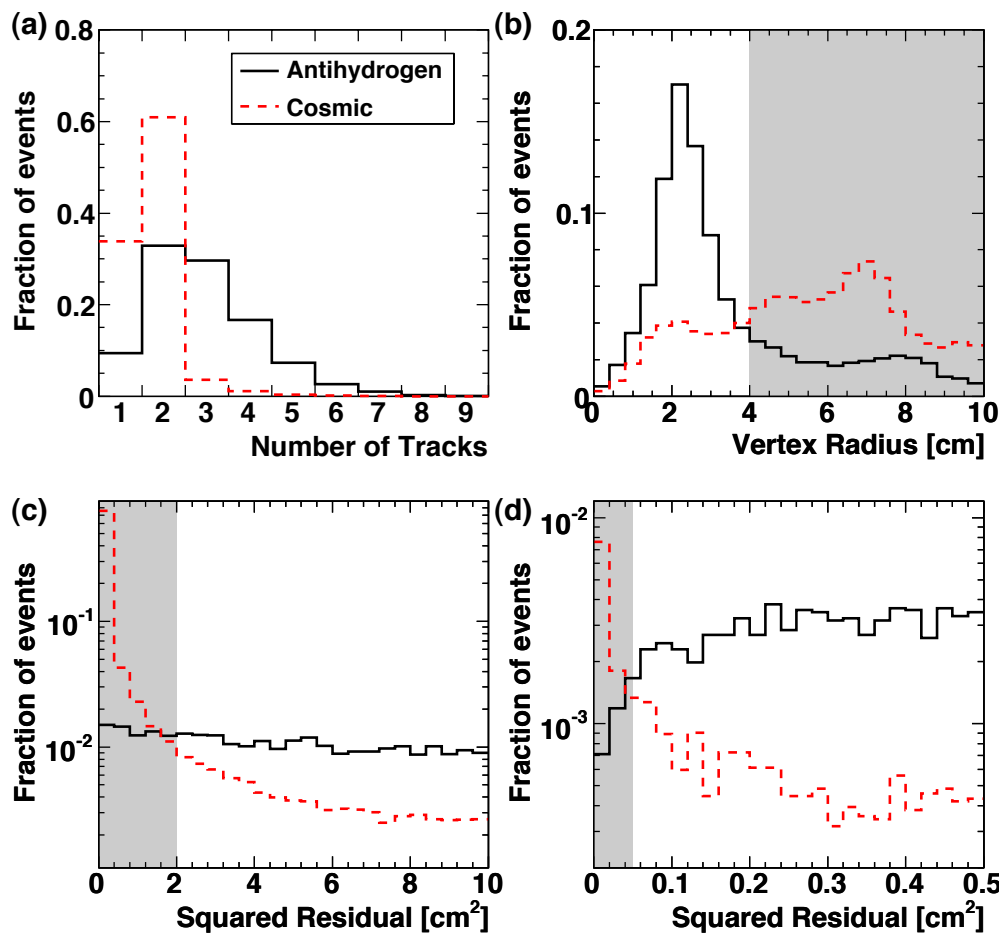


**Figure 8.2:** The measured distributions of (a) the number of identified charged particle tracks, (b) the radial coordinate of the vertex, and the squared residual from a linear fit to the identified positions for the events with (c) two tracks and (d) more than two tracks. The distributions from antihydrogen annihilation are shown in solid black lines and from cosmic rays in dotted red lines. The shaded regions indicate the range of parameters that are rejected to minimize the p-value. (Adapted from Andersen *et al.*, 2010b)

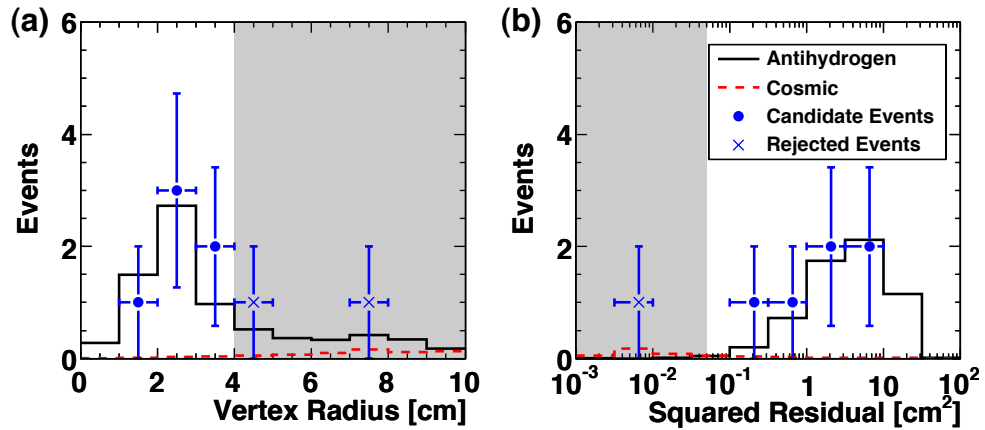


**Figure 8.3:** Comparisons of the distributions of the (a) vertex radius and (b) squared residual for events in the trapping experiment and events from the calibration samples that pass the cuts. The antihydrogen and cosmic graphs have been scaled to match, respectively, the observed number of events in the acceptance region (6) and the expected number of cosmic events in the acceptance region (0.14). Events that fail only the cut under consideration (radius in (a) and residual in (b)) are shown in the shaded region or as cross markers. The size of the error bars indicate the counting error ( $\sqrt{N}$ ). (Adapted from Andresen *et al.*, 2010b)

residuals.

The overall efficiency of detecting and identifying an annihilation is estimated to be  $(40 \pm 7)\%$  from the product of trigger efficiency ( $85 \pm 15\%$ ), the fraction of events that produce a vertex (74%), and the acceptance of the final cuts (65%). The cuts reject 99.5% of the cosmic background, accepting an absolute rate of  $2.2 \times 10^{-2}$  Hz, as determined from the cosmic sample. The total observation time for the 212 trapping experiments was 6.36 s, implying an expected cosmic background of 0.14 events. Were the cuts not applied a total of  $(27 \pm 5)$  cosmic ray events would be expected during a time window of this size.

Throughout the trapping series, 36 detector events were recorded in the 30 ms time window of the magnetostatic trap shutdown. When the cuts were applied to this data, six survived the selection criteria. The characteristics of these *candidate events* were studied in detail. All six had at least three tracks. In Figure 8.3, the candidate events are compared to the distributions of (a)

vertex radius and (b) squared residual values for antihydrogen and cosmic rays. These distributions are taken from the same data as displayed in Figure 8.2, with the appropriate rejection criteria applied, and have been scaled so that the area in the acceptance region matches the observed (antiproton) or expected (cosmic) number of events. Also shown are events that fail only the cut under consideration. While the size of the sample is limited, the events are consistent with the predicted distribution for antiprotons. We also note that the number of events accepted is not overly sensitive to the precise placement of the cuts. The probability of this observation being due to fluctuations in the cosmic background (the p-value) is  $9.2 \times 10^{-9}$ , corresponding to a significance of 5.6 standard deviations. We thus conclude that we observed antiproton annihilations upon release of our magnetic trap in these experiments.

Each of the experimental runs in which a candidate event was identified was closely examined, and the set of six was verified to be representative of the complete 212. No anomalies were found in, for instance, the readings from environment monitoring sensors, positron or antiproton source performance, the background rates of the vertex detector, or the number of annihilations recorded during antihydrogen production.

Concurrent with the trapping experiment, a number of control experiments were carried out. For instance, 121 repetitions of the experiment were carried out without antiprotons in the trap, verifying that the transient electromagnetic fields caused by the quench of the magnets do not induce false annihilation signals. A further 40 were carried out with only positrons present, to ensure that positron annihilations cannot mimic detection of an antiproton.

Finally, it is good practice to ensure that we can account for all the observed events. As stated above, 36 events were observed in the 6.36 s time window, and the expected background signal due to cosmic ray events is  $(27 \pm 5)$ . The six events identified as antiproton annihilations are consistent with a total of  $(15 \pm 4)$  antiproton annihilations, which would cause  $(13 \pm 4)$  events to be detected. Thus assuming the measured rate of cosmic ray events and six annihilation events which pass all cuts, we expect to observe a total of  $(40 \pm 6)$  events in the 6.36 s time window. This number is consistent with the observed number. Note the size of the error bars indicate here are counting errors ( $\sqrt{N}$ ).

### 8.3 Mirror trapping of antiprotons

The magnetostatic trap can act as a trap for charged particles, including bare antiprotons. This arises from the adiabatic conservation of the magnetic moment,  $\mu = E_{\perp}/B$ , of a gyrating particle in a magnetic field (see Chen, 1974, chapter 2). Here  $E_{\perp}$  is the kinetic energy of the particle in the plane transverse to the magnetic field lines and  $B$  the magnitude of the magnetic field. In the magnetostatic trap  $B$  varies along the trajectory of the antiproton. To conserve  $\mu$ , energy is converted between the degrees of freedom perpendicular and parallel to the magnetic field:

$$E_{\parallel} = E_0 \left( 1 - \frac{E_{\perp,0}}{E_0} \frac{B}{B_0} \right), \quad (8.1)$$

where  $E_0 = E_{\parallel} + E_{\perp}$  is the total kinetic energy of the particle and  $E_{\perp,0}$  the perpendicular energy at a point where  $B = B_0$ . The center of the magnetostatic trap is a minimum of  $B$ , so as an antiproton moves away from the center,  $B$  will increase. For antiprotons with a ratio  $E_{\perp,0}/E_0$  greater than a certain value  $E_{\parallel}$  will eventually become zero, which corresponds to an axial turning point in the motion. Thus some particles are reflected from a region of increasing magnetic field. This effect is called *mirror trapping*.

Equation (8.2) can be combined with an electric potential  $\Phi$  to form a pseudo-potential for the antiproton motion:

$$U = E_{\perp,0} \left( \frac{B - B_0}{B_0} \right) + (-e)\Phi. \quad (8.2)$$

Figure 8.4 shows the pseudo-potential calculated for the combined on-axis magnetic field and the clearing field applied to remove antiprotons after mixing. Clearly, low  $E_{\perp,0}$  particles are ejected from the trap by the electric fields which overcomes the force due to the increasing magnetic field. At high values of  $E_{\perp,0}$ , a local minimum develops in the pseudo-potential, where particles can remain trapped. For the particular electric potentials used in these experiments, we estimate that a particle must have  $E_{\perp,0}$  of at least 20 eV to remain trapped in the on-axis field.

Off the axis of cylindrical symmetry, the influence of the octupolar magnetic field produces complex trajectories which cannot be subject to the same

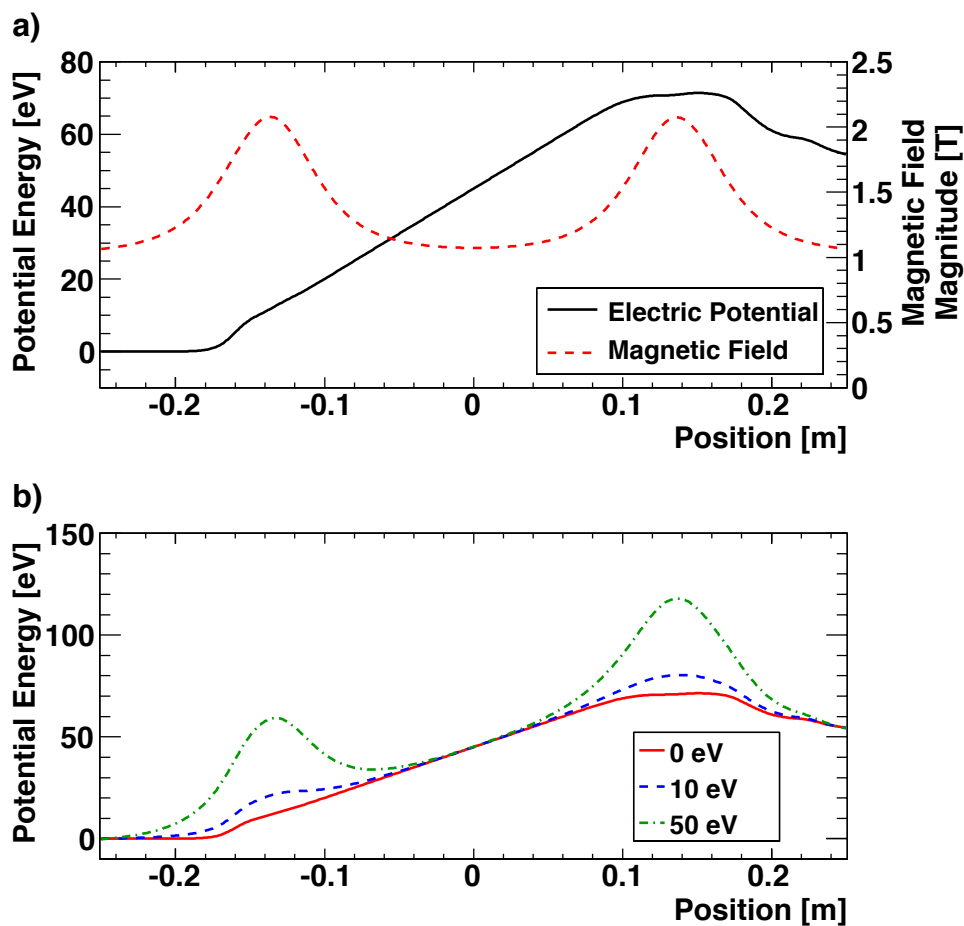


**Figure 8.4:** (a) The on-axis electric potential (solid line) applied to clear antiprotons from the magnetostatic trap, and the on-axis magnetic field (dashed line). (b) The interaction of the magnetic moment of the antiproton with the inhomogeneous magnetic field combine to give an  $E_{\perp}$ -dependent pseudo-potential (see text), three examples with different values of  $E_{\perp,0}$  are shown. On the trap axis particles with and  $E_{\perp,0}$  greater than 20 eV can remain confined in the magnetostatic trap. (Adapted from Andresen *et al.*, 2010b)

analysis. Instead, the trajectories have been calculated numerically. In the numerical simulations antiprotons are given a velocity from a pre-selected distribution and a random position inside the trapping volume. Using the full 3D Lorentz force based on the applied magnetic and electric fields the efficiency of the clearing potential is investigated. We find that no particle with  $E_{\perp,0}$  less than 20 eV remain in the trap, which is the same conclusion as that reached in the analysis of the on-axis pseudo-potential above.

We must consider mechanisms that are capable of producing antiprotons with  $E_{\perp,0}$  of at least 20 eV. Taking the measured antiproton temperature (358 K, 31 meV) and the number of particles in the antiproton plasma, we can calculate the fraction of a thermal distribution with high  $E_{\perp,0}$  and find that it is several orders of magnitude too small to account for the six observed events. Thus, only non-thermal sources of antiprotons are important.

Antiprotons with high parallel kinetic energy are relatively easy to produce, as an antihydrogen atom can be ionized and accelerated by the strong electric fields at the edge of the antihydrogen formation region. In order to convert this parallel kinetic energy into perpendicular energy, the antiproton must undergo a collision. However, in this region the particle density is low enough for antiproton-antiproton collisions to be neglected.

An antiproton can also undergo a collision with a residual gas atom in the trap. In the cryogenic environment of the trap, the residual gas is predominantly hydrogen and helium, and the individual atoms have small velocities compared to mirror-trapped antiprotons. For a head-on collision, in which approximately 20 eV of energy is transferred to the perpendicular degree of freedom, an incident antiproton must have parallel energy greater than about 30 eV. The density of gas atoms is known from the rate of annihilations of stored particles and the rate of hard collisions with antiprotons can be evaluated numerically to be about  $10^{-5}$  Hz. We estimate the probability of such an encounter to be at least five orders of magnitude too low to account for six annihilations.

Our estimate of the probability of producing a mirror-trapped antiproton is extremely small. However, we lack complete knowledge of the spatial and energy distributions of antiprotons during and after the mixing procedure, which means that we cannot rely on these calculations to completely exclude

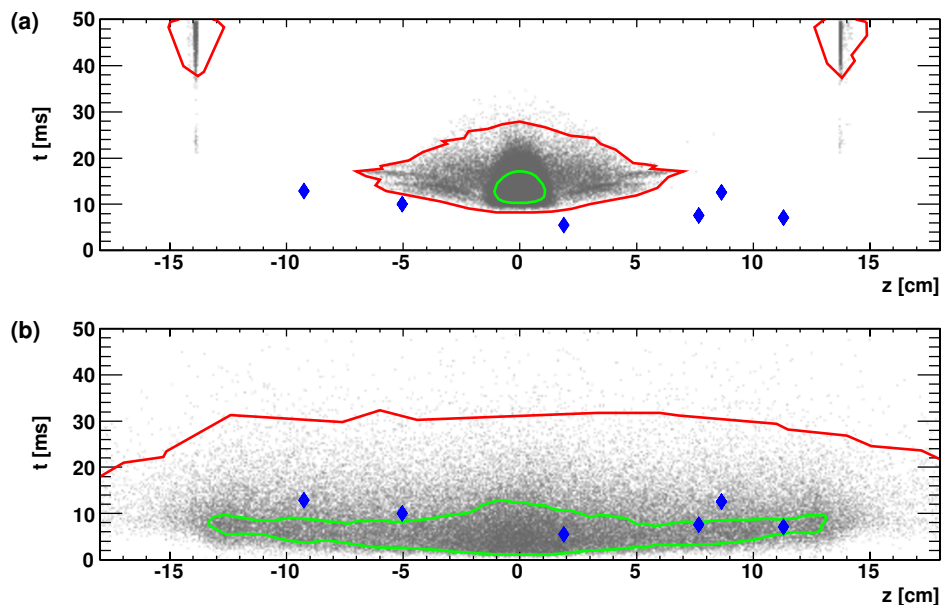


**Figure 8.5:** The time after the start of the magnet shutdown and  $z$ -position relative to the centre of the trap of the simulated annihilations of (a) mirror-trapped antiprotons and (b) antihydrogen atoms released from the magnetostatic trap. Individual simulated annihilations are shown as discrete points, of which there are 86914 in (a) and 62438 in (b). The lines show the contours of constant density which contain 50% (green) and 99% (red) of the density when convolved with the resolution of the detector. The solid diamond-shaped points mark the positions of the six candidate events identified in the trapping experiment. Some mirror-trapped antiprotons impact at  $\pm 14$  cm, where a step in the radius of the electrodes occurs. (Adapted from Andresen *et al.*, 2010b)

the presence of mirror-trapped antiprotons.

## 8.4 Release signatures of antihydrogen and antiprotons

Even if mirror-trapped antiprotons are present as we shut down the magnetic trap, this does not necessarily imply that they cannot be distinguished from antihydrogen. The annihilation vertex detector allows us to determine both the spatial and temporal distributions of annihilations, which can be compared to what would be expected from the release of antihydrogen and mirror-trapped

antiprotons.

A ground state antihydrogen atom can have a kinetic energy of no more than  $0.6 \text{ K} \times k_B$  and remain trapped. Thus, it will move slowly (at most  $100 \text{ ms}^{-1}$ ), and, while the magnetic field is falling, will transit the trap only a small number of times before escaping. During each transit, the magnetic field will change significantly and antihydrogen atoms will not have time to explore the entire trap and find the locations where the depth is lowest. Thus, we expected the  $z$ -distribution of annihilations of antihydrogen atoms to cover the entire  $\sim 20 \text{ cm}$  length of the trap. In contrast, mirror-trapped antiprotons have much higher energy, and move faster than the antihydrogen atoms. They do have time to explore the trap boundaries, and find the location where they are minimally bound — midway between the mirror coils, which is where they are expected to annihilate.

To obtain a quantitative picture of the annihilation distribution of mirror-trapped antiprotons and magnetically confined antihydrogen atoms during the shutdown of the magnetostatic trap another numerical simulation was carried out.

As above, the simulations of mirror-trapped antiprotons were performed by integrating the full 3D Lorentz force. The initial parameters for antiprotons were randomly selected from the set of mirror-trapped antiprotons found to survive the clearing fields. As in the real experiment electric potentials prevented antiprotons from escaping along the  $z$ -axis, and approximately 50% of the antiprotons remain trapped after the currents in the trapping magnets have decayed to zero.

In addition to the antiproton codes, two independent simulations, which modeled the trajectories of antihydrogen atoms subject to the magnetic moment force equation, were developed. The simulations were initialized with antihydrogen atoms evenly distributed in the trap. These atoms were initially either in the ground state, with maximum kinetic energy of  $0.1 \text{ meV}$ , or in the  $n = 25, l = 24, m = 24$  excited state, with maximum kinetic energy  $1.0 \text{ meV}$ . The maximum kinetic energy is larger than the depth of the neutral trap, ensuring that all trappable atoms are considered. Excited states of antihydrogen were allowed to de-excite through spontaneous emission. The atoms were

propagated for between 90 ms and 100 ms before the simulated decay of the magnetic field commences, allowing for the exclusion of transiently-trapped atoms and for randomization of the phase space. After the quench, the simulation continues until the antihydrogen atoms hit the inner surface of the electrodes, leave the trap through the ends, or a further 50 ms has elapsed.

The results are not sensitive to the initial atomic state, except that the initially excited distribution gives a higher fraction of trapped antihydrogen. Figure 8.5 shows the  $z$ -coordinate of the position where the particle impacted the electrode wall on the horizontal axis, and the vertical axis shows the time of the impact relative to the beginning of the current decay. When these points are convolved with a function describing the resolution of the annihilation detector, we obtain a continuous density function. Contours of constant density which contain 50% (green) and 99% (red) of the integral of this function are shown.

As expected from the argument above, the distribution of mirror-trapped antiproton annihilations is concentrated near the centre of the trap, in contrast to the much broader distribution of antihydrogen annihilations. The candidate events, also shown on the figure, clearly lie outside the population of simulated bare antiproton annihilations, and all of the candidate events lie outside the 99% contour. Thus, an upper limit on the fraction of sets of six annihilations drawn from the simulated distributions at  $(z, t)$  positions more extreme than this is  $(10^{-2})^6 = 10^{-12}$ . On the other hand, we observed that half of the events lie inside the 50% contour of the antihydrogen distribution, which is the most likely outcome (with a probability of 0.31), indicating that the candidates are compatible with the release of antihydrogen.

Many parameters have been varied in the simulations of mirror trapped antiprotons to observe their effect on the annihilation distribution. These include introducing tilts and offsets of the magnetic field and using extremely high energy (keV range) antiprotons. We have not found a distribution for which the observed events are not extremely unlikely, and we interpret the results from the simulations as a strong indication that the candidate events are trapped antihydrogen atoms. However, without knowing if the simulations carried out fully represent the real experiment, and without an unambiguous control experiment, we cannot yet definitively claim to have observed trapped

antihydrogen.

At the end of this chapter it is discussed how the simulations can be tested against experiments and how to make an even more unambiguous differentiation between the annihilation signature of mirror-trapped antiprotons and trapped antihydrogen.

## 8.5 Theoretical estimates of the number of trapped antihydrogen atoms

The initial particle temperature and density distributions are well-determined and reproducible enough to allow us to calculate the expected yield of trapped antihydrogen from this experiment. Still, there are many effects that must be included. So the final prediction can only be taken as an order-of-magnitude estimate. We estimate the number of trapped antihydrogen atoms from the simple relationship:

$$\begin{aligned} N_{\text{detected}} &= N_{\text{trapped}} \times f_{\text{detection}} \\ &= N_{\text{produced}} \times f_{0.6\text{K}} \times f_{\text{LFS}} \times f_{\text{detection}}, \end{aligned} \quad (8.3)$$

where  $f_{\text{detection}}$  is the probability of an antiproton annihilation passing all cuts (40%),  $f_{0.6\text{K}}$  is the fraction of atoms produced with energy lower than  $0.6 \text{ K} \times k_B$ , and  $f_{\text{LFS}}$  is the fraction of atoms in trappable low-field seeking states.  $N_{\text{detected}}$ ,  $N_{\text{trapped}}$ , and  $N_{\text{produced}}$  are the number of antihydrogen atoms detected, trapped and produced respectively. Each of the terms will be discussed in turn.

The total number of antihydrogen atoms produced can be estimated by summing the number of annihilation counts over the experimental series and subtracting our estimate for the number of counts due to antiprotons from atoms ionized by the electric field. From this, we determine that approximately  $N_{\text{produced}} \approx 4 \times 10^5$  atoms were produced with a binding energy great enough to survive the electric fields.

Because the mass of the antiproton is so much larger than that of the positron, the kinetic energy of a newly formed antihydrogen atom will be

close to that of the antiproton before combination. This energy has two components: the thermal energy and an energy associated with the magnetron rotation about the axis of the trap due to the crossed electric and magnetic fields (often called an  $E \times B$  rotation). We assume that formation of antihydrogen occurs after the antiproton temperature has equilibrated to the temperature of the positron plasma (194 K). This is justified since the calculated slowing rate of antiprotons in a positron plasma at this temperature and density (Hurt *et al.*, 2008) is much greater than the antihydrogen production rate.

The  $E \times B$  rotation velocity can be calculated from a self-consistent solution to the Poisson-Boltzmann equation. The velocity of the rotation increases further from the axis of the trap, so the radial distribution of points at which antiprotons form antihydrogen can be important. However, at 194 K the thermal velocity of the antiprotons is the dominant contribution, and we take a simple uniform distribution, for which we numerically evaluate the fraction of antiprotons with kinetic energy less than  $0.6 \text{ K} \times k_B$  which gives  $f_{0.6\text{K}} \approx 1.3 \times 10^{-4}$ .

At a temperature of 194 K, the radius of the cyclotron motion of the positron ( $\sim 10^{-7} \text{ m}$ ) is larger than the radius of an antihydrogen atom ( $\sim 10^{-10}$  to  $10^{-8} \text{ m}$ ). Thus, the distribution of magnetic moments will be purely statistical, and the atoms will be evenly divided between high and low-field seeking states (Robicheaux, 2006). So  $f_{LFS} \approx 50\%$ .

Combining these factors an estimate of  $N_{trapped} \approx 26$  antihydrogen atoms were trapped during the course of the 212 repetitions of the trapping experiment. Multiplying this number by the probability for an annihilation of passing all the fiducial cuts we arrive at an estimate of 10 detected atoms.

The simple model can be extended to include the effects of the cascade from highly excited Rydberg states. Higher quantum states can have a larger magnetic moment, and the trapping potential will be deeper for these atoms. As the atom radiatively decays to less excited states (with a lifetime much shorter than the time between antihydrogen production and the observation window (Topçu and Robicheaux, 2006)), the well depth will reduce, becoming 0.6 K when the atom reaches the ground state. As described in (Taylor *et al.*, 2006), antihydrogen atoms that decay near the turning points of their motion will experience a reduction in their total energy. This results in an effective trap depth of as much as a factor of four higher. We must also account for the

possibility that an atom will reach the ground state without passing through an untrapped state. A full discussion of the cascade can be found in (Robicheaux, 2008) and the references therein. Including the cascade, we estimate the number of trappable atoms to be roughly 60, of which about 24 would be expected to pass all cuts when annihilating. We see that the inclusion of this effect makes a more favorable prediction of the trapping probability, and is still within an order of magnitude of the number of candidates observed.

## 8.6 Summary and discussion

ALPHA has conducted a search for trapped antihydrogen by attempting to identify the annihilation of antihydrogen atoms formed in and later released from our magnetostatic trap. The diagnostics incorporated into the ALPHA apparatus allow us to determine and control the experimental parameters to a high level of precision, and permit us to estimate the number of trapped antihydrogen atoms the experiment would be expected to produce.

In a series of 212 antihydrogen trapping experiments, six events which could be positively identified as antiproton annihilations were observed during the rapid shutdown of the magnetostatic trap. These are referred to as antihydrogen candidate events. The number is consistent with  $(15 \pm 4)$  antiproton annihilations and  $(13 \pm 4)$  unidentified detector events. During the total observation time of 6.36 s a total of 36 detector events were observed,  $(27 \pm 5)$  of which are expected to originate from cosmic rays. A simple, order of magnitude, theoretical estimate of the number of trapped antihydrogen is 26 atoms, 85% of which would be expected to trigger an event in the detector. This estimate agrees within a factor of two with the observed number of antiproton annihilations.

Bare antiprotons can become trapped in the magnetostatic trap, and in extreme cases we are unable to clear these from the trapping volume before searching for antihydrogen. Such, so-called mirror trapped antiprotons, would have the same annihilation signature as antihydrogen atoms. In an attempt to exclude the presence of mirror trapped antiprotons in the sample of six annihilation events, simulations are used to compare the release time and location of mirror trapped antiprotons and antihydrogen atoms. The result

of the simulations indicates that the six candidate events occur at time and space coordinates consistent with the expected release signature of trapped antihydrogen, and are very unlikely to be mirror trapped antiprotons. However, without further investigation, we can not definitively claim that we have trapped antihydrogen.

A higher rate of observed events would greatly facilitate study and characterization of the event distribution. Presently, reducing the temperature of the component plasmas seems to offer the most promise to this end.

The evaporative cooling technique described in previous chapters was not applied to these experiments. In its current form, this technique could offer as much as a factor of 40 decrease in the initial antiproton temperature. Though a lower initial antiproton temperature does not directly result in a lower antihydrogen formation temperature in the current antihydrogen formation scheme, it does allow more precise control of the antiproton injection. In addition a lower antiproton temperature minimizes the amount of energy carried into the positron cloud upon injection. The importance of the latter is increased as the positron temperature is lowered.

As mentioned above the measured positron temperature increases from  $(71 \pm 10)$  K to  $(194 \pm 23)$  K after injection of the antiprotons. Preliminary studies indicates that this temperature rise can be made smaller or perhaps eliminated by carefully choosing the parameters of the autoresonant drive used to excite the antiprotons. In addition, achieving lower temperature positrons plasmas appears to be possible, and evaporative cooling of electrons and positrons is starting to be explored in the apparatus.

Attempts to experimentally identify the annihilations release signature of mirror trapped antiprotons can possibly be used to verify the signatures predicted by simulations, and further optimization of the clearing fields is possible. In addition ideas involving directly affecting the release signature of bare antiprotons by applying electric fields are being investigated. Presumably small electric fields would leave the release signature of neutral antihydrogen unaffected.

In summary, for the first time, we have carried out a trapping attempt in which the experimental inputs have been well-determined and theoretic-

cal estimates predict a good probability of detecting trapped antihydrogen. Even very few annihilations can be detected, and there is a good chance future experiments will be able to distinguish antihydrogen annihilations from the annihilation of bare antiprotons by comparing the release signature of the two.

# Outlook

---

In the trapping attempts described in chapter 8 evaporative cooling of the antiprotons was not used to attempt to lower the antihydrogen formation temperature. The main reason for this was the relatively high 100 to 200 K temperature of the positron plasma, which would cause the antiprotons to reheat quickly.

Much work is currently being done to achieve low positron temperatures with the magnetostatic trap energized, and more importantly to avoid the positron temperature to increase when antiprotons are injected. It is likely that low temperature antiprotons will play a role in these efforts. More precise control of the autoresonant antiproton injection can be achieved using lower temperature antiprotons (Barth *et al.*, 2009), and as the temperature of the positron plasma is brought down, the antiproton temperature becomes more important.

The development of evaporative cooling in the ALPHA apparatus required the parallel implementation of a technique to accurately measure the antiproton temperature and pushed hardware development. This is by no means a unique case. Since the start-up in 2006, a wide pallet of tools to diagnose, characterize, and control the experiment has been implemented, and some have been invented to solve specific problems. As a consequence the character of the antihydrogen formation experiments have changed. At first, simply producing antihydrogen inside the magnetostatic trap was a goal in itself, but recently we have been able to focus more specifically on choosing a favorable set of parameters. For positrons and antiprotons the temperature, plasma radius, and density can be controlled within a certain range, and the potential configuration can be tuned to avoid instabilities (Andresen *et al.*, 2009b) or to

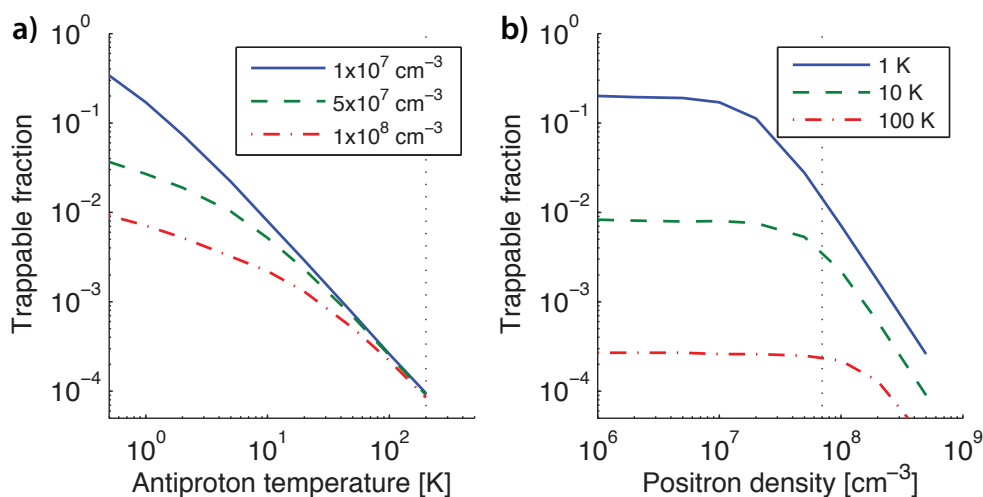


**Figure 9.1:** Fraction of antiprotons with a total kinetic energy below  $0.5 K \times k_B$  vs (a) temperature and (b) positron density. The kinetic energy is calculated by assuming a Boltzmann energy distribution of antiprotons evenly distributed in a positron plasma of radius 1 mm and constant density. The antiprotons rotate with the plasma around the trap axis and thus the rotation velocity adds to their kinetic energy. The vertical dotted lines indicate the temperature and density estimated for the trapping attempts described in chapter 8.

optimize survival of weakly bound atoms. Techniques such as evaporative cooling and radial compression of antiprotons expand the available range of temperatures and densities and thus allows optimization of the antihydrogen formation process.

It is a very difficult task to make an accurate theoretical estimate of the probability of trapping an antihydrogen atom given a certain set of experimental conditions. Estimates, such as that made in section 8.5, are most likely highly inaccurate, but, nevertheless, simple estimates can provide a guideline when designing a better experiment. For instance, it is well known that a cold, dense positron plasma will increase the antihydrogen formation rate and thus enhance antihydrogen production. However, simply increasing the positron density can have a negative effect on the number of atoms formed at very low energies. Due to its large mass, the kinetic energy of the antiproton dominates the kinetic energy of an antihydrogen atom formed from the antiproton. In a positron plasma the antiproton kinetic energy has two components: a thermal

---

component characterized by a temperature and a temperature independent component associated with the magnetron rotation of the plasma. Figure 9.1 shows the fraction of antiprotons with a kinetic energy below  $0.5 K \times k_B$  as a function of temperature or positron density. At low densities ( $10^6 \text{ cm}^{-3}$ ) the magnetron rotation velocity is small, and the thermal kinetic energy dominates, but for high densities ( $10^8 \text{ cm}^{-3}$ ), the effect of rotation is significant for temperatures below  $\sim 100 \text{ K}$ . On the figure, the temperature and density used in the trapping attempts described in chapter 8 is indicated. The positron density could be increased by a factor of 2 or 4 in these experiments, but doing so could easily reduce the trappable fraction of antihydrogen by an order of magnitude. On the other hand decreasing the temperature to  $10 \text{ K}$  would increase the trapping probability dramatically.

Including information about the antihydrogen distribution of atomic states may well change the conclusion of the above estimate, and more elaborate tools to predict the trapping probability certainly exist (Robicheaux, 2008). With the possibilities of diagnosing and tailoring antihydrogen formation and trapping experiments now available, these estimates can be used as a valuable guideline. Producing and trapping antihydrogen is certainly no easy feat, and being in a position where guidance can be put to practical use is big step forward.

*Bon voyage!*  
*Gorm Bruun Andresen,*  
*Aarhus, August 2010.*



# Modeling evaporative cooling - MatLab code

---

MatLab functions used to do the numerical calculations of chapter 6.

## A.1 The collision time constant $\tau_{col}$

The MatLab function below is an implementation of a calculation of the collisional time scale for a cloud of antiprotons of temperature  $T$  and density  $n$ , immersed in a magnetic field of magnitude  $B$ . A detailed description of the calculation can be found in section 4.4.

```

1  % Exact pbar collision time for antiprotons immersed in both
    strong and weak magnetic fields
2  % having both high and low temperatures.
3  % Based on the treatment in [Glinsky et al., 1992] and an
    internal ALPHA note by Joel Fajans (25/2-2009).
4  % Gorm B. Andresen, 2009.
5
6  function t=tau_col(T,B,n)
7
8  %% Constants.
9  eps0=8.854e-12; %Permittivity of free space in F/m.
10 kB=1.3806504e-23; %Boltzmann constant in J/K.
11 e=1.602e-19; %Electron charge in C.
12 m=1.6726e-27; %Proton mass in kg.
13
14 %% Define subfunctions.
```

```

15 %Coulomb Logarithm equivalent.
16 I_SmallB=@(kappa) -sqrt(2*pi)/15*log(kappa/3);
17
18 a=-0.085; bb=-0.017; c=-0.46; d=-1.544;
19 I_Transition=@(kappa) exp(a*log(kappa).^3+bb*log(kappa).^2+c*log(
    kappa)+d);
20
21 I_LargeB=@(kappa) exp(-5*(3*pi*kappa).^0.4/6).*...
22     (1.83./kappa.^(7/15)+20.9./kappa.^(11/15)+0.347./kappa.
23     ^ (13/15)+87.8./kappa.^(15/15)+6.68./kappa.^(17/15));
24 kappa_Small=0.5; kappa_Large=100;
25 I=@(kappa) (kappa<kappa_Small).*I_SmallB(kappa)+(kappa_Large<
26     kappa).*I_LargeB(kappa)+...
27     (kappa_Small<kappa).* (kappa<kappa_Large).*I_Transition(kappa)
28     ;
29
30 %Distance of closest approach:
31 b=@(T) 2*e^2./(4*pi*eps0*kB*T);
32
33 %Thermal velocity:
34 v=@(T) sqrt(2*kB*T/m);
35
36 %Cyclotron frequency:
37 omega_c=@(B) e*B/m;
38
39 %Larmor radius:
40 r_L=@(T,B) v(T)/omega_c(B);
41
42 %Exact Collision frequency (Joel):
43 f=@(T,B,n) n*b(T).^2.*v(T).*I(b(T)./r_L(T,B));
44
45 %% Return collision time (the factor sqrt(2)/5 is applied to
46     match the definition in [Hinton, 1983]):
47 t=sqrt(2)/5./f(T,B,n);

```

## A.2 Numerical calculation of forced evaporative cooling

MatLab function used to do the numerical calculation of forced evaporative cooling (see chapter 6).

```

1  %Numerical model of forced evaporative cooling of antiprotons.
2  %Gorm B. Andresen, 2010.
3  %=====
4  %
5  %Note: All parameters marked (vector) should be column vectors of
      equal length.
6  %
7  %Input parameters:
8  %-----
9  %t_ramp:    Time steps for V_ramp (vector) [s].
10 %V_ramp:    Applied on-axis well depth (vector) [V].
11 %N0:        Initial number [-].
12 %T0:        Initial temperature [K].
13 %R0:        Initial cloud radius [m].
14 %L0:        Initial cloud length [m].
15 %B:         Magnetic field [T].
16 %phi0:      Space charge per particle [V].
17 %heat:      Turns on/off the heating term alpha_heat (1/0).
18 %aperture:  Turns on/off the heating aperture effect (1/0).
19 %
20 %Output parameters:
21 %-----
22 %t:         Time steps for N and T (vector) [s]. Equals t_ramp.
23 %N:         Number remaining (vector) [-].
24 %T:         temperature (vector) [K].
25
26
27 function [t,N,T]=ThesisModel(t_ramp,V_ramp,N0,T0,R0,L0,B,phi0,
      heat,aperture)
28
29 options=odeset('RelTol',1e-8,'AbsTol',1e-8);
30 [t,H]=ode15s(@(t,h) diff_eq(t,h,t_ramp,V_ramp,R0,L0,B,N0,phi0,
      heat,aperture),t_ramp,[N0;T0],options);
31 N=H(:,1);
32 T=H(:,2);
33

```

```

34 function dNT=diff_eq(t,NT,t_ramp,V_ramp,R0,L0,B,N0,phi0,heat,
    aperture)
35 N=NT(1);
36 T=NT(2);
37
38 %Constants.
39 kB=1.3806504e-23; %Boltzmann constant [J/K].
40 e=1.602e-19; %Electron charge in [C]
41 eps0=8.854e-12; %Permittivity of free space [F/m].
42 Rw=22e-3; %Electrode wall radius [mm].
43 gamma=1e-4; %Annihilations per antiproton per second.
44
45
46 %Plasma dimensions:
47 R=R0*sqrt(N0./N);
48 L=L0*sqrt(N/N0);
49
50 %Plasma density:
51 n=1.4*3/2*N^1.5/(pi*R^2*L);
52
53 %On-axis well depth:
54 V0=interp1(t_ramp,V_ramp,t,'linear'); %Vacuum well depth [V].
55 phi=phi0*N; %Space charge potential (estimate) [V].
56 V=V0-phi;
57
58 %Evaporation from center, geometric factor (Debye length/R)^2:
59 lambdaD=sqrt(eps0*kB*T/e^2/n);
60 if aperture
61     f=min((lambdaD/R)^2,1);
62 else
63     f=1;
64 end
65
66 %Eta, lambda, alpha, and alpha_heat:
67 eta=V/(kB*T/e);
68 lambda=1/3*eta*exp(eta);
69 alpha=(eta+1)/(1/2+3/2)-1;
70 alpha_heat=heat*1/(3/2*kB*T)*e^2/(4*pi*eps0)*sqrt(N*N0)/(2*L0);
71
72 %Evaporation time:
73 t_ev=lambda*tau_col(T,B,n)/f;
74

```

```
75 %Differential equations: (First option saves computer fan-power.  
    Remove if low temperatures are required).  
76 if (T<=0.9) .* ( (N/N0)<8e-3)  
77     dT=0;  
78     dN=0;  
79 else  
80     dN=-N/t_ev-gamma*N;  
81     dT=-(alpha-alpha_heat)*T/t_ev;  
82 end  
83  
84 dNT=[dN;dT];
```



# Bibliography

- M. Amoretti, C. Amsler, G. Bonomi, A. Bouchta, P. Bowe, C. Carraro, C. L. Cesar, M. Charlton, M. J. T. Collier, M. Doser, V. Filippini, K. S. Fine, A. Fontana, M. C. Fujiwara, R. Funakoshi, P. Genova, J. S. Hangst, R. S. Hayano, M. H. Holzschneider, L. V. Jørgensen, V. Lagomarsino, R. Landua, D. Lindelöf, E. L. Rizzini, M. Macrí, N. Madsen, G. Manuzio, M. Marchesotti, P. Montagna, H. Pruys, C. Regenfus, P. Riedler, J. Rochet, A. Rotondi, G. Rouleau, G. Testera, A. Variola, T. L. Watson, and D. P. van der Werf. "Production and detection of cold antihydrogen atoms." *Nature*, **419** 456 (2002).
- M. Amoretti, C. Amsler, G. Bonomi, A. Bouchta, P. D. Bowe, C. Carraro, C. L. Cesar, M. Charlton, M. Doser, V. Filippini, A. Fontana, M. C. Fujiwara, R. Funakoshi, P. Genova, J. S. Hangst, R. S. Hayano, L. V. Jørgensen, V. Lagomarsino, R. Landua, D. Lindelöf, E. L. Rizzini, M. Macrí, N. Madsen, G. Manuzio, P. Montagna, H. Pruys, and C. Regenfus. "Positron Plasma Diagnostics and Temperature Control for Antihydrogen Production." *Phys. Rev. Lett.*, **91** 055001 (2003).
- M. Amoretti, C. Amsler, G. Bazzano, G. Bonomi, A. Bouchta, P. Bowe, C. Canali, C. Carraro, C. Cesar, M. Charlton, M. Doser, A. Fontana, M. Fujiwara, R. Funakoshi, P. Genova, J. Hangst, R. Hayano, I. Johnson, L. Jørgensen, A. Kellerbauer, V. Lagomarsino, R. Landua, E. L. Rizzini, M. Macrí, N. Madsen, G. Manuzio, M. Marchesotti, D. Mitchard, F. Ottone, H. Pruys, C. Regenfus, P. Riedler, A. Rotondi, G. Testera, A. Variola, L. Venturelli, Y. Yamazaki, D. van der Werf, and N. Zurlo. "Antihydrogen production temperature dependence." *Physics Letters B*, **583** 59 (2004a).
- M. Amoretti, C. Amsler, G. Bazzano, G. Bonomi, A. Bouchta, P. Bowe, C. Carraro, C. L. Cesar, M. Charlton, M. Doser, V. Filippini, A. Fontana, M. C. Fujiwara, R. Funakoshi, P. Genova, J. S. Hangst, R. S. Hayano, L. V. Jørgensen, V. Lagomarsino, R. Landua, D. Lindelöf, E. L. Rizzini, M. Macrí,

- N. Madsen, G. Manuzio, M. Marchesotti, P. Montagna, H. Pruys, C. Regenfus, P. Riedler, A. Rotondi, G. Rouleau, G. Testera, A. Variola, and D. P. van der Werf. "High rate production of antihydrogen." *Physics Letters B*, **578** 23 (2004b).
- M. Amoretti, C. Amsler, G. Bonomi, A. Bouchta, P. D. Bowe, C. Carraro, C. L. Cesar, M. Charlton, M. Doser, V. Filippini, A. Fontana, M. C. Fujiwara, R. Funakoshi, P. Genova, J. S. Hangst, R. S. Hayano, L. V. Jørgensen, A. Kellerbauer, V. Lagomarsino, R. Landua, D. Lindelöf, E. L. Rizzini, M. Macrí, N. Madsen, G. Manuzio, P. Montagna, H. Pruys, C. Regenfus, A. Rotondi, G. Testera, A. Variola, L. Venturelli, D. P. van der Werf, and Y. Yamazaki. "Dynamics of antiproton cooling in a positron plasma during antihydrogen formation." *Physics Letters B*, **590** 133 (2004c).
- M. Amoretti, C. Amsler, G. Bonomi, P. D. Bowe, C. Canali, C. Carraro, C. L. Cesar, M. Charlton, A. M. Ejsing, A. Fontana, M. C. Fujiwara, R. Funakoshi, P. Genova, J. S. Hangst, R. S. Hayano, L. V. Jørgensen, A. Kellerbauer, V. Lagomarsino, E. Lodi Rizzini, M. Macrì, N. Madsen, G. Manuzio, D. Mitchard, P. Montagna, L. G. C. Posada, H. Pruys, and C. Regenfus. "Search for Laser-Induced Formation of Antihydrogen Atoms." *Phys. Rev. Lett.*, **97** 213401 (2006).
- C. Amsler *et al.* "Review of Particle Physics." *Physics Letters B*, **667** 1 (2008).  
Review of Particle Physics.
- C. D. Anderson. "The Apparent Existence of Easily Deflectable Positives." *Science*, **76** 238 (1932).
- C. D. Anderson. "The Positive Electron." *Phys. Rev.*, **43** 491 (1933).
- M. H. Anderson, J. R. Ensher, M. R. Matthews, C. E. Wieman, and E. A. Cornell. "Observation of Bose-Einstein Condensation in a Dilute Atomic Vapor." *Science*, **269** 198 (1995).
- G. Andresen, W. Bertsche, A. Boston, P. D. Bowe, C. L. Cesar, S. Chapman, M. Charlton, M. Chartier, A. Deutsch, J. Fajans, M. C. Fujiwara, R. Funakoshi, D. R. Gill, K. Gomberoff, J. S. Hangst, R. S. Hayano, R. Hydromako, M. J. Jenkins, L. V. Jørgensen, L. Kurchaninov, N. Madsen, P. Nolan,

- K. Olchanski, A. Olin, A. Povilus, F. Robicheaux, and E. Sarid. "Antimatter Plasmas in a Multipole Trap for Antihydrogen." *Phys. Rev. Lett.*, **98** 023402 (2007).
- G. Andresen, W. Bertsche, P. Bowe, C. Bray, E. Butler, C. Cesar, S. Chapman, M. Charlton, J. Fajans, M. Fujiwara, D. Gill, J. Hangst, W. Hardy, R. Hayano, M. Hayden, A. Humphries, R. Hydomako, L. Jørgensen, S. Kerrigan, L. Kurchaninov, R. Lambo, N. Madsen, P. Nolan, K. Olchanski, A. Olin, A. Povilus, P. Pusa, F. Robicheaux, E. Sarid, S. S. E. Nasr, D. Silveira, J. Storey, R. Thompson, D. van der Werf, J. Wurtele, and Y. Yamazaki. "Antihydrogen formation dynamics in a multipolar neutral anti-atom trap." *Physics Letters B*, **685** 141 (2010a).
- G. B. Andresen, W. Bertsche, A. Boston, P. D. Bowe, C. L. Cesar, S. Chapman, M. Charlton, M. Chartier, A. Deutsch, J. Fajans, M. C. Fujiwara, R. Funakoshi, D. R. Gill, K. Gomberoff, J. S. Hangst, R. S. Hayano, R. Hydomako, M. J. Jenkins, L. V. Jørgensen, L. Kurchaninov, N. Madsen, P. Nolan, K. Olchanski, A. Olin, R. D. Page, A. Povilus, F. Robicheaux, E. Sarid, D. M. Silveira, J. W. Storey, R. I. Thompson, D. P. van der Werf, J. S. Wurtele, and Y. Yamazaki. "Production of antihydrogen at reduced magnetic field for anti-atom trapping." **41** 011001 (2008a).
- G. B. Andresen, W. Bertsche, P. D. Bowe, C. C. Bray, E. Butler, C. L. Cesar, S. Chapman, M. Charlton, J. Fajans, M. C. Fujiwara, R. Funakoshi, D. R. Gill, J. S. Hangst, W. N. Hardy, R. S. Hayano, M. E. Hayden, A. J. Humphries, R. Hydomako, M. J. Jenkins, L. V. Jørgensen, L. Kurchaninov, R. Lambo, N. Madsen, P. Nolan, K. Olchanski, A. Olin, R. D. Page, A. Povilus, P. Pusa, F. Robicheaux, E. Sarid, S. S. E. Nasr, D. M. Silveira, J. W. Storey, R. I. Thompson, D. P. van der Werf, J. S. Wurtele, and Y. Yamazaki. "A novel antiproton radial diagnostic based on octupole induced ballistic loss." *Phys. Plasmas*, **15** 032107 (2008b).
- G. B. Andresen, W. Bertsche, P. D. Bowe, C. C. Bray, E. Butler, C. L. Cesar, S. Chapman, M. Charlton, J. Fajans, M. C. Fujiwara, R. Funakoshi, D. R. Gill, J. S. Hangst, W. N. Hardy, R. S. Hayano, M. E. Hayden, R. Hydomako, M. J. Jenkins, L. V. Jørgensen, L. Kurchaninov, R. Lambo, N. Madsen, P. Nolan,

- K. Olchanski, A. Olin, A. Povilus, and P. Pusa. "Compression of Antiproton Clouds for Antihydrogen Trapping." *Phys. Rev. Lett.*, **100** 203401 (2008c).
- G. B. Andresen, W. Bertsche, P. D. Bowe, C. C. Bray, E. Butler, C. L. Cesar, S. Chapman, M. Charlton, J. Fajans, M. C. Fujiwara, D. R. Gill, J. S. Hangst, W. N. Hardy, R. S. Hayano, M. E. Hayden, A. J. Humphries, R. Hydromako, L. V. Jørgensen, S. J. Kerrigan, L. Kurchaninov, R. Lambo, N. Madsen, P. Nolan, K. Olchanski, A. Olin, A. P. Povilus, P. Pusa, E. Sarid, S. S. E. Nasr, D. M. Silveira, J. W. Storey, R. I. Thompson, D. P. van der Werf, and Y. Yamazaki. "Antiproton, positron, and electron imaging with a microchannel plate/phosphor detector." *Rev. Sci. Inst.*, **80** 123701 (2009a).
- G. B. Andresen, W. Bertsche, C. C. Bray, E. Butler, C. L. Cesar, S. Chapman, M. Charlton, J. Fajans, M. C. Fujiwara, D. R. Gill, W. N. Hardy, R. S. Hayano, M. E. Hayden, A. J. Humphries, R. Hydromako, L. V. Jørgensen, S. J. Kerrigan, J. Keller, L. Kurchaninov, R. Lambo, N. Madsen, P. Nolan, K. Olchanski, A. Olin, A. Povilus, P. Pusa, F. Robicheaux, E. Sarid, S. S. E. Nasr, D. M. Silveira, J. W. Storey, R. I. Thompson, D. P. van der Werf, J. S. Wurtele, and Y. Yamazaki. "Magnetic multipole induced zero-rotation frequency bounce-resonant loss in a Penning–Malmberg trap used for antihydrogen trapping." *Phys. Plasmas*, **16** 100702 (2009b).
- G. B. Andresen, M. D. Ashkezari, M. Baquero-Ruiz, W. Bertsche, P. D. Bowe, C. C. Bray, E. Butler, C. L. Cesar, S. Chapman, M. Charlton, J. Fajans, T. Friesen, M. C. Fujiwara, D. R. Gill, J. S. Hangst, W. N. Hardy, R. S. Hayano, M. E. Hayden, A. Humphries, R. Hydromako, S. Jonsell, L. Kurchaninov, R. Lambo, N. Madsen, S. Menary, P. Nolan, K. Olchanski, A. Olin, A. Povilus, P. Pusa, F. Robicheaux, E. Sarid, D. M. Silveira, C. So, C. H. Storry, R. I. Thompson, D. P. van der Werf, D. Wilding, J. S. Wurtele, and Y. Yamazaki. "Search for Trapped Antihydrogen: First Candidate Events." (2010b). *Manuscript in preparation*.
- G. B. Andresen, M. D. Ashkezari, M. Baquero-Ruiz, W. Bertsche, P. D. Bowe, E. Butler, C. L. Cesar, S. Chapman, M. Charlton, J. Fajans, T. Friesen, M. C. Fujiwara, D. R. Gill, J. S. Hangst, W. N. Hardy, R. S. Hayano, M. E. Hayden, A. Humphries, R. Hydromako, S. Jonsell, L. Kurchaninov, R. Lambo, N. Madsen, S. Menary, P. Nolan, K. Olchanski, and A. Olin. "Evaporative

- Cooling of Antiprotons to Cryogenic Temperatures." *Phys. Rev. Lett.*, **105** 013003 (2010c).
- I. Barth, L. Friedland, E. Sarid, and A. G. Shagalov. "Autoresonant Transition in the Presence of Noise and Self-Fields." *Phys. Rev. Lett.*, **103** 155001 (2009).
- G. Baur, G. Boero, A. Brauksiepe, A. Buzzo, W. Eyrich, R. Geyer, D. Grzonka, J. Hauffe, K. Kilian, M. LoVetere, M. Macrí, M. Moosburger, R. Nellen, W. Oelert, S. Passaggio, A. Pozzo, K. Röhrich, K. Sachs, G. Schepers, T. Seifzick, R. S. Simon, R. Stratmann, F. Stinzinger, and M. Wolke. "Production of antihydrogen." *Physics Letters B*, **368** 251 (1996).
- B. Beck. Ph.D. thesis, University of California, San Diego (1990).
- W. Bertsche, A. Boston, P. D. Bowe, C. L. Cesar, S. Chapman, M. Charlton, M. Chartier, A. Deutsch, J. Fajans, M. C. Fujiwara, R. Funakoshi, K. Gomboroff, J. S. Hangst, R. S. Hayano, M. J. Jenkins, L. V. Jørgensen, P. Ko, N. Madsen, P. Nolan, R. D. Page, L. G. C. Posada, A. Povilus, E. Sarid, D. M. Silveira, D. P. van der Werf, Y. Yamazaki, B. Parker, J. Escallier, and A. Ghosh. "A magnetic trap for antihydrogen confinement." *Nucl. Instrum. Methods Phys. Res., Sect. A*, **566** 746 (2006).
- B. Bransden. *Physics of Atoms and Molecules* (Prentice Hall, Englewood Cliffs, 2003). ISBN 058235692x.
- C. Cesar, G. Andresen, W. Bertsche, P. Bowe, C. Bray, E. Butler, S. Chapman, M. Charlton, J. Fajans, M. Fujiwara, R. Funakoshi, D. Gill, J. Hangst, W. Hardy, R. Hayano, M. Hayden, A. Humphries, R. Hydomako, M. Jenkins, L. Jørgensen, L. Kurchaninov, R. Lambo, N. Madsen, P. Nolan, K. Olchanski, A. Olin, R. D. Page, A. Povilus, P. Pusa, F. Robicheaux, E. Sarid, S. Seif El Nasr, D. Silveira, J. Storey, R. Thompson, D. van der Werf, J. Wurtele, and Y. Yamazaki. "Antihydrogen physics at ALPHA/CERN." *Can. J. Phys.*, **87** 791 (2009).
- C. L. Cesar, D. G. Fried, T. C. Killian, A. D. Polcyn, J. C. Sandberg, I. A. Yu, T. J. Greytak, D. Kleppner, and J. M. Doyle. "Two-Photon Spectroscopy of Trapped Atomic Hydrogen." *Phys. Rev. Lett.*, **77** 255 (1996).

- M. Charlton. "Antihydrogen production in collisions of antiprotons with excited states of positronium." *Phys. Lett. A*, **143** 143 (1990).
- F. Chen. *Introduction to Plasma Physics* (Plenum Press, New York, 1974). ISBN 0306307553.
- R. Davidson. *Physics of Nonneutral Plasmas* (World Scientific Publishing Company, City, 2001). ISBN 1860943020.
- P. A. M. Dirac. "The Quantum Theory of the Electron." *Proceedings of the Royal Society of London. Series A, Containing Papers of a Mathematical and Physical Character*, **117** 610 (1928).
- P. A. M. Dirac. "Quantised Singularities in the Electromagnetic Field." *Proceedings of the Royal Society of London. Series A*, **133** 60 (1931).
- C. F. Driscoll, F. Andereg, D. H. E. Dubin, D.-Z. Jin, J. M. Kriesel, E. M. Hollmann, and T. M. O'Neil. "Shear reduction of collisional transport: Experiments and theory." volume 9, pages 1905–1914 (AIP, 2002).
- G. Y. Drobychev, P. Nédélec, D. Sillou, G. Gribakin, H. Walters, G. Ferrari, M. Prevedelli, G. M. Tino, M. Doser, C. Canali, C. Carraro, V. Lagomarsino, G. Manuzio, G. Testera, S. Zavatarelli, M. Amoretti, A. G. Kellerbauer, J. Meier, U. Warring, M. K. Oberthaler, I. Boscolo, F. Castelli, S. Cialdi, L. Formaro, A. Gervasini, G. Giammarchi, A. Vairo, G. Consolati, A. Dupasquier, F. Quasso, H. H. Stroke, A. S. Belov, S. N. Gninenko, V. A. Matveev, V. M. Byakov, S. V. Stepanov, D. S. Zvezhinskij, M. De Combarieu, P. Forget, P. Pari, L. Cabaret, D. Comparat, G. Bonomi, A. Rotondi, N. Djourelou, M. Jacquy, M. Büchner, G. Tréneq, J. Vigué, R. S. Brusa, S. Mariazzi, S. Hogan, F. Merkt, A. Badertscher, P. Crivelli, U. Gendotti, and A. Rubbia. "Proposal for the AEGIS experiment at the CERN antiproton decelerator (Antimatter Experiment: Gravity, Interferometry, Spectroscopy)." Technical Report SPSC-P-334. CERN-SPSC-2007-017, CERN, Geneva (2007).
- D. H. E. Dubin. "Collisional transport in non-neutral plasmas." volume 5, pages 1688–1694 (AIP, 1998).
- D. H. E. Dubin and T. M. O'Neil. "Trapped nonneutral plasmas, liquids, and crystals (the thermal equilibrium states)." *Rev. Mod. Phys.*, **71** 87 (1999).

- D. L. Eggleston, C. F. Driscoll, B. R. Beck, A. W. Hyatt, and J. H. Malmberg. "Parallel energy analyzer for pure electron plasma devices." *Phys. Fluids B: Plasma Phys.*, **4** 3432 (1992).
- J. Fajans and A. Schmidt. "Malmberg-Penning and Minimum-B trap compatibility: the advantages of higher-order multipole traps." *Nuclear Instruments and Methods in Physics Research Section A: Accelerators, Spectrometers, Detectors and Associated Equipment*, **521** 318 (2004).
- J. Fajans, E. Gilson, and L. Friedland. "Autoresonant (Nonstationary) Excitation of the Diocotron Mode in Non-neutral Plasmas." *Phys. Rev. Lett.*, **82** 4444 (1999).
- J. Fajans, W. Bertsche, K. Burke, S. F. Chapman, and D. P. van der Werf. "Effects of Extreme Magnetic Quadrupole Fields on Penning Traps and the Consequences for Antihydrogen Trapping." *Phys. Rev. Lett.*, **95** 155001 (2005).
- J. Fajans, N. Madsen, and F. Robicheaux. "Critical loss radius in a Penning trap subject to multipole fields." *Physics of Plasmas*, **15** 032108 (2008).
- C. Foot. *Atomic Physics* (Oxford University Press, Oxford Oxfordshire, 2005). ISBN 0198506961.
- M. C. Fujiwara. "Detecting Antihydrogen: The Challenges and the Applications." volume 793, pages 111–121 (AIP, 2005).
- M. C. Fujiwara, M. Amoretti, G. Bonomi, A. Bouchta, P. D. Bowe, C. Carraro, C. L. Cesar, M. Charlton, M. Doser, V. Filippini, A. Fontana, R. Funakoshi, P. Genova, J. S. Hangst, R. S. Hayano, L. V. Jørgensen, V. Lagomarsino, R. Landua, E. Lodi-Rizzini, M. Marchesotti, M. Macrí, N. Madsen, G. Manuzio, P. Montagna, P. Riedler, A. Rotondi, and G. Rouleau. "Three-Dimensional Annihilation Imaging of Trapped Antiprotons." *Phys. Rev. Lett.*, **92** 065005 (2004).
- M. C. Fujiwara, M. Amoretti, C. Amsler, G. Bonomi, A. Bouchta, P. D. Bowe, C. Canali, C. Carraro, C. L. Cesar, M. Charlton, M. Doser, A. Fontana, R. Funakoshi, P. Genova, J. S. Hangst, R. S. Hayano, L. V. Jørgensen, A. Kellerbauer, V. Lagomarsino, R. Landua, E. Lodi-Rizzini, M. Macrí, N. Madsen,

- G. Manuzio, D. Mitchard, P. Montagna, and H. Pruys. "Temporally Controlled Modulation of Antihydrogen Production and the Temperature Scaling of Antiproton-Positron Recombination." *Phys. Rev. Lett.*, **101** 053401 (2008).
- R. Funakoshi, M. Amoretti, G. Bonomi, P. D. Bowe, C. Canali, C. Carraro, C. L. Cesar, M. Charlton, M. Doser, A. Fontana, M. C. Fujiwara, P. Genova, J. S. Hangst, R. S. Hayano, L. V. Jørgensen, A. Kellerbauer, V. Lagomarsino, R. Landua, E. Lodi Rizzini, M. Macrì, N. Madsen, G. Manuzio, D. Mitchard, P. Montagna, L. G. C. Posada, A. Rotondi, and G. Testera. "Positron plasma control techniques for the production of cold antihydrogen." *Phys. Rev. A*, **76** 012713 (2007).
- G. Fussmann, C. Biedermann, and R. Radtke. "Advanced Technologies Based on Wave and Beam Generated Plasmas." In "Proceedings Summer School, Sozopol 1998," page 429 (Kluwer Academic Publishers, Netherlands, 1999).
- G. Gabrielse. "Extremely Cold Antiprotons." *Scientific American*, **267** 78 (1992).
- G. Gabrielse. "Atoms made entirely of antimatter: Two methods produce slow antihydrogen." volume 50 of *Advances In Atomic, Molecular, and Optical Physics*, pages 155 – 217 (Academic Press, 2005).
- G. Gabrielse, X. Fei, K. Helmerson, S. L. Rolston, R. Tjoelker, T. A. Trainor, H. Kalinowsky, J. Haas, and W. Kells. "First Capture of Antiprotons in a Penning Trap: A Kiloelectronvolt Source." *Phys. Rev. Lett.*, **57** 2504 (1986).
- G. Gabrielse, S. L. Rolston, L. Haarsma, and W. Kells. "Antihydrogen production using trapped plasmas." *Physics Letters A*, **129** 38 (1988).
- G. Gabrielse, X. Fei, L. A. Orozco, R. L. Tjoelker, J. Haas, H. Kalinowsky, T. A. Trainor, and W. Kells. "Cooling and slowing of trapped antiprotons below 100 meV." *Phys. Rev. Lett.*, **63** 1360 (1989).
- G. Gabrielse, J. Estrada, J. N. Tan, P. Yesley, N. S. Bowden, P. Oxley, T. Roach, C. H. Storry, M. Wessels, J. Tan, D. Grzonka, W. Oelert, G. Schepers, T. Seifzick, W. H. Breunlich, M. Cargnelli, H. Fuhrmann, R. King, R. Ursin, J. Zmeskal, H. Kalinowsky, C. Wesdorp, J. Walz, K. S. E. Eikema, and T. W.

- Hänsch. "First positron cooling of antiprotons." *Physics Letters B*, **507** 1 (2001).
- G. Gabrielse, N. S. Bowden, P. Oxley, A. Speck, C. H. Storry, J. N. Tan, M. Wes-sels, D. Grzonka, W. Oelert, G. Schepers, T. Sefzick, J. Walz, H. Pittner, T. W. Hänsch, and E. A. Hessels. "Background-Free Observation of Cold Anti-hydrogen with Field-Ionization Analysis of Its States." *Phys. Rev. Lett.*, **89** 213401 (2002a).
- G. Gabrielse, N. S. Bowden, P. Oxley, A. Speck, C. H. Storry, J. N. Tan, M. Wes-sels, D. Grzonka, W. Oelert, G. Schepers, T. Sefzick, J. Walz, H. Pittner, T. W. Hänsch, and E. A. Hessels. "Driven Production of Cold Antihydrogen and the First Measured Distribution of Antihydrogen States." *Phys. Rev. Lett.*, **89** 233401 (2002b).
- G. Gabrielse, N. S. Bowden, P. Oxley, A. Speck, C. H. Storry, J. N. Tan, M. Wes-sels, D. Grzonka, W. Oelert, G. Schepers, T. Sefzick, J. Walz, H. Pittner, T. W. Hänsch, and E. A. Hessels. "Stacking of cold antiprotons." *Physics Letters B*, **548** 140 (2002c).
- G. Gabrielse, A. Speck, C. H. Storry, D. LeSage, N. Guise, D. Grzonka, W. Oel-ert, G. Schepers, T. Sefzick, H. Pittner, J. Walz, T. W. Hänsch, D. Comeau, and E. A. Hessels. "First Measurement of the Velocity of Slow Antihydro-gen Atoms." *Phys. Rev. Lett.*, **93** 073401 (2004).
- G. Gabrielse, P. Larochele, D. Le Sage, B. Levitt, W. S. Kolthammer, I. Kul-janishvili, R. McConnell, J. Wrubel, F. M. Esser, H. Glückler, D. Grzonka, G. Hansen, S. Martin, W. Oelert, J. Schillings, M. Schmitt, T. Sefzick, H. Solt-ner, Z. Zhang, D. Comeau, M. C. George, E. A. Hessels, C. H. Storry, M. Weel, A. Speck, F. Nillius, and J. Walz. "Antiproton Confinement in a Penning-Ioffe Trap for Antihydrogen." *Phys. Rev. Lett.*, **98** 113002 (2007).
- G. Gabrielse, P. Larochele, D. Le Sage, B. Levitt, W. S. Kolthammer, R. Mc-Connell, P. Richerme, J. Wrubel, A. Speck, M. C. George, D. Grzonka, W. Oelert, T. Sefzick, Z. Zhang, A. Carew, D. Comeau, E. A. Hessels, C. H. Storry, M. Weel, and J. Walz. "Antihydrogen Production within a Penning-Ioffe Trap." *Phys. Rev. Lett.*, **100** 113001 (2008).

- M. E. Glinsky and T. M. O'Neil. "Guiding center atoms: Three-body recombination in a strongly magnetized plasma." *Physics of Fluids B: Plasma Physics*, **3** 1279 (1991).
- M. E. Glinsky, T. M. O'Neil, M. N. Rosenbluth, K. Tsuruta, and S. Ichimaru. "Collisional equipartition rate for a magnetized pure electron plasma." *Phys. Fluids B: Plasma Phys.*, **4** 1156 (1992).
- T. W. Hänsch. "Nobel Lecture: Passion for precision." *Rev. Mod. Phys.*, **78** 1297 (2006).
- H. F. Hess. "Evaporative cooling of magnetically trapped and compressed spin-polarized hydrogen." *Phys. Rev. B*, **34** 3476 (1986).
- F. Hinton. *Basic Plasma Physics I*, chapter 1.5 Collisional transport in plasma (North-Holland Publishing Company, Amsterdam, 1983). ISBN 044486427x.
- M. H. Holzscheiter, M. Charlton, and M. M. Nieto. "The route to ultra-low energy antihydrogen." *Physics Reports*, **402** 1 (2004).
- M. Hori, J. Eades, R. S. Hayano, W. Pirkl, E. Widmann, H. Yamaguchi, H. A. Torii, B. Juhász, D. Horváth, K. Suzuki, and T. Yamazaki. "Observation of Cold, Long-Lived Antiprotonic Helium Ions." *Phys. Rev. Lett.*, **94** 063401 (2005).
- J. D. Huba. "NRL Plasma Formulary." Washington, DC 20375 (2009).
- J. L. Hurt, P. T. Carpenter, C. L. Taylor, and F. Robicheaux. "Positron and electron collisions with anti-protons in strong magnetic fields." *Journal of Physics B: Atomic, Molecular and Optical Physics*, **41** 165206 (2008).
- M. J. Jenkins. *Development of an Antihydrogen Trapping Apparatus*. Ph.D. thesis, School of Physical Sciences, Swansea University (2008).
- L. V. Jørgensen, M. Amoretti, G. Bonomi, P. D. Bowe, C. Canali, C. Carraro, C. L. Cesar, M. Charlton, M. Doser, A. Fontana, M. C. Fujiwara, R. Funakoshi, P. Genova, J. S. Hangst, R. S. Hayano, A. Kellerbauer, V. Lagonarsino, R. Landua, E. Lodi Rizzini, M. Macrí, N. Madsen, D. Mitchard,

- P. Montagna, A. Rotondi, G. Testera, A. Variola, and L. Venturelli. "New Source of Dense, Cryogenic Positron Plasmas." *Phys. Rev. Lett.*, **95** 025002 (2005).
- M. Kasevich and S. Chu. "Measurement of the gravitational acceleration of an atom with a light-pulse atom interferometer." *Applied Physics B: Lasers and Optics*, **54** 321 (1992).
- W. Ketterle and N. Van Druten. "Evaporative cooling of trapped atoms." *Adv. At. Mol. Opt. Phys.*, **37** 181 (1996).
- T. Kinugawa, F. J. Currell, and S. Ohtani. "Pulsed Evaporative Cooling of Ion Cloud in an Electron Beam Ion Trap." *Phys. Scripta*, **63** 102 (2001).
- N. Kuroda, H. A. Torii, M. Shibata, Y. Nagata, D. Barna, M. Hori, D. Horváth, A. Mohri, J. Eades, K. Komaki, and Y. Yamazaki. "Radial Compression of an Antiproton Cloud for Production of Intense Antiproton Beams." *Phys. Rev. Lett.*, **100** 203402 (2008).
- D. J. Larson, J. C. Bergquist, J. J. Bollinger, W. M. Itano, and D. J. Wineland. "Sympathetic cooling of trapped ions: A laser-cooled two-species nonneutral ion plasma." *Phys. Rev. Lett.*, **57** 70 (1986).
- N. Madsen, M. Amoretti, C. Amsler, G. Bonomi, P. D. Bowe, C. Carraro, C. L. Cesar, M. Charlton, M. Doser, A. Fontana, M. C. Fujiwara, R. Funakoshi, P. Genova, J. S. Hangst, R. S. Hayano, L. V. Jørgensen, A. Kellerbauer, V. Lagomarsino, R. Landua, E. Lodi-Rizzini, M. Macrí, D. Mitchard, P. Montagna, H. Pruys, C. Regenfus, A. Rotondi, and G. Testera. "Spatial Distribution of Cold Antihydrogen Formation." *Phys. Rev. Lett.*, **94** 033403 (2005).
- P. Mansbach and J. Keck. "Monte Carlo Trajectory Calculations of Atomic Excitation and Ionization by Thermal Electrons." *Phys. Rev.*, **181** 275 (1969).
- S. Maury. "The Antiproton Decelerator: AD." *Hyperfine Interact.*, **109** 43 (1997).
- E. M. McMillan. "The Synchrotron—A Proposed High Energy Particle Accelerator." *Phys. Rev.*, **68** 143 (1945).
- T. J. Murphy and C. M. Surko. "Positron trapping in an electrostatic well by inelastic collisions with nitrogen molecules." *Phys. Rev. A*, **46** 5696 (1992).

- M. M. Nieto and T. Goldman. "The arguments against "antigravity" and the gravitational acceleration of antimatter." *Physics Reports*, **205** 221 (1991).
- T. M. O'Neil. "A confinement theorem for nonneutral plasmas." *Phys. Fluids*, **23** 2216 (1980).
- C. A. Ordonez and D. L. Weathers. "Two-species mixing in a nested Penning trap for antihydrogen trapping." *Physics of Plasmas*, **15** 083504 (2008).
- A. J. Peurrung, J. Notte, and J. Fajans. "Observation of the ion resonance instability." *Phys. Rev. Lett.*, **70** 295 (1993).
- T. J. Phillips. "Antimatter gravity studies with interferometry." *Hyperfine Interactions*, **109** 357 (1997).
- S. A. Prasad and T. M. O'Neil. "Finite length thermal equilibria of a pure electron plasma column." *Physics of Fluids*, **22** 278 (1979).
- D. E. Pritchard. "Cooling Neutral Atoms in a Magnetic Trap for Precision Spectroscopy." *Phys. Rev. Lett.*, **51** 1336 (1983).
- F. Robicheaux. "Simulations of antihydrogen formation." *Phys. Rev. A*, **70** 022510 (2004).
- F. Robicheaux. "Three-body recombination for electrons in a strong magnetic field: Magnetic moment." *Phys. Rev. A*, **73** 033401 (2006).
- F. Robicheaux. "Atomic processes in antihydrogen experiments: a theoretical and computational perspective." *Journal of Physics B: Atomic, Molecular and Optical Physics*, **41** 192001 (2008).
- S. Schlamminger, K.-Y. Choi, T. A. Wagner, J. H. Gundlach, and E. G. Adelberger. "Test of the Equivalence Principle Using a Rotating Torsion Balance." *Phys. Rev. Lett.*, **100** 041101 (2008).
- T. M. Squires, P. Yesley, and G. Gabrielse. "Stability of a Charged Particle in a Combined Penning-Ioffe Trap." *Phys. Rev. Lett.*, **86** 5266 (2001).
- C. H. Storry, A. Speck, D. L. Sage, N. Guise, G. Gabrielse, D. Grzonka, W. Oelert, G. Schepers, T. Sefzick, H. Pittner, M. Herrmann, J. Walz, T. W. Hänsch,

- D. Comeau, and E. A. Hessels. "First Laser-Controlled Antihydrogen Production." *Phys. Rev. Lett.*, **93** 263401 (2004).
- C. L. Taylor, J. Zhang, and F. Robicheaux. "Cooling of Rydberg  $\bar{\text{H}}$  during radiative cascade." *Journal of Physics B: Atomic, Molecular and Optical Physics*, **39** 4945 (2006).
- T. Topçu and F. Robicheaux. "Radiative cascade of highly excited hydrogen atoms in strong magnetic fields." *Phys. Rev. A*, **73** 043405 (2006).
- W.-M. Yao *et al.* "Particle Physics Booklet." (2006).